Spring 5-14-2022

Examination of Ionization in Cesium Diode Pumped Alkali Lasers with an Ion Chamber Diagnostic

Benjamin Oliker
University of New Mexico

Benjamin Oliker
Candidate

Optical Science and Engineering
Department

This dissertation is approved, and it is acceptable in quality and form for publication:
Approved by the Dissertation Committee:

Dr. Wolfgang Rudolph Chairperson

Dr. Timothy Madden

Dr. Greg Pitz

Dr. Paul Schwoebel

Dr. Payman Zarkesh-Ha

Examination of Ionization in Cesium Diode Pumped Alkali Lasers with an Ion Chamber Diagnostic

by

Benjamin Oliker

B.S., Physics, University of Texas, 2006
M.S., Optical Science and Engineering, University of New Mexico, 2012

DISSERTATION

Submitted in Partial Fulfillment of the
Requirements for the Degree of

Doctor of Philosophy
Optical Science and Engineering

The University of New Mexico

Albuquerque, New Mexico

May, 2022

Dedication

To my wife Evangeline

Acknowledgments

I would like to thank the Directed Energy Professional Society (DEPS), the Air Force Research Laboratory (AFRL), and Ball Aerospace for financial support of my graduate education and research. I would like to thank AFRL for the use of laboratory space and equipment.

I have complete gratitude for my advisor Wolfgang Rudolph. He always knew when I attempted to draw conclusions with partial understanding, and he never let me settle for an incomplete answer. By holding high expectations until I rose to meet them, he has given me confidence in my scientific ability.

I give great thanks to my mentors at AFRL, Greg Pitz, Tony Hostutler, and Timothy Madden. Your guidance and friendship have helped me build a fulfilling career. I could not have had success in the laboratory without Eric Guild and Donald Stalnaker, and I could not have had success building theory and simulation without Hal Cambier. Thank you all.

I would like to thank my parents, Michael and Valerie. My dad passed along to me his love of science and at least part of his innate creativity. My mom has always had unwavering belief in me, even when the choices I made were less than perfect.

And most importantly, I would like to thank my wife, Evangeline, and my four daughters, Hannah, Lilly, Gracie, and Charlotte. You have all been patient and encouraging with my late nights and slow progress. Eva, I am in awe of everything we have accomplished since I started this degree. I think we can relax for the first time since our honeymoon. Thank you for all the happiness and love in my life. Girls, you have my permission to be whatever type of scientist you want to be when you grow up! (Or anything else that truly makes you happy.)

Examination of Ionization in Cesium Diode Pumped Alkali Lasers with an Ion Chamber Diagnostic

by

Benjamin Oliker

B.S., Physics, University of Texas, 2006
M.S., Optical Science and Engineering, University of New Mexico, 2012

Ph.D., Optical Science and Engineering, University of New Mexico, 2022

Abstract

Diode pumped alkali lasers (DPALs) are leading candidates for future high power applications, with many potential utilities for the military, aerospace, communications, and scientific diagnostics. A critical step in their development is measurement and understanding of unwanted ionization processes that occur inside the laser, which decrease efficiency, reduce the usable alkali population, and increase the heat load. In this dissertation, direct measurement of the ionization rate of a cesium DPAL gain medium are made for the first time, via application of an ion chamber diagnostic. Measured ionization rates are compared against the predictions of a computer simulation of the multi-step ionization mechanism, developed using processes described in the open literature. Comparisons are made across the following parameter ranges: pump powers from 0.1 - 1.2 W, intensities of 8 - 100 W/cm^2, cesium densities of 0.3 -

2×10^{12} cm^{-3}, pressures of 750 - 810 torr, temperatures of 45 - 70 °C, and either pure helium or a 6:1 mixture of helium and methane (14% methane). The simulation is demonstrated to accurately predict the low level of ionization to within an order-of-magnitude. The rate of ionization is shown to be slow compared to pump absorption, with a maximum of less than one ionization event for every one million pump photons absorbed (<1 ppm). Simultaneous fluorescence and ion chamber measurements indicate that a collisional neutral-particle process that populates highly-excited Rydberg energy states, such as secondary energy pooling, warrants further investigation. For example, fluorescence measurements will be shown to have minimal impact due to application of 300 V on the electrodes (sufficient to cause current saturation), indicating that Rydberg states are populated via a neutral particle process, rather than via electron / ion recombination, as has been previously suggested.

Ion chambers will be shown to be effective diagnostics for DPAL ionization rate measurement. Plasma production rates in the experiment were orders-of-magnitude above typical conditions, so additional research was done to ensure the accuracy of the diagnostic in this high plasma density regime. Standard ion chamber operation is at plasma densities sufficiently low that space-charge effects are negligible. However, at high density, it will be shown that the following processes occur: (1) space-charge limited ion drift, (2) Debye shielding preventing the electric field from penetrating a bulk plasma region, and (3) ambipolar diffusion across the bulk with possibly elevated electron temperature. This will be demonstrated through development of a numerical simulation of the ion chamber governing equations, known as the Thomson model, and validating it against test results with varying cesium density and beam position between the electrodes. Through test and simulation, it will be shown that although a variety of processes occur only in a high density ion chamber, none of these processes prevent accurate measurement of ionization rate under DPAL conditions.

Contents

Glossary

ϵ	Electrical permittivity
e	Elementary charge
k	Boltzmann constant
I	Planck's constant
h	Current
J	Current density
I_{sat}	Saturation current
V_{sat}	Saturation voltage
V_a	Applied voltage at the electrodes of an ion chamber
d	Electrode spacing
A_p	Cross-sectional area of the plasma along the axis between the electrodes
Q	Ionization Rate
$Q(x)$	Spatially varying ionization rate in the axis between the electrodes
$n(x)_{i/e}$	Spatially varying ion / electron density

$E(x)$	Spatially varying electric field
$\mu_{i/e}$	Ion / electron mobilities
$D_{i/e}$	Ion / electron diffusion constants
C_R	Ion / electron bimolecular recombination rate
n_{min}	Minimum plasma density that is in the high density regime
V_{min}	Minimum voltage to overcome space-charge effects
I_{tot}	Total current
I_s	Ion chamber signal current without background leakage current
R_1	Resistor between the biased electrode and the power supply
R_2	Resistor between the second electrode and ground
R_{leak}	Effective resistance associated with leakage current
C_1	Capacitance of the electrodes
C_2	Capacitance from the biased electrode to the grounded ion chamber walls
C_3	Capacitance from the second electrode to the grounded ion chamber walls
R_{L2}	Effective resistance associated with transient leakage current
C_L	Effective capacitance associated with transient leakage current
α	Relaxation parameter
s	Sum of the radii of two collision partners
ΔE_{hfs}	Hyperfine splitting between total angular momentum F components

S_{ab}	Transition strength factor from state b to a
γ_a	Pressure broadening due to collisions with particle a
δ_a	Pressure shifting due to collisions with particle a
τ_{ab}	Fluorescent lifetime for transition from state b to a
σ_{so}	Spin-orbit mixing collision cross-section
σ_q	Quenching collision cross-section
σ_{ep}	Energy pooling collision cross-section
σ_{pen}	Penning ionization collision cross-section
σ_{photo}	Photoionization cross-section
σ_{SO}	Spin-orbit mixing collision cross-section

Chapter 1

Introduction

1.1 Diode Pumped Alkali Lasers

A high energy laser (HEL) capable of transmitting a beam great distances while maintaining power density has broad applications for the military, aerospace, communications, and scientific diagnostics. Generating such a beam in a system that is also efficient, reliable, compact, and has an acceptable cost, is not easy. Most HEL research can be put into one of two categories: (1) gas phase lasers, such as gas dynamic CO_2, hydrogen floride, and the chemical oxygen iodine laser (COIL), or (2) solid state lasers, such as Nd:YAG rod lasers and Yb:silica fiber amplifiers. However, a leading candidate in the development of system with a good balance of size, weight, and power (SWaP) is a hybrid between both categories, the diode pumped alkali laser (DPAL). This laser system was invented in 2003 [1], and it is the first gas / solid-state hybrid to be heavily researched. It combines the advantages of a solid state system, including a convenient electrical energy source, efficient and reliable diode optical pumping, and a simple and robust lasing scheme, with the benefits of a gas phase system, mainly power scalability due to rapid heat removal by flowing of the gain medium. A DPAL also has shorter output wavelengths than most other

HELs (which happen to coincide with atmospheric transmission windows) and high quantum efficiency; a cesium DPAL outputs 894.6 nm light with a 4.7% quantum defect, a rubidium DPAL outputs 795.0 nm light with a 1.9% quantum defect, and a potassium DPAL outputs 770.1 nm light with a 0.44% quantum defect. Currently, the highest power demonstration of a DPAL was in a flowing potassium system with 1.5 kW output and an optical-to-optical efficiency of 48%. [2] (Optical-to-optical efficiency is the output laser power divided by the incident pump power.)

A DPAL is a hybrid laser since it combines a gas phase gain medium and solid state diode pumping. A simplified diagram of a DPAL system is shown on the right side of Fig. 1.1. Fresh gas (an alkali and buffer gas mixture) flows into the gain medium, where it is excited by many small diode optical pump lasers (tuned to the D_2 spectral line, 852.3 nm for cesium). Next, that energy is converted to a slightly longer wavelength (along the D_1 spectral line, 894.6 nm for cesium), and extracted as efficiently as possible as a single laser beam with optimum beam quality. Excess heat from the lasing process rapidly flows out of the beam, which is essential to maintaining beam quality. Excitation of the DPAL output beam is done in the typical laser manner; absorption of sufficient pump light results in a population inversion between an excited state in the alkali gas and the ground state, which causes the gas to become an optical amplifier (via stimulated emission), called a gain medium. The gain medium is wrapped by a resonator, which is shown in the diagram as two mirrors. The resonator traps a small amount of fluorescence from the gain medium, then repetitively reflects that light back, amplifying the signal on each pass until it saturates to a steady-state. The resonator in the diagram has a high reflectivity (HR) mirror and an output coupler (OC), which is a partially reflecting mirror that emits a fraction of the beam as an output, and another fraction as feedback to the gain medium. Steady-state output is reached when the amplification the laser beam receives in a round-trip through the resonator equals optical loss, the main loss being the output beam. The diagram shows the resonator as a two-mirror linear resonator,

but other more complex optical systems, such as ring resonators, are possible as well. The most common resonator type for a high power laser with good beam quality is an unstable resonator, which typically use a graded reflectivity mirror as an output coupler. (An unstable resonator is used since it can maintain single mode operation with a wide beam diameter in the gain medium. [3]) Also, the diode pumps are shown in the diagram arranged orthogonal to the output beam, but other geometries are common as well, such as end-pumping.

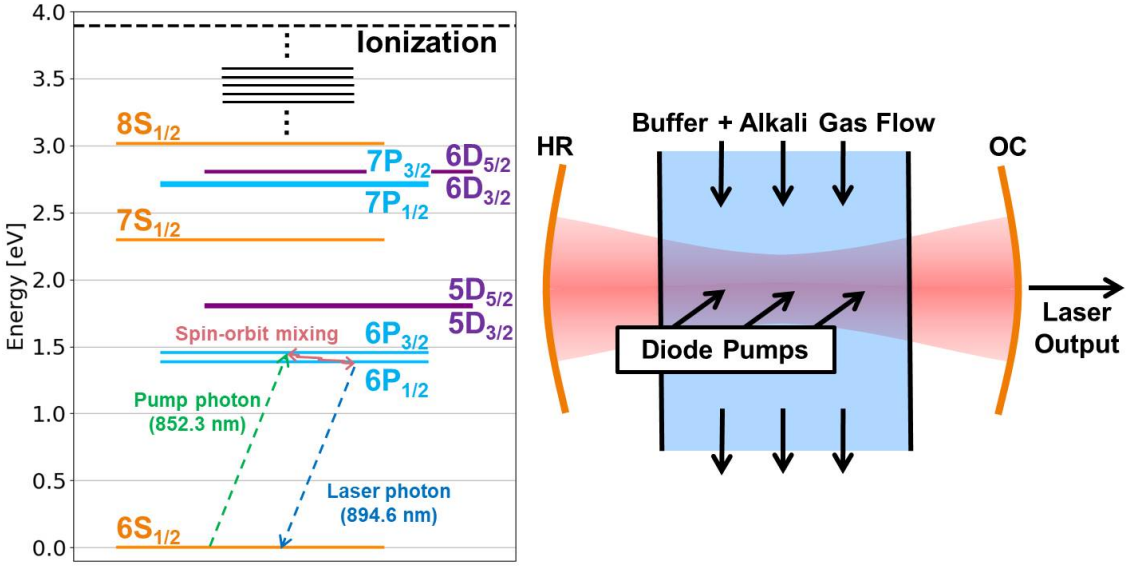

Figure 1.1: Overview of the physics and geometry of DPAL. [Left] Energy-state diagram of cesium energy states showing the DPAL lasing mechanism of (1) pump photon absorption on the D_2 line, (2) spin-orbit mixing of the $6P$ states due to buffer gas collisions, and (3) laser photon emission on the D_1 line. Higher energy states are shown as well that are involved in unwanted ionization processes. [Right] Geometrical diagram of a flowing DPAL system showing (a) an alkali and buffer gas mixture moving through the gain medium, (b) absorption from many diode pump sources, and (c) emission of a single laser beam from a resonator consisting of two mirrors, a high reflector (HR) and an output coupler (OC).

An energy-state diagram of the basic DPAL lasing process is shown on the left side of Fig. 1.1. The laser action in the gain medium is performed by alkali gas, which has been demonstrated with cesium, rubidium, and potassium. However, most

of the gaseous gain medium consists of noble gas or hydrocarbon buffer gas in the typical range of $1 - 10$ atm, and the alkali content is only a few parts-per-million (ppm) or less. The light of many diode stack lasers is absorbed by the alkali gas. The diodes are highly energy efficient; however, each has poor beam quality. (The diodes cannot be used directly as an HEL since their poor beam quality would cause rapid divergence of the beam during propagation.) The diodes are finely tuned to what is historically known in spectroscopy as the D_2 absorption line of the alkali, which causes excitation to the $nP_{3/2}$ state. Population is then rapidly transferred to the thermally connected state $nP_{1/2}$ via collisions with the buffer gas. Finally, laser photons are emitted along the D_1 transition of the alkali to the ground state, $nS_{1/2}$. The rapid transfer of population (via spin-orbit mixing) from $nP_{3/2}$ to $nP_{1/2}$ is necessary to create a population inversion along the D_1 transition; it enables the system to reach a condition where it simultaneously absorbs pump light on the D_2 transition (852.3 nm for cesium) and amplifies laser light on the D_1 transition (894.6 nm for cesium). The buffer gas is necessary in the system for two reasons, (1) to pressure broaden the absorption lines to match diode pump emission and (2) to increase the spin-orbit mixing rate of the nP levels. The desired laser kinetics of DPAL involve only the three lowest levels, as shown in the cesium energy-state diagram in Fig. 1.1; however, unwanted collisional and photon processes can steal energy away from the lasing mechanism and cause excitation past $nP_{3/2}$, possibly to ionization.

Typical DPAL buffers are hydrocarbons and noble gases, and in the current experiment, methane and helium have been investigated. Helium is widely used for two main reasons: (a) it efficiently pressure broadens the pump absorption spectrum at 852 nm and (b) it has a low index of refraction which minimizes thermal aberration. Methane is widely used because it has been shown to efficiently spin-orbit mix the pump and laser energy states ($6P_{3/2}$ and $6P_{1/2}$) while causing minimal quenching from these states to ground. (Quenching is a collisional process that causes population

to relax to a lower energy state, releasing heat.) [4] [5] In the current, experiment buffer gas mixtures near 1 atm with either pure helium or a mixture of 84% helium and 14% methane have been investigated.

1.2 Open Questions in DPAL Research

Many avenues of research are underway in the development of DPAL technology. Continual improvement of diode pump spectral linewidth and SWaP is on-going. In 2016, fiber-coupled pump modules built by DILAS Inc. were demonstrated with >400 W output and <60 pm (<30 GHz) spectral width at 766 nm for potassium DPAL. Each module contained eight diode bars, each with a volume Bragg grating (VBG), which were individually temperature controlled to lock the emission spectrum. [6] Work has begun to demonstrate power scalability while maintaining beam quality. Shaffer *et al.* have developed contactless diagnostics capable of making direct measurement of thermal aberration that occurs during DPAL operation. [7]. Effort is being invested in developing techniques to protect resonator windows from corrosive alkali gas via material selection and gas flow pattern. Fletcher *et al.* identified multiple window materials resistant to alkali-induced effects [8]. Development of flow systems with consistent and controlled alkali gas content is underway. Zhdanov *et al.* demonstrated a closed-loop potassium system and measured improved efficiency at higher flow rates [9]. Yacoby *et al.* also observed increased efficiency at high flow rates in a closed-loop cesium system, and they furthered the investigation to show that the cause was alkali density dependence on flow velocity rather than thermal degradation [10]. Hydrocarbons are often used as DPAL buffer gas since many are efficient at spin-orbit mixing of the pump and laser states, but have a relatively low rate of quenching these states; however, the rate of unwanted reaction between excited state alkali and hydrocarbon is an open area of research [11].

Laser induced ionization in buffered alkali gases has been observed and analyzed

since before the invention of DPAL; yet,the details of these processes and impacts on DPAL operation are not fully understood. Concerns that energy wasted by ionization processes could potentially limit power scaling of DPAL have been greatly relieved by demonstration of efficient CW lasing at high total power, high intensity, and high alkali density [2]. Concern was further reduced after Wallerstein demonstrated agreement between fluorescence measurements of a potassium DPAL gain medium pumped at 1-2 kW and predictions based on ionization kinetic simulation [12]. The model was used to extrapolate to intensities of 100 kW/cm^2 and potassium densities of 10^{16} cm^{-3}, showing $< 10\%$ ionization throughout the parameter space. However, evidence of DPAL efficiency reduction due to ionization was observed by Zhadanov *et al.* [13]. The authors demonstrated significant output power increase in a potassium DPAL with 4% methane compared to pure helium buffer gas, and they argued that the likely cause of the difference was ionization behavior.

Testing and analysis have already shown that DPAL can operate efficiently at high power with minimal degradation due to ionization. However, the full parameter space of DPAL operating conditions has not been explored at high power, such as various buffer gas combinations, pressures, and alkali densities. Continued improvement of experimentally validated ionization modeling can be used to examine the viability of DPAL in these various regimes before costly experiments are initiated. Also, all high power regimes are impacted to some extent by ionization. Inclusion of ionization in high fidelity DPAL design software, such as the General Aerodynamic Simulation Program (GASP), written by Aerosoft Inc., has already begun. This effort improves accuracy and enables design of high power systems that avoid issues associated with ionization, such as reduced pump absorption, decreased lasing efficiency, and increased heat generation.

All previous experimental examinations of DPAL ionization have been indirect. The analysis has focused on explanation of observed laser behavior (such as output power, absorption, and fluorescence) with energy state rate equation modeling based

on known processes. Many of these investigations have shown convincing evidence that ionization was the source of the observed changes; however, this approach can never instill the same level of confidence as a direct measurement.

An important area of DPAL research is furthering the understanding of the processes causing ionization via direct detection of charged particle generation.

1.3 Direct DPAL Ionization Rate Measurement with an Ion Chamber

In this thesis, the utility of DPAL ionization rate measurement with an ion chamber is examined and demonstrated in laser excited cesium gas. An ion chamber is a diagnostic that uses electrodes to extract charged particles from a gas to make a direct ionization rate measurement via current saturation. The application of an ion chamber diagnostic to a DPAL gain medium is demonstrated for the first time. Results of both ion chamber and fluorescent measurements are used to evaluate and expand our understanding of the mechanisms resulting in DPAL ionization. The benefits and limitations of ion chamber measurement for future higher power DPAL experiments are examined.

The fundamental topic in this research was ionization processes that occur in DPAL. However, use of an ion chamber to make the measurements required significant attention to be given to the diagnostic itself. The central reason for this was that the ion chamber needed to be operated significantly far from typical conditions, which is discussed further in Section 1.5. The ionization rate in DPAL is well above standard ion chamber use; the highest measured rates in the experiment were seven orders-of-magnitude higher than what a commercial ion chambers can measure. The complex processes that occur at high ionization rate and high plasma density in an ion chamber were examined in detail to show that accurate measurements can still

be made. Also, typical ion chamber use involves measurement of uniform ionizing radiation that fills the space between the electrodes; however, in the DPAL diagnostic geometry, the excitation is localized in the laser beam.

The modeling and experimental research in this thesis is generally divided into two related subjects: (1) analysis of ionization mechanisms that occur in laser excited cesium gas and (2) viability of ion chamber operation at high plasma density and localized ionization, which is necessary for use as a direct DPAL ionization rate diagnostic.

1.4 Ion Chambers

An ion chamber, also called an ionization chamber, is a diagnostic commonly used for radiation dosimetry. The diagnostic consists of an ionization rate measurement across a volume of gas between two electrodes, as shown in Fig. 1.2. Because of its robust and simple design, it has been in continual use for a period that already spans three centuries. The equations governing the motion of ionized particles across the system were first defined and analyzed by J.J. Thomson in 1899 [14]. The work contributed to his 1906 Nobel prize for theoretical and experimental investigations on the conduction of electricity by gases. Well over 100 years later, the ion chamber remains a commercial product commonly used in the fields of nuclear power, nuclear medicine, and environmental radiation monitoring.

Three related diagnostics for determining the flux of ionizing radiation are described in Fig. 1.2, the ion chamber, the proportional counter, and the Geiger-Müller counter. All of the diagnostics are based on exposing a volume of gas to the ionizing radiation of interest, then measuring changes to conductivity; however, each operates in a different voltage regime. The ion chamber is operated at the lowest voltage range. The device is used to measure the rate that ionization occurs in the

gas volume (the total rate integrated over the volume between the electrodes). It does this by measuring the saturation current, which is the nearly constant current response across the voltage range. The saturation current is directly proportional to ionization rate in this regime, since the voltage is high enough to attract all charged particles to their respective electrodes with negligible recombination loss, yet low enough to prevent field-induced ionization. An ion chamber is generally used to measure larger radiation doses than the counters, since it measures a continuous current, rather than individual ionization events. The proportional counter and Geiger-Müller counter operate in the higher voltage ranges. Both devices count radiation particles by utilizing avalanche ionization, which is a process that causes a measurable current surge initiated by a single ionization event. Avalanche ionization occurs in a sufficiently high electric field that free electrons accelerate quickly enough that they liberate additional electrons during particle collisions, which causes exponential signal growth. Proportional counters are able to measure the energy of the incident radiation, and Geiger-Müller counters are able to detect extremely low doses.

Characteristic ion chamber measurements that were recorded during this investigation are shown for three different laser powers on a semi-log plot in Fig. 1.3. The pump excitation laser powers used in this test ranged from 0.2 - 1.2 W, and higher powers caused increased gas ionization rates. The shapes of the plotted voltage versus current measurements are typical for an ion chamber, known as "saturation curves". The saturation region occurred at voltages between roughly 100 - 500 V. The rate of saturated current flow is a direct measurement of the total ionization rate between the electrodes. In this regime, current is drawn out by the electrodes at a rate equal to the rate plasma is produced by ionization processes. In the regime below saturation, the gas is ionized at the same rate, but since the electric field is lower, the ions and electrons move slowly, providing sufficient opportunity for recombination and reducing the measured current. The data shown in Fig. 1.3 was

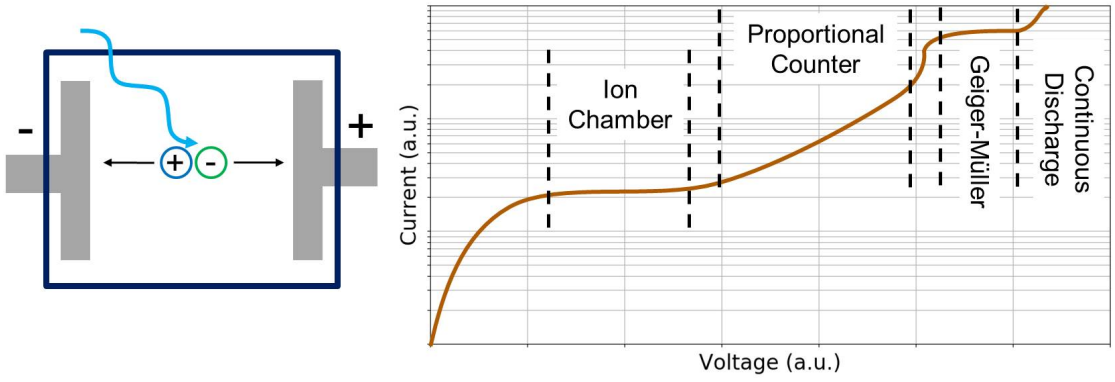

Figure 1.2: Fundamentals of ion chambers and other gas ionization detectors. [Left] Diagram of a typical parallel plate ion chamber showing radiation entering into the chamber, ionizing the gas between the plates, then the electron / ion pairs are pulled to their respective electrode. Current saturation indicates that charged particles are pulled sufficiently fast that negligible recombination occurs. [Right] Qualitative $I(V)$ curve showing different gas ionization detector regimes. The parameter space labeled "ion chamber" is of interest in this thesis.

only measured to 500 V; however, at slightly higher voltage, field-induced ionization was observed to occur, which causes a sharp increase in the current response of the system.

1.5 Open Questions in Ion Chamber Research

Ion chambers are well-established technology for monitoring radiation levels in work areas around nuclear sources. This requires detection of radiation at significantly lower levels than exist in a DPAL gain medium. For example, the IC3 handheld ion chamber from Rotem Industries typically measures ionizing radiation in the range of 10^{-4}-10^{2} R/h, which corresponds to ionization rates of $2.7\times(10^{1}$-$10^{7})$ cm^{-3}s^{-1}. The ionization rates in the current experiment are 10^{12}-10^{14} cm^{-3}s^{-1}, which are up to 7 orders-of-magnitude above the range of the commercial ion chamber.

Behavior of ion chambers has been thoroughly characterized at the low ionization

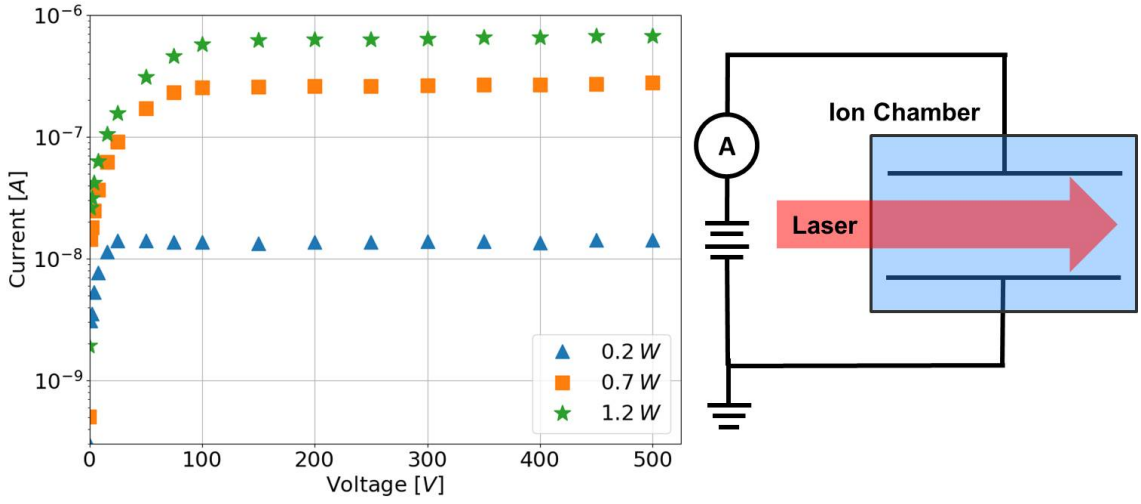

Figure 1.3: Examples of ion chamber electrical and optical geometry and measurements. [Left] Example ion chamber measurements at varying laser powers. The chamber was a 7.7 cm long cell filled with 875 torr of a 6:1 helium:methane mixture and 2.2×10^{12} cm^{-3} cesium, excited to ionization with pump intensities of 15-100 W/cm^2. The results demonstrate current saturation for applied voltages between roughly 100 - 500 V. [Right] Simplified circuit diagram of an ion chamber diagnostic used to measure the ionization rate of laser excited gas, including a voltage source, an ammeter, and electrodes inside an ion chamber, surrounding the laser excited gas.

rates relating to human health (discussed further in Sec. 2.2). Dosimetry in this regime will be referred to as the "typical operating condition" of an ion chamber. Ionization rates in this regime create sufficiently low plasma density that the charged particles have minimal influence on each other.

The central question to be answered in ion chamber analysis in this thesis is: Do any high density plasma effects impact the ability of an ion chamber to accurately measure DPAL ionization rates?

Operation at high plasma density is uncommon; however, the 1952 analysis of Boag & Wilson has been the authoritative work on the subject for 70 years. The authors generated ionization rates of 2×10^{14} cm^{-3}s^{-1} with a 1.2 MeV electron beam produced with a Van de Graaff generator. They created an analytic model of a high

density ion chamber based on the well-established Thomson model, and showed that it accurately predicted measurements under the following conditions: (a) negligible impact of diffusion and (b) uniform ionization filling the gap between the electrodes. However, DPAL operating conditions violate both restrictions.

To examine the processes in a high plasma density ion chamber, the analysis of Boag & Wilson needed to be extended to include diffusion and allow for a spatially localized ionization source (the focused pump laser beam). This has been accomplished by developing a finite-difference simulation of the ion chamber, then validating predictions of voltage versus current, called "saturation curves", with experimental measurement. This analysis will be used to demonstrate the following: (a) a variety of processes occur only in a high density ion chamber, (b) these processes are well understood since they are natural consequences of the Thomson model with diffusion, and (c) none of these processes prevent accurate measurement of ionization rate under DPAL conditions.

The DPAL ionization rate is significantly higher than standard operating conditions of an ion chamber. To trust the diagnostic in this regime, the details of high plasma density operation must be understood and shown to allow valid measurement of ionization rates.

1.6 Dissertation Objectives and Thesis Outline

The goal of this dissertation is to improve understanding of DPAL ionization mechanisms through the use of an ion chamber diagnostic. DPAL has been demonstrated with three different alkali gases: cesium, rubidium, and potassium. The dissertation will focus on cesium DPAL due to: (a) interest in cesium ionization generated by the results of Zhdanov *et al.* [15], which are discussed further in Ch. 2, (b) interest in development of cesium DPAL systems at higher powers, (c) similarity of ionization

mechanisms between all the alkali gases, discussed further in Ch. 4, and (d) availability of experimental equipment. Experiments will involve excitation of cesium gas with various buffer gas mixtures using a Ti:sapphire pump laser tuned to 852.3 nm. Measurements will not involve full DPAL operation, since it would have increased the complexity of the system with a laser resonator and oscillation of a beam at 894.6 nm. The ionization mechanism is not expected to be substantially different with excitation from a single wavelength (pump only at 852.3 nm), compared to excitation from two simultaneous wavelengths (pump and laser at 852.3 and 894.6 nm), which is discussed further in Ch. 4.

The objectives of the thesis are:

1. Evaluate the current understanding of ionization mechanisms that occur in a cesium diode pumped alkali laser (DPAL) gain medium by comparing direct ionization rate measurements with an ion chamber to predicted rates based on known processes.

    - Construct an ion chamber around a laser-excited, buffered, cesium gas, and measure ionization rate with varying optical power, cesium density, and buffer gas mixture.
    - Simultaneously monitor various fluorescence lines during ion chamber operation for additional verification of the ionization mechanism and validity of the diagnostic.
    - Develop a computational simulation to predict ionization rate based on cesium ionization processes published in the open literature.
    - Assess understanding of DPAL ionization mechanisms by comparing theoretical predictions and experimental measurements, quantifying accuracy of the computational tool, and making suggestions on how DPAL ionization models can be improved.

2. Determine if an ion chamber can be used for direct ionization rate measurement of a DPAL gain medium, considering the rate is multiple orders-of-magnitude above standard operating conditions.

    - Record measurements with an ion chamber at the high plasma densities created in a DPAL; measure saturation curves (current measurements with varying voltage, below and above saturation) with varying cesium density and location of focused laser spot.
    - Develop a computational simulation of the motion of ion and electrons from generation in the laser beam to extraction at their respective electrodes, based on the Thomson model and the analysis of Boag & Wilson, and validate it with experimental measurements.
    - Analyze simulated high plasma density behavior to identify unique processes, determine if any hinder DPAL ionization rate measurement, and use the results to guide future diagnostic use.

The remainder of the dissertation is split into five additional chapters and five appendices. Chapter 2 provides additional information on the basis of the research by summarizing previous research in DPAL ionization and ion chamber operation. Chapter 3 details construction, testing, and simulation of the ion chamber diagnostic. In this chapter, it is demonstrated that an ion chamber is an effective tool for measurement of DPAL ionization rate despite generation of significantly higher plasma density than typical operation. Chapter 4 describes development of a predictive simulation of laser-excited cesium ionization inside the ion chamber based on known processes published in the open literature. Chapter 5 overviews all measurements using an ion chamber and spectrometer, compares the results against theoretical predictions, and uses the results to understand cesium DPAL ionization mechanisms. Finally, Chapter 6 summarizes all results and draws conclusions. Appendix A provides extra information on the electrical and mechanical details of the experimental

apparatus. Appendix B contains the detailed description of the computational simulation of the Thomson model including diffusion. Appendix C contains additional information necessary to fully describe the computational simulation of the ionization mechanism in the ion chamber experiment. Appendix D is an archive of results of all ion chamber measurements. Appendix E includes comparison plots of all ion chamber measurements and simulation predictions across parameter spaces of either varying pump excitation power or varying cesium density.

Chapter 2

Previous Work

The goal of this chapter is to detail key learnings of previous work and motivate the current research. The chapter is split into two sections: Sec. 2.1 provides an overview of research into DPAL ionization, and Sec. 2.2 describes examinations of ion chamber operation, particularly at high plasma density.

2.1 Previous Examinations of DPAL Ionization

Concern over ionization effects in DPAL has a simple foundation: (a) alkali metals have the lowest ionization energy of any group on the periodic table (the lowest being cesium at 3.89 eV), and (b) DPAL requires rapid energy cycling (absorption of a pump photon and emission of a laser photon) through a relatively small number of alkali atoms. Based on these facts alone, it seems probable that processes could exist to concentrate the energy of three pump or laser photons into a single alkali valance electron, causing it to ionize. And, before DPAL interest began, research already existed showing that these processes occur. In 1970, Measures showed that efficient plasma generation can occur by laser excitation of a pure potassium gas (without any buffer) through a process he called laser interaction based on resonance saturation

(LIBORS) [16]. Measures explained his observations based on a cycle of super-elastic collisions of free electrons and excited alkali, followed by electron impact ionization, which can create a run away-process and rapid ionization in the absence of buffer gas to efficiently quench the high-temperature free-electrons. Tam & Happer were the first to generate "laser snow" by resonantly exciting cesium gas with 10 torr of hydrogen buffer, causing a white glow indicating ionization, and causing CsH particles to fall from the beam path. The formation of the precipitant was catalyzed by the laser since it excited the alkali and decreased the activation energy of the chemical reaction. [17]. Relatively low voltage plasma formation (due to avalanche ionization) for alkali in roughly 1 atm of noble gas has been observed, making it useful as the working fluid in magneto-hydrodynamic (MHD) power generation. It was found that breakdown of the gases was represented well by a modified form of Paschen's law in which only the alkali gas ionized, and the noble-gas buffer remained neutral. [18] [19] [20] An excellent overview of energy transfer processes between laser excited cesium atoms, other atomic alkali, and noble gases with analysis of the temperature dependence is provided by Vadla *et al.* [21].

The first thorough examination of ionization processes in a DPAL was made by Wu [22]. He found that variations in laser output power of rubidium gas with helium buffer during a 1 ms Ti:Sapphire pump pulse corresponded to timescales consistent with known collisional and photon ionization processes. He found that the main impact of ionization was a reduction in the usable alkali population for laser action, so he found that ionization caused reduced efficiency when alkali density was below optimum, and he also found that ionization actually improved efficiency when alkali density was above optimum. Knize *el al.* focused their attention on photon excitation processes in DPAL and a cesium exciplex laser, and warned that a high pressure system may be susceptible to rapid ionization if broadening rates for high lying states are sufficiently large [23]. Markosyan & Kushner simulated a wide range of chemistry that can occur in a cesium DPAL, including numerical calculation

of electron impact cross-sections [24]. They demonstrated the capability of super-elastic electron collisions increasing electron temperature and leading to significant ionization. Wallerstein tracked many fluorescent lines during high power ($1 - 2\,\mathrm{kW}$) diode pumping and lasing of a flowing potassium DPAL with pure helium and with small levels of methane ($< 7\%$) [12]. He examined variations with intensities up to $60\,\mathrm{kW/cm^2}$ and alkali densities up to $2 \times 10^{14}\,\mathrm{cm^{-3}}$. Wallerstein developed a kinetics model which incorporated energy exchange between nine different energy states, and showed that it was in agreement with measurements of fluorescent power across the wide parameter space. He observed more than an order-of-magnitude greater fluorescence for many states in the pure helium system compared to the system with methane, and found that this was consistent with possible increased methane quenching of high lying states; however, he pointed out that super-elastic electron collisions were not included in the analysis and warranted further investigation.

In addition, recent experimental evidence may show efficiency reduction due to ionization in a potassium DPAL with pure helium buffer gas [13]. Zhadanov *et al.* saw a $5\times$ increase in power output in the same potassium DPAL laser run with 4% methane added to the buffer gas compared to pure helium. Zhadanov *et al.* as well as other authors, Waichman and Cambier & Madden, have attributed this result to rapid quenching of excess kinetic energy in the free electron plasma by the hydrocarbon. [25] [26] The authors developed rate equation models of the potassium system and showed that a cycle of super-elastic collisions of free electrons and excited alkali, followed by electron impact ionization, becomes the dominant ionization process if energy removal from free-electrons is too slow. Cambier & Madden examined the electron energy spectrum in detail to show that the same nonlinear excitation processes can cause the spectrum to have a significantly larger high energy tail than a thermal Maxwell distribution, further exacerbating the impact of the nonlinear processes.

Significant increase to interest in DPAL ionization occurred when Zhdanov *et*

al. measured a "roll-over" in output power of a static-cell cesium DPAL. When the authors pumped the cell with a CW beam they observed maximum power output with about 70 W input and decreased output with higher powers. They did not observe a roll-over effect with pulsed pumping. [15]. Oliker *et al.* showed with three-dimensional simulation that known ionization processes and thermal lensing could have had an impact on output power, but were insufficient to cause the observed roll-over in the CW experiment [27]. Barmashenko *et al.* came to a similar conclusion, and they also showed that alkali-hydrocarbon reactions can degrade output power, but are unlikely to cause roll-over [28]. Endo *et al.* demonstrated that similar power output roll-over is caused by increasing cell temperature, which results in alkali density increasing through an optimum [29]. The experiment of Zhdanov *et al.* had much higher average power during CW operation than when pulsed, leading to higher convective and radiative heating of the walls and additional cesium vaporization, which was the likely cause of the observed roll-over during CW lasing.

There have been multiple examinations of plasma density in rubidium DPAL gain media over the past decade [30] [31] [32], which involved a similar ion chamber setup to what is described in this dissertation. The authors used chopped laser light and a lock-in amplifier to measure current excited by the laser induced plasma. However, the authors did not use the ion chamber to measure saturation current and ionization rate. Instead, they applied a voltage ramp up to 10 V, and examined the slope in the voltage versus current curve, and from this, made conclusions on steady-state plasma density. However, the conclusions were based on analysis that did not consider Debye shielding or other high density plasma effects, and it was unclear from their results what density regime was present. The reported peak plasma densities may have been much lower than what was actually present, since the maximum 10 V probe would not be sufficient to interact with the core of a high density plasma.

Novel contributions to DPAL understanding in this dissertation are due to measurement and analysis via an ion chamber. The investigations of Wu [22] and

Zhadanov *et al.* [13] examined DPAL ionization indirectly, by showing that ionization processes accounted for observed changes to DPAL power output and fluorescence. The current investigation provides a direct measurement of the charged particle production rate, which reduces ambiguity and improves confidence in the results.

By comparing measurements and predictions of ionization rates, it will be shown that known cesium ionization mechanisms and rates are in good agreement with observations. However, multiple measurements will be shown that indicate that secondary energy pooling has a larger role than previously considered and warrants further investigation. For example, simultaneous ion chamber and fluorescence measurements showed that population of high Rydberg energy states is nearly constant with or without a significant electric field. This indicates that the production of these high lying states is not due to ion / electron recombination, as has been previously suggested, and is likely due to secondary energy pooling involving neutral particle collisions.

2.2 Previous Examinations of High Plasma Density Ion Chambers

Analysis of ion chambers has focused on the Thomson model, which is a set of governing differential equations and boundary conditions, developed over a hundred years ago [14]. The model describes generation of charged particles, motion due to diffusion or drift (caused by the electric field), and finally either recombination or extraction as current at the electrodes. The outputs of the model solved to steady-state are the measured current across the chamber, and spatially dependent maps of ion density, electron density, and electric field. The Thomson model is discussed in detail in Ch. 3. Despite the long history of the model, exact analytic solutions have

proven difficult, and useful information has only been gleaned with varying levels of approximation.

Most analysis with the Thomson model has focused on typical, low plasma density ion chamber operation, which was critical in establishing its validity. The work that guided ion chamber use through the Manhattan Project and early nuclear energy development was highlighted by Mie [33], Seeliger [34], Seeman [35], Townsend [36], Thomson & Thomson [37], and Boag & Wilson [38]. These authors showed that ion chambers with a wide range of geometries and gases were well characterized by the Thomson model using the following approximations: (i) negligible space-charge, (ii) negligible diffusion, (iii) limited recombination, and (iv) spatially uniform ionizing radiation. Since that time, Rosen and George [39] have developed solutions without restriction on recombination, Chabod [40] has developed a perturbation technique to create solutions from non-uniform radiation fields, and Ridenti *et al.* [41] have shown agreement to measured saturation curves, i.e. voltage versus current below and above saturation. Excellent overviews of ion chamber technology include books by Boag [42] and Knoll [43].

Few authors have examined high plasma density effects in ion chambers. The principal work on the subject was by Boag & Wilson [38]. They developed a relationship between current and voltage, expressed in Eq. (2.1). The equation is based on the Thomson model, and can be used to predict the saturation curve of a high plasma density ion chamber. To derive the result, the authors used the following two assumptions: (a) negligible diffusion and (b) spatially uniform ionization filling the volume between the electrodes. (As was previously discussed in Sec. 1.5, standard operating conditions of a DPAL violate both of these assumptions.) Note that Eq. (2.1) will be examined further in Sec. 3.3.4.

$$I(V) = I_{sat}\sqrt[4]{\frac{4\epsilon V_a^2}{ed^4Q}\frac{\mu_e\mu_i}{\mu_e+\mu_i}}; \quad V < V_{sat}$$
$$I(V) = I_{sat}; \qquad\qquad\qquad\qquad V \geq V_{sat} \tag{2.1}$$

In the equation, I_{sat} is the saturation current, V_a is the voltage applied to the electrodes, d is the electrode spacing, Q is the ionization rate with units of $cm^{-3}s^{-1}$, $\mu_{i/e}$ are the ion / electron mobilities, ϵ is permitivity (in SI units), and e is the elementary charge. Their analysis showed that the plasma splits into two regions below saturation: (1) a space-charge limited ion flow region that experiences the electric field and (2) a bulk plasma region with near-zero electric field due to Debye shielding. However, since Boag & Wilson didn't include diffusion in their analysis, they did not fully describe how current passes through the bulk or the details of the transition between the bulk and the space-charge limited flow.

Huyse *et al.* [44] analyzed various processes that can occur at high density, and provided appropriate limitations if each is to be avoided. Multiple authors have analyzed the effect of space-charge on low density ion chambers. Boag showed how space-charge can alter the volume of gas in the chamber contributing to measured current, particularly if a guard ring is used. (A guard ring is a second set of electrodes surrounding the main electrodes; it is used to increase the uniformity of the inner electric field.) [45] Chabod refined his solution to the Thomson model to allow low-level space-charge effects in his perturbation technique. [46]

Dosimetry for FLASH radiotherapy is a growing field interested in the high plasma density ion chamber regime. [47] Researchers have found that short, high-dose bursts are effective in treating tumors, while reducing harm done to neighboring healthy tissue. The ionization rates involved in measuring doses of FLASH radiotherapy with an ion chamber are similar to what occurs in a DPAL gain medium (roughly 100 Gy/s time-averaged, equivalent to an ionization rate of 10^{13} $\mathrm{cm^{-3}s^{-1}}$). McManus *et al.* compared dosimetry results with an ion chamber to measurements

with a graphite calorimeter to show that current saturation was achieved for average dose rates of 0.17 Gy/s, but current was only 4% of saturation with a field strength of 600 V/cm for doses of 50.41 Gy/s. [48]

In this dissertation, the Thomson model with diffusion is solved with computer simulation, which allowed for results without simplifying assumptions or constraints. The simulations show the role of diffusion in moving current through the bulk plasma region and into the space-charge limited ion flow region. The research of Boag & Wilson is extended to allow for arbitrary ionization spatial profiles, which is necessary for localized laser excitation. Simulated saturation curves (measurements of voltage versus current below and above saturation) are compared against measurements in a variety of situations to validate the accuracy of the simulation. The experimental and simulation results demonstrate that an ion chamber is a viable diagnostic at the high plasma densities generated in a DPAL gain medium.

Additionally, multiple techniques for defining the separating point between low and high plasma density regimes have been previously suggested, which have been shown to be in agreement with the simulation developed during the current analysis. One method is to define high density to be a plasma with Debye length equal to or smaller than the electrode spacing [44], which is shown in Eq. (2.2) where n_{min} is the minimum density causing plasma effects, k is the Boltzmann constant, and T is temperature. For an ion chamber with a 1 cm spacing at room temperature, this condition is met at plasma densities greater than 10^4 cm^{-3}. Another technique is to estimate space-charge effects from the Mott-Gurney law based on ionization rate, ion mobility, and electrode spacing, then determine the minimum voltage required to overcome the space-charge, which is shown in Eq. (2.3) where V_{min} is the voltage to match space-charge. Based on nominal ion mobility of 10 cm^2/V and an electrode spacing of 1 cm, 100 V is the minimum necessary to negate space-charge effects of slow moving ions created at a rate of 2×10^{11} cm^{-3}s^{-1}. [44] One important modification of this estimation, discussed again later, is that if ionization occurs in

a small region compared to the volume of the ion chamber, lateral spreading of the plasma lowers the volume averaged ionization rate. It will be shown in Ch. 3 that standard DPAL operating conditions are in the high density regime based on either definition.

$$n_{min} = \frac{\epsilon kT}{e^2 d^2} \tag{2.2}$$

$$V_{min} = \sqrt{\frac{eQd^4}{4\epsilon_0 \mu}} \tag{2.3}$$

2.3 Chapter Summary

Significant research has already been done on ionization processes in DPAL and ionization rate measurement using ion chambers. Prior research into DPAL ionization is extended in this dissertation by (a) novel application of an ion chamber to make direct measurements of charged particle generation rates, and (b) by building a model of laser induced ionization in cesium gas based on previously examined and measured processes, then quantifying the agreement between theory and measurement.

Research into high plasma density ion chambers is built upon by developing and validating a computer simulation of the full Thomson model with diffusion (the well established governing equations of an ion chamber) without any of the typical restrictions. This has been done to demonstrate that an ion chamber is an accurate diagnostic for the DPAL ionization rate, which is significantly above standard operating conditions.

Chapter 3

Ion Chamber Diagnostic at High Plasma Density

The goals of this chapter are to: (a) detail the experimental apparatus and data collection method, and (b) to demonstrate through experimentation and simulation that an ion chamber is an accurate tool for measurement of DPAL ionization rates, which are multiple orders-of-magnitude above standard operation, as described previously in Sec. 1.5. In Sec. 3.1, the hardware used in the experiment is described, including the pump laser, the ion chamber, and the fluorescence monitoring optics. In Sec. 3.2, an overview is provided of the simulation tool developed to examine details of high density ion chamber behavior. And in Sec. 3.3, the ion chamber simulation is shown to be accurate by comparing it to experimental results while varying multiple parameters. Next, both experimental and simulation results are analyzed to show that additional processes occur at high plasma density, but none interfere with accurate DPAL ionization rate measurement.

3.1 Experimental Apparatus and Procedure

An ion chamber was built that was capable of measuring the ionization rate of the cesium vapor gain medium in a diode pumped alkali laser. The ion chamber is shown in Figure 3.1, and additional images and detailed discussion are in Appendix A. The ion chamber was filled with either pure helium or a 6:1 mixture of helium to methane at 700 torr and 25 °C. The cell contained a few grams of pure cesium metal, which created a vapor pressure that could be controlled by the cell temperature, and was at most slightly less than 1 ppm. The gas mixture was typical for a DPAL gain medium. The trace amount of cesium gas was excited with high intensity light from a Ti:Sapphire laser, tuned to the D_1 absorption line at 852 nm, which generated a dense plasma between the electrodes.

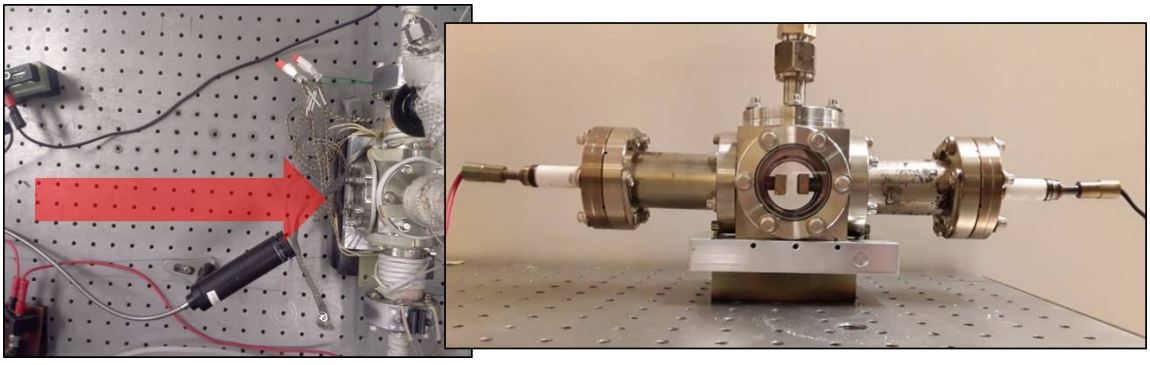

Figure 3.1: Ion chamber containing cesium and buffer gas with windows and electrodes. [Left] Top view of setup including indication of Ti:Sapphire 852.3 nm pump laser propagation axis, electrical connections to the electrodes from the power supply (not shown), and the fiber optic and beam tube used to collect fluorescence for measurement with a spectrometer. [Right] Front view of ion chamber showing electrode spacing.

The walls of the ion chamber were stainless steel with uncoated fused silica windows in the front and back, separated by 7.7 cm. The electrodes entered the cell electrically isolated via alumina ceramic breaks. The electrodes were copper with cross-sections of 0.9×6.9 cm, and the spacing between electrodes was 1.0 ± 0.05 cm.

The cell was baked at 180 °C under vacuum for one day. Next cesium was added in a nitrogen glove box, and the cell was evacuated with a turbo pump. Finally it was filled with 600 torr of ultra high purity helium and 100 torr of ultra high purity methane from Airgas, sealed, and leak tested. The vapor density of the cesium was controlled by heating the cell to temperatures in the range of 45-70 °C, causing cesium densities of 10^{11}-10^{13} cm^{-3}. The cell was wrapped in heaters and insulation, and the temperature was set using proportional-integral-derivative (PID) contollers with thermocouples on the bottom flange and on the cell wall near the biased electrode. Condensation of cesium on the windows was prevented by using a heat gun on the windows before each test. The heaters were found to add noise to the electrode measurements, so the heaters were turned off during testing. The temperature was found to decrease by ∼1 °C during the two minute data collection periods.

The cesium gas was excited with a Coherent MBR 110 Ti:sapphire tuned to the peak absorption wavelength of 852.3 nm and with a maximum power of 1.2 W. The spectral width of the pump beam was monitored during testing with a Yokogawa AQ6370 optical spectrum analyzer to be 0.04 nm FWHM, which was slightly narrower than the pressure broadened absorption spectrum of the gas. A Thorlabs BP209 laser beam profiler was used to measure the intensity on the celll, shown in Figure 3.2, and show that the beam was nearly collimated during propagation inside the cell, with a measured beam area increase of 5%. The horizontal and vertical beam diameters shown in Fig. 3.2 correspond to the $1/e^2$ points of an elliptical Gaussian fit. The beam was linearly polarized, and if a power less than the maximum was needed, then it was attenuated with a polarizing beam splitter and a half waveplate to minimize thermal lensing; the maximum measured extinction was greater than 97%. The beam spectrum was monitored during testing with a Yokogawa AQ6370 optical spectrum analyzer, with an example measurement shown in Fig. 3.2. The beam was measured to have 7-8% transmission loss through the front or back window on the cell.

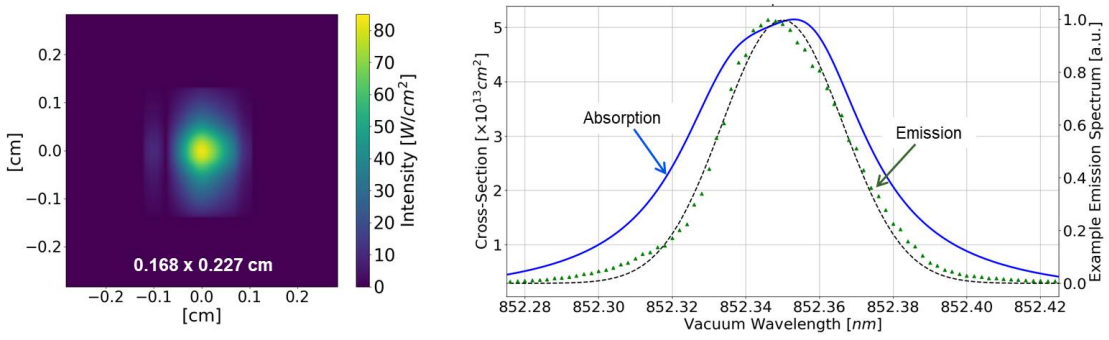

Figure 3.2: Pump laser measurements [Left] Measured intensity profile at 1.1 W, and [Right] Measured emission spectrum with a Gaussian fit (FWHM = 0.039 nm) and a calculated absorption lineshape for a 6:1 mixture of helium and methane at 759 torr and 323 K.

The alkali density in the cell was determined by measuring percent transmission of the pump beam at a series of incident powers, which will be discussed further in Section 5.1. The range of alkali densities that were included in the test were restricted to those with measurable transmission through 7.7 cm of gas. Fluorescence was monitored with an Acton SpectraPro 2750 from Princeton / Roper, which is a 750 mm Czerny-Turner monochomator with a 1200 grooves/mm grating blazed at 500 nm. The spectra were recorded with a liquid nitrogen cooled Spec-10 visible and near-infrared (NIR) charge coupled device (CCD) detector. A green filter was sometimes used to remove fluorescence above 500 nm. Fluorescence was monitored from a small volume near the front window of the ion chamber. It was collected by a 2.5 cm diameter, 5.0 cm focal length lens. The lens imaged the volume onto a fiber collector by being placed 10 cm from each, held in position at the end of a beam tube from the fiber, as shown in Fig. 3.1. The lens was adjusted to image fluorescence from the beam center by maximizing signal.

A complete circuit diagram of the ion chamber diagnostic is shown in Fig. 3.3. The circuit diagram is split into a power supply and ammeter and three additional regions, A, B, and C. Regions A and B include electrical components that were

explicitely added in the system, and Region C represents current leakage from the electrodes to the grounded walls of the system.

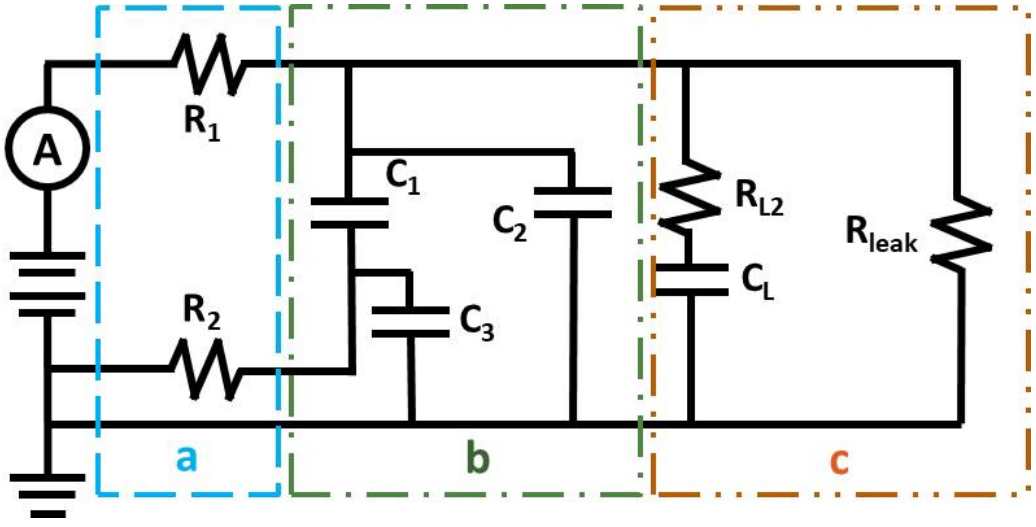

Figure 3.3: Diagram of the circuit accounting for observed transients and steady-state. Region a: Resistors added to circuit to prevent electrical arcing. Region b: Capacitance of electrode and alumina ceramic breaks. Region c: Resistance and capacitance from the biased electrode to the cell walls, which cause the observed leakage current. $R_1 = 1.54$ MΩ, $R_2 = 1.48$ MΩ, $C_1 = 1$ pF, $C_2 =$ 41 pF, $C_3 = 41$ pF, $R_{L2} =$ 7-8 GΩ, $C_L =$ 25-30 pF, $R_{leak} =$ 4-7 GΩ

The power supply shown in Fig. 3.3 was a Keithley 2410, which had a built-in ammeter and the ability to be computer controlled via LabView software. The system was calibrated using a known resistor in the range of nA $-$ μA. Region A of Fig. 3.3 represents two resistors, 1.54 and 1.48 MΩ, which were connected between the power supply and the electrodes to prevent a short circuit if electrical arcing occurred. Region B includes components in the system which behave as capacitors, which are the electrodes and the electrical breaks around the electrodes. The capacitance of the electrode itself was calculated to be 1 pF based on the 1 cm spacing and the minimal dielectric behavior of the gases. The alumina ceramic electrical breaks are insulators between the electrodes and the grounded ion chamber walls. The capacitance of the electrical breaks was measured to be 41 ± 17 pF. The details of the capacitance measurement are provided in Appendix A. The last region shown in

Fig. 3.3 represents the observed behavior of current leakage. The leakage current was observed to change temporally for roughly 0.2 s before reaching a steady-state. This situation was electrically represented by the combination of resistors and capacitors. Measurement of the response of the system to a rapid change in voltage is shown in Fig. 3.4, which shows the effects of the leakage current.

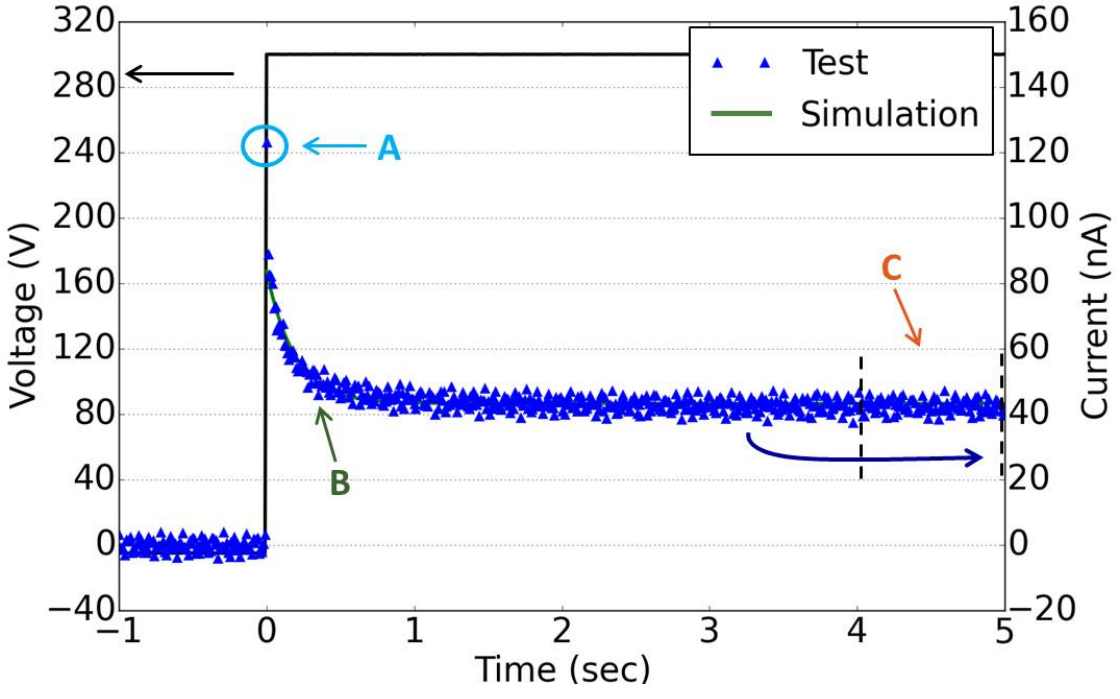

Figure 3.4: Measured current response to step-function applied voltage without laser excitation. Point A: Single high data point due to a fast transient response <0.01 s. Region B: Slow transient response of roughly 0.2 s. Region C: Steady-state leakage current measured between 4-5 s.

The circuit shown in Fig.3.3 was shown to well-represent the measurements shown in Fig. 3.4. The measurement shown in Fig. 3.4 was taken without laser excitation, so it is only the background electrical response of the system. The measurement exhibits three distinct features: (a) a fast transient that was <0.01 s, (b) a slow transient that lasted about 0.2 s, and (c) a steady-state leakage current. The fast transient was due to rapid charging of the electrode and alumina ceramic breaks

(Region B in Fig. 3.3). The slow transient and non-zero steady-state current are caused by resistance and capacitance of the leakage current (Region C in Fig. 3.3). The circuit diagram shown in Fig. 3.3 was simulated with the Simulation Program with Integrated Circuit Emphasis (SPICE), which was accessed on the internet via www.partsim.com/simulator on 10 FEB 2019. The results of the circuit simulation are overlayed on the measurement in Fig. 3.4, demonstrating agreement between measurement and simulation.

The exact mechanism of the current leakage is unknown; however, three observations were made about the leakage at steady-state: (a) the current was directly proportional to the applied voltage, (b) the current increased with increasing cesium vapor density, and (c) the current corresponded to resistances of 4-7 GΩ. The leakage current was likely due to a small layer of cesium condensing on the alumina ceramic break.

Current measurements with the ion chamber were the sum of background leakage and signal from ionized gas. The following steps were taken to isolate the signal from the background. A LabView data collection program was written to apply a set number of voltages to the chamber, hold each for 5 s, and measure current response at 100 Hz. Typically 20 different voltages were applied, so data collection lasted a little less than 2 minutes. To avoid transient background effects, measurements were all done at steady-state, which was defined to be the average current between 4-5 s after applying a voltage. Next, the resistance associated with the steady-state leakage current, R_{leak}, was measured using the LabView data collection program without laser excitation. After this, the laser was applied to the gas in the ion chamber, and the total current response, I_{tot}, was measured with the LabView data collection program to applied voltage, V_a. Finally, Eq. (3.1) was used to determine the ion chamber signal without background leakage, I_s. Eq. (3.1) represents the circuit shown in Fig. 3.3 at steady-state, such that all capacitors have charged and become open circuits, and with the addition that gas ionization has caused I_{sig} across

the electrodes. The resistor in the equation, R_1, was the 1.54 MΩ resistor between the power supply and the ion chamber. Since $R_{leak} >> R_1$, the $\frac{R_1}{R_{leak}}$ term is negligible, but it was included in the calculation for completeness.

$$I_s = I_{tot}\left(1 + \frac{R_1}{R_{leak}}\right) - \frac{V_a}{R_{leak}} \tag{3.1}$$

Multiple tests were done to show that measurements of I_s were only due to gas ionization. First, it was shown that the laser did not generate current due to the external photoelectric effect, potentially caused by illumination of the electrodes. The ion chamber showed zero I_s under the following conditions: (1) no applied laser, (2) laser off-resonant at 815 nm between electrodes, (3) laser at 815 nm with the grounded electrode illuminated, and (4) laser at 815 nm with the biased electrode illuminated. Next, the chamber showed significant signal (40× the leakage current) when the laser was turned to resonance at 852.3 nm. The photoelectric effect was not expected since the work function of the copper electrodes is roughly 5 eV [49], which is significantly larger than the energy of an 815 nm photon (1.52 eV). The second test that was done was an evaluation of the breakdown voltage, above which the current multiplying effect of field-induced ionization occurs. Breakdown was observed with initiation at voltages between 400 and 900 V. The breakdown voltage was inversely proportional to cesium vapor pressure. Similar observations have been made previously in cesium / helium mixtures as well as for other alkali and rare Earth gases. [18] [20] Field-induced ionization was observed to occur independent of laser excitation, and it was seen to be accompanied by a purple glow in the corners of the electrodes. The electrodes were not electro-chemically polished, and the edges were not chamfered, which increased the field in localized regions and likely reduced breakdown voltage. All ion chamber results discussed in this paper were measured below the breakdown voltage.

3.2 Ion Chamber Governing Equations and Finite-Difference Simulation

The high plasma density ion chamber experiment has been simulated to (a) demonstrate that the Thomson model accounts for measured saturation curves, $I(V)$, and (b) examine the processes that arise to ensure that none prevent accurate measurement. For example, before the simulation was developed, there was a concern that space charge could condense the electric field to a sufficiently small region of the plasma that it could create field-induced ionization; however, our results show that this effect is minimal.

A set of differential equations and boundary conditions make up the Thomson model, which governs the ion density $n_i(x,t)$, electron density $n_e(x,t)$, electric field $E(x)$ assuming an ionization rate $Q(x)$ and applied voltage V_a. In steady state and one (x) dimension, it reads:

$$\frac{dn_i}{dt} = Q(x) - C_R n_i(x) n_e(x) - \frac{d}{dx}[\mu_i E(x) n_i(x)] + D_i \frac{d^2}{dx^2} n_i(x) = 0 \tag{3.2}$$

$$\frac{dn_e}{dt} = Q(x) - C_R n_i(x) n_e(x) + \frac{d}{dx}[\mu_e E(x) n_e(x)] + D_e \frac{d^2}{dx^2} n_e(x) = 0 \tag{3.3}$$

with the boundary conditions

$$n_i(0) = n_e(d) = 0 \tag{3.4}$$

$$\frac{d^2 n_i(d)}{dx^2} = \frac{d^2 n_e(0)}{dx^2} = 0 \tag{3.5}$$

and the following constraint linking the field to the applied voltage.

$$\frac{d}{dx}E(x) = \frac{e}{\epsilon_0}[n_i(x) - n_e(x)] \tag{3.6}$$

$$V_a = \int_0^d E(x)dx \tag{3.7}$$

Here the subscript i represents ions, the subscript e represents either free-electrons or negative ions, C_R is the bimolecular recombination coefficient, μ is mobility, D is the diffusion coefficient, d is the electrode spacing, and V_a is the voltage applied to the electrodes. The bimolecular recombination coefficient is described further in Sec. 4.8 and in Appendix B. The reaction requires a collision between an ion and an electron, so it is dependent on the density of both particles. The geometry represented by the equations has the surface of the high potential electrode at $x = 0$ and the surface of the low potential electrode at $x = d$, such that ions are pulled by the electric field in the $+x$ direction and electrons are pulled in the $-x$ direction.

The first two equations of the Thomson model (3.2 and 3.3) are based on conservation of positive and negative charges with terms for charge generation, recombination, drift due to the influence of the electric field, and diffusion due to density gradients. Equation (3.6) is Gauss's law and Eq. (3.7) is the restriction that the integrated field must equal the applied voltage.

The first boundary condition, Eq. (3.4), is typical of the Thomson model. In most applications, diffusion is ignored, which causes Eqs. (3.2 and 3.3) to become first-order, and only one boundary condition is required. Equation (3.4) shows that the density of ions at the high potential electrode and the density of electrons at the low potential electrode are both zero. This condition is caused by the electric field causing the particles to drift away from these electrodes. This condition is valid even

in the case where diffusion dominates over drift, since any particles that diffuse to the electrodes rapidly recombine, which is discussed further in Sec. 3.3.6.

By including diffusion in the Thomson model, Eqs. (3.2 and 3.3) become second-order, which require an additional boundary condition. Equation (3.5) is the boundary condition for charged particles reaching the electrode that is electrically attractive. The boundary condition indicates that diffusion does not occur across the boundary, only particle drift into the electrode due to the field at the surface.

The first two equations of the Thomson model, Eqs. (3.2 and 3.3), show that at steady-state, current is constant between the electrodes. This is derived by first subtracting the two equations from each other, which results in the following.

$$\frac{d}{dx}[\mu_i E(x) n_i(x) + \mu_e E(x) n_e(x) - D_i \frac{dn_i}{dx}(x) + D_e \frac{dn_e}{dx}(x)] = 0 \tag{3.8}$$

Since the derivative is zero at each point between the electrodes, the quantity inside the brackets must be a constant. Therefore, current density, J, is a constant at steady-state, defined be Eq. (B.6), and it is the sum of drift and diffusion of both ions and electrons. And, since we are only considering variation in one axis, x, we are assuming that the plasma has a uniform cross-section, A_p, in the other two axes, z & y. Therefore, current, $I = JA_p$, is a constant as well.

$$J = e\mu_i E(x) n_i(x) + e\mu_e E(x) n_e(x) - eD_i \frac{dn_i}{dx}(x) + eD_e \frac{dn_e}{dx}(x) \tag{3.9}$$

The saturation behavior of an ion chamber can be shown by manipulating Eq. (3.2) or Eq. (3.3) as well. Equation (3.2) can be rearranged to form the following.

$$Q(x) - C_R n_i(x) n_e(x) = \frac{d}{dx}\left[\mu_i E(x) n_i(x) - D_i \frac{dn_i}{dx}(x)\right] \tag{3.10}$$

Integrating both sides from $x = 0$ to $x = d$, and multiplying by the elementary charge, e, creates

$$e \int_0^d [Q(x) - C_R n_i(x) n_e(x)]\, dx = J_i(d) - J_i(0) \tag{3.11}$$

where J_i is the current density due only to ion motion, defined by $J_i(x) = e\mu_i E(x) n_i$ (x) $-eD_i \frac{dn_i}{dx}(x)$. Since current density at an electrode is only due to the charged particle attracted to that electrode, $J_i(0) = 0$ and $J_i(d) = J$. Using this result and multiplying by A_p, results in the following equation.

$$eA_p \int_0^d [Q(x) - C_R n_i(x) n_e(x)]\, dx = I \tag{3.12}$$

Equation 3.12 demonstrates that the current measured by an ion chamber is equal to the integrated ionization rate, $e \int_0^d Q(x)dx$, reduced by recombination. As voltage increases, it causes the ions and electrons to increase in velocity, which decreases their densities, and reduces total recombination loss, $eA_p \int_0^d C_R n_i(x) n_e(x) dx$. If voltage is sufficient to cause saturation, then it indicates that recombination has been reduced to a negligible level, and the saturation current equals the integrated ionization rate, which is shown by Eq. (3.13).

$$V_a \geq V_{sat}; \quad I_{sat} = eA_p \int_0^d Q(x)dx \tag{3.13}$$

Details of the computational tool developed to investigate the high plasma density ion chamber experiments are provided in Appendix B. The simulation involves one-dimensional discretization of the 1 cm axis between the electrodes, and an iterative finite-difference technique to determine steady-state solutions of the Thomson model for: (a) ion density, $n_i(x)$, (b) electron density, $n_e(x)$, and (c) electric-field, $E(x)$.

The simulation incorporates the full Thomson model without any approximation, which results in the following processes naturally occurring: (a) space-charge limited ion flow, (b) Debye shielding and separation of a bulk plasma region with near-zero electric field, and (c) ambipolar diffusion across the bulk plasma. Discussion is also provided on the values of the physical constants used in the model for mobility, diffusion, and bimolecular recombination.

3.3 High Plasma Density Ion Chamber Model Validation and Analysis

3.3.1 Comparison of Experimental and Simulation Results

A series of simulation results is shown in Figure 3.5. The parameters used correspond to experimental measurements of an ion chamber under a constant level of laser excitation, and with four different applied voltages. Each row of plots in the figure correspond to a different applied voltage: 0.1, 50, 120, and 200 V. The left column of plots shows the steady-state values of the electric field, electron density, and ion density. The right column of plots shows the four contributions to current from Eq. (B.6) multiplied by the plasma cross-section (A_p), ion drift, electron drift, ion diffusion, and electron diffusion. The black dotted line in the plots shows the total current, which is a constant across the electrodes at steady-state. The excitation beam in the simulation was a uniform beam with a width of 0.12 cm. The beam edges are identified in the plots with gold dotted lines. Similar simulations were made with a Gaussian excitation profile and matching total ionization rate, which yielded similar results, but with more gradual changes in behavior near the beam edges.

Effects that occur at high plasma density were apparent in the simulation results,

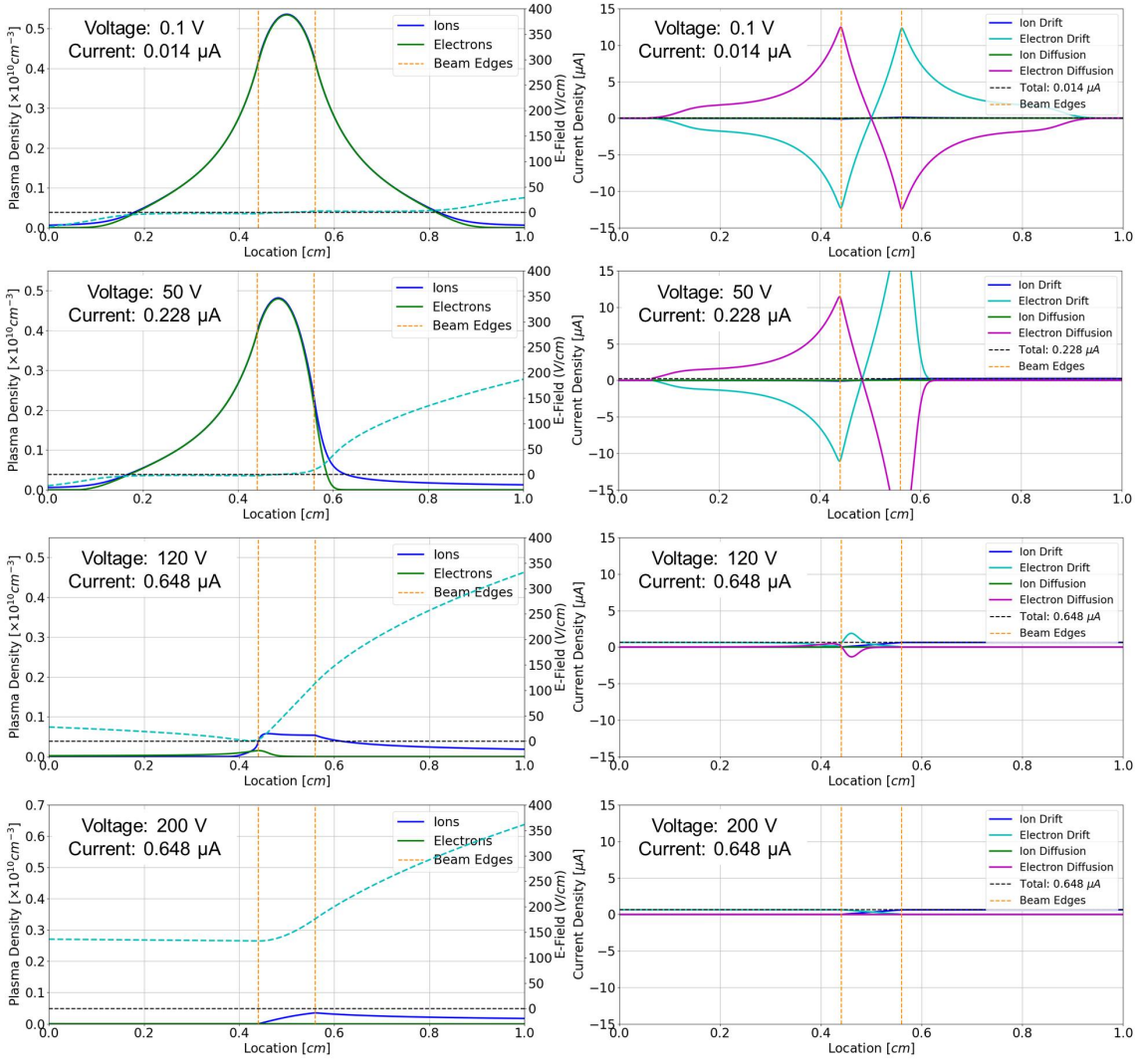

Figure 3.5: Series of simulations of the high plasma density ion chamber with increasing applied voltage: 0.1. 50, 120, and 200 V. [Left Column] Steady-state solutions of ion and electron density (left y-axis) and electric field (right y-axis). [Right Column] Steady-state solutions of current density. The predicted currents are listed on each graph; the total simulated ionization correspond to a current of 0.648 μA, which the system saturated to at voltages of 120 V or greater. Each component of current is shown independently, ion drift = $eA_p\mu_i E(x)n_i(x)$, electron drift = $eA_p\mu_e E(x)n_e(x)$, ion diffusion = $-eA_p D_i \frac{dn_i}{dx}(x)$, and electron diffusion = $eA_p D_e \frac{dn_e}{dx}(x)$.

which demonstrated that the complex processes were natural consequences of the Thomson model. In a low density chamber, space-charges and their effect on the

Table 3.1: Parameters used in simulation results shown in Figure 3.5, matching experimental conditions as closely as possible

Parameter	**Value**
Gas Temp.	338 K
Electron Temp.	3000 K
Cesium Density	3.5×10^{12} cm^{-3}
Plasma Cross-Sec., A_p	0.9×7.7 cm
Beam Location	Centered between electrodes
Pump Power	1.2 W
Beam Diameter	0.12 cm

electric field distribution are negligible. However, at sufficiently high density, space-charge effects are important, such as Debye shielding and ambipolar diffusion.

It is apparent in Fig. 3.5 that if the applied voltage is insufficient (<150 V) to overcome potentials due to space-charges, then the plasma is separated into a two regions: (a) an ion flow region near the negative electrode with a significant electric field, space charge limited ion motion, and near zero electron density, and (b) a bulk plasma with near zero electric field and nearly identical density fields of ions and electrons exhibiting ambipolar diffusion. This is exactly the situation described by Boag & Wilson [38]. The field across the ion flow region was shown to increase toward the negative electrode, causing: (a) ions to accelerate and (b) a reduction in ion density. These two effects balanced each other to maintain constant current density. This situation is also in agreement with Mott & Gurney [50], who studied single carrier crystals with all charge entering the region through the electrode. However, by including diffusion in the simulation, the results of Boag & Wilson have been extended to demonstrate the mechanism for current flowing through the bulk plasma (region b) and into the space-charge limited ion flow (region a).

The simulation results showed that opposite charges generally moved together through the bulk plasma (ambipolar diffusion), since any deviation from uniformity creates a strong localized field that pulled the charges back together. The plots of

current density in Fig. 3.5 demonstrate that the bulk plasma allowed a slight electric field to be present, which enabled current to pass through, and which balanced the effect of diffusion. At an applied voltage of $V_a = 200$ V the ionization chamber was in the saturation regime for this particular ionization rate. This situation is shown in Fig. 3.5(d). The bulk plasma vanished, shown by the positive electric field filling the space between the electrodes. The overlap of the ion and electron densities was greatly diminished, which caused recombination to be dramatically decreased to a negligible level. The progression of steady-state solutions with increasing voltage demonstrated that high density plasma interaction effects were expected to occur, and it was expected that at sufficiently high applied voltage, the field would penetrate through the plasma, recombination would become negligible, and the saturation current would become equal to the ionization rate.

Measurement and simulation of saturation curves for two different ionization rates in the regime of high plasma density are shown in Fig. 3.6. The ionization rate was varied by changing the Cs vapor temperature from 323 to 338 K resulting in a Cs density change from 1.2 to 3.5×10^{12} cm^{-3}. The laser power was kept constant. The measured saturation currents were 0.033 and 0.648 μA . The ionizing volume was approximated as a uniform cylinder with a diameter of 0.12 cm (beam $1/e$ diameter) and a length of 7.7 cm (window-to-window distance), which corresponded to average ionization rate densities of 2.4 and 46×10^{12} cm^{-3}s^{-1}.

Multiple parameters in the simulation were varied within the range of uncertainty, which demonstrated that the experimental measurements were bounded by simulation predictions. The parameters that were varied were electron temperature ($T_e =$ 338 - 3000 K), the plasma cross-sectional area ($A_p = 6.9$ - 13.9 cm^2), and location of the laser beam between the electrodes ($x = 0.5$ - 0.7 cm, with $x = 0$ at the high potential electrode).

The uncertainty in the electron temperature was due to generation at temperatures significantly above the neutral gas density, followed by rapid energy loss to

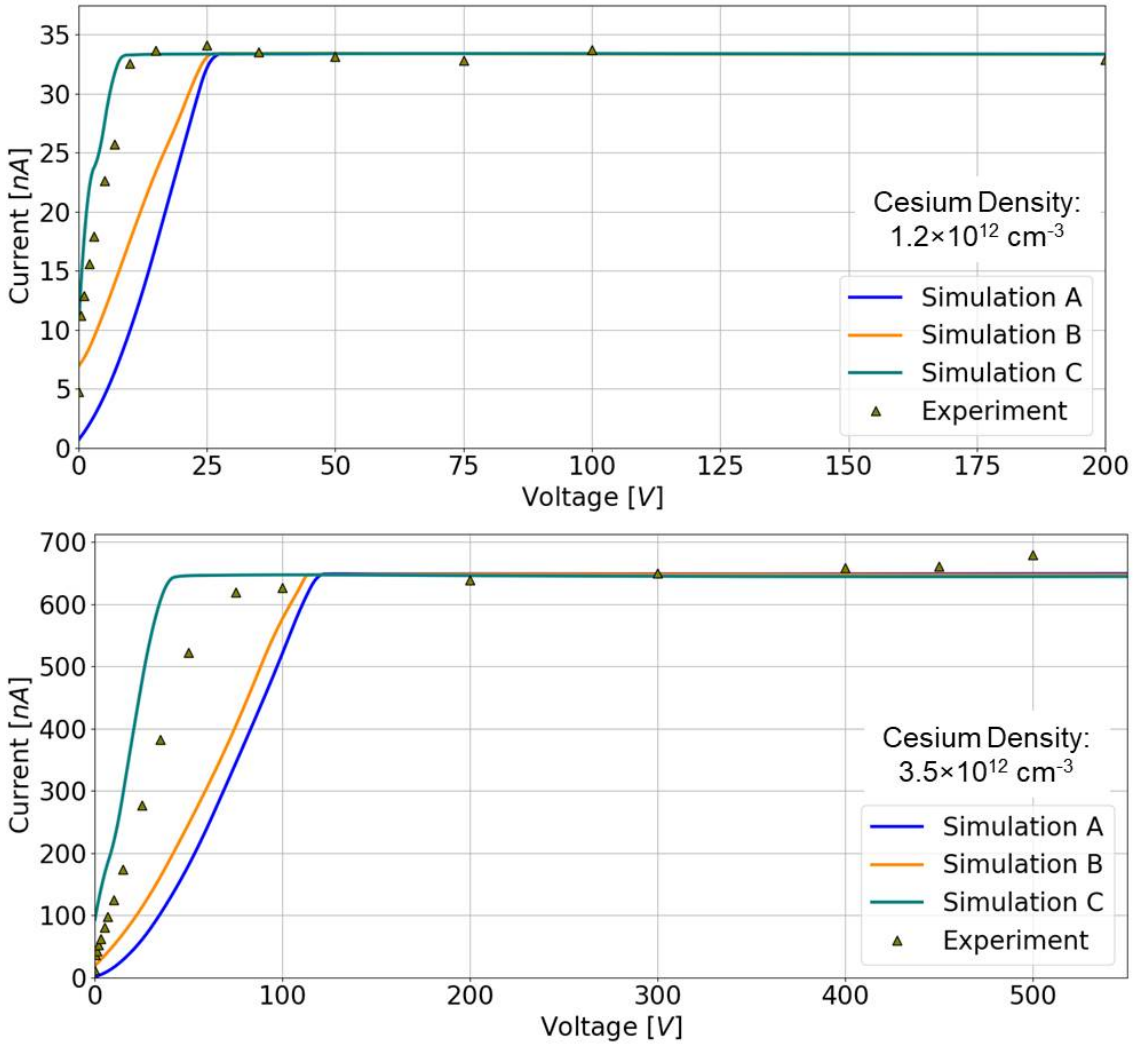

Figure 3.6: Measured and simulated saturation curves for two different ionization rates, corresponding to saturation currents of 0.033 and 0.648 μA and average ionization rate densities of 2.4 and 46×10^{12} cm^{-3}s^{-1}. The simulations were performed with variation within uncertainty of the following parameters: Simulation A: $T_e = 338$ K, $A_p = 0.9 \times 7.7$ cm^2, $x = 0.5$ cm; Simulation B: $T_e = 3000$ K, $A_p = 0.9 \times 7.7$ cm^2, $x = 0.5$ cm; Simulation C: $T_e = 3000$ K, $A_p = 1.8 \times 7.7$ cm^2, $x = 0.7$ cm.

buffer gas. Free electrons were generated in the system with excess kinetic energy of roughly 0.5 eV, which correspond to temperatures of 5500 K. The excess energy is due to the ionization mechanism (Penning ionization or photoionization from energy states near the $7P$ level), which is discussed in detail in Ch. 4. The electron

temperature was simulated as spatially uniform for simplicity and because it was the worst-case-scenario for the influence of electron temperature on the motion of the plasma. The electron temperature impacts the diffusion coefficient of the electrons via the Einstein relation, $eD_e = \mu_e k T_e$, which is the typical relationship between diffusion, mobility, and temperature. The elevated electron temperature was incorporated in the simulation as an increased electron diffusion constant, which caused increased diffusion of both ions and electrons in the bulk plasma via ambipolar diffusion. The uncertainty in electron temperature was simulated as either 338 K, which matched the neutral gas temperature, or 3000 K, which was approximately half of the free electron generation temperature.

The uncertainty in the cross-sectional area of the plasma in the experiment was due to lateral plasma motion. The details of lateral plasma motion cannot be incorporated into a one-dimensional simulation. Instead, the extent of the lateral motion was considered as an uncertainty and simulated as a plasma cross-sectional area that was larger than the excitation beam. The cross-sectional area was estimated to be between 1 - 2$\times$ the area of the electrodes, which was $A_p = 0.9 \times 7.7 = 6.9$ cm^2 or $1.8 \times 7.7 = 13.9$ cm^2. Lateral spread of the plasma is caused by two processes: (a) the electric field bent around the bulk plasma and (b) ions repelled by the space-charge region.

The uncertainty of the positioning of the beam between the electrodes was due to difficulty in alignment. The spacing between the electrodes was 1 cm, and the $(1/e)$ beam diameter was 0.12 cm. The positioning of the ion chamber around the beam was adjusted such that the beam was half way between the clipping points on the electrodes. The position of the beam centered between the electrodes was confirmed by observing the visible line of fluorescence in cesium gas along the beam path. However, the error in the beam positioning may have been ± 0.2 cm, and this uncertainty was incorporated into the simulation with beam center at either x=0.5 cm (centered between electrodes) or at $x = 0.7$ cm from the high potential

electrode.

The following three features of the measured saturation curves were replicated in simulation: (1) off-set current, (2) saturation voltage, and (3) saturation current. The off-set current was the current measured when a small voltage, 0.5 V, was applied. (The current was observed to be near zero when 0 V was applied, and rapidly increase to the off-set value with <0.5 V applied.) Simulations with either T_e = 3000 K or the laser beam center at $x = 0.7$ cm showed an off-set. The saturation voltage is the minimum applied voltage required to cause current saturation. The three simulations shown in Fig. 3.6 bound the saturation voltage and then plateau at the saturation current.

In further testing and simulation, agreement was demonstrated that changing the position of the pump laser beam between the electrodes shifted the saturation voltage, but did not significantly alter the saturation current. Comparison of measured and simulated saturation curves with beam center at either $x = 0.2$ cm or $x = 0.8$ cm is shown in Fig. 3.7. The intention of this test was for a qualitative comparison of changes in position, due to significant uncertainty in the position of the beam during testing. Additionally, the small difference in measured saturation current may be due to small laser power or thermal changes between the two tests. The results show agreement between test and simulation that saturation voltage is proportional to the transit distance of the ions (from the beam to the low potential electrode). This is understandable since it shows that higher voltage is required to collect low mobility ions at a longer distance. Measurements of steady-state current were made using an oscilloscope across resistor, R_2, which was done so that time-dependent behavior could be examined as well, which is described in Sec. 3.3.2.

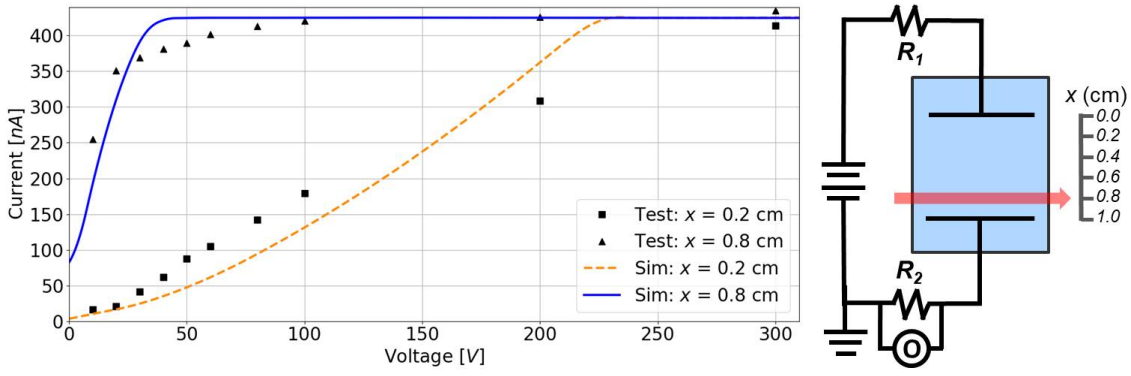

Figure 3.7: Qualitative comparison of ion chamber behavior while varying position of the pump laser beam between the electrodes. [Left] Measured and simulated saturation curves with the beam position varied between $x = 0.2$ and $x = 0.8$ cm. [Right] Diagram of the ion chamber and laser geometry with the beam at $x = 0.8$ cm. Measurements were made using an oscilloscope around resistor, $R_2 = 1.48$ MΩ.

3.3.2 Temporal Behavior Measurement and Analysis

The time-dependent behavior of the ion chamber was examined using an oscilloscope and a chopped laser beam, with results shown in Fig. 3.8. The diagnostic setup matched the diagram shown on the right in Figure 3.7. The excitation laser was held at a constant power throughout the experiment, and it was chopped at 10 Hz. The time-dependent laser power transmitted through the chopper was monitored with a photodiode, and it is shown as the black line in both plots in Fig. 3.8. Voltage applied to the cell was held constant, and each measurement of temporal current response was averaged 64 times. A comparison was made between the laser beam center held at $x = 0.2$ or 0.8 cm.

The results in Fig. 3.8 show that when the pump laser beam center is at $x = 0.2$ cm, and applied voltage was <50 V, the current decay once the laser was removed had a long tail. However, the decay was nearly instantaneous with the laser at $x =$

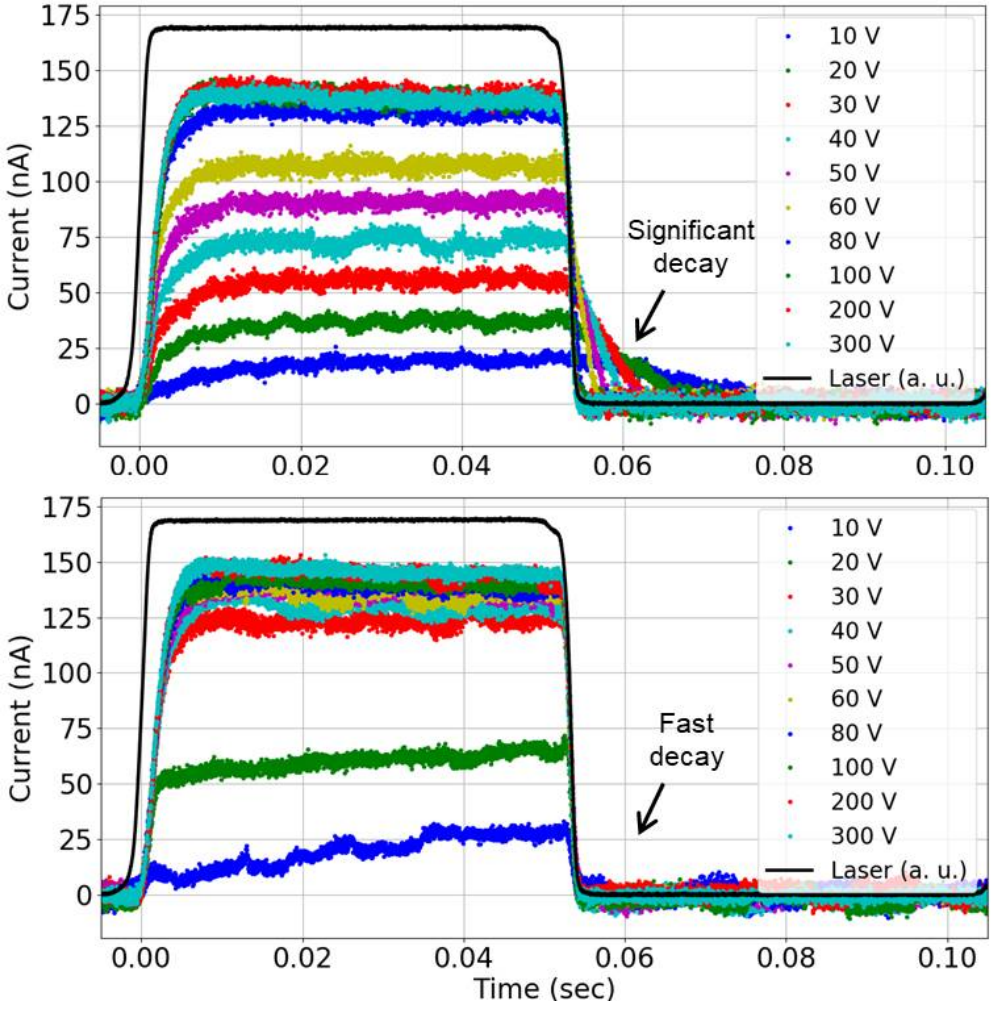

Figure 3.8: Time-resolved current response to pulsed excitation. A series of measurements were done with varying applied voltage on the ion chamber. [Top] Measurements with the pump laser centered at $x = 0.2$ cm, which demonstrated a significant signal decay time at low applied voltage. [Bottom] Measurements with the pump laser centered at $x = 0.8$ cm, which demonstrated a rapid signal decay time at all voltages.

0.8 cm for all applied voltages. This behavior can be explained by examining the ion transit time. With the beam at $x = 0.2$ cm and a low applied voltage, the ions slowly moved about 0.8 cm to the low potential electrode, which caused the noticeable tail on the current decay. When a high voltage was applied, the ions increased velocity,

and the decay time dropped. And, when the beam was at $x = 0.8$ cm, the ion transit distance was only about 0.2 cm, and the decay was immediate, even with a low applied voltage.

The decay time constant of the current across the ion chamber was similar to what was expected based on ion transit time. The current decay was fit with the function $I = A \exp({}^{-t}/_{\tau})$, where t is time and τ is the decay time constant. The measured decay time constants are shown in Figure 3.9. Error bars on the measurements were due to RMS deviation from the exponential fit. The time constants are only significant when the beam was at $x = 0.2$ cm and a low voltage was applied. The estimated transit time of an ion 0.8 cm from beam center to the negative electrode is shown as the black line. The velocity of the ion was based on the expected mobility of 9.1 cm^2/Vs at 333 K and the electric field neglecting space charge, $E = \frac{V_a}{d}$. Space charge likely played a role in the ion transit time, which may account for the difference between the measured and estimated current decay constants. However, the simple temporal analysis (ignoring space-charge) shows that the order-of-magnitude of the measured signal decay time was expected based on ion mobility. The mobility rate of a cesium ion through a helium and methane mixture is discussed further in Appendix B.

3.3.3 Measured Variation of Saturation Current with Electrode Bias

In the ion chamber, one electrode was biased and the other was nearly grounded (separated from ground by resistor $R_2 = 1.48$ MΩ, which was minimal compared to the resistance across the gap between the electrodes). The cell walls were electrically grounded via a strap connecting it to the grounded optical bench. The electric field across the ionized region in the laser beam were equivalent whether the biased electrode is positive or negative compared to ground. However, at high ionization

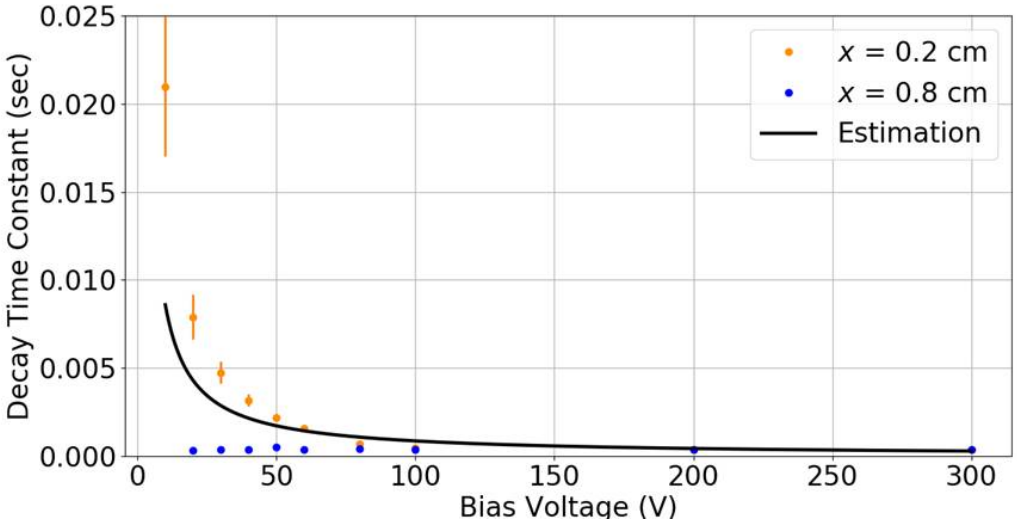

Figure 3.9: Measured and estimated time constants, τ, for ionization signal to decay after the pump laser beam is blocked. Measurements were made with the beam center at x = 0.2 and 0.8 cm. The estimated time constant corresponds to x = 0.2 cm.

rate, differences in measured saturation current were observed with the polarity of the bias.

Example measurements of saturation current with positive or negative bias are shown in Figure 3.10. These results are repeated in Appendix D along with all other ion chamber measurements. It was observed that at an ionization rate of 46×10^{12} cm^{-3}s^{-1}, the saturation current was 9% higher when the biased electrode was positive, rather than negative. Additionally, with a ionization rate of 19×10^{12} cm^{-3}s^{-1}, the current was 4% higher with positive bias. At rates of 7×10^{12} cm^{-3}s^{-1} or less, the difference in bias had a $< 1\%$ effect.

The bias-dependent behavior is believed to be caused by a small fraction of charged particles escaping the electric field between the parallel plate electrodes, and it is diagramed in Fig. 3.11. The field decreases rapidly outside of the parallel plates; however, it does not drop to zero. The difference between the positive

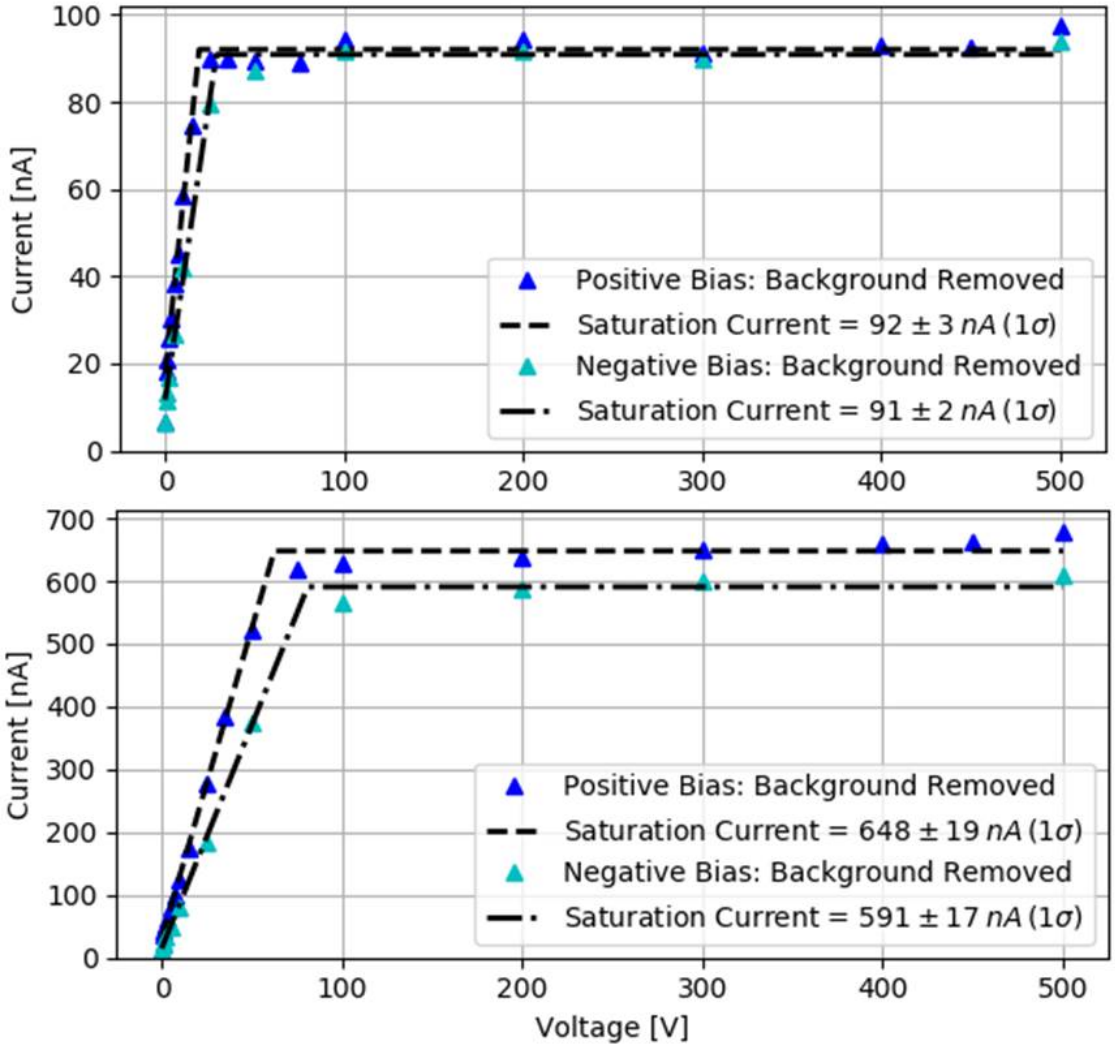

Figure 3.10: Comparisons of saturation curves measured with the biased electrode having a positive or negative voltage compared to ground. [Top] Measurement at cesium density of 1.8×10^{12} cm^{-3}, laser power of 1.2 W, and ionization rate of $7{\times}10^{12}$ cm^{-3}s^{-1}, demonstrating 1% difference in saturation current with bias. [Bottom] Measurement at cesium density of 3.5×10^{12} cm^{-}3, laser power of 1.2 W, and ionization rate of $46{\times}10^{12}$ cm^{-3}s^{-1}, demonstrating 9% difference in saturation current with bias.

and negative bias is due to the multiple orders-of-magnitude difference in mobility between electrons and ions. If the biased electrode is positive, then the small electric field outside the plates is sufficient to cause any escaped electrons to reverse

direction and be collected at the electrode. However, if the biased electrode is negative, the field is too weak to alter the course of an escaped ion sufficiently, and it ultimately collides with the grounded chamber wall. This result indicates that a positive bias should be used in high density ion chamber measurements, which was done throughout the results shown in this dissertation.

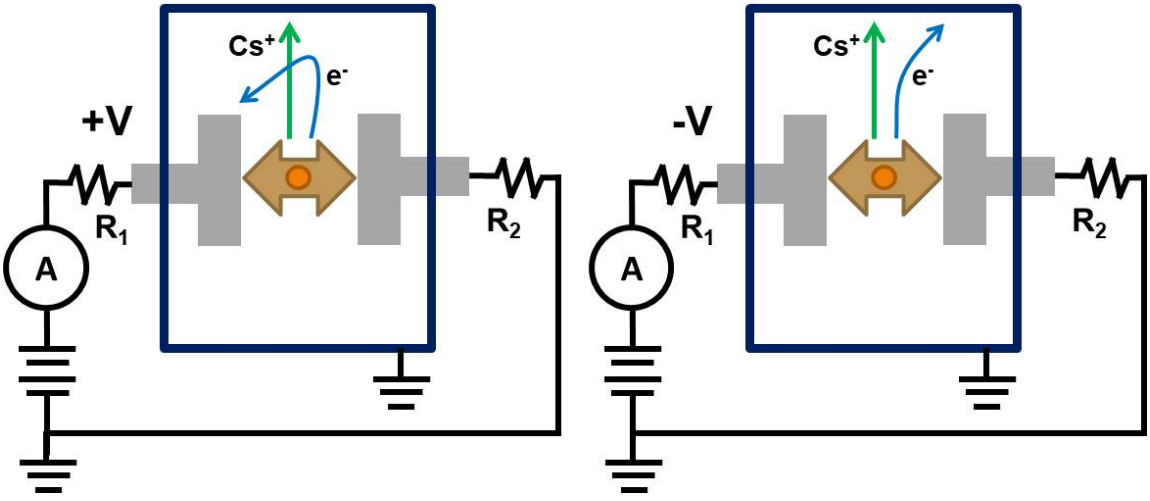

Figure 3.11: Diagram of observed bias-dependent behavior. The main signal is shown as arrows pointing away from the pump laser beam in the center of the chamber; this represents electrons and ions moving to their respective electrode. A representative path is shown for an electron, e^-, and an ion, Cs^+, which escape the parallel plates [Left] The high mobility electron is drawn to the positively biased electrode due to the small field at the edge of the chamber, and it contributes to the measured signal. [Right] Both the ion and electron collide with the grounded cell wall, and do not contribute to the measured signal.

3.3.4 Verification of Simulation Results

To verify that the physics of the Thomson model have been correctly coded into the simulation, the output of the simulation has been compared against the analytic analysis of Boag & Wilson. [38] They derived Eq. (2.1) for predicting the saturation curve of a high plasma density from the Thomson model under the following conditions: (1) uniform ionization from electrode-to-electrode (2) free-electrons are the

negative charge carriers, rather than negative ions, and (3) negligible diffusion. To generate the equation, Boag & Wilson predicted the distance into the plasma that the electric field would reach, then defined regions of bulk plasma with negligible electric field and space-charge limited ion flow. They argued that the ion flow region would have negligible recombination and that the bulk plasma would have roughly uniform density and recombination. Based on this, they showed that the current drawn would be a fraction of the saturation current calculated by the width of the ion flow region divided by the total distance between the electrodes.

The results of our one-dimensional simulation have been compared against the equation derived by Boag & Wilson, shown in Fig. 3.12. The main difference between the two models is that the one-dimensional simulation includes diffusion. The simulation assumed that uniform excitation occurred over a $0.9 \times 7.7 \times 0.97\,\mathrm{cm}$ volume. Ionization was simulated filling 97% of the space between the electrodes, since filling 100% caused numerical instability. The ionization rate in the simulation was $6.0 \times 10^{11}\,\mathrm{cm^{-3}s^{-1}}$, which corresponded to a saturation current of $0.648\,\mu\mathrm{A}$. The electron temperature was 3000 K, which accentuated the impact of ambipolar diffusion and determine if diffusion caused a difference in the predicted saturation curve.

The saturation curves from the analytic equation derived by Boag & Wilson and the full simulation, which includes diffusion, were nearly identical. The differences in the simulation results were a reduced saturation current ($< 3\%$) and a 39 nA off-set current. These minor differences are likely due to the impact of diffusion. The similarity of the analytic and simulated results is verification that the code was implemented correctly. An example simulation result with an applied voltage of 50 V is shown on the right side of Fig. 3.12.

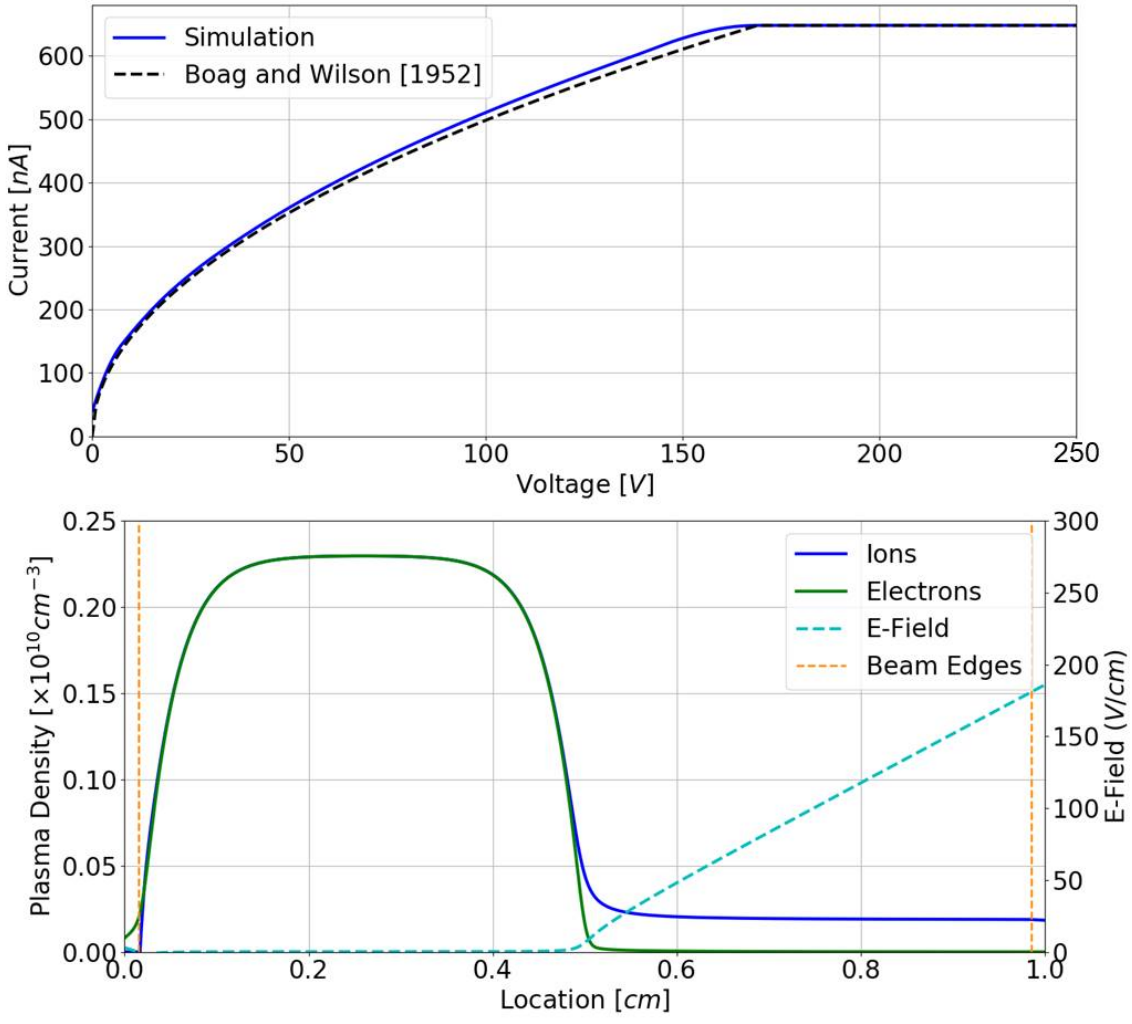

Figure 3.12: [Top] Comparison of analytic and simulated saturation curves for near uniform ionization. The analytic prediction derived by Boag & Wilson is Eq. (2.1). [Bottom] Example simulation with an applied voltage of 50 V.

3.3.5 Sensitivity Study: Mobility and Recombination Rate

A simulation sensitivity study was done to examine parameters that are predicted to impact the slope of the saturation curve at high density. This was done to determine if a high density ion chamber might be able to be used to measure physical properties of a plasma besides ionization rate. The two parameters investigated were mobility, μ_i (which also determines diffusion coefficient through the Einstein relation), and the

recombination rate, C_R (which also impacts the peak plasma density). The predicted saturation curves of the nominal case, a case where ion mobility was decreased by a factor-of-two, and a case where the recombination rate coefficient was increased by a factor-of-two are shown in Figure 3.13. Mobility was decreased from 9.1 to 4.6 cm^2/Vs and recombination was increased from 1.0 to 2.0×10^{-7} cm^3/s, which is discussed further in Appendix B. The nominal case was identical to Simulation B shown on the right side of Figure 3.6, and the other cases have equivalent parameters except mobility or recombination. The results show sensitivity of the system to mobility, but not the recombination rate. This indicates that a measurement of the slope in a high density ion chamber could be used to measure ion mobility; however, it cannot be used to measure recombination rate or plasma density, since significant variations of the quantities cause only minor change to the saturation curve. It should be noted that the sensitivity study was all done in the high plasma density regime, and the sensitivity of these parameters is likey to be different at significantly lower plasma density. For example, at low plasma density, the slope of the saturation curve is likely to be highly sensitve to the recombination rate, but at high density, the system is insensitive.

Multiple measurements of plasma density in rubidium DPAL gain media have been published over the past decade [30] [31] [32]. Each test had a similar setup which involved a pulsed ion chamber. The authors used a chopped laser light and a lock-in amplifier to measure current excited by the laser induced plasma. From these measurements, they drew conclusions about the peak density of the plasma contained between the electrodes. However, their argument ignored space-charge, and could only be valid in a low plasma density regime. The authors applied a maximum of 10 V to the ion chamber, which did not achieve saturation behavior, which makes it unclear what density regime was present. The conclusions of the reports would be inaccurate in a high density regime since Debye shielding would have protected the bulk plasma from the field that was used to measure it.

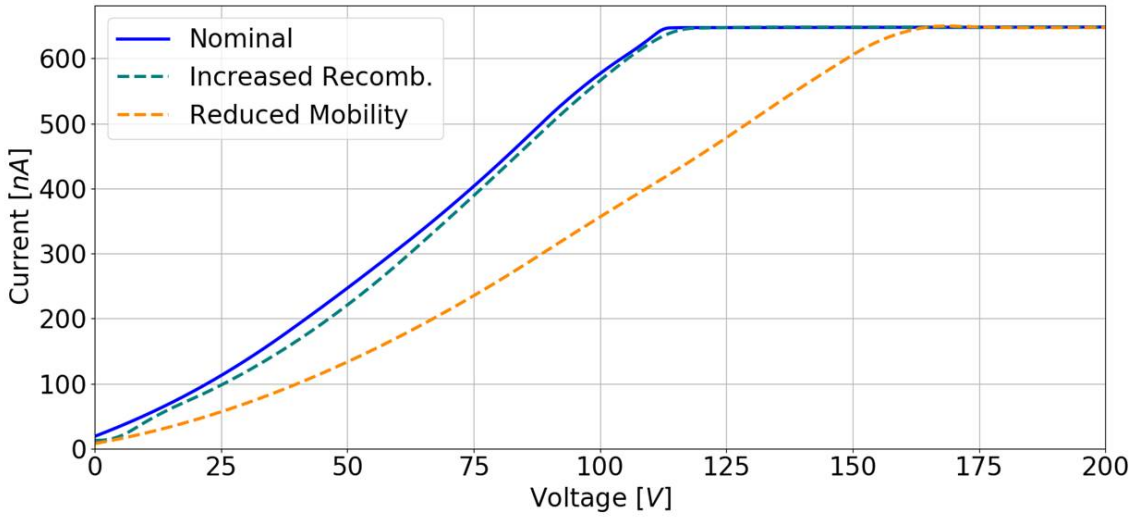

Figure 3.13: Results of numerical simulation sensitivity study. Simulated current versus applied voltage for three sets of parameters: (a) [solid blue] Nominal parameters, $\mu_i = 9.1$ cm^2/Vs, $C_R = 1.0{\times}10^{-7}$ cm^3/s, (b) [cyan dashed] Increased recombination, $\mu_i = 9.1$ cm^2/Vs, $C_R = 2.0{\times}10^{-7}$ cm^3/s (caused the peak plasma density to drop by 25%), (c) [orange dashed] Decreased mobility, $\mu_i = 4.6$ cm^2/Vs, $C_R = 1.0{\times}10^{-7}$ cm^3/s

3.3.6 Electrode Surface Chemistry

It is unlikely that the surface chemistry between cesium ions and copper electrodes altered measurements in the ion chamber under investigation; however, these processes could impact the accuracy of other ion chamber measurements using different materials. If the ion has sufficient energy to cause ionization when it strikes an electrode, then it creates a higher signal than would be measured otherwise. This can occur due to secondary electron emission, also called Auger emission, or negative ion sputtering. Secondary electron emission was unlikely in the current experiment due to the low ionization energy of cesium, 3.89 eV, compared to the work function of the copper electrodes, roughly 5 eV for either copper or copper oxide [49], and due to the low kinetic energy of the ions in the thick buffer gas. Negative ion sputtering has been observed by bombardment of a copper electrode with heavy cesium ions,

knocking free negative copper ions. However, this process has only been observed with a high energy cesium ion beam (1.1 keV) and only with about 2% efficiency. [51]

3.4 Chapter Summary and Conclusions

An ion chamber operated with high plasma density has been investigated with experiment and simulation. Conditions atypical for ion chamber operation, but similar to what is encountered in a Cs DPAL were studied. The ionization rates investigated were between 10^{12}-10^{14} $cm^{-3}s^{-1}$, 7 orders-of-magnitude above standard ion chamber operation. The main question to be answered was whether the saturation current under these conditions (due to a laser beam focused between two electrodes) could still be used to measure the ionization rate.

Modeling the behavior of such an ion chamber required accounting for carrier recombination, diffusion, and drift, as well as localized ionization within the pump laser beam. A numerical algorithm was developed to solve the well known governing equation of the system, the Thomson model, without any simplifying assumptions. The results showed that a variety of processes occur only at high plasma density, such as space-charge limited ion flow, Debye shielding preventing the electric field from penetrating a bulk plasma region, and ambipolar diffusion across the bulk with possibly elevated electron temperature. The results also showed that if sufficient voltage can be applied to the system to cause saturation, without electric field exceeding the threshold for breakdown, then the saturation current is a direct measure of the ionization rate. No processes alter the accuracy of the diagnostic; for example, Debye shielding does not cause strong localization of voltage drop at the plasma edge or significant reduction of the breakdown voltage.

An ion chamber was built to validate numerical simulations. Saturation curves

were measured for different ionization rates (varied by changing the Cs vapor density at constant laser power), and with changing the location of the ionizing region (laser focus) between the electrodes. Agreement between measurement and simulation demonstrated that the complex processes at high density are well described by the Thomson model, which increased confidence in the accuracy of the diagnostic.

In summary, an ion chamber at high plasma density was found to be an effective direct diagnostic for ionization rate measurement. The following recommendations are made to ensure accuracy. (1) Use of an ion chamber is only possible if current saturation is achieved below the breakdown voltage. Optimum design to achieve this includes (a) minimal ionized volume and (b) plasma generation as close to the ion collecting electrode as possible. The simulation of the Thomson model can be used to predict if an ion chamber geometry will satisfy this condition. (2) The biased electrode should be positive compared to the grounded walls, which allows collection of any high mobility electrons that escape the region between the electrodes.

Chapter 4

Prediction of Pump Laser Induced Ionization Rate

The fundamental objective of the investigation was to quantify how well laser induced ionization processes are understood in a cesium DPAL by directly measuring laser induced ionization rates, and comparing to expected rates based on collisional and photon excitation processes that have been previously reported. The first part of accomplishing this goal was to review pertinent literature, tabulate known ionization processes, and develop a simulation that could predict the measured total ionization rate. This chapter details the development of the simulation of pump laser induced ionization in an ion chamber. Further simulation details, including a table of all parameters and full specification of all solved equations is included in Appendix C.

4.1 Simulation of Ionization at a Point in the Ion Chamber

Laser induced ionization after resonant excitation in a cesium gas is known to occur due to multistep processes involving collisions or photon energy transfer. Due to the complexity of the processes and the experimental setup, prediction of the saturation current measured in the ion chamber required computational simulation.

The behavior of the laser excited gas at each point in the simulation was determined by solving a system of ordinary differential equations (ODEs). The full set of equations is provided in Appendix C. The inputs to the equations were incident spectrally-resolved pump power, beam diameter, cesium density, buffer gas composition, temperature, and pressure. The equations included the following processes: spectral pump absorption, fluorescence, spin-orbit mixing, quenching, energy pooling, Penning ionization, and photoionization. Solutions to the system of ODEs were steady-state populations for the eleven energy states shown in Fig. 4.1, pump absorption, and most importantly, ionization rate. The labeling of the eleven states in ascending energy order as $n_0, n_1, ..., n_{10}$ is shown.

The system of ODEs in Appendix C, Eqs. (C.5 - C.15), is a system of 11 equations wtth 11 unknown variables. The first 10 equations are the ODEs, and the 11th is a conservation of mass equation showing that the total population density of all energy states of cesium must equal the cesium density. The ODE equations each have the form (written for example energy state n_j) $\frac{dn_j}{dt} =$, which is followed by expressions for the rate of all processes adding to or subracting from the population of state n_j. The equations are then solved at steady-state, which indicates that each temporal derivative is equal to zero. Finding the values of n_0 to n_{10} that cause all of the equations to be equal to zero is referred to as "root solving". This operation has been accomplished computationally using the Python 2.7 function "scipy.optimize.fsolve"

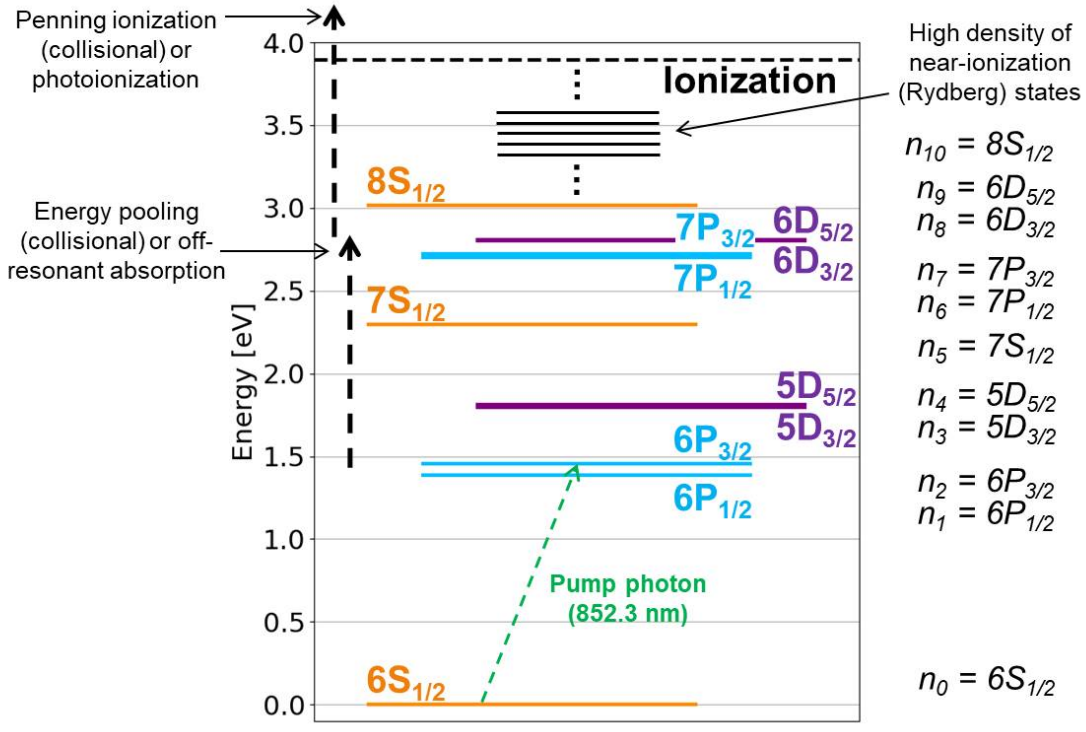

Figure 4.1: Cesium energy-state diagram showing collisional and photon pathways to ionization after 852.3 nm absorption from the ground state.

from Scipy 1.2.1 using the Powell Hybrid Method. Based on the incident pump laser intensity and the state of the gas (temperature, pressure, density, and composition), the system of ODEs is solved to predict the behavior of the system at a point in the ion chamber.

An approximation made in the ionization model that ions and electrons are immediately pulled to the electrodes once they are generated. This assumption is accurate for an ion chamber operated above saturation, since in this regime, recombination is negligible. The model also ignores the finite rate at which fresh cesium diffuses into the beam after cesium ions have been drawn to the electrodes, since diffusion is negligible for the beam widths and ionization rates investigated. Ion mobility in a 6:1 mixture of helium to methane at 854 torr and 333 K has been estimated to be

9.1 cm^2/Vs (see Appendix B). The diffusion coefficient is approximately determined by mobility via the Einstein relation, which corresponds to a diffusion constant of 0.25 cm^2/s. Estimating the rate of fresh cesium diffusion into the beam has been done in the same manner as Sheldon Wu by estimating the rate of diffusive transport by $\Delta n D/\Lambda^2$, where Δn is the density difference between cesium inside and outside the beam, D is the diffusion coefficient, and Λ is the characteristic length, which is $r/2.4$ where r is the beam radius [22]. Using this formula at the highest ionization rate in this analysis, 1.4×10^{13} $cm^{-3}s^{-1}$, in a cesium density of 2.2×10^{12} cm^{-3}, and with a beam radius of 0.06 cm, results in a cesium density reduction of less than 2% in the beam to cause diffusion to replenish cesium as fast as ions drift to the electrodes. The 2% reduction was significantly lower than uncertainty in experimental measurements.

The analysis strategy for handling uncertainty in kinetic rate constants was to use the worst-case-scenario, meaning the rate in the range of uncertainty that would cause maximum ionization. This was done to simulate an upper bound on the theoretical ionization rate, which will be discussed further in analysis of the comparison of measurements and prediction in Sec. 5.3. For example, this meant that rates for collisional Penning ionization and cross-sections for photoionization used in simulation corresponded to the largest measurements of rates that have been published, discussed in Section 4.7. Additionally, this meant that relaxation rates were minimized. For example, rates for quenching from states above $6P$ are not well known, so these relaxation rates were not included in the simulation (the rates were effectively set to zero), and only fluorescent decay has been included, discussed in Section 4.4.

4.2 One-Dimensional Simulation of the Geometry of the Ion Chamber

The geometry of the experiment required one-dimensional simulation to account for pump power variation along the propagation axis of the ion chamber. The 7.7 cm propagation axis was typically discritized into 21 mesh points (zm_0 to zm_{20}) with 20 cells between (z_0 to z_{19}). This mesh density was found to result in less than 1% error compared to simulation with 1000 mesh points in simulations at high pump power and alkali density.

Each cell in a simulation had the same alkali density, buffer gas mixture, pressure, and temperature. The difference between the cells was the incident spectrally-resolved pump beam, $I_\nu(\nu, zm_j)$, which is defined at the mesh points zm_j between cells. The behavior of each cell was calculated in series, beginning with the cell at the entrance window. The incident pump spectrum was input into the system of ODEs, Eqs. (C.5 - C.15), which were solved to determine the populations of all energy states and the ionization rate, $Q(z_i)$ (units = $\mathrm{cm}^{-3}\mathrm{s}^{-1}$) in cell z_i. Based on the populations, changes to the pump spectrum due to absorption in the cell were calculated to determine the incident pump spectrum on the following cell. This process was repeated until the behavior of the system was calculated in each cell in the system.

The outputs of the simulation were: (a) spectrally resolved pump intensity at each mesh point (including the spectrum transmitted through the system), (b) populations of all energy states in each cell, and (c) ionization rate from each cell. The contributions from each cell were summed to determine predicted saturation current, I_{sat} measured by the ion chamber, shown by Eq. 4.1, where A_{beam} is the pump laser beam cross-sectional area, and Δz is the uniform mesh spacing.

$$I_{sat} = eA_{beam} \sum_{i=0}^{n} Q(z_i)\Delta z \tag{4.1}$$

Example simulation outputs are shown in Figure 4.2 when input pump power is 1.2 W and cesium density is 2.2×10^{12} cm^{-3}. The predicted ion chamber saturation current was 131 nA, which was predicted by numerically integrating the simulated ionization rate curve.

4.3 Pump Laser Absorption

Spectrally-resolved pump intensity was calculated at each mesh point along the pump propagation axis. The simulated pump spectrum was a Gaussian function with full width at half maximum (FWHM) and center frequency based on experimental measurements. The pump emission spectrum and gas absorption spectrum were resolved on a dense uniform grid of 10,000 points, centered on the pump center frequency, and with a total width of 6× the measured FWHM. The cesium absorption spectrum has been calculated based on pressure broadening and shifting by the buffer gas constituents and cesium hyperfine spectral structure. Details of absorption spectrum calculation are in C.1 based on information compiled by Daniel Steck [52] and Pitz *et al.* [53]. An example of the spectral behavior incorporated in the ion chamber simulation is shown in Figure 4.3. The plot shows the incident and transmitted pump spectrum as well as the absorption spectrum with hyperfine structure.

An assumption inherent to one-dimensional simulation is uniformity of behavior in the two axes that are not discretized. This is handled in the simulation by assuming that the pump beam is perfectly collimated with uniform circular intensity profile at a specified diameter. In comparison of experimental to simulated results, the simulated

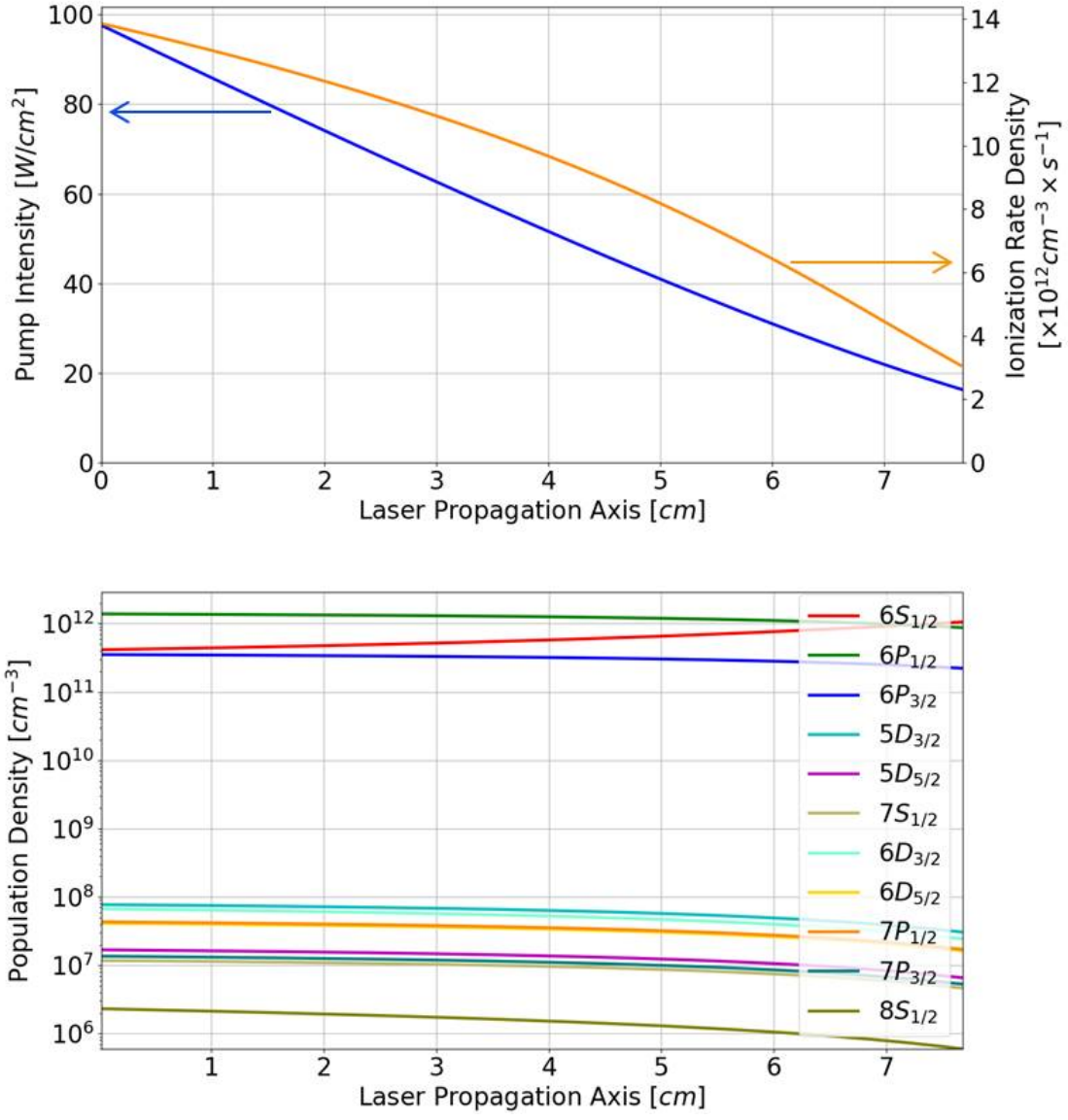

Figure 4.2: Example simulation results with input pump power = 1.2 W, temperature = 343 K, cesium density = 2.2×10^{12} cm^{-3}, and buffer gas = 6:1 mixture of helium to methane at 806 torr. The total integrated ionization rate over the 0.087 cm^3 excited volume (with a beam diameter of 0.12 cm) was 8.2×10^{11} Hz, which is equivalent to a predicted saturation current of 131 nA.

beam diameter was the $1/e$ point of the Gaussian fit to experimental intensity profile measurements. Matching the $1/e$ diameter was chosen since a circular uniform beam

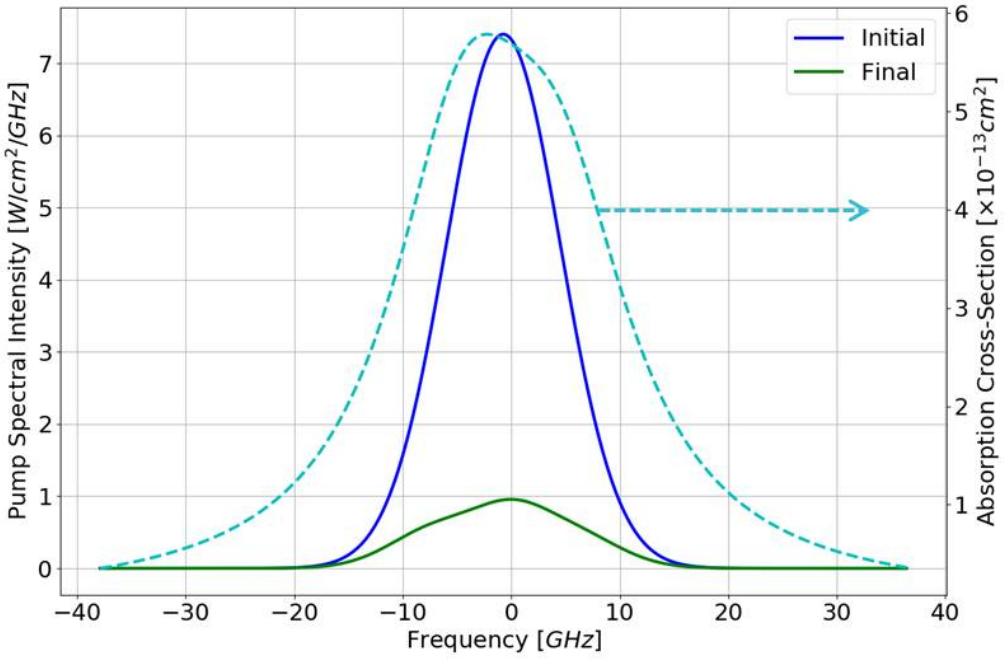

Figure 4.3: Example spectral intensity of the laser and the Cs absorption cross-section [dashed line] as a function of $\nu - \nu_0$ where ν_0 is the respective center frequency. The incident [blue solid line] and transmitted [green solid line] laser spectra are shown. The absorption spectrum was calculate at temperature = 343 K, cesium density = 2.2×10^{12} cm^{-3}, and buffer gas = 6:1 mixture of helium to methane at 806 torr with asymmetry due to hyperfine structure.

and a Gaussian beam that share this width have the same total power and peak intensity. This is considered a highest-ionization or worst-case scenario since the uniform beam has much more area at the peak intensity compared to the Gaussian.

4.4 Fluorescence and Quenching

Relaxation from upper energy states has been incorporated into simulation as fluorescence and collisional quenching. Fluorescent decay from each energy state in the

system (shown in Fig. 4.1) with branching ratios to lower states, if the transition is allowed, are listed in Table C.2 of Appendix C.2.

Quenching is a collisional process that results in an excited cesium dropping in energy with a release of heat. It was included in simulation only from the $6P$ states in collision with methane. Quenching due to collisions between cesium atoms has a significant cross-section, but the low density of cesium compared to buffer gas causes the rate to be negligible. The cesium $6P$ quenching cross-section due to collisions with helium has been measured to be $<10^{-19}$ cm^2 [54], which has a negligible effect on the system.

The cross-section for collisions with methane has been included based on measurements of the upper-bound of rubidium / methane quenching, which were 1.9×10^{-19} cm^2. [5] The rubidium measurement was shown to be more than an order-of-magnitude smaller than previous measurements, which was achieved through careful handling of radiation trapping, and similar measurements in cesium have not been made. The quenching was small compared to the fluorescence rate from the $6P$ levels, but it was included for completeness.

Wallerstein suggested that quenching from the high states may be significant; however, the rates are not well known. [12] Quenching rates from above the $6P$ states have not been included in simulation. Inclusion of quenching from high energy states would cause a decrease in the predicted ionization rate, which is discussed further in Sec. 5.3. All cross-sections used in simulation are listed in Table C.3.

The rates of collisional processes in this report, such as quenching, have been calculated by multiplying collision cross-sections by the mean relative thermal velocity of the collision partners, as shown in Eq. (4.2), where R is the rate (units = cm^3/s), σ is the collision cross-section, $v_r(T)$ is the temperature dependent relative velocity, and $m_{1,2}$ are the masses of the collision partners. The kinetic equations, Eqs. (C.5 - C.15), use v_r to represent relative velocity between two colliding cesium atoms, $v_{r,He}$

between a cesium and a helium, and v_{r,CH_4} between a cesium and a methane.

$$R = \sigma v_r(T), \text{ where } v_r(T) = \sqrt{\frac{8kT}{\pi}\left(\frac{1}{m_1} + \frac{1}{m_2}\right)} \tag{4.2}$$

4.5 Spin-Orbit Mixing

Spin-orbit mixing of the $6P$ energy levels has a significant impact on pump absorption in cesium gas if methane is present, and it has been included in simulation. The $6P$ energy levels are close enough that they are thermally linked, and their rates are related through the law of detailed balance, as shown in Eq. (4.3), where $\sigma_{so,1\leftarrow 2}$ is the spin-orbit mixing cross-section from $6P_{3/2}$ to $6P_{1/2}$, $\sigma_{so,2\leftarrow 1}$ is the reverse rate, and ΔE is the difference in energy between the states, which is 554 cm^{-1} for cesium.

$$\sigma_{so,1\leftarrow 2} = 2\sigma_{so,2\leftarrow 1}\exp(-\Delta E/kT) \tag{4.3}$$

4.6 Excitation from the $6P$ States

Energy pooling is a collisional process between two excited cesium atoms in the $6P$ states, resulting in one being promoted to a doubly excited state and the other relaxing to ground ($6S_{1/2}$). Pooling targets excitation to states that are nearly resonant with the sum of the energy in the collision partners, which are the states $7P$, $6D$, and $8S$ in cesium. Energy pooling can be endo- or exothermic, with a small preference for exothermic, which is determined by the energy defect of the reaction, ΔE (defined to be the difference between the sum of the collision partners and the final highly excited state). Measurements of energy pooling between the first excited P levels of a range of alkali have been tabulated and analyzed by Wallerstein *et al.* [55]. They

found that rates were largely independent of the alkali gas, and was clearly dependent on ΔE. They fit all of the measured data to develop the empirical formula in Eq. (4.4) where σ_{ep} is the energy pooling cross-section. The fit included measurements in the temperature range of 350 - 597 K. Fifteen different energy pooling reactions were included in the simulation between all combinations of the two initial states and five final states, with cross-sections listed in Table C.3. Pooling rates that have not been measured previously were estimated using Eq. (4.4). Also, the total energy pooling rates for all combinations of collisions between the $6P$ states are defined by Eqs. (4.5).

$$\sigma_{ep} \approx \begin{Bmatrix} 3.58 \pm 1.8 \times 10^{-14} \exp\left[-0.71 \pm 0.28 \left({}^{\Delta E}/_{kT}\right)\right]; \text{ if } \Delta E > 0 \\ 1.60 \pm 0.5 \times 10^{-14} \exp\left[+0.84 \pm 0.04 \left({}^{\Delta E}/_{kT}\right)\right]; \text{ if } \Delta E < 0 \end{Bmatrix} \tag{4.4}$$

$$\sigma_{ep,11} = \sum_{i=6}^{10} \sigma_{ep,0i\leftarrow 11}, \sigma_{ep,12} = \sum_{i=6}^{10} \sigma_{ep,0i\leftarrow 12}, \sigma_{ep,22} = \sum_{i=6}^{10} \sigma_{ep,0i\leftarrow 22} \tag{4.5}$$

There are no resonant transitions from the $6P$ energy states with 852 nm pump light; however, it is possible for photon excitation to occur via the far wing of an absorption line. The closest resonance is between the $6P_{1/2}$ state and the $6D$ states, which has an offset of about 10 THz. These processes have not been included in ionization modeling since they are expected to be negligible compared to energy pooling at pressures near 1 atm and intensities less than 100 W/cm^2. This estimation assumes a Lorentian lineshape and the high estimate of the pressure broadening coefficient for the $6D$ states of 55 MHz/torr used by Knize *et al.* [23]. Excitation due to off-resonant absorption may be important at higher pressures and intensities, and it is more important in rubidium due to closer proximity of resonance. Wallerstein *et al.* show that further investigation of the lineshape is needed to determine if non-Lorentzian features in the wings could cause significant absorption. [55]

4.7 Collisional and Photon Ionization Processes

Penning ionization can occur during a collision between a cesium at an energy state $7P$ or higher and the relatively large population of excited cesium in the $6P$ states, resulting in one cesium becoming ionized, and one relaxing to the ground state. The process was examined thoroughly in rubidium by Barbier and Chéret [56]. The authors found Penning ionization to be a highly efficient ionization mechanism (near gas kinetic). Measurements showed slightly faster rates for D states compared to S states, and for states with different orbital number. Rates from P states could not be measured with the experimental setup; however, these rates are expected to be similar. Barbier and Chéret also measured atomic Penning ionization to be roughly two orders-of-magnitude faster than associative or Hornbeck-Molnar ionization. (Associative and Hornbeck-Molnar ionization are processes that involve molecular cesium dimer formation.) Similar rates have not been measured for cesium; however, since orbital number was not found to be a significant factor, collisional ionization processes are expected to be similarly fast. Penning ionization has been incorporated in the simulation at $\sigma_{pen} = 5 \times 10^{-8}$ cm^3/s, shown in Table C.3, which corresponds to the highest measurement of Barbier and Chéret. Associative and Hornbeck-Molnar ionization has not been included since these were found to be negligible compared to Penning ionization.

Absorption of a single 852 nm pump photon from any cesium state $7P$ or higher results in photoionization. Measurements and theoretical predictions in potassium by Zatsarinny & Tayal [57] and in rubidium by Duncan *et al.* [58] generally show good agreement. These results generally show that a high estimate of the photoionization cross-section from the $7P$, $6D$, and $8S$ states in cesium (resulting in roughly 0.5 eV of excess energy) is $\sigma_{photo} = 0.2 \times 10^{-16}$ cm^2, which was also the estimate used by Knize *et al.* [23]. This cross-section has been incorporated into ionization simulation, as shown in Table C.3. The photoionization rate at the DPAL laser wavelength,

895 nm, are expected to have similar photoionization cross-sections to the DPAL pump wavelength of 852 nm.

Nonlinear two-photon absorption of 852 nm light from the cesium $6P$ energy states directly causes ionization. This process was examined by Geltman [59] who calculated a rate of 5.9×10^{-29} cm^4/W. This process has not been incorporated into simulation since it has a negligible effect on DPAL operation.

Ionization rate at a point in the ion chamber, was calculated based on the Penning and photon ionization rates. First, in cell z_i, ODE Eqs. (C.5 - C.15) were solved to steady-state to calculate the predicted populations of the highly excited states n_6 to n_{10}. Eqs. (C.5 - C.15) include terms for population leaving states n_6 to n_{10} due to Penning and photon ionization. The ODEs assume that the system is inside an ion chamber at saturation, so there are no terms for recombination of ions and electrons. Second, once the populations of states n_6 to n_{10} have been calculated, Eq. (4.6), is used to calculate the ionization rate, $R_{ion}(z_i)$, in cell z_i from those states due to Penning and photon ionization. In the ionization rate calculation, the total pump laser intensity I_{pump} at mesh point zm_i is used to calculate the photoionization rate inside cell z_i. This is a numerical approximation, which ignores pump intensity reduction as the pump propagates through cell z_i, from mesh point zm_i to zm_{i+1}. However, error associated with this approximation is decreased by reducing the uniform mesh spacing, Δz, and sufficient mesh density was used in analysis to cause negligible error, as described in Sec. 4.2.

$$R_{ion}(z_i) = \left\{ \sigma_{photo} \frac{I_{pump}(zm_i)}{h\nu} + \sigma_{pen} v_r \left[n_1(z_i) + n_2(z_i) \right] \right\} \sum_{i=6}^{10} n_i(z_i) \tag{4.6}$$

4.8 Electron / Ion Recombination

Electron / ion recombination is critical in determination of plasma density in a CW DPAL; however, an ion chamber is not the appropriate tool for measuring this rate. It was shown in Sec. 3.3.5 that recombination in a high plasma density ion chamber has minimal impact on voltage versus current measurements above and below saturation. Recombination collisions require a third body to remove excess energy. The third body can be a photon in radiative recombination; however, these rates are slow. [22] In Appendix B, the three-body recombination rate of cesium ions, free-electrons, and buffer gas was estimated to be 1.0×10^{-7} cm^3/s for a mixture of 676 torr helium and 113 torr methane at 338 K, which corresponds to a recombination time of 100 μs for plasma densities of 10^{11} cm^{-3}. Multiple authors have investigated molecular dissociative recombination in alkali gas, and have shown that the rate is fast. However, this process is limited by the rate of molecular ion generation, which, as Cambier & Madden argue, involves multiple factors each with significant uncertainty. [26] [60] [61] [62] [63]

4.9 Analytic Analysis of Ionization Rate Dependence

Measurement and simulation of ion chamber saturation current will be described in Ch. 5 with variation in pump laser power and cesium density. However, the expected dependence can be understood without a computational tool, particularly the dependence on cesium density, n_{Cs}.

The dominant multistep ionization process in the model is pump photon absorption, followed by two collisions (energy pooling and Penning ionization). Therefore, the dependence of the ionization rate at a single point in the ion chamber on cesium

density is predicted to be cubic, $Q(z) \propto n_{Cs}^3$. This is because it involves an excited cesium in a $6P$ state colliding with two more excited cesium in $6P$ states (each of which is linearly dependent on cesium density). However, the ion chamber measures the total ionization rate integrated along the optical axis, $I_{sat} = eA_{beam} \int_0^L Q(z)dz$, where A_{beam} is the cross-sectional area of the pump laser beam and L is the 7.7 cm path length of the ion chamber. The ion chamber measurement has a different n_{Cs} dependence than a single point, due to the integration. The integrated dependence is quadratic rather than cubic. The drop from cubic to quadratic is because increasing cesium density has two impacts: (a) it increases the ionization at each point touched by pump light by n^3, and (b) it causes the pump light to be absorbed into a smaller volume with an n^{-1} dependence. The inverse relationship between cesium density and ionized volume reduced the dependence of the total ionization rate from n_{Cs}^3 to n_{Cs}^2.

For example, the functional form of pump absorption is complicated due to saturation of the $6P_{3/2}$ state (discussed below); however, if saturation effects are ignored, then the equation simplifies to

$$Q(z) = Cn_{Cs}^3 \exp\left(-\sigma_{abs} n_{Cs} z\right) \tag{4.7}$$

the integral of which is

$$\int_0^L Q(z)dz = Cn_{Cs}^2 \left[1 - \exp\left(-\sigma_{abs} n_{Cs} L\right)\right] \tag{4.8}$$

This example shows that even though the ionization rate at a point is dependent on n_{Cs}^3, the saturation current measured by the ion chamber is dependent on n_{Cs}^2 (assuming that the optical axis of the ion chamber is long enough that $\exp\left(-\sigma_{abs} n_{Cs} L\right) \approx 0$).

The expected dependence of saturation current on laser pump power is more complicated, due to saturation effects of the $6P_{3/2}$ state. At low pump intensity (and low power) the population of the $6P_{3/2}$ state increases linearly with intensity. However, as the state fills up with population, the ability of the gas to absorb pump light decreases, and the state becomes "saturated". The dependence of $6P_{3/2}$ population on pump power is linear at low intensity and near zero above saturation. This causes the predicted dependence of ionization rate on pump power to vary from cubic to near zero, depending on pump intensity. Due to the complications of pump saturation, the relationship between pump power and ion chamber saturation current will be predicted with simulation, rather than analytic analysis.

Note that the pump laser saturation intensity of the system is estimated by $\frac{h\nu}{\sigma_{abs}\tau_{20}}$ to be roughly 15 W/cm^2, where h is Planck's constant, ν is the pump frequency (352 THz), σ_{abs} is the absorption cross-section ($\sim 5 \times 10^{-13}$ cm^2 for a 6:1 mixture of helium to methane at 343 K and 806 torr), and τ_{20} is the fluorescent lifetime (30.5 ns). Since ion chamber testing has been done at pump intensites around saturation (8 - 100 W/cm^2) the dependence of ion chamber saturation current on pump power is expected to vary over the measurement range.

4.10 Chapter Summary

A simulation of the energy-state kinetic processes that occur in a laser excited cesium gas has been built, based on known processes discussed in literature. The simulation is one-dimensional and accounts for variation of pump laser power due to absorption along the optical path between the ion chamber electrodes. The dominant ionization process in the model has three steps: (1) pump photon absorption from the ground state, $6S_{1/2}$, to the $6P_{3/2}$ state, (2) collisional energy pooling to a highly excited Rydberg state, and finally (3) collisional Penning ionization. The simulation will be used to compare current theoretical understanding of laser induced cesium ionization

against ion chamber measurements, discussed in Ch. 5. However, based on analytic analysis, the predicted dependence of ion chamber saturation current on variation in cesium density is $I_{sat} \propto n_{Cs}^2$. The parameters and kinetic equations used in the simulation are listed in Appendix C.

Chapter 5

Ionization Measurement and Comparison to Prediction

The goals of this chapter are to compare measurements of cesium pump laser induced ionization and fluorescence to predictions based on theoretical processes, then use those results to analyze understanding of the underlying mechanisms.

Ionization due to 852 nm laser excitation in a cesium gas is due to complicated multi-step process with multiple dependencies, and an ion chamber examines the final result, which is the total ionization rate of the beam between the electrodes. To quantify our understanding of the ionization mechanism, results of ion chamber testing with the apparatus described in Chapter 3, have been compared to results of ion chamber simulation described in Chapter 4. The results have been compared in absolute value, and in relative trends with varying pump power, varying cesium density, and with two different buffer gas mixtures, either pure helium or a 6:1 helium to methane ratio. The comparison of relative trends provides information on whether photon processes or collisional processes dominate the multi-step ionization mechanism. Analysis of ion chamber results, as well as fluorescence measurements shown in Section 5.2, are analyzed in Section 5.3.

5.1 Ion Chamber Measurements, Predictions, and Uncertainty Quantification

Uncertainty in both experimental and simulation results has been analyzed to enable comparison.

Uncertainty in measured saturation current was based on current fluctuations due to electrical noise, as well as consistency of the saturation current. Each applied voltage was maintained for five seconds, the measured current was the average over the final second (as discussed in Section 3.1), and this was used to determine an uncertainty for each data point, ϵ_p. Next, examining only data points above the saturation voltage, the average current was defined as the saturation current, and the RMS deviation from the average was defined as the error in saturation consistency, ϵ_c. Using the maximum value of the data point error for a saturation curve, $\bar{\epsilon_p}$, the two sources of error were combined with a root-sum-square (RSS) to get the total error (one standard deviation, 1σ) in a saturation current measurement, $\epsilon_t = \sqrt{\bar{\epsilon_p}^2 + \epsilon_c^2}$.

Uncertainty in the simulation results was due to seven measured parameters that were inputs into the simulation, listed in Table 5.1, and it was quantified via Monte Carlo analysis by running many simulations with random variation of parameters with uncertainty. The analysis was split up into two types of uncertainty: (1) epistemic (also called systematic) or (b) aleatory (also called random).

Epistemic uncertainties in a diagnostic are due to a unknown quantities that are constant between tests; whereas, aleatory uncertainties vary shot-to-shot. For example, uncertainty in power meter measurements was both epistemic and aleatory. Epistemic uncertainty of $\pm 3\%$ was due to resolution and calibration of the power meter, and aleatory uncertainty of an additional $\pm 3\%$ was due to the maximum observed random laser fluctuations during any two-minute ion chamber data collection. Each uncertainty bar on a simulation data point shown in Figures 5.1 -

Table 5.1: Sources of uncertainty in measured experimental parameters

Parameter	**Epistemic / Systematic**	**Aleatory / Random**
Pump spectrum center wavelength	±0.01 nm (Normal dist.)	Uniform over range of meas.
Pump spectrum FWHM	N/A	Uniform over range of meas.
Pressure at room temperature	700 torr ±5% (Normal dist.)	N/A
Beam diameter	N/A	Uniform over range of meas.
Power meter measurements	±3% (Normal dist.)	±3% (Normal dist.)
Window loss	7-8% (Uniform dist.)	N/A
Cesium density	N/A	Based on transmission meas.

5.3 shows one standard deviation in predicted saturation current based 64 random draws of the parameters listed in Table 5.1. Analysis of data relative data trends in pump power and cesium density incorporated aleatory uncertainty only, and analysis of absolute variation between experiment and simulation results incorporated both epistemic and aleatory uncertainty. The inclusion of epistemic uncertainty was only a minor increase, since the largest contribution was due to aleatory uncertainty in alkali density and beam diameter.

The parameter in the system with the largest uncertainty was cesium density. The density of the cesium gas was varied by changing the temperature of the ion chamber. The expected relationship between cesium density and temperature is exponential and given by Eq. (5.1). [52] [64] The relationship has an accuracy of ±5% from 298-550 K for the vapor pressure of cesium evaporated from the liquid state. In the equation, P is the cesium vapor pressure in torr (omit the 2.881 term for units of atm) and T is the temperature in K.

$$log_{10}P = 2.881 + 4.165 - \frac{3830}{T} \tag{5.1}$$

Cesium density was the only parameter in Table 5.1 that was not measured directly; it was determined indirectly through pump beam transmission measurement. Cesium density was determined as part of the Monte Carlo uncertainty analysis. For each random draw of the first six parameters in Table 5.1, the appropriate cesium density was determined to be the alkali density that caused the simulated pump transmission to best match measured pump transmission. Measurements of incident pump power versus transmitted pump power are shown in Appendix D.

The cesium densities determined via pump transmission, were in good agreement with calculated densities based on ion chamber temperature. Temperature was maintained using two proportional-integral-derivative (PID) contollers with thermocouples on the outside of the ion chamber. (One on the bottom of the system and one on the side wall near the biased electrode. The thermocouple on the wall was kept 10 °C hotter to prevent condensation on the electode.) The system temperature corresponding to the cesium density transmission measurements was consistently 5 °C above the temperature of the thermocouple on the side wall of the chamber. The 5 °C difference may be due to higher temperatures inside the ion chamber, modification Eq. (5.1) due to evaporation from stainless steel chamber walls rather than liquid cesium alone, or due to slight nonuniformity of the alkali gas in the chamber.

Comparisons of experimental and simulated ion chamber saturation current are shown in Figures 5.1 - 5.3. In the plots, experimental results are shown with blue stars and simulated results are shown with green triangles. The plots are logarithmic for two reasons: (1) the saturation current was measured to vary by nearly 4 orders-of-magnitude across the parameter space, and (2) a power law dependence on a log-log plot is determined by the slope of a straight line. The experimental and simulated data has been fit with straight lines on the log-log plot, which is shown as

black dashed lines. The slope of the best fit line is shown in the legend of the plots with uncertainty based on the vertical error bars. Only data points with saturation current greater than 2 nA have been included in the linear fit, since these points have a higher signal-to-noise ratio. Data trends at low power or low cesium density have very large uncertainty since many of the data points were excluded from the linear fit.

In Figure 5.1, results are shown with varying pump power and either low or high temperature and cesium density. In Figure 5.2, results are shown with varying temperature and alkali density and either low or high pump power. All three figures show results with a buffer gas mixture of 6:1 helium to methane; however, Figure 5.3 also shows a comparison to results with pure helium buffer gas. The uncertainty bars in all three figures are due to aleatory uncertainty only since this is appropriate for determining relative trends.

Including epistemic uncertainty causes the maximum saturation current to be measured at 648 nA ±2% and simulated at 99 nA±45%, which occurred at a pump power of 1.2 W (0.97 W absorbed) and a cesium density of 2.2×10^{12} cm^{-3}. The measured rate is 6.5× higher than the simulated rate; however, both agree that ionization is a rare occurrence with less than one ionization occurring for every one million absorbed photons. (Measured ionization events compared to pump photon absorption was 0.97 ppm and the predicted frequency was 0.15 ppm.)

Results in Figure 5.1 show that measurements of saturation current are significantly higher (6.5× higher) at the maximum alkali density measured, and both experiment and simulation are in agreement that saturation current has roughly a squared dependence on pump power ($I_{sat} \propto P_{pump}^2$). The data has been fit with a straight line on the log-log plot; however, data points near the highest powers measured show deviation from the straight line. The deviation from linearity is due to saturation of the $6P_{3/2}$ state.

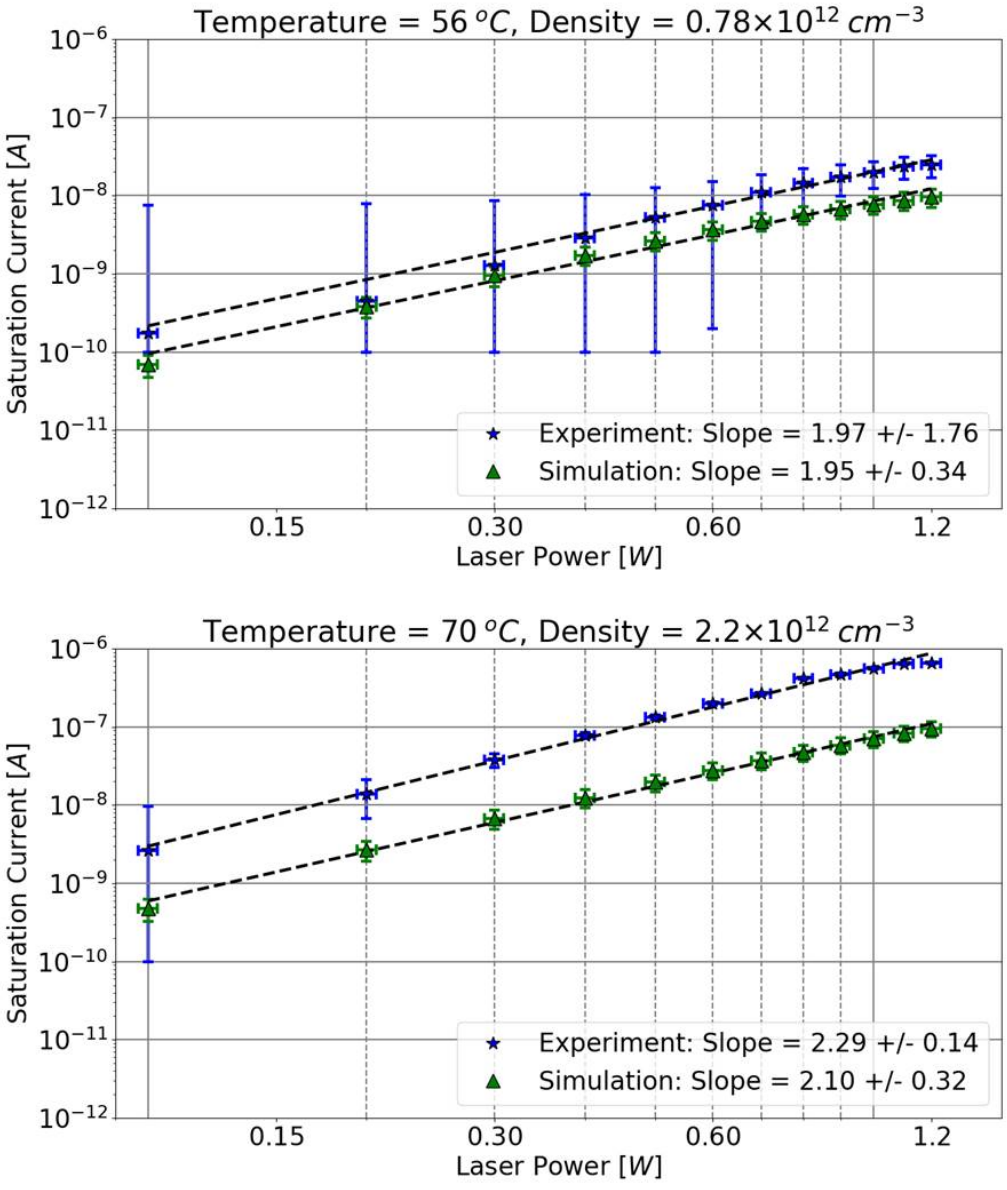

Figure 5.1: Measured and simulated saturation current in an Cs ion chamber for different powers of the ionizing laser at low and high Cs density. The Cs density was changed by changing the ion chamber temperature. The dashed lines are power laws $I_{sat} \propto P_{pump}^{\kappa}$, where κ is listed as "slope".

Results in Figure 5.2 show disagreement between experiments and simulation results; the experimental results show that saturation current has roughly a cubic

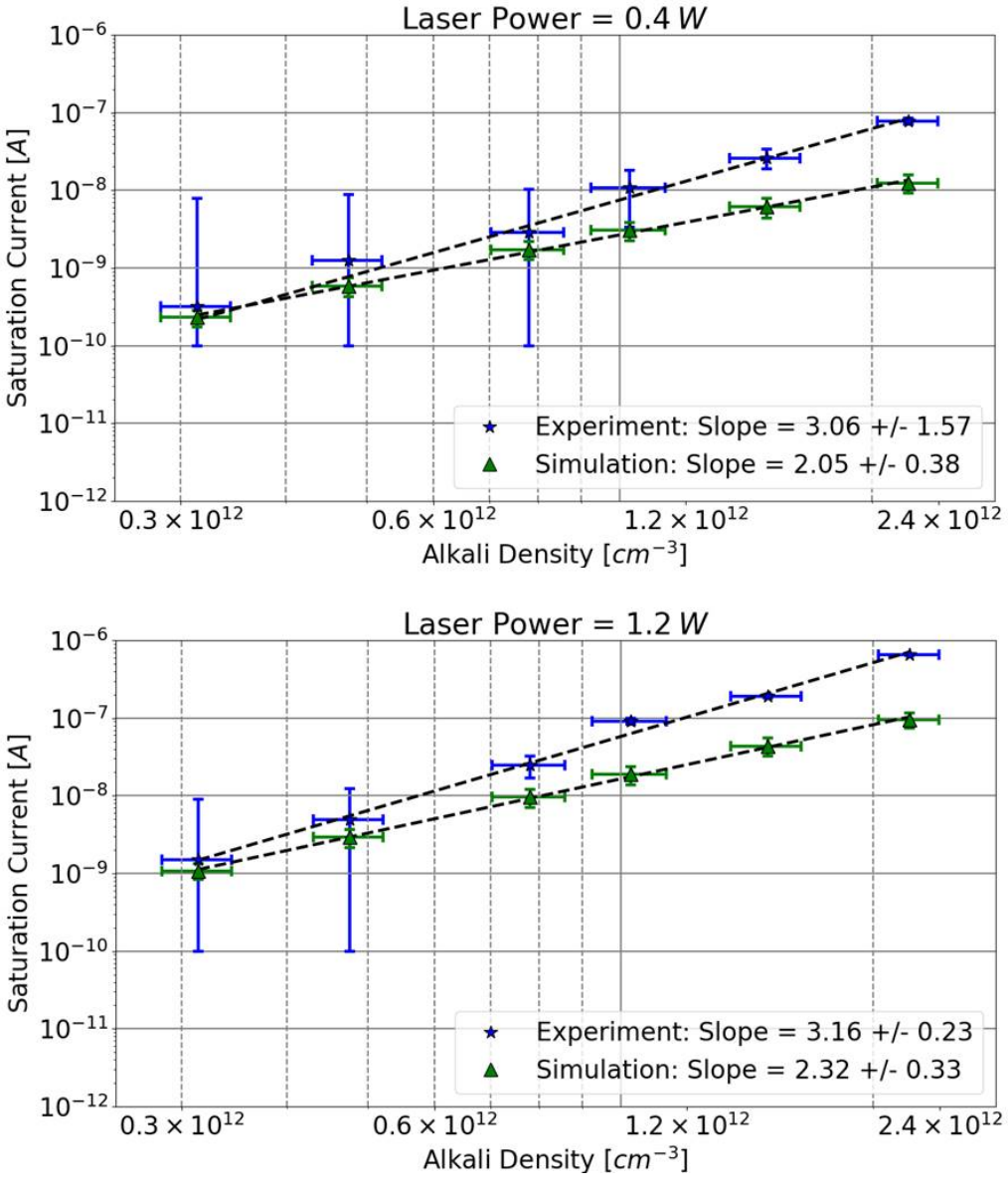

Figure 5.2: Measured and simulated saturation current in an Cs ion chamber Cs density at low and high pump laser power. The Cs density was changed by changing the ion chamber temperature. The dashed lines are power laws $I_{sat} \propto n_{Cs}^{\kappa}$, where κ is listed as "slope".

dependence on cesium density (Measurement: $I_{sat} \propto n_{Cs}^{3}$); whereas, the simulation results predict that saturation current should have roughly a quadratic dependence

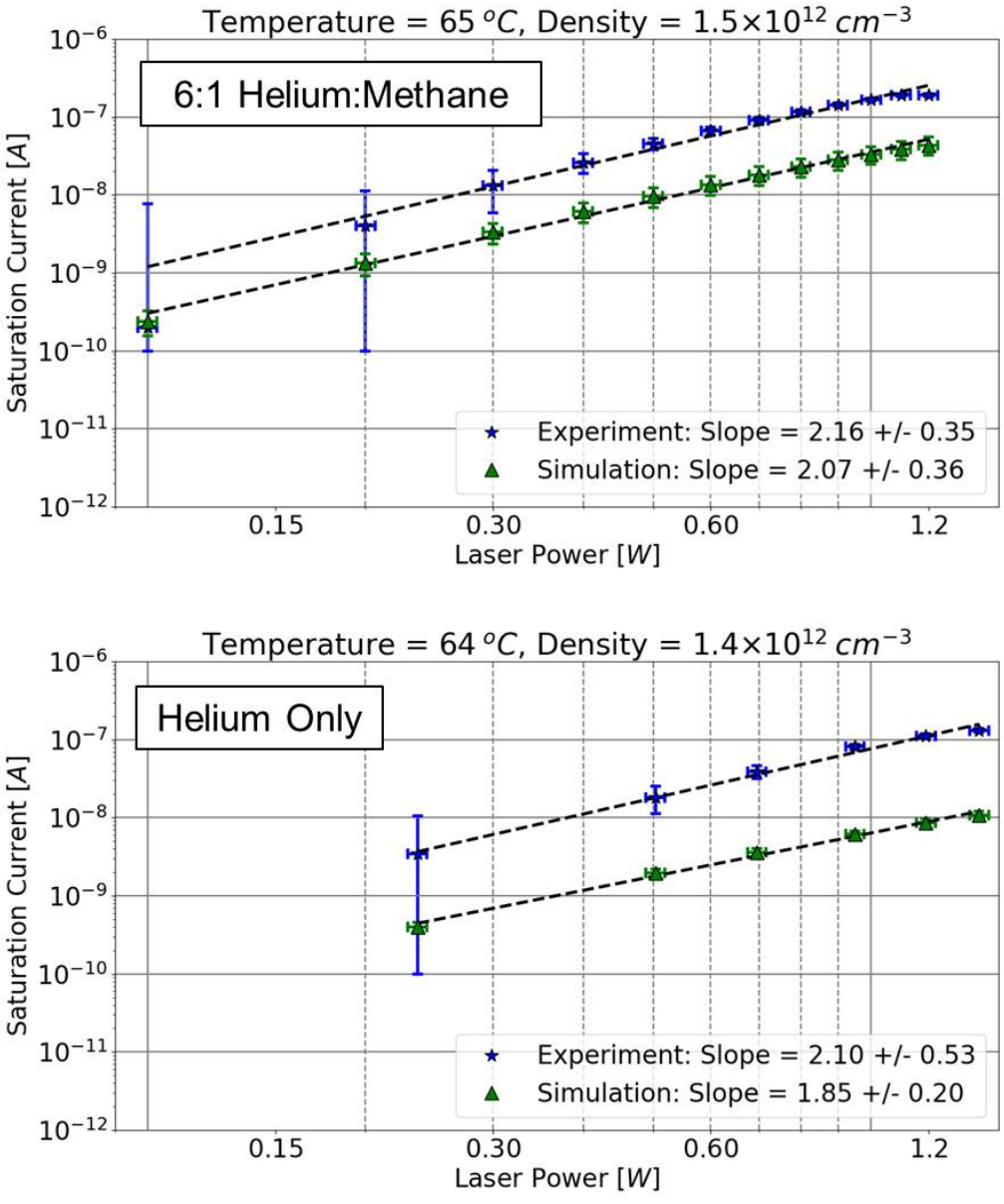

Figure 5.3: Measured and simulated saturation current in an Cs ion chamber with varying buffer gas composition. The dashed lines are power laws $I_{sat} \propto P_{pump}^{\kappa}$, where κ is listed as "slope".

on cesium density (Simulation: $I_{sat} \propto n_{Cs}^2$).

The comparison between different buffer gases in Figure 5.3 shows similar behav-

ior in both cases; saturation current was about 2× higher with the helium / methane mixture compared to pure helium, and the relative trend ($I_{sat} \propto P_{pump}^2$) was equivalent. A drop in the saturation current without methane was predicted in simulation results since methane causes spin-orbit mixing of the $6P$ states, which allows for a larger population of excited cesium, since the population can be spread between the $6P_{1/2}$ and $6P_{3/2}$ states, which leads to increased ionization.

5.2 Fluorescence Measurements

Fluorescence measurements were made simultaneously with ion chamber measurements. Fluorescent lines were monitored for three transitions, $7P_{3/2} \rightarrow 6S_{1/2}$ at 455 nm, $7P_{1/2} \rightarrow 6S_{1/2}$ at 459 nm, and $7D_{5/2} \rightarrow 6P_{3/2}$ at 697 nm, as shown in Figure 5.4.

As discussed in Ch. 3, fluorescence was collected from a small volume near the center of the beam at the entrance window of the ion chamber. The fluorescent light was fiber coupled to a spectrometer to examine each fluorescent transition individually. The measured spectra are shown in Appendix D. The total power in a fluorescent transition was found by fitting a Lorentzian profile to the measured fluorescent line and integrating it. The error associated with this measurement has been calculated from the RMS difference between the Lorentzian and the measured spectrum. The measured power in each fluorescent line has been normalized to the highest power recorded during the test. This enabled examination of the relative changes in fluorescence at the front of the cell due to variations in pump laser power and cesium density.

The measured trends in fluorescent power variation of all three transitions is shown in Fig. 5.5 on a log-log plot. The plot on the left shows relative fluorescence change with varying laser pump power at cesium density of 3.6×10^{12} cm^{-3}. The

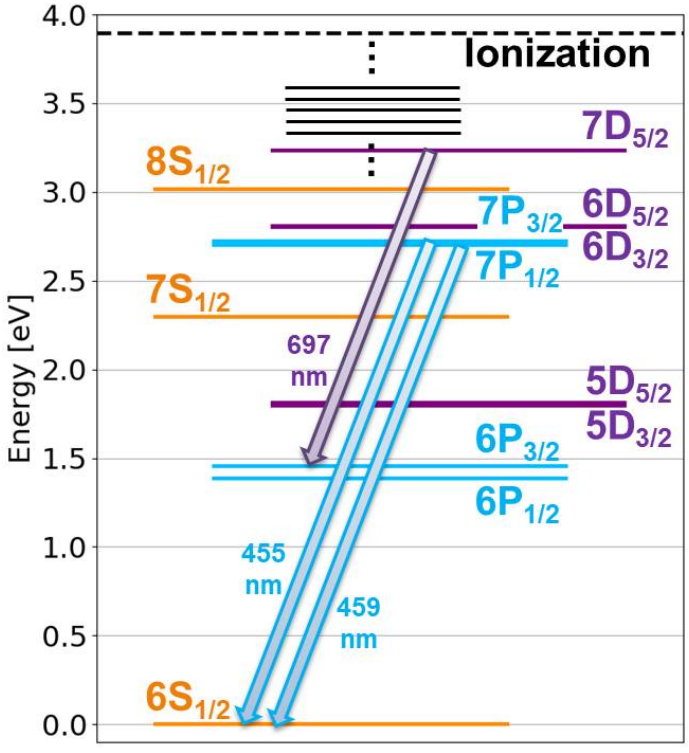

Figure 5.4: Cesium energy state diagram showing the three tracked fluorescent transitions and the eleven states included in simulation plus the $7D_{5/2}$ state.

results do not show a line on the log-log plot, which indicates that the relationship is not well represented by a power law. This trend was expected due to saturation of the $6P$ states. The plot on the right shows relative fluorescence change with varying cesium density at pump laser power of 1.2 W. The data shows that fluorescent power, P_f of all three transitions increases as cesium density increases with an exponent of 2.5-3.5 ($P_f \propto n_{Cs}^{2.5-3.5}$).

Changes in fluorescence due to the application of an electric field from the ion chamber was examined. Differences in measurement with and without 300 V are

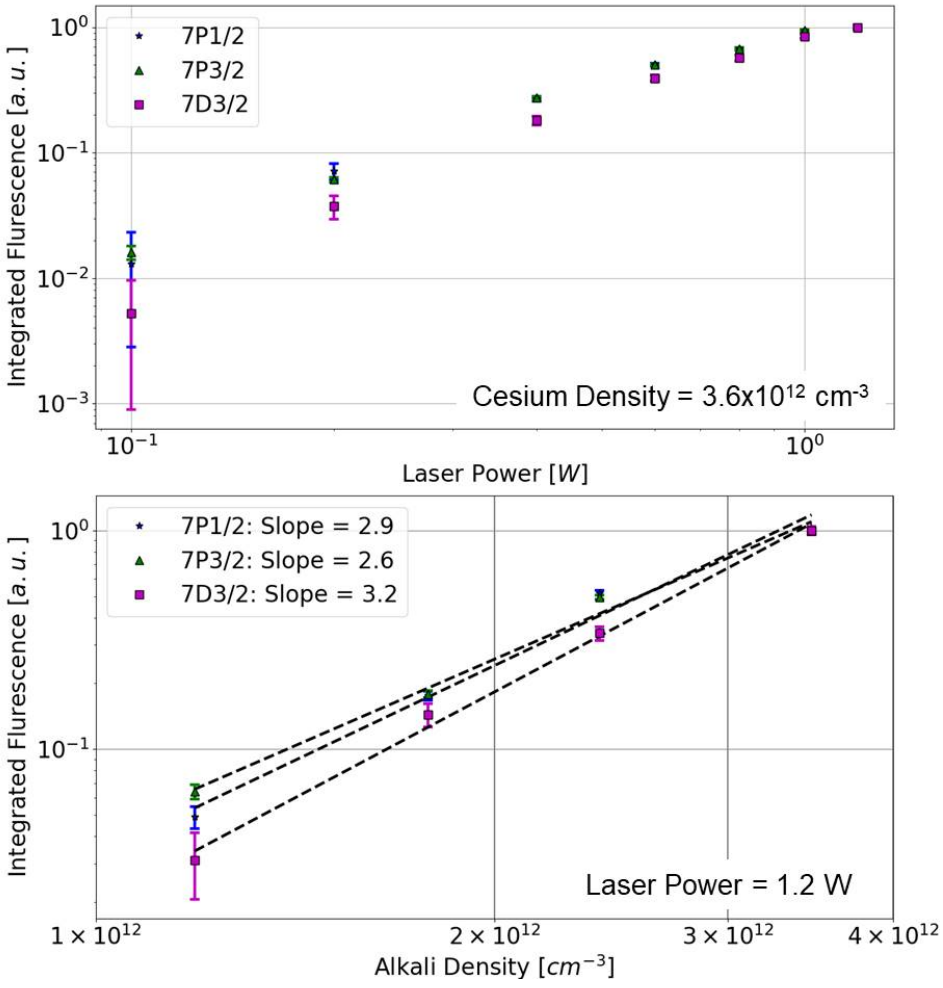

Figure 5.5: Summary of fluorescence measurements of the $7P_{1/2}$, $7P_{3/2}$, and $7D_{5/2}$ states. Integrated fluorescent power was determined by fitting measured spectral lineshapes to a Lorentzian profile and integrating. The measurements are normalized to the highest measurement for each spectral line. [Top] Measurements with varying laser pump power and cesium density of 3.6×10^{12} cm^{-3}. [Bottom] Measurement with varying cesium density and laser power of 1.2 W. The dashed lines are power laws $P_f \propto n_{Cs}^{\kappa}$, where κ is listed as "slope".

shown in Figure 5.6. The 300 V field was sufficient to cause current saturation. Fluorescence was observed to remain nearly constant, with at most a 20% decrease at high cesium density.

The 20% decrease in fluorescence with the application in voltage is consistent

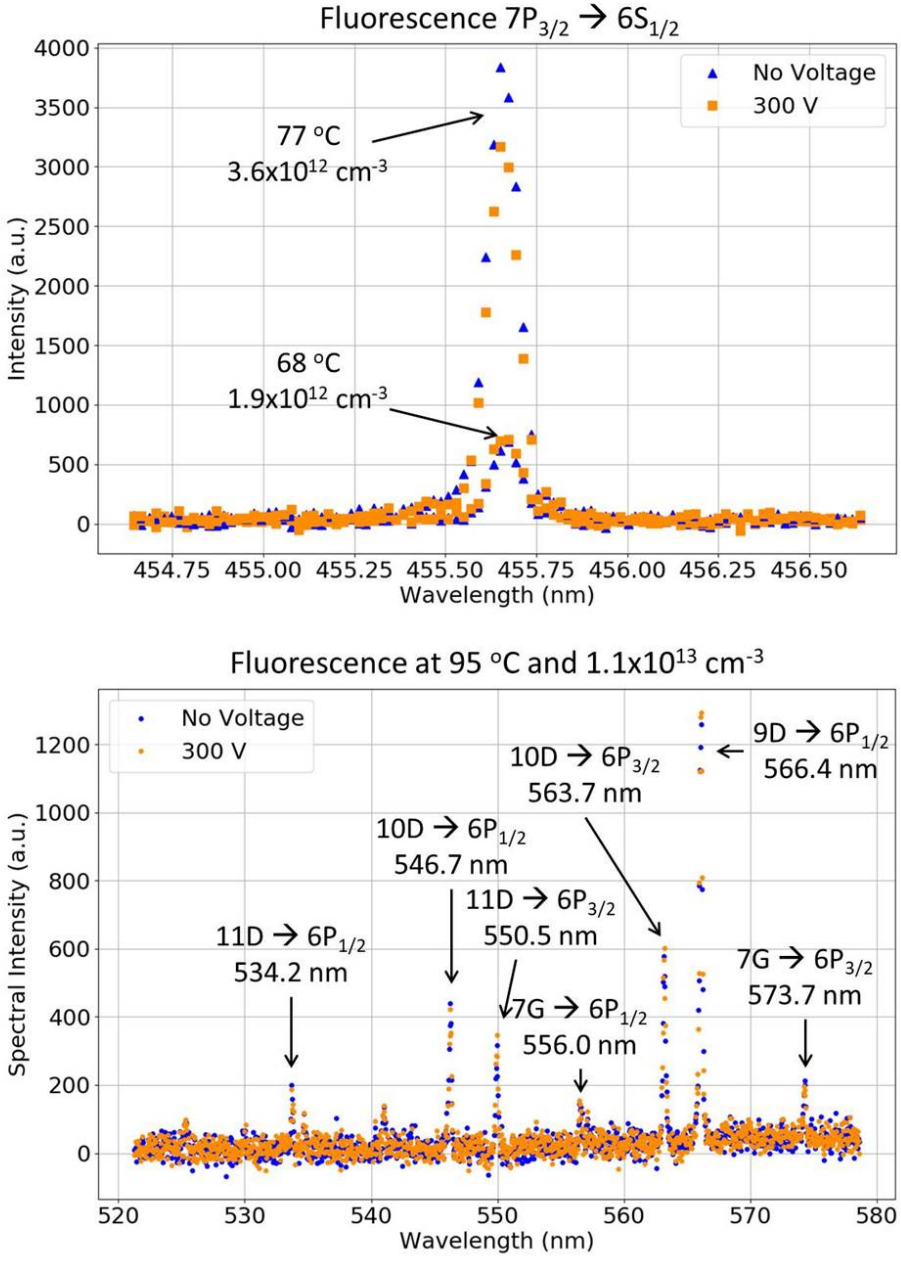

Figure 5.6: Fluorescence measurements at a pump power of $1.2\,W$ with and without $300\,V$ applied to the electrodes showing a maximum variation of less than 20%

with estimations made in Sec. 4.1 of cesium density reduction in the pump beam path due to diffusion of fresh cesium from around the beam to replace cesium ions

pulled to the electrodes. This process was not included in simulation since it was estimated to cause at most a negligible 2% reduction in cesium density. However, ion chamber measurements shown in Sec. 5.1 show higher ionization than predicted by simulation, which would increase the impact of diffusion. A reduction in cesium density of about 7% is expected to decrease fluorescence by 20% due to the measured relationship shown in Figure 5.5.

Fluorescence from many highly excited Rydberg energy states was nearly unchanged by application of an electric field sufficient to cause current saturation. This indicates that the dominant process populating these states is not electron / ion recombination, as has been previously suggested [55]. This is because an ion chamber operated at saturation has caused drift of charged particles to the electrodes to be significantly faster than recombination. If the Rydberg states were mainly populated by recombination, then the impact of the ion chamber would be to remove the process creating the populations, which would significantly diminish fluorescence. Creation of Rydberg states in the system may be do to secondary energy pooling from the $5D$ and $7S$ states, as discussed in Section 5.3. Fluorescence from many Rydberg states is shown in 5.6. This measurement was done with the ion chamber at 95°C, which caused a sufficiently high cesium density that minimal pump transmission was allowed. The alkali density is estimated to be $1.1 \times 10^{13}\,\mathrm{cm}^{-3}$ based on the temperature using the expected relationship. [52]

5.3 Analysis of DPAL Ionization Rate

5.3.1 Comparison of Measurements and Predictions

Ion chamber measurements and simulation predictions agree that ionization is rare with less than one ionization event per one million absorbed pump photons (<1 ppm). However, measured rates were larger than expected; the largest disagreement between

modeling and simulation was 6.5× at the highest pump power of 1.2 W and the highest cesium density of 2.2×10^{12} cm^{-3}. The measured rate was 0.97 ppm and the predicted rate was 0.15 ppm. Multiple possible causes of the larger measured ionization rate than expected have been investigated.

Relative changes in ionization rate were measured while varying laser pump power and cesium density, which provided information about the ionization mechanism. Measurements and simulation were in agreement that saturation current increased as the square of the pump power ($I_{sat} \propto P_{pump}^2$). This was evidence that the role of photons in the ionization model was correct. However, measurements and simulation were in disagreement on the dependence of saturation current on cesium density; the measured dependence was cubic (Measurement: $I_{sat} \propto n_{Cs}^3$), and the predicted dependence was quadratic (Simulation:$I_{sat} \propto n_{cesium}^2$). This was evidence that the ionization model may be missing a collisional process.

The reason that the measured $I_{sat} \propto n_{Cs}^3$ dependence suggests that the ionization model is missing a collisional process can be understood based on the following.

As was previously discussed in Sec. 4.9, the main multistep ionization process in the model was: (1) pump photon absorption, (2) collisional energy pooling, (3) collisional Penning ionization. This process required collisions between three excited cesium atoms, and therefore, the predicted dependence of the ionization rate at a single point in the ion chamber on cesium density was cubic, $Q(z) \propto n_{Cs}^3$. However, as discussed in Sec. 4.9, since the saturation current of the ion chamber was proportional to the total integrated ionization rate, $\int_0^L Q(z)dz$, along the 7.7 cm optical path through the ion chamber, the predicted dependence of the measured saturation was decreased to $I_{sat} \propto n_{Cs}^2$. (The reduction from n_{Cs}^3 to n_{Cs}^2 is due to reduced absorption length as cesium density increases.)

If an additional collisional process was missing from the ionization model, it would increase the dependence of saturation current from n_{Cs}^2 to n_{Cs}^3. The dominant

ionization pathway would then involve collisions between four excited cesium atoms, and ionization at a point would have a fourth-order dependence, $Q(z) \propto n_{Cs}^4$. The measured saturation current would still be one order less, so it would be $I_{sat} \propto n_{Cs}^3$.

5.3.2 Investigation of Discrepancies Between Measurements and Predictions

Besides a missing collisional process, other possible causes of the higher than expected ionization rate and increased cesium density dependence have been investigated. The processes that have been investigated are:

1. Secondary energy pooling, which is possibly the missing collisional process in the ionization model
2. Sensitivity of ionization to nonuniformity of the cesium gas
3. Effects of plasma transport to the electrodes
4. Radiation trapping
5. Stark effect due to the applied electric field
6. Inverse-bremsstrahlung photon absorption by the plasma.

Processes that occur in a high density ion chamber were investigated in Ch. 3. It was found that even at high density where space charge is significant, there are no processes that alter saturation current measurement. For example, it was found that Debye shielding does not cause a significant increase to the electric field by restricting it to a small localized region. This processes was examined to ensure that it does not cause field induced ionization.

Radiation trapping is a process in which a pump photon is fluoresced and re-absorbed elsewhere in the gas, possibly multiple times. This process would cause an increase to the dependence of ionization rate on cesium density; however, it is unlikely to have had a significant effect since the pump absorption length in the experiment, > 0.7 cm, was much longer than the beam diameter, < 0.2 cm.

Perturbations of the cesium atoms due to the electric field, known as the Stark effect, occurred in the experiment; however, the impacts were likely negligible. Generally, the Stark effect occurs when an applied electric field alters the energy states of a particle by pulling the electrons and nucleus in opposite directions. In the experiment, a maximum electric field of 500 V/cm was applied to the cesium gas. This is 6 orders-of-magnitude smaller than the field experienced by the ground-state valance electron due to the nucleus, which is approximately 214 MV/cm (based on a cesium atomic radius of 2.6 $\mathring{A}$ [65].) The applied electric field is expected to cause a decrease in the ionization potential. This has been measured by Klots & Compton to have the following relationship (Eq. 5.2) with $a = 1.90 \pm 0.03$, which is just slightly below the semiclassical value of 2. [66] [67] In the equation, ΔE is the change in ionization energy, $E_H = 27.211$ eV is the Hartree energy (approximately the electric potential of hydrogen or twice the ionization potential), F_a is the applied electric field, and $F_H = 512.4$ MV/cm is the Hartree field (approximately the field experienced by the electron of a ground state hydrogen electron). The calculated ionization potential decrease of cesium in the experiment due to the applied field of 500 V/cm is 0.4% from 3.89 to 3.87 eV, which is not expected to cause a significant change to 852 nm laser induced ionization.

$$\frac{\Delta E}{E_H} = a\sqrt{\frac{F_a}{F_H}} \tag{5.2}$$

Multiple impacts on photoionization rates due to the Stark effect have been previously observed; however, none of these effects are expected to have been important in

the current experiment. An effect resulting from Stark shifting has been observed in photoionization of alkali gas in a strong electric field with radiation near the ionization threshold. [68] Freeman and Economou showed that stable Stark-shifted states exist above the threshold, which do not ionize. Conversely, they showed that unstable Stark-shifted states exist below the threshold, which rapidly ionize. This process causes electric-field dependent resonances to appear in the spectrum of the photoionization cross-section near threshold. This process is not expected to be significant in DPAL ionization since photoionization from the $7P$ states or higher excites cesium well-above the ionization threshold. Klots & Compton observed electric-field enhancement of photoionization from S and F states in cesium gas. [66] [67] The authors attributed the increased ionization to Stark mixing, which is an effect where the electric field causes slight blending of states with opposite polarity. Without the field, populating the S and F states caused minimal ionization since the states have small photoionization cross-sections. The electric field resulted in population mixing to states with larger photoionization cross-sections, increasing the total ionization rate. Stark mixing is unlikely to have been significant in the current experiment, since collisions with the buffer gas was much more efficient at mixing energy state population. (Klots & Compton did their experiment in a cesium beam with no buffer gas.)

The Stark effect causes absorption lineshapes to shift and broaden with an applied electric field. The effect is more pronounced for high Rydberg states. For example, the Stark shift for a 500 V/cm field is expected to be 1.1 pm on the $10D_{5/2}$ state and 200 pm on the $18D_{5/2}$ state [69]. The Stark effect is unlikely to be a major impact on this experiment since it is a small effect on most cesium states and lineshape perturbation has a smaller effect on collisional processes compared to photon absorption.

Inverse-bremsstrahlung is a process that allows charged particles to absorb incident radiation. The process requires a collision partner to perturb and oscillate the

charged particle, enabling it to accept the energy of the photon as increased kinetic energy. This effect is efficient at high plasma density, and is key to laser fusion; however, it is minimal at the range of plasma densities in the experiment, which are estimated to be $< 10^{10}\, cm^{-3}$ [70] [71].

5.3.3 Secondary Energy Pooling

Secondary energy pooling is a collisional excitation process between a $6P$ state and a higher energy state, which results in formation of a highly excited Rydberg state that is still below the ionization limit, as shown in Figure 5.7. This process could occur in collisions between the $6P$ states and either the $5D$ or $7S$ states, which would be formed after relaxing from higher states, $6D$, $7P$, and $8S$, formed during initial energy pooling.

Rates for this process have not been measured; however, it is expected that the total cross-sections would be much larger than the pooling processes between two $6P$ states since the final state is nearly resonant with many Rydberg levels. The expected collision cross-sections are shown in Table 5.2. The rates have been calculated using Eq. (4.4), based on transitions from $5D$ to $8P$, $7D$, $9S$, $5F$, and $5G$, and from $7S$ to 74 different states from 3.68 – 3.84 eV. The energy states are based on transitions tabulated by Sansonetti [72]. Ionization from the highly excited Rydberg states may be faster due to Hornbeck-Molnar ionization and associative Penning ionization, since the Rydberg states are near or above the ionization limit of the cesium dimer (3.19 eV [73]). However, rubidium measurements indicate that direct Penning ionization is dominant over Hornbeck-Molnar and associative Penning ionization. [56]

Secondary energy pooling was likely an important step in the cesium ionization mechanism, based on both ion chamber and fluorescence measurements; however, it was unlikely to fully explain the gap between measured and predicted saturation current. The cross-sections of secondary energy pooling rates are 1-2 orders-

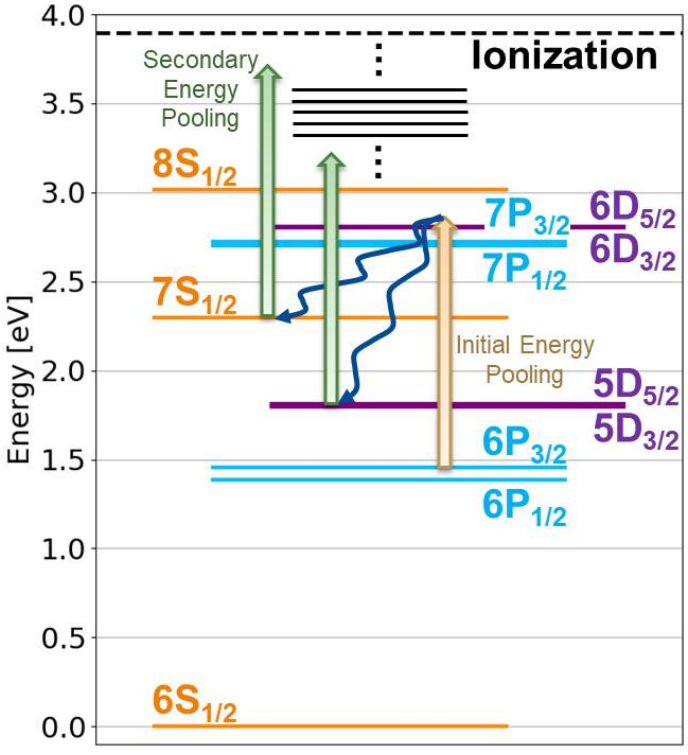

Figure 5.7: Cesium energy state diagram showing initial energy pooling, followed by radiative or collisional decay to the $5D$ or $7S$ energy states, then secondary energy pooling to states near the ionization limit.

Table 5.2: Estimated secondary energy pooling collision cross-sections based on calculations from Equation Set 4.4 published by Wallerstein *et al.* [55]

Secondary Pooling Reaction	**Total Cross-Section** [$\times 10^{-16}$ **cm**^{2}]
$6P_{1/2} + 5D_{3/2} \rightarrow Cs^{**} + 6S_{1/2}$	797
$6P_{3/2} + 5D_{3/2} \rightarrow Cs^{**} + 6S_{1/2}$	342
$6P_{1/2} + 5D_{5/2} \rightarrow Cs^{**} + 6S_{1/2}$	764
$6P_{3/2} + 5D_{5/2} \rightarrow Cs^{**} + 6S_{1/2}$	402
$6P_{1/2} + 7S_{1/2} \rightarrow Cs^{**} + 6S_{1/2}$	3712
$6P_{3/2} + 7S_{1/2} \rightarrow Cs^{**} + 6S_{1/2}$	7522

of-magnitude larger than similar pooling rates between two $6P$ states; however, the cross-sections are lower than the Penning ionization cross-section of 12900×10^{-16} cm^2 (Table C.3) used in simulation. Since the populations of the states above $6P$ were all similar (which is shown in Figure 4.2) Penning ionization was expected to occur

faster than secondary pooling. Based on these rate estimations, secondary energy pooling was expected to increase the total ionization rate and dependence on cesium density, but not fully account for differences between measured and simulated ion chamber results.

Multiple aspects of fluorescence measurements further indicated that secondary energy pooling was an important process in cesium ionization. First, the expected dependence of $7P$ fluorescence on cesium density was quadratic due to energy pooling between two $6P$ states; however, the measured fluorescence dependance had an exponent of 2.5 - 3.5 ($P_f \propto n_{Cs}^{2.5-3.5}$), which is shown in Figure 5.5. This result may be explained by secondary energy pooling or by alkali nonuniformity, which is discussed in the next paragraph. Second, the dependence of fluorescence on cesium density from $7P$ and $7D$ was nearly the same. The $7P$ states can be populated directly by energy pooling from $6P$ collisions; whereas, $7D$ cannot. The observation that fluorescence from all of these states has roughly equivalent cesium dependence indicates that significant mixing of the Rydberg states occurred. This is consistent with rapid secondary pooling followed by cascading population between high energy states. Third, fluorescence from Rydberg states was not significantly impacted by application of a strong electric field, which was sufficient to cause current saturation, as shown in Figure 5.6. This indicates that the Rydberg states are not populated by electron / ion recombination, since current saturation indicates that recombination is negligible compared to drift of the charged particles to the electrodes. Measurements of Rydberg energy state fluorescence support evidence shown in ion chamber testing that secondary energy pooling is an important mechanism in ionization of cesium gas after laser excitation.

5.3.4 Sensitivity to Cesium Nonuniformity

Saturation current of the ion chamber is highly sensitive to nonuniformity of the cesium gas, which is likely the dominant cause of the discrepancy between measured and simulated results. The sensitivity was demonstrated by test results; the range of cell temperatures investigated was 25°C (8% change in absolute temperature), which showed an order-of-magnitude change in average cesium density and three orders-of-magnitude change in saturation current. Ion chamber simulation assumed that cesium density was uniform across the cell; however, nonuniformity could have been caused by evaporation / condensation at window or electrode surfaces. (Cesium was removed from the ion chamber windows before each test series using a heat gun, and heater rope was wrapped around the window flanges; however, condensation to a level not noticable to the human eye could have formed.) If there were small regions that the beam passed through with slightly higher cesium density, it would cause a significant increase to the total ionization.

The significant impact of nonuniformity on measured saturation current was demonstrated in simulation, shown in Fig. 5.8. Two simulations were compared, one with uniform cesium density and one with nonuniform cesium density. Both simulation had 1.2 W of pump laser light incident on the ion chamber and 11% transmission. The simulation with uniform cesium density resulted in a saturation current of 99 nA, and the simulation with nonuniform density resulted in 648 nA (6.5× increase).

The simulations shown in Fig. 5.8 correspond to the highest measurement made with the ion chamber, and demonstrate that nonuniform alkali density could account for the higher-than-predicted saturation current, while still maintaining the measured 11% pump transmission. The nonuniformity in cesium density was set to a maximum of 11×10^{12} cm^{-3} at the cell windows, decaying over a distance of roughly 1 cm to 1×10^{12} cm^{-3}. The density profile was chosen arbitrarily since the details of the

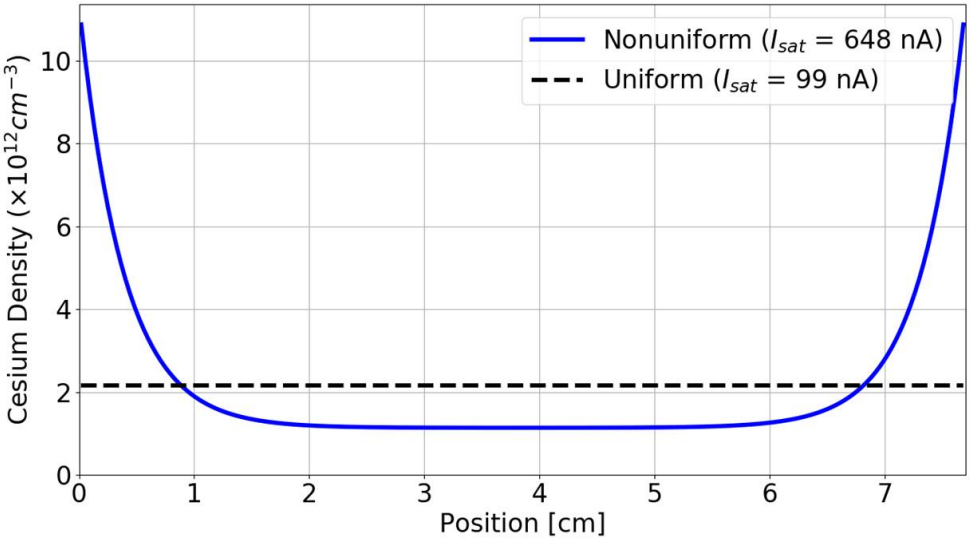

Figure 5.8: Comparison of ion chamber simulations with uniform and nonuniform cesium density. The nonuniform cesium density is modeled as increased density near the windows. The simulations have 1.2 W incident pump laser power and 11% transmission. The of the that have equal pump absorption, but 6.5× variation in saturation current

possible nonuniformity are not well known.

5.3.5 Predicted Ionization Rate in a High Power DPAL

The main interest in DPAL technology involves efficient and excellent beam quality operation at high power, many orders-of-magnitude above the 1.2 W Ti:sapph laser used in this investigation. To provide information for this regime, the ion chamber simulation was extrapolated. A simulation was executed at possible high power conditions, which included cesium density of 10^{15} cm^{-3} and pump intensity of 57 kW/cm^2. The results showed 85% pump absorption (over a 7.7 cm optical path length) and $< 2\%$ conversion of absorbed pump photons to ionization events. This demonstrates that the rate of ionization even in a high power DPAL is predicted

to be low. However, an ion chamber is not the appropriate diagnostic for processes that occur after ionization, since the system alters the plasma as it draws charged particles to the electrodes. Because of this, processes such as super-elastic electron collisions coupled to electron impact ionization, were not investigated or included in simulation, and further analysis is recommended.

5.4 Chapter Summary

Results of simulataneous measurements with an ion chamber and a fluorescence spectrometer were compared against simulation predictions based on known ionization processes. Agreement and discrepancies between the results were identified and analyzed to quantify understanding of DPAL ionization mechanisms and suggest areas requiring further investigation.

The simulated ionization processes were shown to accurately predict ionization to within an order-of-magnitude in the following parameter ranges: pump powers up to 1.2 W, peak intensities up to 100 W/cm^2, and average cesium densities up to 2.2×10^{12} cm^{-3}. Both test results and prediction were in agreement that the ionization rate is slow compared to pump absorption, with less than one ionization event for every one million pump photons absorbed (<1 ppm) across the ranges investigated.

However, while test and simulation agreed to within an order-of-magnitude, the largest discrepancy in predicted saturation current was 6.5×, which is significant. At the maximum pump laser power and cesium density, the measured saturation current was 648 nA ±2% and simulation predicted at 99 nA±45%.

Relative variation of ion chamber saturation current was measured as the following two variables were changed: pump laser power and cesium gas density (controlled by changing the ion chamber temperature). Experimental and simulation results

were in agreement that the saturation current of the ion chamber has a roughly quadratic dependence on pump power ($I_{sat} \propto P_{pump}^2$). Disagreement was shown for the dependence on cesium density; the measured dependence was roughly cubic (Measurement: $I_{sat} \propto n_{Cs}^3$) and the predicted dependence was roughly quadratic (Simulation: $I_{sat} \propto n_{Cs}^2$). Measurements done in pure helium and in a 6:1 helium to methane mixture showed similar behavior between the buffer gases.

Multiple potential causes of the discrepancies between measurement and simulation were investigated (higher-than-expected saturation current and stronger dependence on cesium density). The most likely cause of the difference was nonuniformity of the cesium gas. The system was shown to have high sensitivity to small changes in density, which may have been caused by condensation on windows or electrodes. Additionally, a missing neutral-particle collisional processes, possibly secondary energy pooling, may be missing from the ionization model.

Fluorescence measurements resulted in further evidence for a missing collisional process that is significant to ionization. First, fluorescence from $7P$ and $7D$ states was shown to have similar relative increase with increasing cesium density, despite the $7D$ state being significantly higher in energy than the $7P$ state. This indicates that a collisional process may be rapidly mixing the highly excited states. Second, fluorescence from many Rydberg states was shown to be minimally impacted by application of 300 V (greater than the saturation voltage). This indicates that the Rydberg states are populated by a neutral particle process, not electron / ion recombination, which has been previously suggested.

The simulation has been extrapolated to high power with cesium density of 10^{15} cm^{-3} and pump intensity of 57 kW/cm^2. The results showed that ionization remains slow with <2% of absorbed pump photons result in an ionization event. However, processes that occur after ionization, such as super-elastic electron collisions coupled to electron impact ionization, may be important at higher power. These processes have not been examined or incorporated into simulation, and further investigation is

recommended.

Chapter 6

Summary and Outlook

6.1 Summary

An ion chamber diagnostic was shown to be an effective tool in measurement of the laser induced ionization rate of a buffered cesium gas excited along the D_2 transition (852 nm), which is the typical setup of a cesium diode pump alkali laser (DPAL) gain medium. This study was the first direct measurement of the ionization rate in a DPAL gain medium, since saturation current measured by an ion chamber is equal to the total charged particle generation in the gas between the electrodes. Both experimentation and simulation were in agreement that the rate is slow compared to pump absorption; measured and predicted ionization rate was less than one ionization event for every one million pump photons absorbed (<1 ppm) at pump powers up to 1.2 W, peak intensities up to 100 W/cm^2, and average cesium densities up to 2.2×10^{12} cm^{-3}.

The ability of an ion chamber to accurately measure DPAL ionization rates, which are mulitple orders-of-magnitude higher than typical operating conditions, was evaluated with test and simulation. A finite-difference simulation of the Thom-

son model with diffusion was developed to examine the details of operation at high ionization rate and high plasma density. Measurements of saturation curves ($I(V)$ curves measured below and above saturation) were compared to simulations results. The observed behavior was shown to be in agreement with theoretical predictions of the model with variation in cesium density (significantly impacting ionization rate) and location of focused laser spot. Measurements of time-dependent current with a chopped excitation beam were shown to be in agreement with theoretical time constants based on ion transit time. The simulation demonstrated that certain processes only occur in a high plasma density ion chamber, such as space-charge limited ion flow, Debye shielding, and ambipolar diffusion. However, none of these processes impacted the ability of an ion chamber to accurately measure ionization rate, provided the geometry and conditions of the experiment allow current saturation to occur at a lower voltage than field-induced breakdown. The simulation can be used to design an ion chamber experiment to minimize saturation voltage, which is generally accomplished by (a) minimizing the ionized volume and (b) generating plasma as close to the ion collecting electrode as possible. Also, positive electrode bias was found to be necessary at high ionization rate to collect any free electrons that escape the region between the parallel plates.

Ionization occurs in a cesium gas when the equivalent energy of 2.7 pump photons is condensed into a single valance electron. The mechanism for this to occur is a multistep process involving many energy states and both collisional and photon interactions. To quantify understanding of this mechanism, test results with ion chamber and fluorescence diagnostics were compared against predictions of ionization simulation based on known processes. Comparisons were made across the following parameter ranges: pump powers from 0.1 - 1.2 W, intensities of 8 - 100 W/cm^2, cesium densities of 0.3 -2$\times 10^{12}$ cm^{-3}, pressures of 750 - 810 torr, temperatures of 45 - 70°C, and either pure helium or a 6:1 mixture of helium and methane (14% methane). Many competing processes were incorporated into ionization simulation, but the

dominant pathway was three steps: (1) photon absorption to the $6P_{3/2}$ state (spin-orbit mixed with the $6P_{1/2}$ state in the presence of methane), (2) collisional energy pooling to the $7P$, $6D$, or $8S$ states, and finally (3) collisional Penning ionization. This model was shown to accurately predict the low level of ionization to within an order-of-magnitude; however, there were discrepancies between the measured and simulated results.

At the maximum pump laser power, 1.2 W, and the maximum cesium density, 2.2×10^{12} cm^{-3} (70 °C), the measured saturation current was 648 nA ±2% and simulation predicted at 99 nA±45%. The results agree on the order-of-magnitude of the effect, which is more than 6 orders below pump photon absorption. (Measurements show 0.97 ionization event occurring for every one million pump photons absorbed, and 0.15 events were predicted.) However, the maximum difference between measured and predicted ionization rate was 6.5×, which is significant.

The relationship between ion chamber saturation current and either pump laser power or cesium gas density were measured and analyzed. Experimental and simulation results were in agreement that the saturation current of the ion chamber has a roughly quadratic dependence on pump power ($I_{sat} \propto P_{pump}^2$) over the range investigated. Measurements and simulation were in disagreement on the dependence of saturation current on average cesium density; the measured dependence was roughly cubic (Measurement: $I_{sat} \propto n_{Cs}^3$) and the predicted dependence was roughly quadratic (Simulation: $I_{sat} \propto n_{Cs}^2$). Measurements done in pure helium and in a 6:1 helium to methane mixture showed similar ionization rates, with a lower ionization rate measured and expected in pure helium due to poor spin-orbit mixing of the $6P$ states causing reduced capacity of excited cesium.

Multiple sources of discrepancy between measured and predicted saturation current were analyzed (both the absolute difference, maximum 6×, and the relative dependence on cesium density, n_{Cs}^2 vs. n_{Cs}^3). The mostly likely cause was nonuniform cesium density in the ion chamber. The ionization rate was shown to have signifi-

cant sensitivity to cesium density, and even small variations (possibly near the ion chamber windows or electrodes) could account for the discrepancies in ion chamber results. However, the higher-than-expected dependence of saturation current on cesium density could also be partially attributed to a missing neutral-particle collisional processes, which we are referring to as "secondary energy pooling". An important multistep ionization mechanism with this process would be: (1) photon absorption to the $6P$ states, (2) initial energy pooling to the $7P$, $6D$, or $8S$ states, followed by relaxation to the $5D$ or $7S$ states (3) secondary energy pooling to high Rydberg states near the ionization limit, and (4) collisional Penning ionization. Rates for secondary energy pooling were estimated, and it was shown that it is not likely to fully account for discrepancies between test and simulation; however, it is a fast process that may have contributed to observations and further investigation is recommended.

Fluorescence measurements were made simultaneously with ion chamber measurements, which showed further evidence for the importance of secondary energy pooling. Fluorescence from $7P$ and $7D$ states was monitored from a small volume near the entrance window of the ion chamber. The measured dependence on cesium density was higher-than-expected, consistent with ion chamber measurements. Also the dependence of $7P$ and $7D$ states was roughly equivalent, despite the $7D$ state being significantly higher in energy than the $7P$ state. Both of these observations are consistent with excitation to Rydberg states via secondary energy pooling, then cascading of energy between highly excited states, including $7P$ and $7D$, during relaxation. Also, fluorescence measurements were minimally impacted by application of 300 V on the electrodes, which was sufficient to cause current saturation of the ion chamber. This indicates that Rydberg states are populated via a neutral particle process, such as secondary energy pooling, rather than via electron / ion recombination, as has been previously suggested.

Simulation results have been extrapolated to a potential high power DPAL condition with cesium density of 10^{15} cm^{-3} and pump laser intensity of 57 kW/cm^2. The

simulation resulted in <2% of absorbed pump photons causing an ionization event. However, further investigation is recommended to ensure that a high power DPAL does not operate in a plasma regime that did not occur in the current experiment with a 1.2 W pump laser power. At sufficiently high plasma density, processes which occur after ionization, such as super-elastic electron collisions coupled to electron impact ionization, can become important. Continued testing at higher power can be done to establish parameter bounds (such as maximum alkali density) to ensure that DPAL is operated in conditions that minimize any harmful ionization effects.

Direct ionization rate measurement of a laser excited cesium gas with an ion chamber has been demonstrated and analyzed for the first time. The ion chamber diagnostic has been shown to be effective, despite operation at significantly higher ionization rates than it is typically used. Measured ionization rates are in order-of-magnitude agreement with predictions based on known collisional and photon processes. However, further investigation of DPAL ionization rates with an ion chamber at higher power is recommended to examine the roles of cesium nonuniformity, secondary energy pooling, and processes which occur after ionization, such as super-elastic electron collisions coupled to electron impact ionization.

6.2 Outlook

Further testing of a DPAL with an ion chamber diagnostic at increased laser power is recommended. Multiple lessons learned during current testing should be used to guide future work:

1. The simulation of plasma transport to the electrodes described in this dissertation can be used to design high power tests. This will ensure that current saturation is reached at a lower voltage than field-induced ionization. For example, the beam diameter of the DPAL may need to be restricted so that

the distance that ions need to travel to reach the low potential electrode is minimized.

2. It is recommended to use a flowing DPAL system with alkali-free gas purges over the windows to ensure that window condensation cannot occur, which minimizes any alkali density nonuniformity. Any inhomogeneity that does occur can be measured by recording an image of fluorescence along the optical path, since any high density spots will have more fluorescence than expected.

3. To ensure that no charged particles escape the electrodes, a positive bias voltage should be applied and the height of the electrodes should be much larger than the beam diameter. This is particularly important if the high power operation includes significant radiation trapping that can extend the ionized volume.

4. The rate and impact of secondary energy pooling should be further investigated during testing with simultaneous fluorescence and ion chamber measurements. Appropriate filters should be used to remove pump and laser light while passing all fluorescent lines of interest. The collecting optics should be calibrated to measure the absolute population differences between states that are populated by initial energy pooling ($6D$, $7P$, and $8S$), states that contribute to secondary energy pooling ($5D$ or $7S$), and high Rydberg near-ionization states that result from secondary energy pooling.

5. Although an ion chamber is not the appropriate diagnostic to measure the rate of processes which occur after ionization, such as super-elastic electron collisions coupled to electron impact ionization, it can be used to identify the regimes where these processes are important. An ion chamber draws plasma out of the DPAL beam path to the electrodes. So, if the plasma does not have a significant role, then applying a voltage to the electrodes will not have a significant effect on the DPAL power output. However, if plasma processes are causing a degradation to the output power of the DPAL, then applying

a voltage is predicted to increase the power output. It is recommended to operate a high power DPAL in an ion chamber, then record changes to output power with the application of a saturating electric field. This test can be done while varying parameters, such as pump laser intensity and cesium density, to establish regimes where plasma processes degrade DPAL power output.

Appendix A

Electrical and Mechanical Build of the Ion Chamber Diagnostic

A.1 System Layout

Images of the test system, including the pump laser, ion chamber, and fluorescence monitor are shown in Figure A.1, which are supplemental to images shown in Section 3.1. The images show the entire beam path from the Coherent MBR 110 Ti:sapphire laser source to the ion chamber. The beam exited the laser source slightly divergent (nearly collimated). The polarized beam next propagated through a Faraday isolator to prevent any back reflections. Next, a portion of the beam (≈10%) was split-off and focused into a fiber coupled Yokogawa AQ6370 optical spectrum analyzer (OSA), which was monitored during testing to ensure spectral stability. The beam then reflected off two flat mirrors. The beam was next focused by a 100 cm lens that focused the beam slightly in front of the ion chamber. The divergence of the beam through the 7.7 cm path length of the ion chamber resulted in a beam area increase of 5%, which can be seen in beam profile measurements shown in Figure A.2. The beam was attenuated using a half-wave plate and polarizing beam splitter (PBS).

This technique created negligible thermal lensing, which is demonstrated by the beam profiles shown in Figure A.3 that do not show a change in beam diameter with attenuation. The beam finally propagated to the ion chamber. The transmitted beam through the ion chamber was either blocked by a beam dump or it was absorbed by a power meter. Additionally, the beam power just before it reached the ion chamber was measured before each test. Or, a flat mirror was used at 45°, 10 cm before the ion chamber, and the beam was directed either to a Thorlabs BP209 laser beam profiler or a knife edge to measure the diameter at an equivalent plane to the center of the ion chamber.

Fluorescence was monitored during simultaeous ion chamber operation. This was done with an Acton SpectraPro 2750 from Princeton / Roper, which is a 750 mm Czerny-Turner monochomator with a 1200 grooves/mm grating blazed at 500 nm. The device used a liquid nitrogen cooled Spec-10 visible and near-infrared (NIR) charge coupled device (CCD) detector. A green filter was sometimes used to remove fluorescence above 500 nm. Fluorescence was monitored from a small volume near the front window of the ion chamber, which was ensured by slightly adjusting the lens position to maximize signal. It was collected by a 2.5 cm diameter, 5.0 cm focal length lens. The lens imaged the volume onto a fiber collector by being placed 10 cm from each, held in position at the end of a beam tube from the fiber.

Electrical measurements were supplied, controlled, and monitored by a Keithley 2410 power supply with internal ammeter. A LabView program was developed to automate data collection, as described in Section 3.1. Two resistors, 1.54 and 1.48 MΩ, were inserted between the power supply and electrodes to prevent short circuiting if electrical arcing occurred.

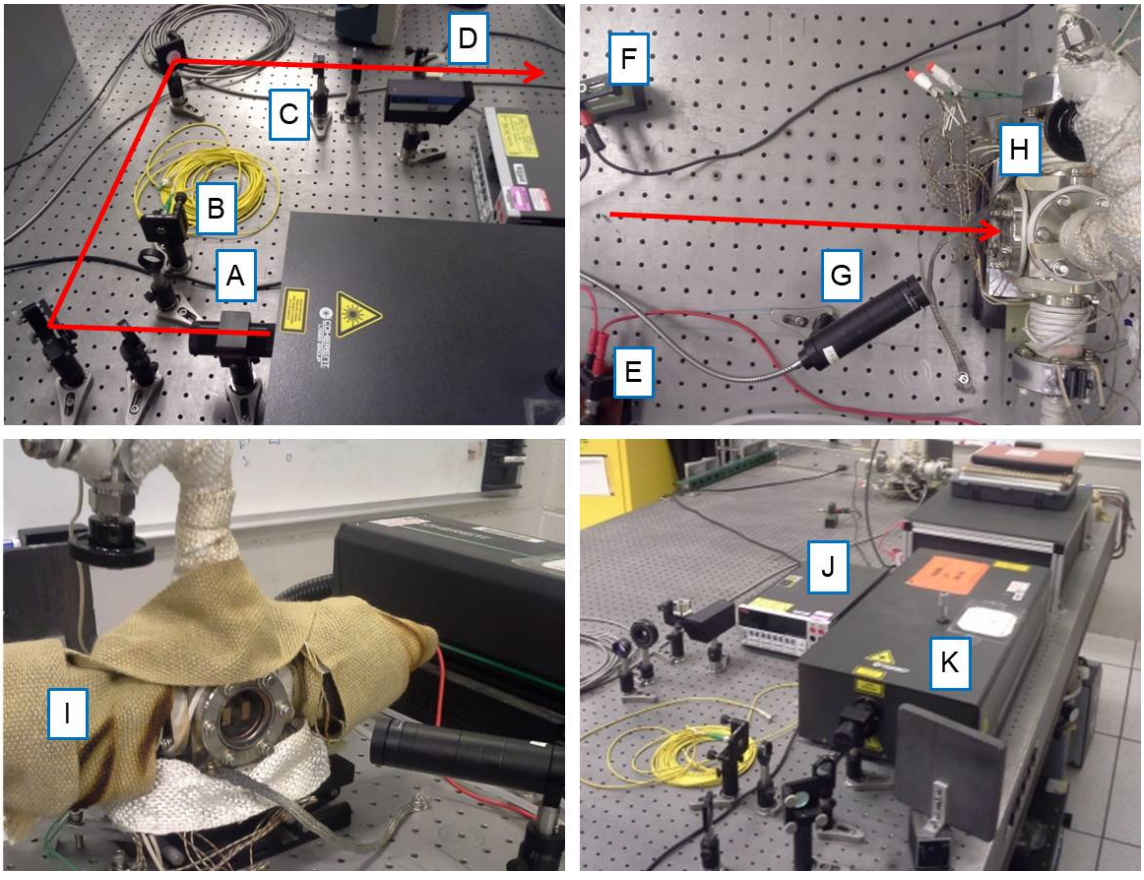

Figure A.1: Images of test system; A = Optical isolator, B = Fiber coupling for optical spectrum analyzer (OSA), C = Lens with 100 cm focal length, D = Half-wave plate and polarizing beam splitter (PBS) for beam attenuation, E = 1.54 MΩ resistor, F = 1.48 MΩ resistor, G = Fiber coupling for fluorescence spectrometer with beam tube and a 5 cm focal length lens, H = Ion chamber, I = Thermal insulation on ion chamber, J = Power supply, and K = Ti:sapphire laser

A.2 Capacitance Measurement of Ion Chamber Power Feedthroughs

Circuit analysis of the ion chamber system was discussed in detail in Section 3.1. It was shown that the temporal current response of the system to a rapid change in voltage can be explained by: (1) a fast transient (<1 ms) created by the capacitance of the electrodes and the power feedthroughs and (2) a slower transient (≈20 ms)

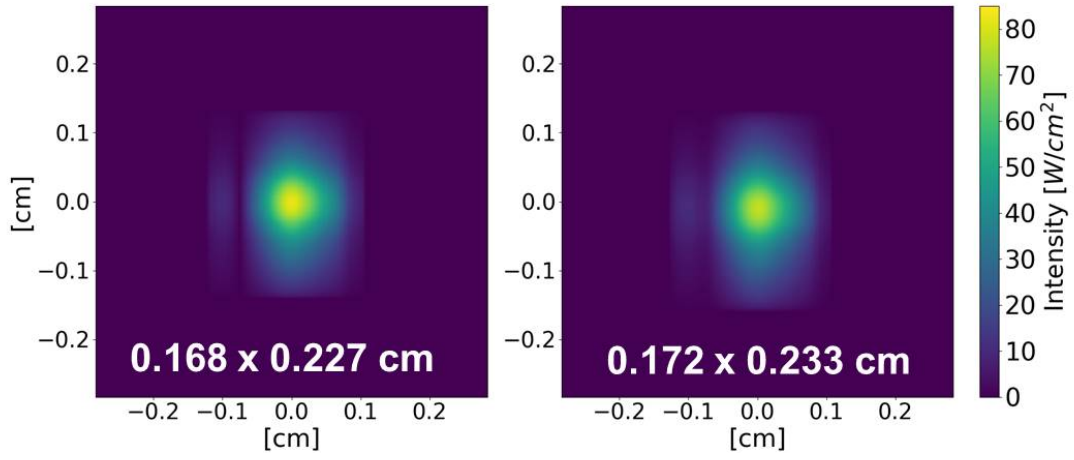

Figure A.2: Beam profile measurements showing slight divergence through the cell; [Left] Profile at the front of the ion chamber; [Right] Profile at the back of the ion chamber after 7.7 cm of propagation

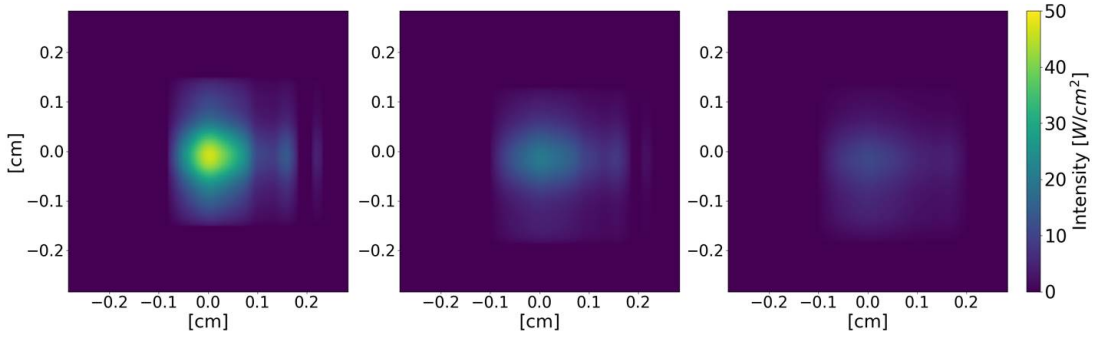

Figure A.3: Beam profile measurements showing beam attenuation with the PBS and half-wave plate; [Left] Profile at 0.91 W (no attenuation); [Center] Profile at 0.50 W, [Right] Profile at 0.30 W

created by capacitance associated with current leakage from the electrodes to the grounded chamber walls. The capacitance of the electrodes was estimated to be 1 pF based on the 1 cm electrode spacing and minimal dielectric behavior of the gases. The power feedthroughs allowed the electrodes to enter the ion chamber while maintaining a vacuum seal and electrical isolation from the grounded chamber walls. This was done by having an alumina ceramic break between the electrodes and walls,

which electrically behaves as a capacitor. Measurement of the capacitance of each power feedtrhough is described in this section.

The measurements were performed by connecting an oscilloscope around each capacitor (with some additional known resistors), and measuring the temporal response of the system to a 1 V step-function change in voltage using an oscilloscope. However, the measurement was made more difficult because the capacitance of the oscilloscope was larger than the capacitance of the power feedthroughs. The background circuit, including the internal resistance and capacitance of the oscilloscope, is shown in Figure A.4. The oscilloscope was in series with a known resistor, 1.54 MΩ, and it was in parallel with another known resistor, 1.48 MΩ. The simplified, equivalent circuit is also shown in Figure A.4, which adds the two parallel resistors together as a single effective resistor of 2.1 MΩ. The theoretical current response of the system is provided by Equation A.1 for an RC circuit in parallel. The equation shows the temporal evolution of the current, $i(t)$, across resistor, R_2, which is the current that would be measured with the oscilloscope. In the equation, V, is the step function applied voltage at time $t = 0$. The best fit of the measured current response using Equation A.1 is shown in Figure A.4, which was used to measure the internal capacitance of the oscilloscope with uncertainty due to the RMS difference between the measured and the theoretical data. By using this method, the internal capacitance of the oscilloscope was measured to be 186±7 pF. The measured capacitance was larger than the capacitance specified by the manufacturer, which is likely due to additional capacitance of wires and connectors.

$$i(t) = \frac{V}{\alpha R_2}\left(1 - \exp\left[\frac{-\alpha t}{R_1 C}\right]\right) \qquad \text{where } \alpha = \frac{R_1}{R_2} + 1 \tag{A.1}$$

The capacitance of the power feedthroughs was measured with a similar technique. The background circuit shown in Figure A.4 was connected to a power feedthough in parallel with the oscilloscope. By connecting the power feedthrough

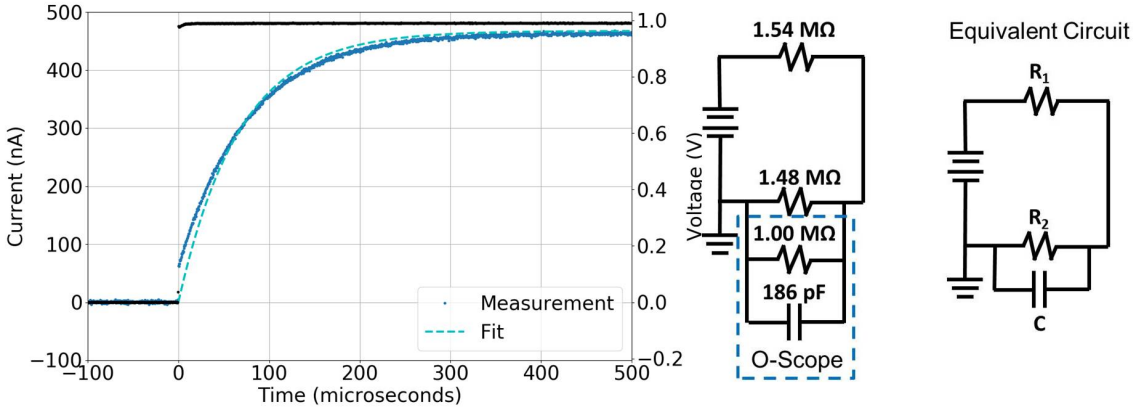

Figure A.4: [Left] Measured background current response to a step-function applied voltage on the oscilloscope; [Right] Circuit diagrams of the background test system, including the internal voltage and capacitance of the oscilloscope, as well as the simplified equivalent circuit which shows a single resistor, R_2 =2.1 MΩ, as the sum of the two parallel resistors

and the oscilloscope in parallel, the two capacitors act as a single circuit element with total capacitance equal to the sum of the individual components. So, the circuit with the added power feedthrough capacitor still reduces to the equivalent circuit shown in Figure A.4 and the theoretic current response is still provided by Equation A.1. The measured current response of the system with each power feedthrough is shown in FigureA.5. The change in the time constant of the response is due to the added capacitance of the power feedthrough. The measured capacitance of the power feedthrough on the biased electrode was 41±17 pF, and the power feedthrough on the grounded electrode was 41±16 pF.

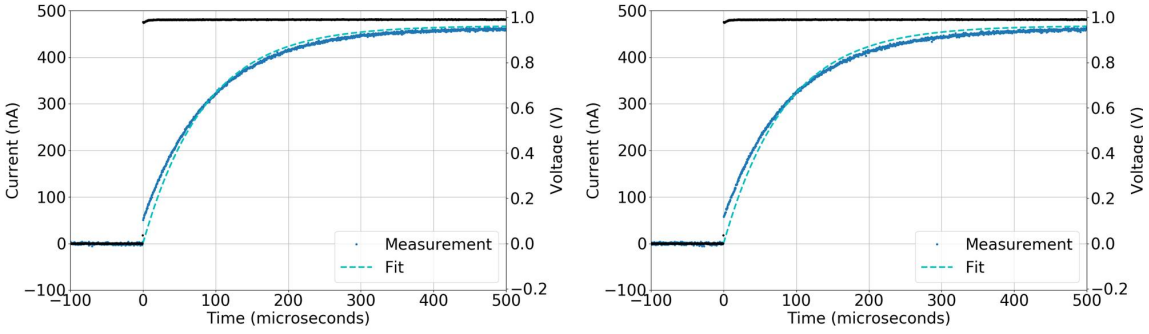

Figure A.5: Measured current response with the capacitor under test added in parallel to the oscilloscope, as shown in Figure A.4. [Left] Measurement of capacitance of the power feedthrough on the grounded electrode. [Right] Measurement of capacitance of the power feedthrough on the biased electrode.

Appendix B

Computational Simulation of the Full Thomson Model

One-dimensional, steady-state solutions of the full Thomson model, Eqs. (3.2 - 3.5), with diffusion have been found by discretizing the axis between the electrodes, then applying an iterative finite-difference technique. The model requires the following inputs: applied voltage, V_a, and spatially varying ionization rate, $Q(x)$, and generates the following outputs: ion densty, $n_i(x)$, electron density, $n_e(x)$, and electric field, $E(x)$. The simulations all used a 1 cm electrode separation, which was meshed with a one-dimensional uniform grid. It was found that 3001 grid points provided sufficient resolution; this corresponds to a grid separation of 3.33 μm, which was smaller than a Debye length at the highest plasma densities simulated. The numerical technique involved the following steps. **(1) Initialize:** Initialize solutions with the following constant values: $E = V_a/d$ and $n_i = n_e = 0$, where d is the electrode spacing. **(2) Begin iteration with finite-difference solve:** Using the current values of the solutions, $E^{(i)}(x)$, $n_i^{(i)}(x)$, and $n_e^{(i)}(x)$, where superscript (i) indicates the ith iteration, and using the central-difference approximations shown in Eq. (B.1) (where superscript j denotes the jth point in the grid)

$$\begin{aligned} \frac{dn}{dx} &\approx \frac{n^{j+1} - n^{j-1}}{2\Delta x} \\ \frac{d^2n}{dx^2} &\approx \frac{(n^{j+1} - n^j) - (n^j - n^{j-1})}{\Delta x^2} \end{aligned} \tag{B.1}$$

solve the tri-diagonal system of equations

$$\begin{aligned} \left[\frac{\mu_i}{2\Delta x}E^j + \frac{D_i}{\Delta x^2}\right] n_i^{j-1} + \left[C_R n_e^j - \mu_i\left(\frac{dE}{dx}\right)^j - \frac{2D_i}{\Delta x^2}\right] n_i^j + \\ \left[\frac{-\mu_i}{2\Delta x}E^j + \frac{D_i}{\Delta x^2}\right] n_i^{j+1} = -Q^j \\ \left[\frac{-\mu_e}{2\Delta x}E^j + \frac{D_e}{\Delta x^2}\right] n_e^{j-1} + \left[C_R n_i^j + \mu_e\left(\frac{dE}{dx}\right)^j - \frac{2D_e}{\Delta x^2}\right] n_e^j + \\ \left[\frac{\mu_e}{2\Delta x}E^j + \frac{D_e}{\Delta x^2}\right] n_e^{j+1} = -Q^j \end{aligned} \tag{B.2}$$

with boundary conditions

$$\begin{aligned} n_i(0) = 0 \therefore n_i^1 = 0 \\ \frac{d^2n_i}{dx^2}(d) = 0 \therefore n_i^N = 2n_i^{N-1} - n_i^{N-2} \\ \frac{d^2n_e}{dx^2}(0) = 0 \therefore n_e^1 = 2n_e^2 - n_e^3 \\ n_e(d) = 0 \therefore n_e^N = 0 \end{aligned} \tag{B.3}$$

Use the Thomas algorithm [74] to invert the matrix and solve the system of equations, since this is a computationally efficient method for tri-diagonal matrices. The results of this step are density fields, $n_i'(x)$ and $n_e'(x)$. Note that the application of the boundary conditions reduces the size of the tri-diagonal matrix from $N \times N$ to $N-2 \times N-2$. **(3) Relax density field solutions:** Apply Eq. (B.4) to generate updated density fields for the next iteration, $n_i^{(i+1)}(x)$ and $n_e^{(i+1)}(x)$.

$$n^{(i+1)}(x) = (1-\alpha)n^{(i)}(x) + \alpha n'(x) \tag{B.4}$$

Relaxation restricts the allowable amount of change per iteration, which maintains stability of the numerical method. Allow the value of the relaxation parameter, α, to change on each iteration. It was found that if the following two conditions were met, the simulation remained stable: (a) $\alpha < 2 \times 10^{-5}$ and (b) $\Delta n_{max} < 10^6\ \mathrm{cm}^{-3}$, where Δn_{max} is the maximum change in density at any point on the computational mesh. Due to the strong relaxation, it was found that the technique often required approximately 400,000 iterations to converge. Possible acceleration techniques that may decrease computational time are Ng and Anderson acceleration [75] [76] [77]. **(4) Calculate updated E-field:** Calculate the updated electric field by numerically integrating the updated density fields according to the following equation.

$$\begin{aligned} \bar{E}(x) &= \frac{e}{\epsilon_0}\int_0^x [n_i(x') - n_e(x')]dx' \\ E_0 &= \frac{V_{applied}}{d} - \frac{1}{d}\int_0^d \bar{E}(x)dx \\ E(x) &= \bar{E}(x) + E_0 \end{aligned} \tag{B.5}$$

(5) Check for convergence and repeat steps 2-5 if necessary: Calculate current density across the numerical mesh, $J(x)$, according to Eq. (B.6). From the first two equations of the Thomson model, Eqs. (3.2 and 3.3), it can be shown that at steady-state, current density between the electrodes is constant. Calculate the average and root-mean-square (RMS) variation of the current density along the computational mesh. If the variation is less than 0.5%, then the simulation is considered converged and complete, and if not, then repeat steps 2-5.

$$J(x) = \mu_i E(x) n_i(x) + \mu_e E(x) n_e(x) - D_i \frac{dn_i}{dx}(x) + D_e \frac{dn_e}{dx}(x) \tag{B.6}$$

Important parameters in the ion chamber simulation are mobilities, diffusion constants, and electron / ion recombination rate. The relationship between mobility and diffusion coefficients is shown by the Einstein relation, $eD = \mu kT$. The variation of mobility with temperature and pressure or the variation of mobility between different particles can be estimated with the relation shown in Eq. (B.7) [78], where s is the sum of the radii of the two collision partners, P is pressure, and m_i is the mass of collision partner i.

$$\mu \propto \frac{\sqrt{T}}{s^2 P}\sqrt{\frac{1}{m_1}+\frac{1}{m_2}} \tag{B.7}$$

Diffusion and mobility of a gas mixture is defined by Blanc's law, shown in Eq. (B.8) [79], where D_{mix} is the diffusion constant of the gas mixture, D_i is the diffusion constant of the ith constituent, and f_i is the mole fraction of the ith constituent.

$$\frac{1}{D_{mix}} = \sum_i \frac{f_i}{D_i} \tag{B.8}$$

The mobility of cesium ions in helium gas has been measured to be $15.5\pm1\text{cm}^2/\text{Vs}$ at 1 atm and 273 K [80] and $18.5 \pm 0.5\ \text{cm}^2/\text{Vs}$ at 1 atm and 450 - 550 K [81]. These measurements are in agreement due to the temperature scaling $\mu \propto \sqrt{T}$ from Eq. (B.7). No measurement of cesium mobility in methane has been made, so the mobility constant has been estimated based on the scaling in Eq. (B.7). A cesium ion has a mass of 132.9 AMU and a radius of 1.7 $\mathring{A}$ [65], a helium atom has a mass of 4.0026 AMU and a radius of 0.31 $\mathring{A}$ [82], and a methane molecule has a mass of 16.043 AMU and a radius of 2.0 $\mathring{A}$ [83]. Based on these sizes and at 1 atm and 273 K, the mobility of a cesium ion in methane is approximately $2.4\,\text{cm}^2/\text{Vs}$ and the mobility of a cesium ion in a 6:1 mixture of helium and methane is approximately $8.7\ \text{cm}^2/\text{Vs}$. Free electron mobility is multiple orders-of-magnitude higher than ion

mobility [84]. Electron mobility has been simulated with the value 1000 cm^2/Vs. Neither helium nor methane generate negative ions at the energy levels present in the laser induced cesium plasma, in which electrons are freed with energy <1 eV. [85] [86]

Electron / ion recombination requires a third body to remove excess energy, as was previously discussed in Sec. 4.8. The rate of cesium recombination when helium is the third body has been measured to be 4×10^{-29} cm^6/s at 625 K [87]. The rate is expected to be faster when methane is the third body due to the larger size and available vibrational modes; however, the rate has not been measured. The recombination rate of ionized methane has been used in the simulation, which has been calculated to be near 10^6 cm^3/s at 1 atm and 300 K, equivalent to $4 \times 10^{-26} cm^6/s$ [88]. The recombination rate when a free electron is the third body has been measured to be 3×10^{-9} $cm^6 s^{-1} K^{4.5}$ [89], which has not been included in the simulation since it is slower than the heavy particle recombination rate at the temperatures and plasma densities in the experiment. The expected temperature dependence of heavy particle mediated recombination is $T^{-2.5}$ [90]. Based on these published rates, the recombination rate used in simulation was 1.0×10^{-7} cm^3/s, which was calculated for a 676 torr helium and 113 torr methane mixture at 338 K. For plasma densities of 10^{11} cm^{-3}, the recombination time is roughly 100 μs. Note that the third body in the recombination process can be a photon; however, radiative recombination is significantly slower than collisional.

Appendix C

Model of Laser Excited Cesium Gas Ionization

C.1 Cesium $6P_{3/2}$ Absorption Cross-Section

Simulation of the pressure-dependent cesium $6P_{1/2}$ absorption cross-section included hyperfine energy level splitting due to electron / nucleus angular momentum coupling, including the well known splitting of the ground state that is now used in the definition of the second. (The frequency splitting is exactly 9,192,631,770 Hz.) Equations defining hyperfine splitting (Set C.1) were defined by Steck [52] and equations for the combined absorption spectrum from each hyperfine component (Set C.2) were defined by Pitz & Perram [91]. Splitting due to the magnetic octupole or any higher terms have been ignored since they are negligible at the pressure regimes examined. Hyperfine splitting corresponds to total angular momentum F, which is the vector sum of total electron angular momentum J and total nuclear angular momentum I. The cesium ground state, $6S_{1/2}$ is split into two states, corresponding to $J = 1/2$, $I = 7/2$, and F" $= 3$ or 4. The pump state, $6P_{3/2}$ is split into four states, corresponding to $J = 1/2$ or $3/2$, $I = 7/2$, and $F' = 2$, 3, 4, or 5. In Eqs. (C.1), ΔE_{hfs} is

the energy splitting between total angular momentum F components, and all other parameters are defined in Table C.1, and the electric quadrupole term only applies to the $J = 1.5$ ($6P_{3/2}$) splitting. Summing the components of the hyperfine spectrum is done with Eqs. (C.2), which is summed over transition from the two lower states F" = 3 or 4 to the four upper states $F' = 2$, 3, 4, or 5. This requires knowledge of the relative hyperfine transition strength factors, $S_{F'F"}$, as well as the thermal distribution between the ground state splitting, $f_{F"}$, defined in Table C.1, where $E(F")$ is the relative energy above the lowest F" state. In the equation set, $\sigma(\nu)$ is the frequency resolved absorption cross section, $g_J = 2J + 1$ is the degeneracy of the fine structure component, λ is wavelength ($\frac{c}{\nu}$), A_{21} is the spontaneous emission rate, $\nu_{F\leftarrow' F"}$ is the line center of the $F \leftarrow' F$" transition (varied by pressure shifting according to the rates listed in Table C.1), and $g_\nu(\nu, \nu_{F'\leftarrow F"})$ is the normalized lineshape of the transition component. The lineshape was approximated to be a Lorentzian with a width defined by the pressure of the buffer gas and broadening cross-sections shown in Table C.1; a Lorentzian lineshape is appropriate for the pressure regimes included in this study. Scaling pressure broadening and shifting rates from temperature, T_1, to temperature, T_2, is done by multiplying the rate at T_1 by $\sqrt{T_1/T_2}$.

$$\begin{aligned} \Delta E_{hfs} &= \frac{1}{2} A_{hfs} K + B_{hfs} \frac{\frac{3}{2}K(K+1) - 2I(I+1)J(J+1)}{4I(2I-1)J(2J-1)} \\ K &= F(F+1) - I(I+1) - J(J+1) \end{aligned} \tag{C.1}$$

$$\begin{aligned} \sigma(\nu) &= \sum_{F"} \sum_{F'} \left(\frac{g_{J'}}{g_{J"}}\right) \left(\frac{\lambda^2}{8\pi}\right) A_{21} S_{F'F"} g_\nu(\nu, \nu_{F'\leftarrow F"}) f_{F"} \\ f_{F"} &= \frac{(2F"+1)\exp[-E(F")/kT]}{\sum_{F"}(2F"+1)\exp[-E(F")/kT]} \end{aligned} \tag{C.2}$$

Spectral pump absorption in propagation from mesh point zm_j to subsequent point zm_{j+1} was calculated using Equation C.3, which is the Beer-Lambert law

applied to each spectral line separately assuming that the spectral absorption cross-section, $\sigma(\nu)$, is constant across the mesh cell between the points. In the equation, $I_\nu(\nu, z)$ is the spectral pump intensity at plane z (units = $\mathrm{cm}^2/\mathrm{Hz}$) and Δz is the distance from zm_j to zm_{j+1}. The factor of $\frac{1}{2}$ is due to the degeneracy of states n_0 and n_2. The reduction in the integated pump spectrum indicates that energy has been deposited in the gas volume contained in the cell between mesh points zm_j and zm_{j+1}. The excitation rate of state n_2 due to pump absorption was calculated with Equation C.4, where $W_{pump}(z_i)$ is the pump excitation density of the cell between mesh points zm_j and zm_{j+1} (units = $\mathrm{cm}^{-3}\mathrm{s}^{-1}$). At the pump intensities investigated in this report, photoionzation is less than one part-per-million (ppm) compared to pump absorption from the ground state, so absorption due to photoionization has not been included in the simulation.

$$I_\nu(\nu, zm_{j+1}) = I_\nu(\nu, zm_j) \exp\left[\left(n_0 - \frac{1}{2}n_2\right)\sigma(\nu)\Delta z\right] \tag{C.3}$$

$$W_{pump}(z_i) = \frac{1}{\Delta z}\left(\int_0^\infty \frac{I_\nu(\nu, zm_i)}{h\nu}d\nu - \int_0^\infty \frac{I_\nu(\nu, zm_{i+1})}{h\nu}d\nu)\right) \tag{C.4}$$

C.2 Cesium Ionization Model Kinetic Parameters

Table C.1: Cesium $6P_{3/2}$ absorption cross section parameters.

Parameter	**Symbol**	**Value**	**Reference**
Magnetic Dipole Constant, $6S_{1/2}$	$A_{6S_{1/2}}$	$h\cdot$ 2.2981579425 GHz (exact)	[52]
Magnetic Dipole Constant, $6P_{3/2}$	$A_{6P_{3/2}}$	$h\cdot$ 50.28827(23) MHz	[52]
Electric Quadrupole Constant, $6P_{3/2}$	$B_{6P_{3/2}}$	$h\cdot$ -0.4934(17) MHz	[52]
Einstein A Coefficient, $6P_{3/2}$	A_{21}	32.8 MHz $[1/(30.499 \pm 0.070)$ ns]	[92] [52] [93] [72]
Strength Factor, $4 \leftarrow 5$	S_{45}	11/18	[52]
Strength Factor, $4 \leftarrow 4$	S_{44}	7/24	[52]
Strength Factor, $4 \leftarrow 3$	S_{43}	7/72	[52]
Strength Factor, $4 \leftarrow 2$	S_{42}	0	[52]
Strength Factor, $3 \leftarrow 5$	S_{35}	0	[52]
Strength Factor, $3 \leftarrow 4$	S_{34}	15/56	[52]
Strength Factor, $3 \leftarrow 3$	S_{33}	3/8	[52]
Strength Factor, $3 \leftarrow 2$	S_{32}	5/14	[52]
Pressure Broadening Rate (Helium)	γ_{He}	20.59 ± 0.06 MHz/torr at 313 K	[53]
Pressure Broadening Rate (Methane)	γ_{CH_4}	25.84 ± 0.0 MHz/torr at 313 K	[53]
Pressure Shifting Rate (Helium)	δ_{He}	0.69 ± 0.01 MHz/torr at 313 K	[53]
Pressure Shifting Rate (Methane)	δ_{CH_4}	-8.86 ± 0.02 MHz/torr at 313 K	[53]

Table C.2: Cesium fluorescence parameters.

Symbol	**Initial State**	**Final State**	**Rate [MHz]**	**Lifetime [ns]**	**Branching Ratio**	**Reference**
τ_{10}	$6P_{1/2}$	$6S_{1/2}$	28.6	34.9	1.0	[92] [52] [93] [72]
Total Radiative Lifetime [ns]				**34.9**		
τ_{20}	$6P_{3/2}$	$6S_{1/2}$	32.8	30.5	1.0	[92] [52] [93] [72]
Total Radiative Lifetime [ns]				**30.5**		
τ_{31}	$5D_{3/2}$	$6P_{1/2}$	0.913	1100	0.90	[94] [93] [72]
τ_{32}	$5D_{3/2}$	$6P_{3/2}$	0.107	9350	0.10	[94] [93] [72]
Total Radiative Lifetime [ns]				**980**		
τ_{42}	$5D_{5/2}$	$6P_{3/2}$	0.781	1280	1.0	[95] [93] [72]
Total Radiative Lifetime [ns]				**1280**		
τ_{51}	$7S_{1/2}$	$6P_{1/2}$	6.23	161	0.35	[96] [93]
τ_{52}	$7S_{1/2}$	$6P_{3/2}$	11.4	87.7	0.65	[96] [93]
Total Radiative Lifetime [ns]				**56.7**		
τ_{60}	$7P_{1/2}$	$6S_{1/2}$	0.793	1260	0.13	[97] [93] [72]
τ_{63}	$7P_{1/2}$	$5D_{3/2}$	1.59	629	0.27	[96] [93]
τ_{65}	$7P_{1/2}$	$7S_{1/2}$	3.52	284	0.60	[96] [93]
Total Radiative Lifetime [ns]				**169**		
τ_{70}	$7P_{3/2}$	$6S_{1/2}$	1.84	544	0.26	[97] [93] [72]
τ_{73}	$7P_{3/2}$	$5D_{3/2}$	0.13	7700	0.02	[96] [93]
τ_{74}	$7P_{3/2}$	$5D_{5/2}$	1.10	910	0.15	[96] [93]
τ_{75}	$7P_{3/2}$	$7S_{1/2}$	4.05	247	0.57	[96] [93]
Total Radiative Lifetime [ns]				**140**		
τ_{81}	$6D_{3/2}$	$6P_{1/2}$	12.7	78.7	0.82	[96]
τ_{82}	$6D_{3/2}$	$6P_{3/2}$	2.66	376	0.17	[96]
τ_{86}	$6D_{3/2}$	$7P_{1/2}$	0.090	11000	0.01	[96]
τ_{87}	$6D_{3/2}$	$7P_{3/2}$	0.0086	120000	0.00	[96]
Total Radiative Lifetime [ns]				**64.7**		
τ_{92}	$6D_{5/2}$	$6P_{3/2}$	15.2	65.8	1.00	[96]
τ_{97}	$6D_{5/2}$	$7P_{3/2}$	0.063	15870	0.00	[96]
Total Radiative Lifetime [ns]				**65.5**		
$\tau_{10,1}$	$8S_{1/2}$	$6P_{1/2}$	2.04	490	0.21	[96]
$\tau_{10,2}$	$8S_{1/2}$	$6P_{3/2}$	3.60	278	0.37	[96]
$\tau_{10,6}$	$8S_{1/2}$	$7P_{1/2}$	1.38	725	0.14	[96]
$\tau_{10,7}$	$8S_{1/2}$	$7P_{3/2}$	2.62	382	0.27	[96]
Total Radiative Lifetime [ns]				**104**		

Table C.3: Cesium energy state kinetics parameters. Units on cross-sections and uncertainty are $\times 10^{-16}$ cm^2.

Process	**Sym.**	**Cross Sec.**	**Unc.**	**Temp.**	**Refs.**
Spin-Orbit Mixing (Methane) $6P_{3/2} + CH_4 \rightarrow 6P_{1/2} + CH_4$	$\sigma_{so,1\leftarrow 2}$	21.36	0.01	298 K	[4] [98]
Quenching (Methane) $6P_{1/2} + CH_4 \rightarrow 6S_{1/2} + CH_4$	$\sigma_{q,0\leftarrow 1}$	0.019	Upper Bound	313 K	[5]
Quenching (Methane) $6P_{3/2} + CH_4 \rightarrow 6S_{1/2} + CH_4$	$\sigma_{q,0\leftarrow 2}$	0.019	Upper Bound	313 K	[5]
Energy Pooling $2\,6P_{1/2} \rightarrow 6S_{1/2} + 6D_{3/2}$	$\sigma_{ep,06\leftarrow 11}$	130	30	337-365 K	[99] [100]
Energy Pooling $2\,6P_{1/2} \rightarrow 6S_{1/2} + 6D_{5/2}$	$\sigma_{ep,07\leftarrow 11}$	80	40	337-365 K	[99]
Energy Pooling $2\,6P_{1/2} \rightarrow 6S_{1/2} + 7P_{1/2}$	$\sigma_{ep,08\leftarrow 11}$	38	18	337-365 K	[99]
Energy Pooling $2\,6P_{1/2} \rightarrow 6S_{1/2} + 7P_{3/2}$	$\sigma_{ep,09\leftarrow 11}$	13	4	337-365 K	[99]
Energy Pooling $2\,6P_{1/2} \rightarrow 6S_{1/2} + 8S_{1/2}$	$\sigma_{ep,0,10\leftarrow 11}$	0.33	0.17	337-365 K	[99]
Energy Pooling $6P_{1/2} + 6P_{3/2} \rightarrow 6S_{1/2} + 6D_{3/2}$	$\sigma_{ep,06\leftarrow 12}$	49	Est.	350-597 K	[55] [101]
Energy Pooling $6P_{1/2} + 6P_{3/2} \rightarrow 6S_{1/2} + 6D_{5/2}$	$\sigma_{ep,07\leftarrow 12}$	58	Est.	350-597 K	[55] [101]
Energy Pooling $6P_{1/2} + 6P_{3/2} \rightarrow 6S_{1/2} + 7P_{1/2}$	$\sigma_{ep,08\leftarrow 12}$	2.4	Est.	350-597 K	[55]
Energy Pooling $6P_{1/2} + 6P_{3/2} \rightarrow 6S_{1/2} + 7P_{3/2}$	$\sigma_{ep,09\leftarrow 12}$	4.7	Est.	350-597 K	[55]

Energy Pooling $6P_{1/2} + 6P_{3/2} \rightarrow 6S_{1/2} + 8S_{1/2}$	$\sigma_{ep,0,10\leftarrow 12}$	4.6	Est.	350- 597 K	[55]
Energy Pooling $2\,6P_{3/2} \rightarrow 6S_{1/2} + 6D_{3/2}$	$\sigma_{ep,06\leftarrow 22}$	27	9	337- 365 K	[99] [100]
Energy Pooling $2\,6P_{3/2} \rightarrow 6S_{1/2} + 6D_{5/2}$	$\sigma_{ep,07\leftarrow 22}$	56	28	337- 365 K	[99]
Energy Pooling $2\,6P_{3/2} \rightarrow 6S_{1/2} + 7P_{1/2}$	$\sigma_{ep,08\leftarrow 22}$	1.8	0.8	337- 365 K	[99]
Energy Pooling $2\,6P_{3/2} \rightarrow 6S_{1/2} + 7P_{3/2}$	$\sigma_{ep,09\leftarrow 22}$	1.8	0.9	337- 365 K	[99]
Energy Pooling $2\,6P_{3/2} \rightarrow 6S_{1/2} + 8S_{1/2}$	$\sigma_{ep,0,10\leftarrow 22}$	5.2	2.2	337- 365 K	[99]
Penning Ionization $Cs^{**} + 6P \rightarrow 6S_{1/2} + Cs^{+} + e^{-}$	σ_{pen}	12900	Est.	470 K	[56]
Photoionization $Cs^{**} + h\nu \rightarrow Cs^{+} + e^{-}$	σ_{photo}	0.2	Est.	N/A	[23] [55] [58] [57]

C.3 Cesium Ionization Model Kinetic Equations

$$\begin{aligned}\frac{dn_1}{dt} = &-\left(\frac{1}{\tau_{10}} + \sigma_{q,0\leftarrow 1} v_{r,CH_4} n_{CH_4} + \sigma_{so,2\leftarrow 1} v_{r,CH_4} n_{CH_4}\right) n_1 - 2\sigma_{ep,11} v_r n_1^2 - \\ &- \sigma_{ep,12} v_r n_1 n_2 + \sigma_{so,1\leftarrow 2} v_{r,CH_4} n_{CH_4} n_2 + \frac{n_3}{\tau_{31}} + \frac{n_5}{\tau_{51}} + \frac{n_8}{\tau_{81}} + \frac{n_{10}}{\tau_{10,1}} - \\ &- \sigma_{pen}(n_6 + n_7 + n_8 + n_9 + n_{10}) n_1\end{aligned} \tag{C.5}$$

$$\begin{aligned}\frac{dn_2}{dt} =& W_{pump} + \sigma_{so,2\leftarrow 1} v_{r,CH_4} n_{CH_4} n_1 - \sigma_{ep,21} v_r n_1 n_2 - \\ &- \left(\frac{1}{\tau_{20}} + \sigma_{q,0\leftarrow 2} v_{r,CH_4} n_{CH_4} + \sigma_{so,1\leftarrow 2} v_{r,CH_4} n_{CH_4}\right) n_2 - 2\sigma_{ep,22} v_r n_2^2 + \\ &+ \frac{n_3}{\tau_{32}} + \frac{n_4}{\tau_{42}} + \frac{n_5}{\tau_{52}} + \frac{n_8}{\tau_{82}} + \frac{n_9}{\tau_{92}} + \frac{n_{10}}{\tau_{10,2}} - \\ &- \sigma_{pen}(n_6 + n_7 + n_8 + n_9 + n_{10}) n_2\end{aligned} \tag{C.6}$$

$$\frac{dn_3}{dt} = -\left(\frac{1}{\tau_{31}} + \frac{1}{\tau_{32}}\right) n_3 + \frac{n_6}{\tau_{63}} + \frac{n_7}{\tau_{73}} \tag{C.7}$$

$$\frac{dn_4}{dt} = -\frac{n_4}{\tau_{42}} + \frac{n_7}{\tau_{74}} \tag{C.8}$$

$$\frac{dn_5}{dt} = -\left(\frac{1}{\tau_{51}} + \frac{1}{\tau_{52}}\right) n_5 + \frac{n_6}{\tau_{65}} + \frac{n_7}{\tau_{75}} \tag{C.9}$$

$$\begin{aligned}\frac{dn_6}{dt} =& \sigma_{ep,06\leftarrow 11} v_r n_1^2 + \sigma_{ep,06\leftarrow 12} v_r n_1 n_2 + \sigma_{ep,06\leftarrow 22} v_r n_2^2 - \\ &- \left(\frac{1}{\tau_{60}} + \frac{1}{\tau_{63}} + \frac{1}{\tau_{65}}\right) n_6 + \frac{n_8}{\tau_{86}} + \frac{n_{10}}{\tau_{10,6}} - \\ &- \sigma_{pen} v_r (n_1 + n_2) n_6 - \sigma_{photo} \frac{I_{pump}}{h\nu} n_6\end{aligned} \tag{C.10}$$

$$\begin{aligned}\frac{dn_7}{dt} =& \sigma_{ep,07\leftarrow 11} v_r n_1^2 + \sigma_{ep,07\leftarrow 12} v_r n_1 n_2 + \sigma_{ep,07\leftarrow 22} v_r n_2^2 - \\ &- \left(\frac{1}{\tau_{70}} + \frac{1}{\tau_{73}} + \frac{1}{\tau_{74}} + \frac{1}{\tau_{75}}\right) n_7 + \frac{n_8}{\tau_{87}} + \frac{n_9}{\tau_{97}} + \frac{n_{10}}{\tau_{10,7}} - \\ &- \sigma_{pen} v_r (n_1 + n_2) n_7 - \sigma_{photo} \frac{I_{pump}}{h\nu} n_7\end{aligned} \tag{C.11}$$

$$\begin{aligned}\frac{dn_8}{dt} =&\sigma_{ep,08\leftarrow 11} v_r n_1^2 + \sigma_{ep,08\leftarrow 12} v_r n_1 n_2 + \sigma_{ep,08\leftarrow 22} v_r n_2^2 - \\ &- \left(\frac{1}{\tau_{81}} + \frac{1}{\tau_{82}} + \frac{1}{\tau_{86}} + \frac{1}{\tau_{87}}\right) n_8 - \sigma_{pen} v_r (n_1 + n_2) n_8 - \\ &- \sigma_{photo} \frac{I_{pump}}{h\nu} n_8\end{aligned} \tag{C.12}$$

$$\begin{aligned}\frac{dn_9}{dt} =&\sigma_{ep,09\leftarrow 11} v_r n_1^2 + \sigma_{ep,09\leftarrow 12} v_r n_1 n_2 + \sigma_{ep,09\leftarrow 22} v_r n_2^2 - \\ &- \left(\frac{1}{\tau_{82}} + \frac{1}{\tau_{87}}\right) n_9 - \sigma_{pen} v_r (n_1 + n_2) n_9 - \sigma_{photo} \frac{I_{pump}}{h\nu} n_9\end{aligned} \tag{C.13}$$

$$\begin{aligned}\frac{dn_{10}}{dt} =&\sigma_{ep,0,10\leftarrow 11} v_r n_1^2 + \sigma_{ep,0,10\leftarrow 12} v_r n_1 n_2 + \sigma_{ep,0,10\leftarrow 22} v_r n_2^2 - \\ &- \left(\frac{1}{\tau_{10,1}} + \frac{1}{\tau_{10,2}} + \frac{1}{\tau_{10,6}} + \frac{1}{\tau_{10,7}}\right) n_{10} - \sigma_{pen} v_r (n_1 + n_2) n_{10} - \\ &- \sigma_{photo} \frac{I_{pump}}{h\nu} n_{10}\end{aligned} \tag{C.14}$$

$$n_0 = n_{total} - \sum_{i=1}^{10} n_i \tag{C.15}$$

Appendix D

Full Set of Ion Chamber Measurements

During each test series, the conditions tabulated in Section D.1 for the cesium cell and Ti:Sapph pump beam were measured. Uncertainty in the conditions has been quantified, which has been incorporated into simulation and uncertainty in predictions of ionization rate. Each test series has been labeled alphabetically A-L. Test series A and B were recorded in September 2017, and involved pure helium buffer gas. Test series C-H were recorded in January 2018, and involved a 6:1 mixure of helium to methane buffer gas. Test series I-L were recorded in May 2018, and involved a 6:1 mixure of helium to methane buffer gas, as well as simultaneous fluorescence and ion chamber measurements. Each test series was recorded in roughly an hour, and involved maintaining constant thermal conditions. The temperature was controlled by maintaining the temperature at two thermocouples. The first thermocouple was located on the base of the cesium cell, and the second was located on a side tube that surrounded a power feed-through for an electrode. The second thermocouple was maintained at ten degrees above the first electrode to help prevent condensation of cesium on the cell windows. The cesium density and corresponding temperature

inside the cell were measured through analysis of pump beam absorption. Comparisons of measurements and predictions of pump absorption are shown in Section D.2. The nominal values of cesium density and temperature inside the cell correspond to the average of Monte Carlo uncertainty quantification, and the minimum and maximum values correspond to one standard deviation (1σ). The inside cell temperature correspond to cesium density through the relationship defined by Steck [52]. The temperature inside the cell was typically a few degrees hotter than either thermocouple. The tabulated center wavelength measurements and uncertainty account for the 0.05 ± 0.01 nm off-set measured in the optical spectrum analyzer. Multiple measurements of the pump beam intensity profile were taken with either a beam profiler or with a knife-edge measurement, recorded at multiple times throughout each test day. The beam diameter reported corresponds to the $1/e$ point of the Gaussian fit. The measurements were fit in the horizontal and vertical axes separately, and the reported diameter is the geometric mean of the two measurements. The beam profile measurements are shown in Sec. D.3. Sections D.4 and D.5 summarize results of all electrode measurements. Additionally, measurements of fluorescent power in multiple spectral lines is shown in Sec. D.6, which were recorded simultaneously with ion chamber test series I-L.

D.1 Parameters during Ion Chamber Testing

Table D.1: Measured test parameters including uncertainty from test series A, buffer gas = helium only, thermocouple 1 = 40 °C, thermocouple 2 = 50 °C.

Parameter	**Nominal**	**Minimum**	**Maximum**
Beam Diameter ($1/e$) [cm]	0.160	0.150	0.169
Center Wavelength [nm]	852.334	852.322	852.346
Pump Spectrum FWHM [nm]	0.040	0.036	0.044
Alkali Density [cm^{-3}]	0.74×10^{12}	0.68×10^{12}	0.80×10^{12}
Temperature Inside Cell [°C]	55.7	54.7	56.7

Table D.2: Measured test parameters including uncertainty from test series B, buffer gas = helium only, thermocouple 1 = 50 °C, thermocouple 2 = 60 °C.

Parameter	**Nominal**	**Minimum**	**Maximum**
Beam Diameter ($1/e$) [cm]	0.160	0.150	0.169
Center Wavelength [nm]	852.339	852.325	852.353
Pump Spectrum FWHM [nm]	0.034	0.032	0.036
Alkali Density [cm^{-3}]	1.4×10^{12}	1.3×10^{12}	1.5×10^{12}
Temperature Inside Cell [°C]	64.0	63.1	64.9

Table D.3: Measured test parameters including uncertainty from test series C, buffer gas = 6:1 mixture He:CH_4, thermocouple 1 = 35 °C, thermocouple 2 = 45 °C.

Parameter	**Nominal**	**Minimum**	**Maximum**
Beam Diameter ($1/e$) [cm]	0.121	0.100	0.140
Center Wavelength [nm]	852.325	852.312	852.338
Pump Spectrum FWHM [nm]	0.036	0.034	0.038
Alkali Density [cm^{-3}]	0.32×10^{12}	0.27×10^{12}	0.36×10^{12}
Temperature Inside Cell [°C]	45.1	43.5	46.7

Table D.4: Measured test parameters including uncertainty from test series D, buffer gas = 6:1 mixture He:CH_4, thermocouple 1 = 40 °C, thermocouple 2 = 50 °C.

Parameter	**Nominal**	**Minimum**	**Maximum**
Beam Diameter ($1/e$) [cm]	0.121	0.100	0.140
Center Wavelength [nm]	852.324	852.311	852.336
Pump Spectrum FWHM [nm]	0.037	0.035	0.038
Alkali Density [cm^{-3}]	0.47×10^{12}	0.41×10^{12}	0.54×10^{12}
Temperature Inside Cell [°C]	50.1	48.4	51.7

Table D.5: Measured test parameters including uncertainty from test series E, buffer gas = 6:1 mixture He:CH_4, thermocouple 1 = 45 °C, thermocouple 2 = 55 °C.

Parameter	**Nominal**	**Minimum**	**Maximum**
Beam Diameter ($1/e$) [cm]	0.121	0.100	0.140
Center Wavelength [nm]	852.325	852.312	852.338
Pump Spectrum FWHM [nm]	0.037	0.035	0.039
Alkali Density [cm^{-3}]	0.78×10^{12}	0.67×10^{12}	0.88×10^{12}
Temperature Inside Cell [°C]	56.3	54.6	58.0

Table D.6: Measured test parameters including uncertainty from test series F, buffer gas = 6:1 mixture He:CH_4, thermocouple 1 = 50 °C, thermocouple 2 = 60 °C.

Parameter	**Nominal**	**Minimum**	**Maximum**
Beam Diameter $(1/e)$ [cm]	0.121	0.100	0.140
Center Wavelength [nm]	852.327	852.312	852.342
Pump Spectrum FWHM [nm]	0.045	0.041	0.048
Alkali Density [cm^{-3}]	1.0×10^{12}	0.91×10^{12}	1.2×10^{12}
Temperature Inside Cell [°C]	60.0	58.4	61.6

Table D.7: Measured test parameters including uncertainty from test series G, buffer gas = 6:1 mixture He:CH_4, thermocouple 1 = 55 °C, thermocouple 2 = 65 °C.

Parameter	**Nominal**	**Minimum**	**Maximum**
Beam Diameter $(1/e)$ [cm]	0.121	0.100	0.140
Center Wavelength [nm]	852.329	852.316	852.342
Pump Spectrum FWHM [nm]	0.048	0.046	0.049
Alkali Density [cm^{-3}]	1.5×10^{12}	1.3×10^{12}	1.7×10^{12}
Temperature Inside Cell [°C]	64.9	63.3	66.4

Table D.8: Measured test parameters including uncertainty from test series H, buffer gas = 6:1 mixture He:CH_4, thermocouple 1 = 60 °C, thermocouple 2 = 70 °C.

Parameter	**Nominal**	**Minimum**	**Maximum**
Beam Diameter $(1/e)$ [cm]	0.121	0.100	0.140
Center Wavelength [nm]	852.325	852.313	852.337
Pump Spectrum FWHM [nm]	0.035	0.033	0.036
Alkali Density [cm^{-3}]	2.2×10^{12}	1.9×10^{12}	2.6×10^{12}
Temperature Inside Cell [°C]	70.2	68.0	74.4

Table D.9: Measured test parameters including uncertainty from test series I, buffer gas = 6:1 mixture He:CH_4, thermocouple 1 = 50 °C, thermocouple 2 = 60 °C, simultaneous measurement of fluorescence and ion chamber.

Parameter	**Nominal**	**Minimum**	**Maximum**
Beam Diameter $(1/e)$ [cm]	0.115	0.109	0.120
Center Wavelength [nm]	852.347	852.332	852.362
Pump Spectrum FWHM [nm]	0.030	0.027	0.033
Alkali Density [cm^{-3}]	1.2×10^{12}	1.1×10^{12}	1.3×10^{12}
Temperature Inside Cell [°C]	61.9	60.9	62.8

Table D.10: Measured test parameters including uncertainty from test series J, buffer gas = 6:1 mixture He:CH_4, thermocouple 1 = 55 °C, thermocouple 2 = 65 °C, simultaneous measurement of fluorescence and ion chamber.

Parameter	**Nominal**	**Minimum**	**Maximum**
Beam Diameter ($1/e$) [cm]	0.115	0.109	0.120
Center Wavelength [nm]	852.334	852.322	852.346
Pump Spectrum FWHM [nm]	0.036	0.034	0.038
Alkali Density [cm^{-3}]	1.8×10^{12}	1.6×10^{12}	1.9×10^{12}
Temperature Inside Cell [°C]	67.3	66.1	68.5

Table D.11: Measured test parameters including uncertainty from test series K, buffer gas = 6:1 mixture He:CH_4, thermocouple 1 = 60 °C, thermocouple 2 = 70 °C, simultaneous measurement of fluorescence and ion chamber.

Parameter	**Nominal**	**Minimum**	**Maximum**
Beam Diameter ($1/e$) [cm]	0.115	0.109	0.120
Center Wavelength [nm]	852.339	852.327	852.351
Pump Spectrum FWHM [nm]	0.035	0.033	0.036
Alkali Density [cm^{-3}]	2.4×10^{12}	2.2×10^{12}	2.6×10^{12}
Temperature Inside Cell [°C]	71.4	70.2	72.6

Table D.12: Measured test parameters including uncertainty from test series L, buffer gas = 6:1 mixture He:CH_4, thermocouple 1 = 65 °C, thermocouple 2 = 75 °C, simultaneous measurement of fluorescence and ion chamber.

Parameter	**Nominal**	**Minimum**	**Maximum**
Beam Diameter ($1/e$) [cm]	0.115	0.109	0.120
Center Wavelength [nm]	852.339	852.327	852.350
Pump Spectrum FWHM [nm]	0.033	0.031	0.034
Alkali Density [cm^{-3}]	3.5×10^{12}	3.0×10^{12}	3.9×10^{12}
Temperature Inside Cell [°C]	76.6	74.9	78.4

D.2 Measurements of Pump Absorption

Figures D.1 - D.12 show measurements of pump laser absorption. The measurements were used to determine the cesium density of the cell. The measurements were part of the Monte Carlo error analysis previously discussed in Sec. 5.1. Each test series (A - L) was assigned a nominal cesium density and one standard deviation (1σ) uncertainty, listed in Sec D.1. Each figure shows a series of transmitted pump laser power measurements with varying incident power. Each point on the curve was recorded at a roughly five minute interval from the previous measurement during ion chamber testing. The temperature and cesium density of the system was nearly constant during testing, but differences between simulated and measured pump laser transmission is likely due to thermal and cesium density fluctutations.

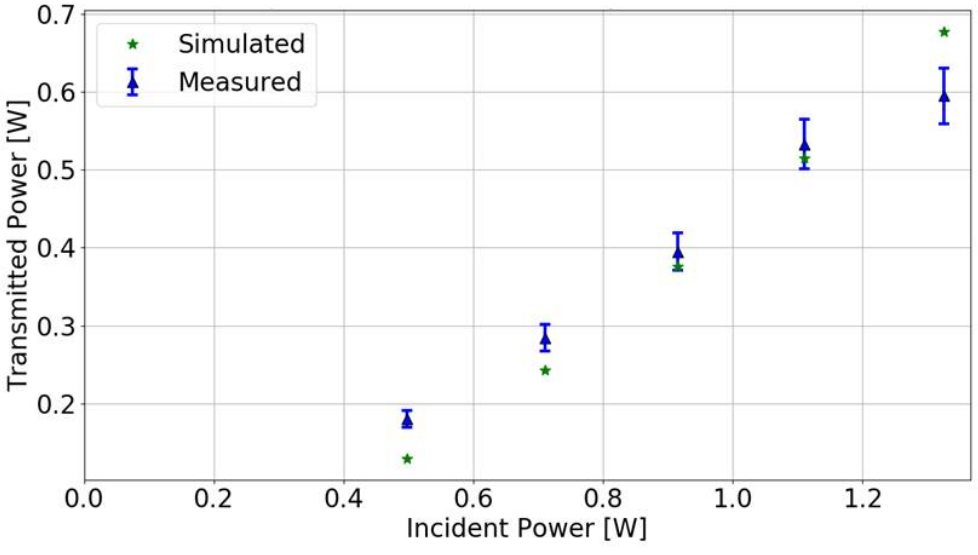

Figure D.1: Test Series A: Comparison of pump absorption measurements and simulated results at nominal conditions.

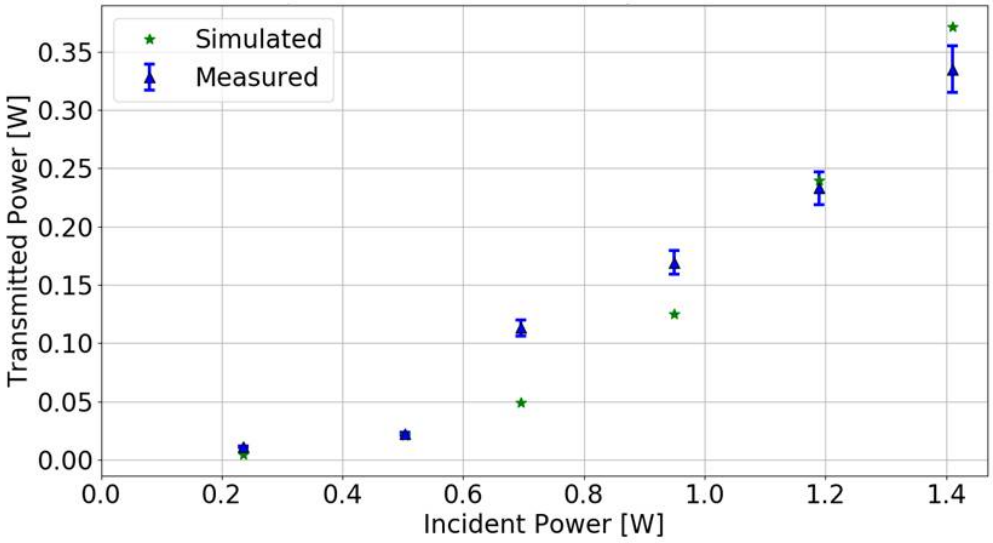

Figure D.2: Test Series B: Comparison of pump absorption measurements and simulated results at nominal conditions.

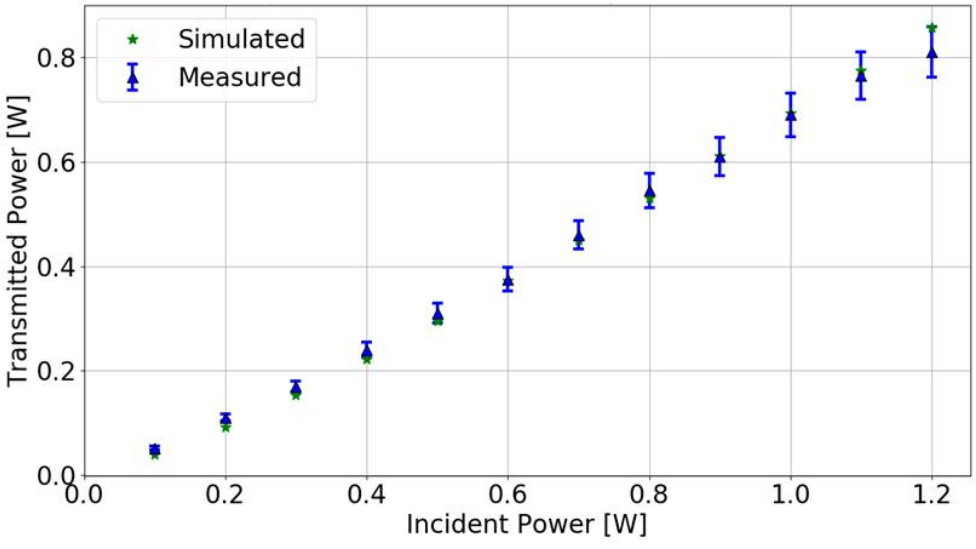

Figure D.3: Test Series C: Comparison of pump absorption measurements and simulated results at nominal conditions.

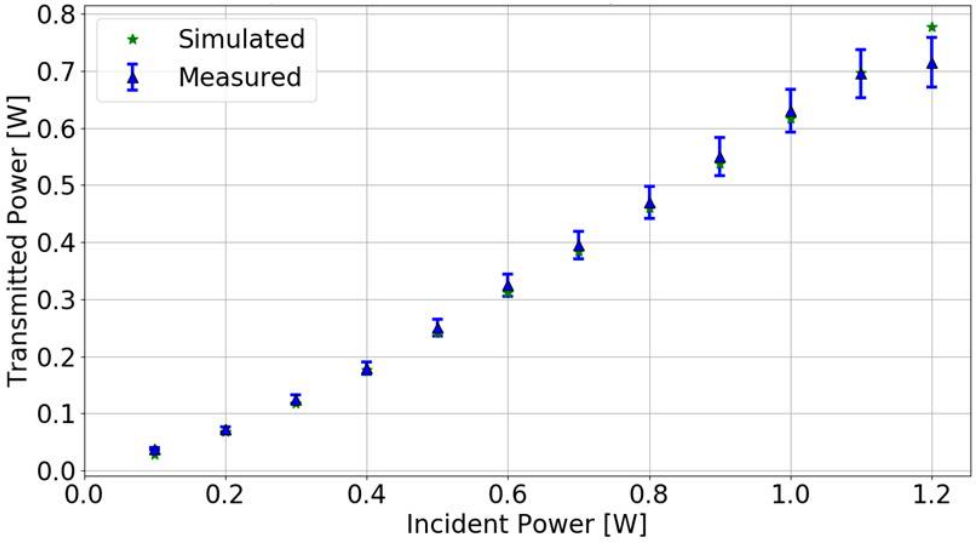

Figure D.4: Test Series D: Comparison of pump absorption measurements and simulated results at nominal conditions.

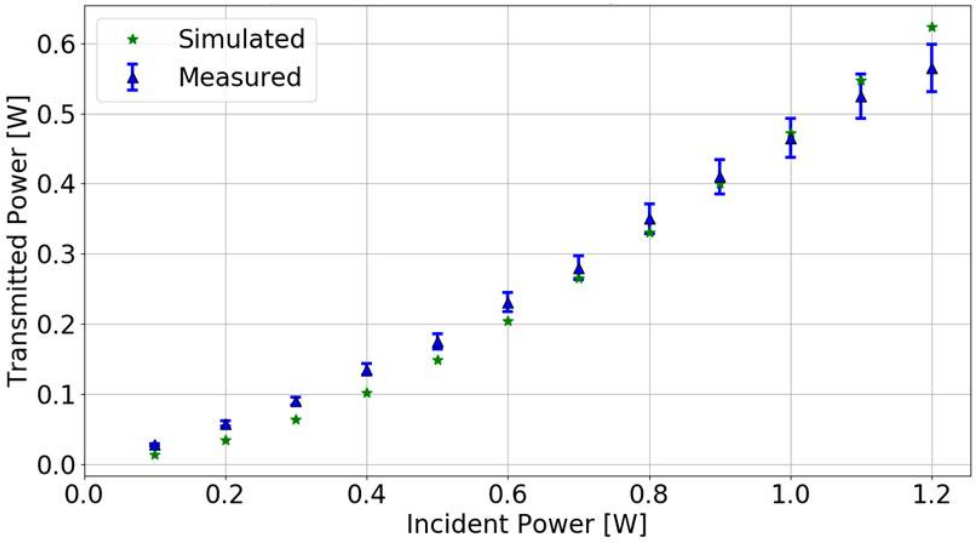

Figure D.5: Test Series E: Comparison of pump absorption measurements and simulated results at nominal conditions.

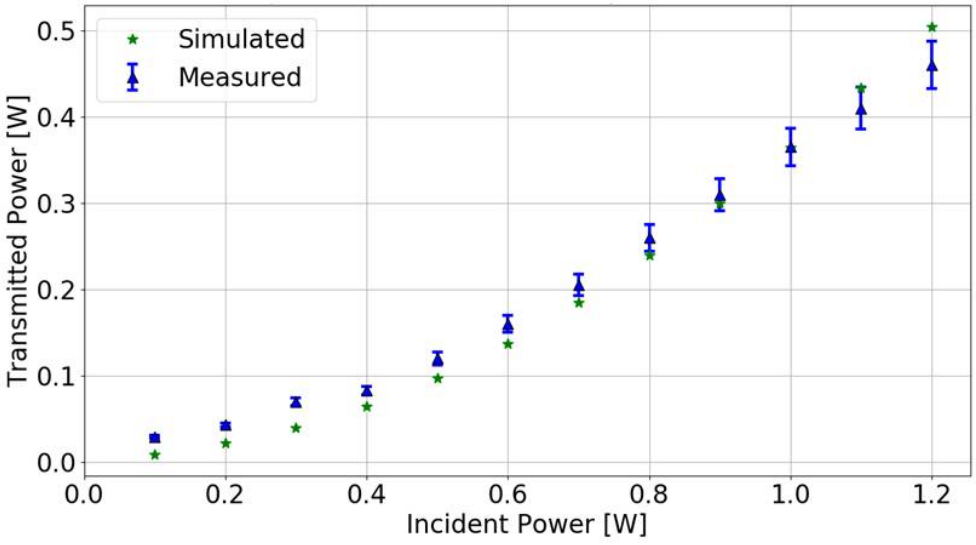

Figure D.6: Test Series F: Comparison of pump absorption measurements and simulated results at nominal conditions.

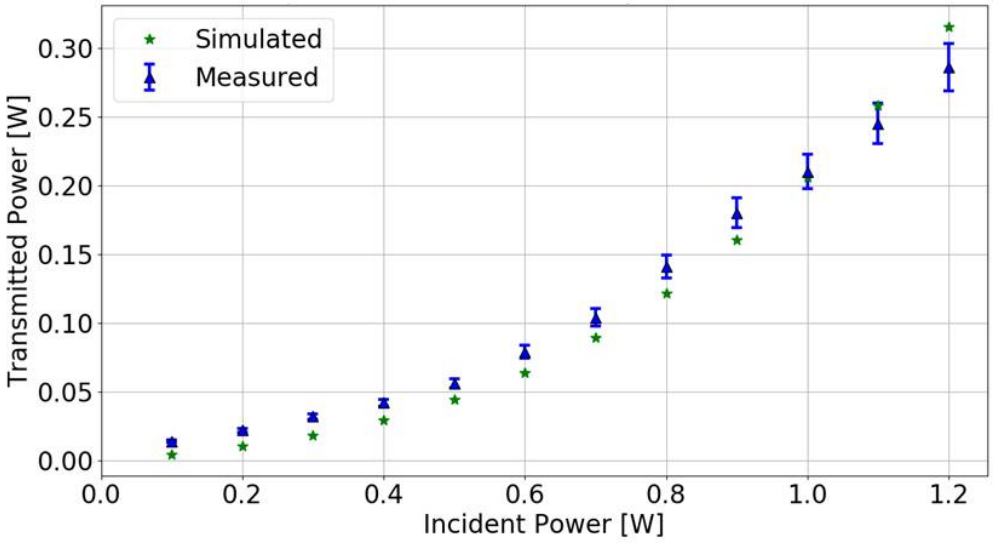

Figure D.7: Test Series G: Comparison of pump absorption measurements and simulated results at nominal conditions.

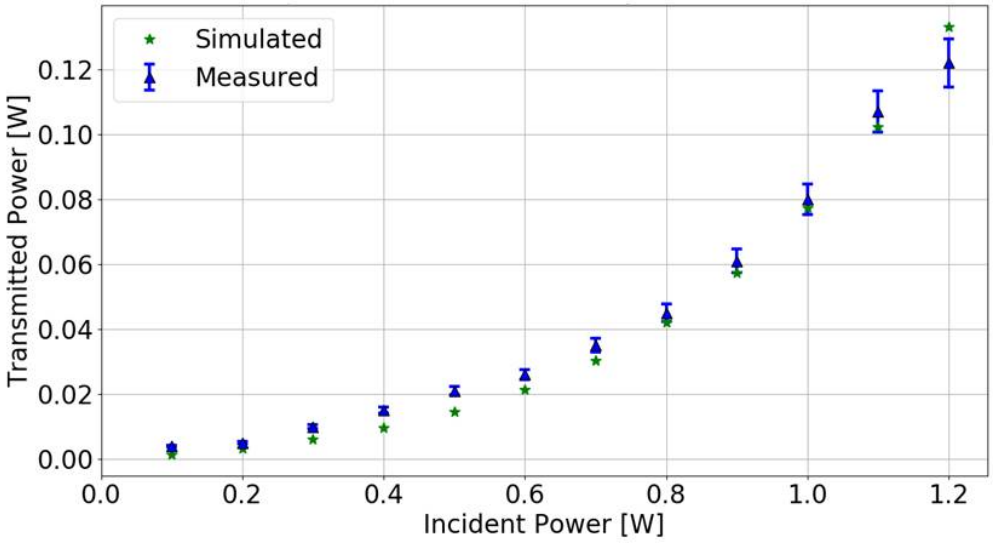

Figure D.8: Test Series H: Comparison of pump absorption measurements and simulated results at nominal conditions.

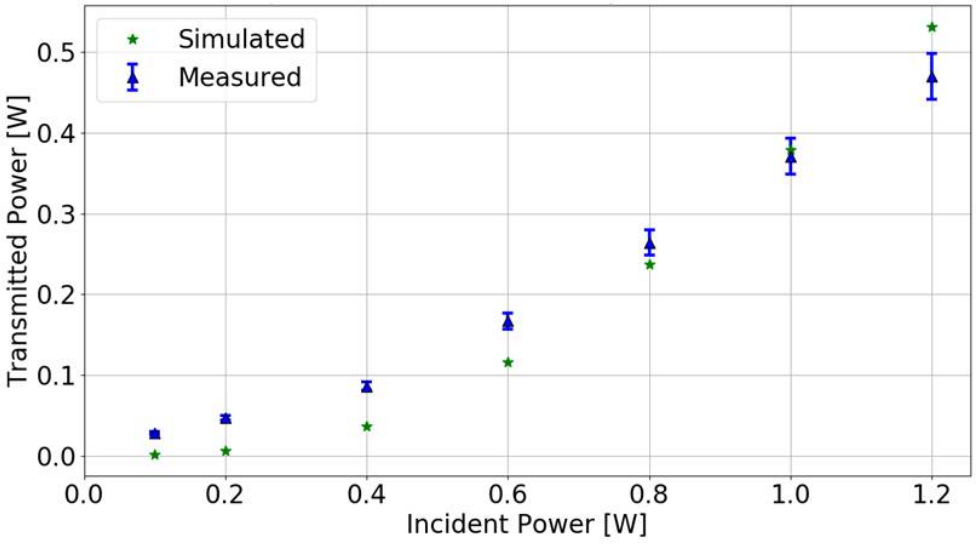

Figure D.9: Test Series I: Comparison of pump absorption measurements and simulated results at nominal conditions.

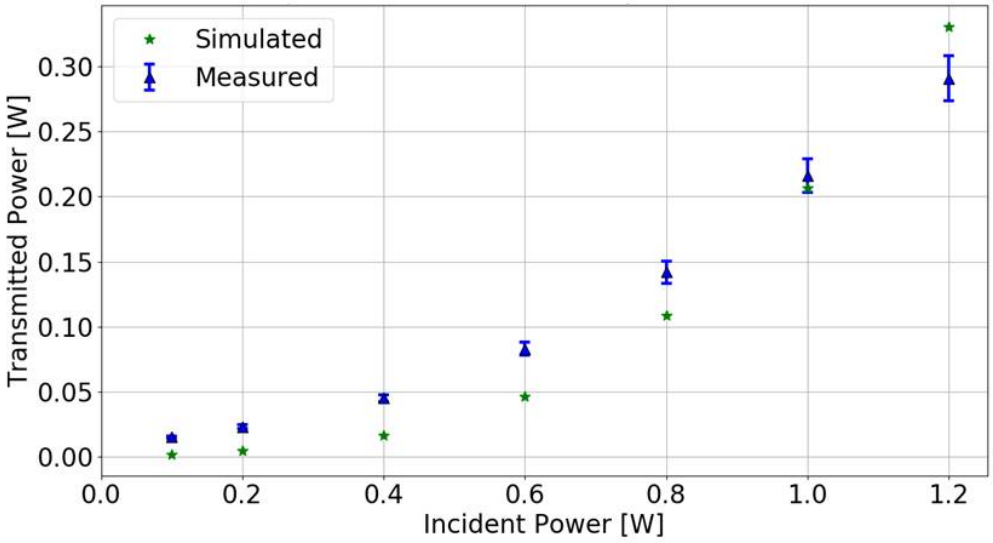

Figure D.10: Test Series J: Comparison of pump absorption measurements and simulated results at nominal conditions.

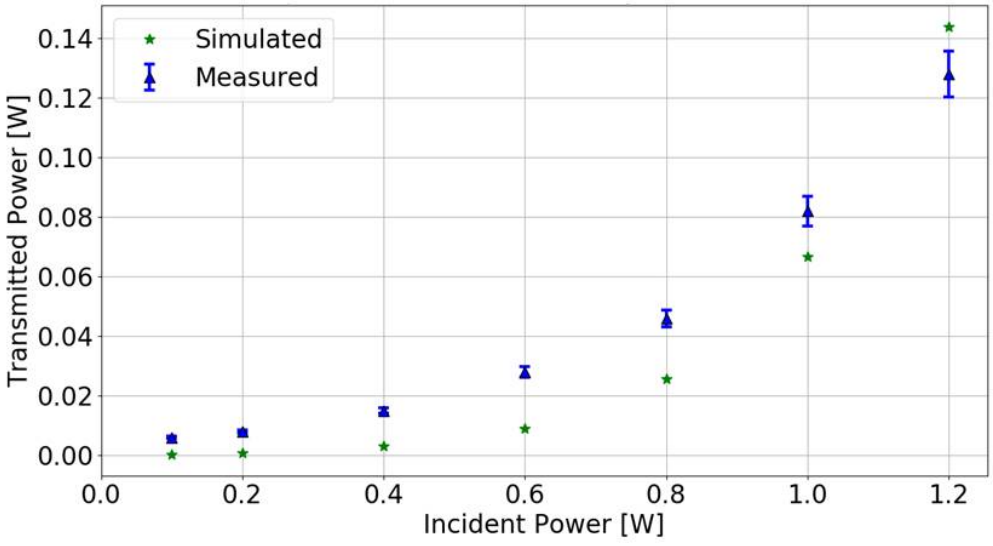

Figure D.11: Test Series K: Comparison of pump absorption measurements and simulated results at nominal conditions.

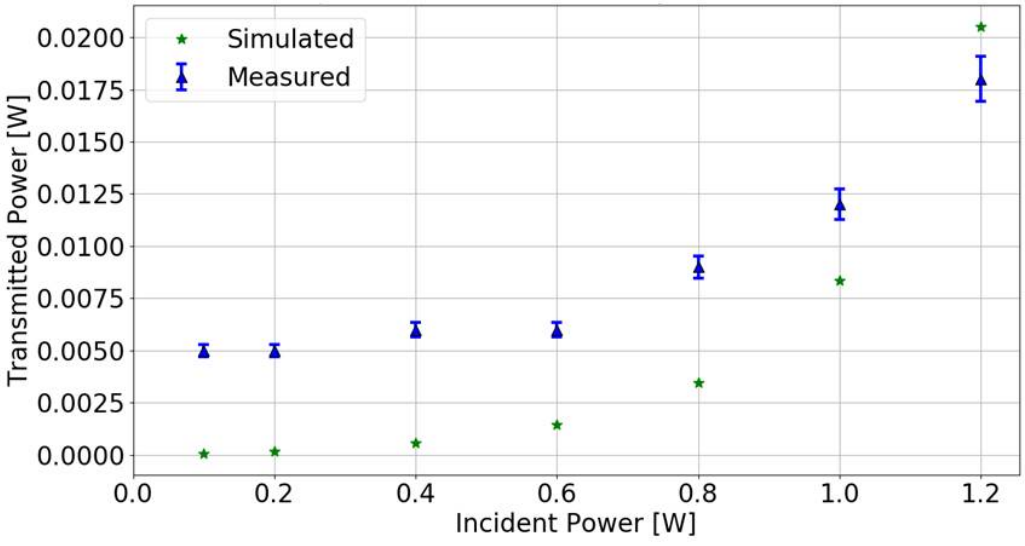

Figure D.12: Test Series L: Comparison of pump absorption measurements and simulated results at nominal conditions.

D.3 Measurements of Beam Profiles

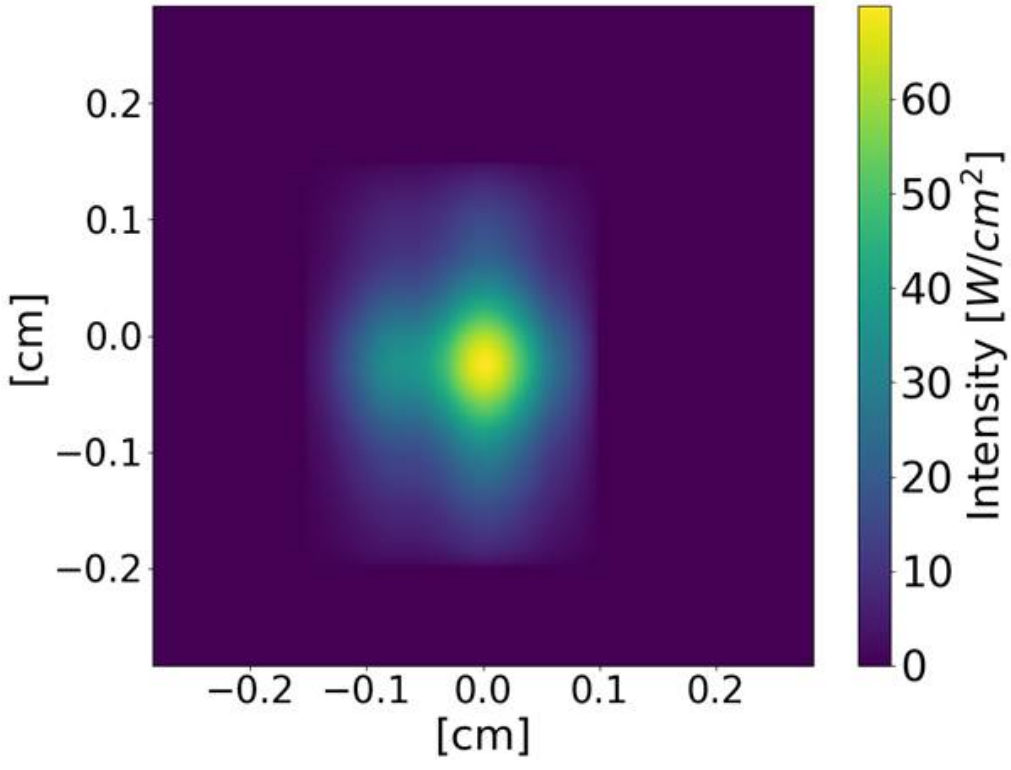

Figure D.13: Test Series A-B: Beam profile measurement (Before test series 1)

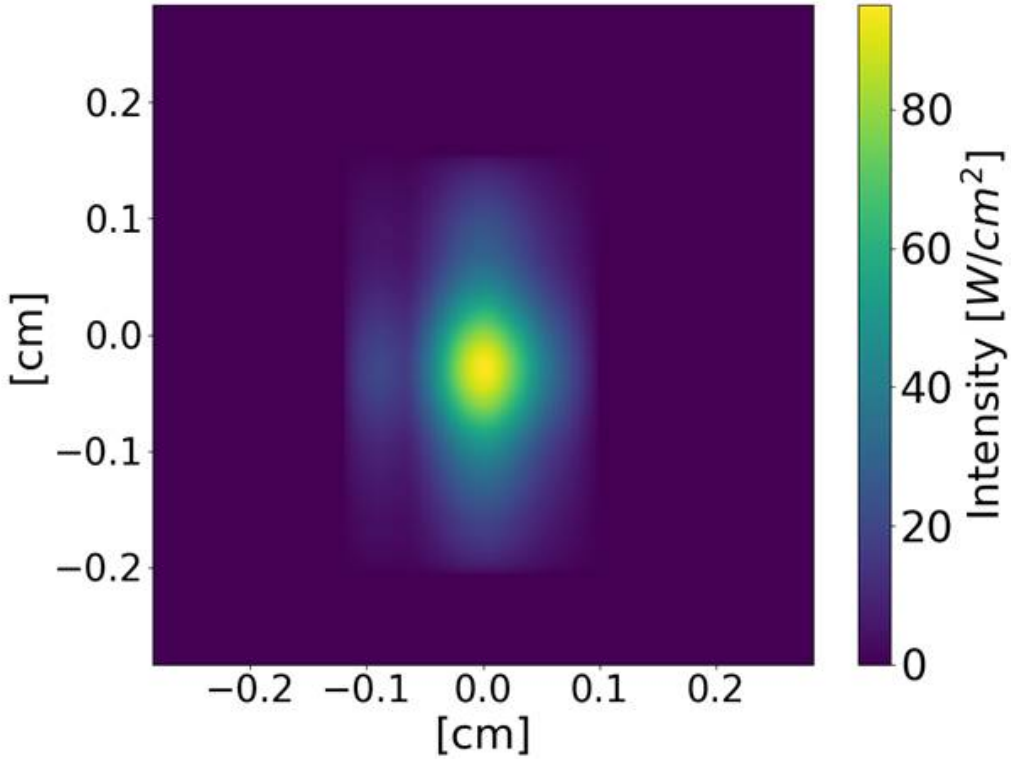

Figure D.14: Test Series A-B: Beam profile measurement (After test series 2)

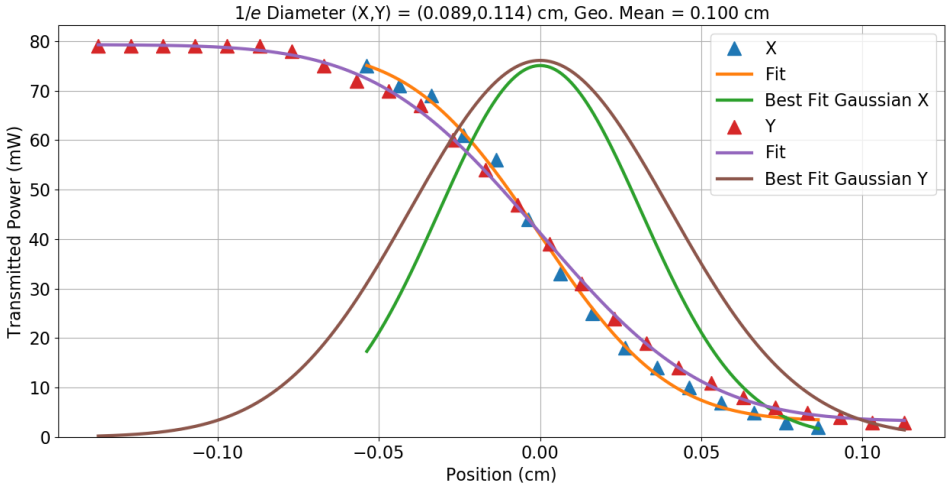

Figure D.15: Test Series C-H: Beam profile measurement using knife edge before testing

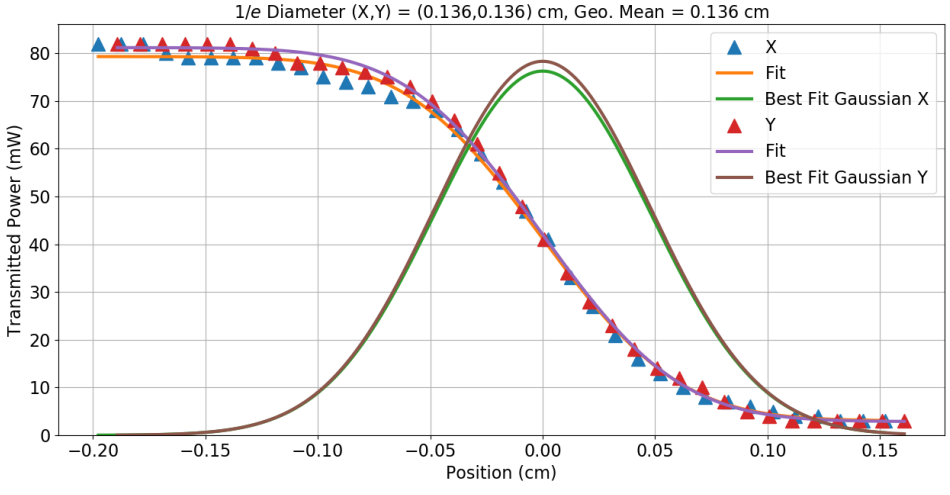

Figure D.16: Test Series C-H: Beam profile measurement using knife edge in the middle of testing

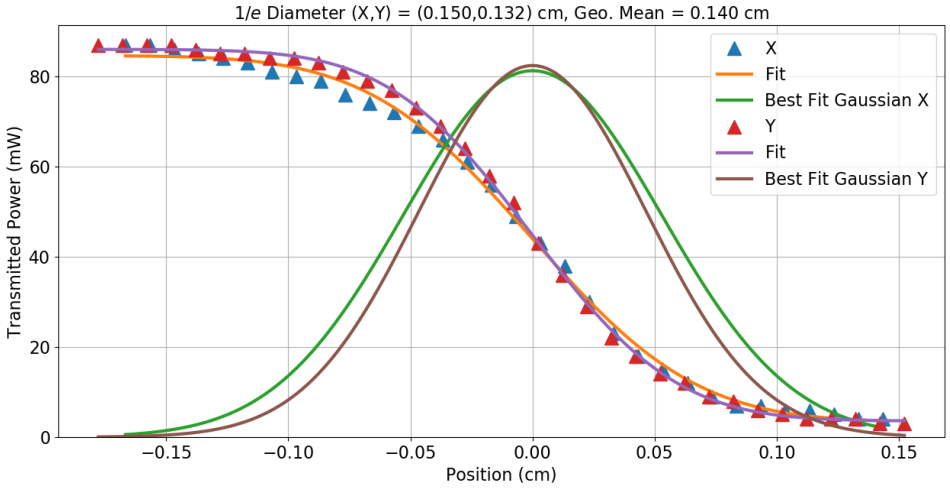

Figure D.17: Test Series C-H: Beam profile measurement using knife edge at the end of testing

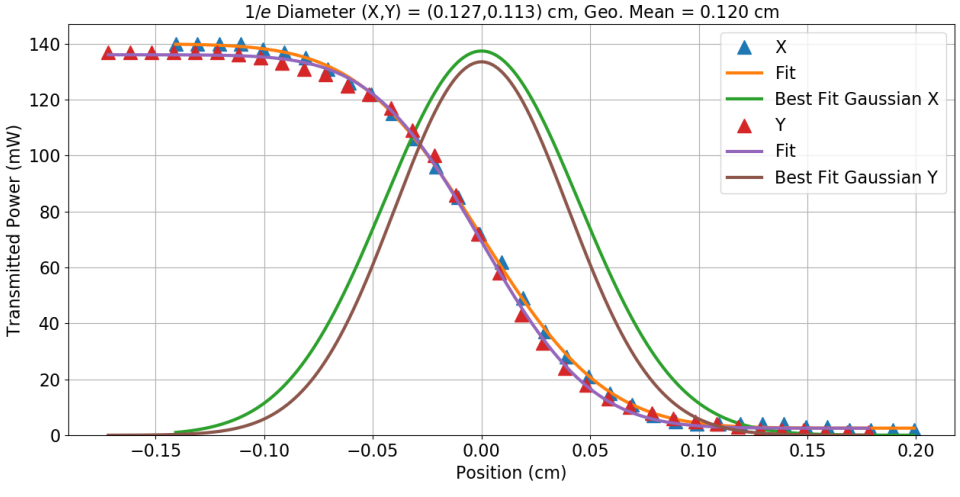

Figure D.18: Test Series I-L: Beam profile measurement using knife edge before testing

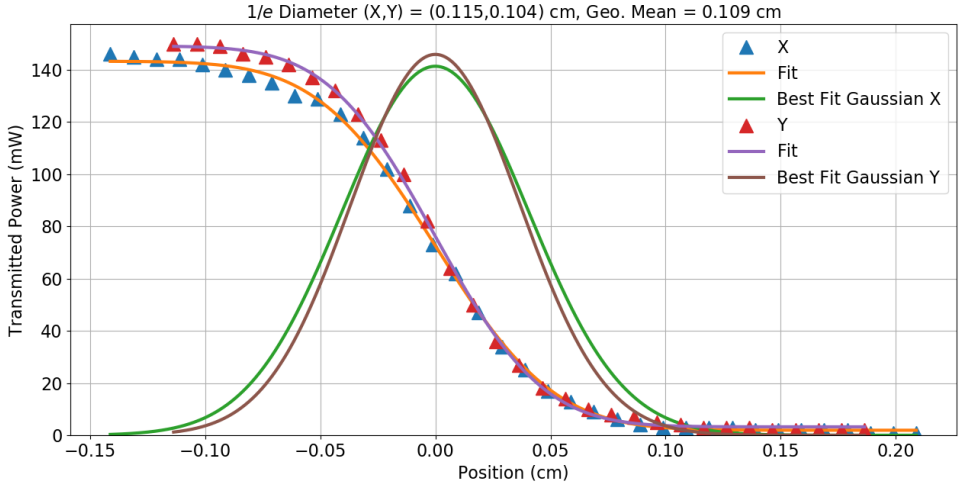

Figure D.19: Test Series I-L: Beam profile measurement using knife edge at the end of testing

D.4 Tabulated Ion Chamber Measurements

Table D.13: Results of ion chamber measurements in test series A - D

Test	**Temp.**	**Density**	**Pump Power**	**Off-Set**	**Sat. Voltage**	**Sat. Current**
[N/A]	**[°C]**	**[cm^{-3}]**	**[W]**	**[nA]**	**[V]**	**[nA]**
A1	56	0.74×10^{12}	0.5	0.0	2	2.1
A2	56	0.74×10^{12}	0.7	0.6	2	4.0
A3	56	0.74×10^{12}	0.9	2.5	5	5.8
A4	56	0.74×10^{12}	1.1	4.3	7	7.7
A5	56	0.74×10^{12}	1.3	5.1	8	12
B1	64	1.39×10^{12}	0.2	2.0	10	3.4
B2	64	1.39×10^{12}	0.5	4.2	12	18
B3	64	1.39×10^{12}	0.7	8.8	12	39
B4	64	1.39×10^{12}	1.0	14.2	19	80
B5	64	1.39×10^{12}	1.2	16.4	22	111
B6	64	1.39×10^{12}	1.4	15.6	28	131
C1	45	0.32×10^{12}	0.1	0.2	3	0.2
C2	45	0.32×10^{12}	0.2	0.0	3	0.1
C3	45	0.32×10^{12}	0.3	0.3	3	0.3
C4	45	0.32×10^{12}	0.4	0.3	3	0.4
C5	45	0.32×10^{12}	0.5	0.4	4	0.6
C6	45	0.32×10^{12}	0.6	0.5	4	0.6
C7	45	0.32×10^{12}	0.7	0.5	4	0.8
C8	45	0.32×10^{12}	0.8	0.5	3	0.9
C9	45	0.32×10^{12}	0.9	0.7	5	1.0
C10	45	0.32×10^{12}	1.0	0.7	4	1.2
C11	45	0.32×10^{12}	1.1	0.6	4	1.5
C12	45	0.32×10^{12}	1.2	0.9	4	1.4
D1	50	0.47×10^{12}	0.1	0.1	4	0.3
D2	50	0.47×10^{12}	0.2	0.2	4	0.4
D3	50	0.47×10^{12}	0.3	0.3	4	0.7
D4	50	0.47×10^{12}	0.4	0.7	4	1.3
D5	50	0.47×10^{12}	0.5	0.6	4	1.6
D6	50	0.47×10^{12}	0.6	1.0	4	2.3

Table D.14: Results of ion chamber measurements in test series D - G

Test	**Temp.**	**Density**	**Pump Power**	**Off-Set**	**Sat. Voltage**	**Sat. Current**
[N/A]	**[°C]**	**[cm^{-3}]**	**[W]**	**[nA]**	**[V]**	**[nA]**
D7	50	0.47×10^{12}	0.7	1.3	4	2.9
D8	50	0.47×10^{12}	0.8	1.6	5	3.4
D9	50	0.47×10^{12}	0.9	1.7	5	3.8
D10	50	0.47×10^{12}	1.0	2.0	5	4.5
D11	50	0.47×10^{12}	1.1	2.4	5	5.2
D12	50	0.47×10^{12}	1.2	2.1	4	5.0
E1	56	0.78×10^{12}	0.1	0.2	3	0.2
E2	56	0.78×10^{12}	0.2	0.6	4	0.6
E3	56	0.78×10^{12}	0.3	0.8	4	1.4
E4	56	0.78×10^{12}	0.4	1.3	4	2.9
E5	56	0.78×10^{12}	0.5	1.8	6	5.2
E6	56	0.78×10^{12}	0.6	2.8	8	7.6
E7	56	0.78×10^{12}	0.7	3.5	9	11
E8	56	0.78×10^{12}	0.8	4.4	10	15
E9	56	0.78×10^{12}	0.9	4.9	11	17
E10	56	0.78×10^{12}	1.0	5.6	12	20
E11	56	0.78×10^{12}	1.1	6.1	13	24
E12	56	0.78×10^{12}	1.2	6.7	13	24
F1	60	1.03×10^{12}	0.1	0.0	3	0.2
F2	60	1.03×10^{12}	0.2	0.7	3	0.9
F3	60	1.03×10^{12}	0.3	1.5	5	3.0
F4	60	1.03×10^{12}	0.4	3.1	9	11
F5	60	1.03×10^{12}	0.5	4.5	13	18
F6	60	1.03×10^{12}	0.6	6.2	16	27
F7	60	1.03×10^{12}	0.7	7.1	17	36
F8	60	1.03×10^{12}	0.8	8.3	19	46
F9	60	1.03×10^{12}	0.9	9.5	22	56
F10	60	1.03×10^{12}	1.0	10.3	23	65
F11	60	1.03×10^{12}	1.1	12.2	26	76
F12	60	1.03×10^{12}	1.2	14.2	27	91
G1	65	1.49×10^{12}	0.1	0.5	4	0.5
G2	65	1.49×10^{12}	0.2	1.5	7	4.0
G3	65	1.49×10^{12}	0.3	3.2	14	13
G4	65	1.49×10^{12}	0.4	5.0	18	26
G5	65	1.49×10^{12}	0.5	7.3	24	45
G6	65	1.49×10^{12}	0.6	9.2	29	67

Table D.15: Results of ion chamber measurements in test series G - L

Test	**Temp.**	**Density**	**Pump Power**	**Off-Set**	**Sat. Voltage**	**Sat. Current**
[N/A]	**[°C]**	**[cm^{-3}]**	**[W]**	**[nA]**	**[V]**	**[nA]**
G7	65	1.49×10^{12}	0.7	11.4	33	92
G8	65	1.49×10^{12}	0.8	13.1	37	117
G9	65	1.49×10^{12}	0.9	14.1	39	143
G10	65	1.49×10^{12}	1.0	14.9	41	167
G11	65	1.49×10^{12}	1.1	15.9	43	189
G12	65	1.49×10^{12}	1.2	17.0	42	189
H1	70	2.21×10^{12}	0.1	1.1	15	2.4
H2	70	2.21×10^{12}	0.2	2.8	20	14
H3	70	2.21×10^{12}	0.3	4.9	33	38
H4	70	2.21×10^{12}	0.4	8.5	52	78
H5	70	2.21×10^{12}	0.5	9.6	61	133
H6	70	2.21×10^{12}	0.6	13.5	79	201
H7	70	2.21×10^{12}	0.7	13.5	84	265
H8	70	2.21×10^{12}	0.8	16.3	106	418
H9	70	2.21×10^{12}	0.9	17.6	105	470
H10	70	2.21×10^{12}	1.0	16.5	110	555
H11	70	2.21×10^{12}	1.1	16.4	116	645
H12	70	2.21×10^{12}	1.2	19.3	111	647
I1+	62	1.19×10^{12}	1.2	10.8	10	33
I1-	62	1.19×10^{12}	1.2	6.5	14	32
J1+	67	1.78×10^{12}	1.2	17.8	19	92
J1-	67	1.78×10^{12}	1.2	11.6	29	91
K1+	71	2.40×10^{12}	1.2	28.4	37	258
K1-	71	2.40×10^{12}	1.2	18.5	54	248
L1+	77	3.47×10^{12}	1.2	30.6	62	648
L1-	77	3.47×10^{12}	1.2	14.3	81	591

D.5 Ion Chamber Measurements

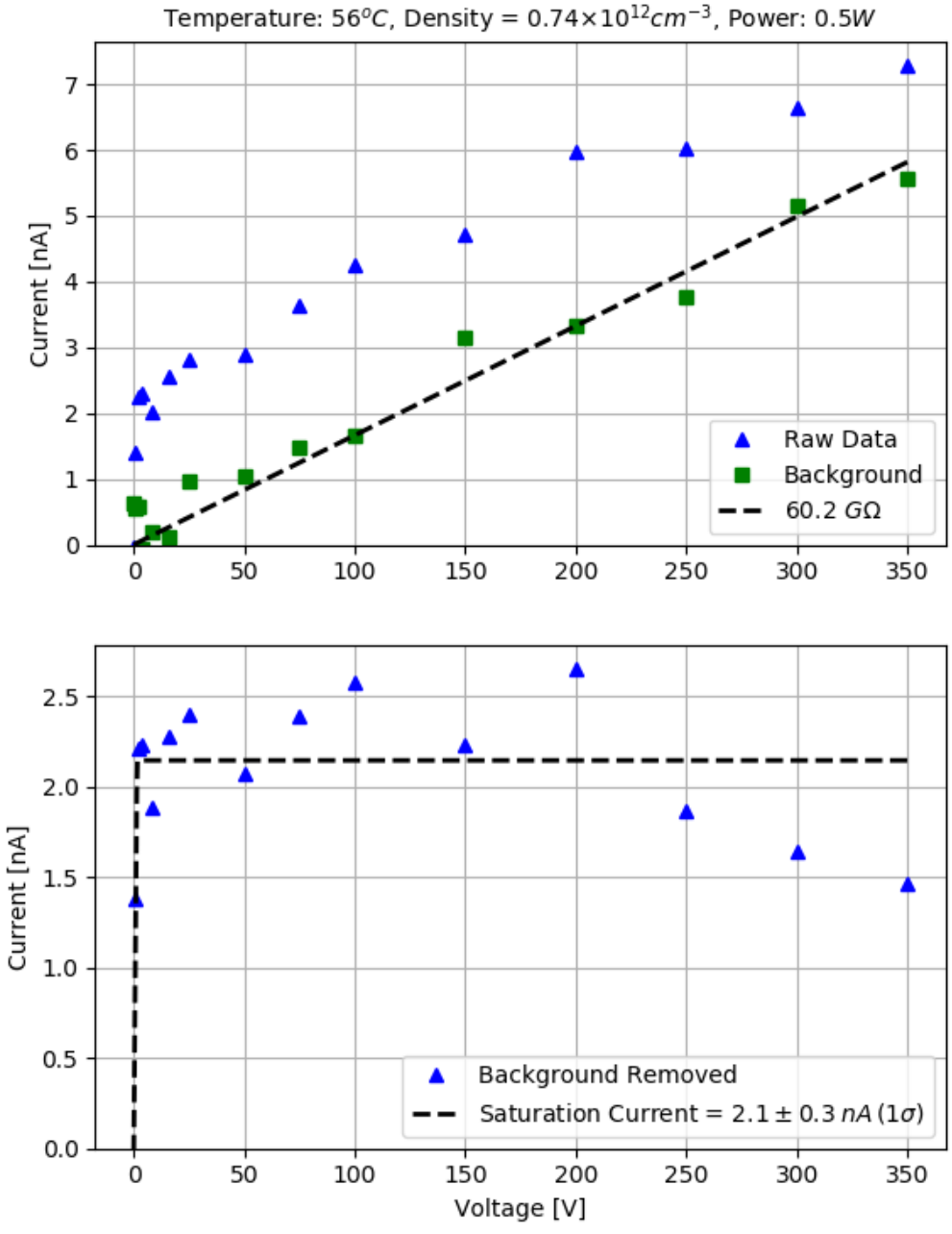

Figure D.20: Electrode measurement A1

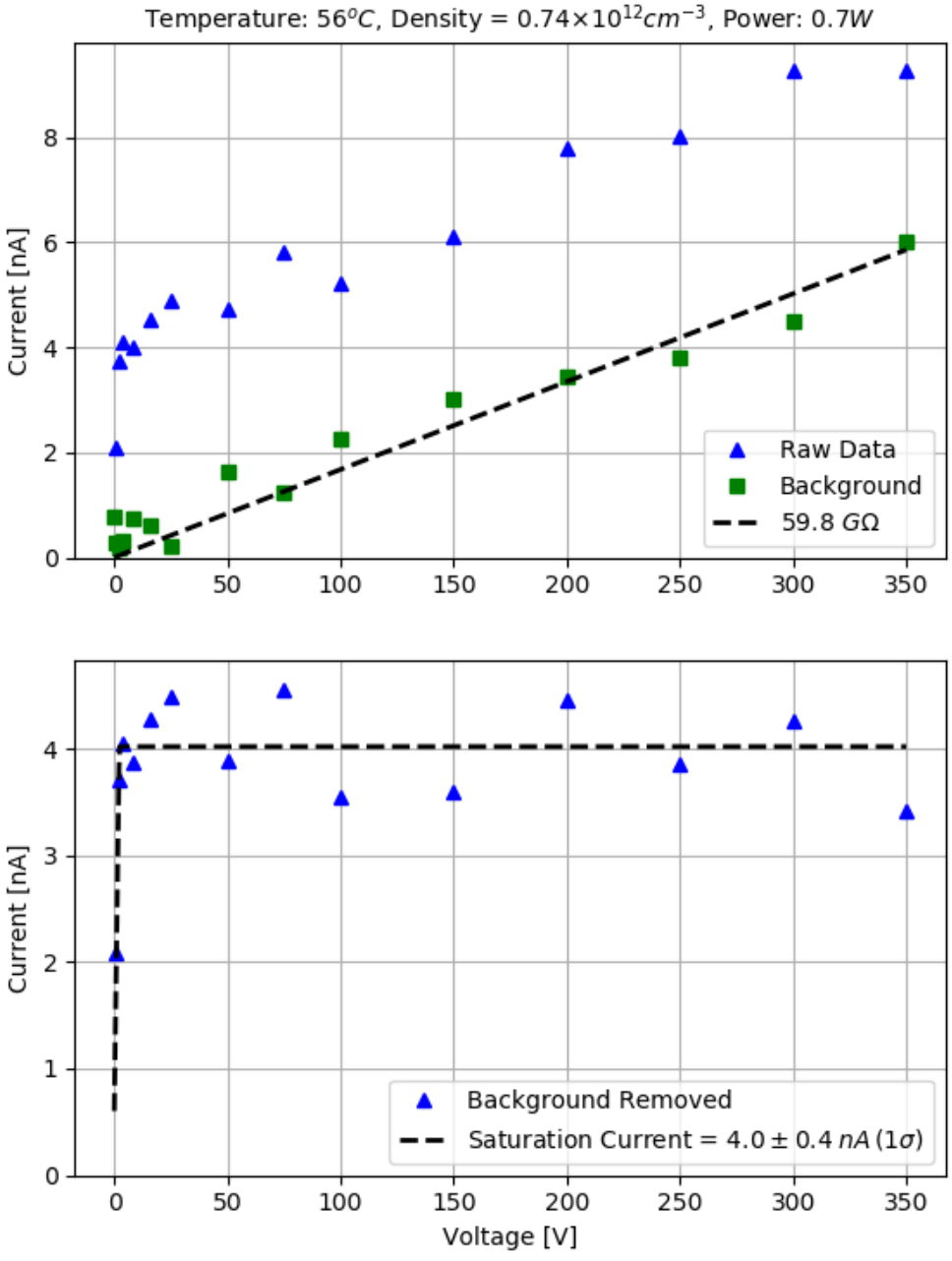

Figure D.21: Electrode measurement A2

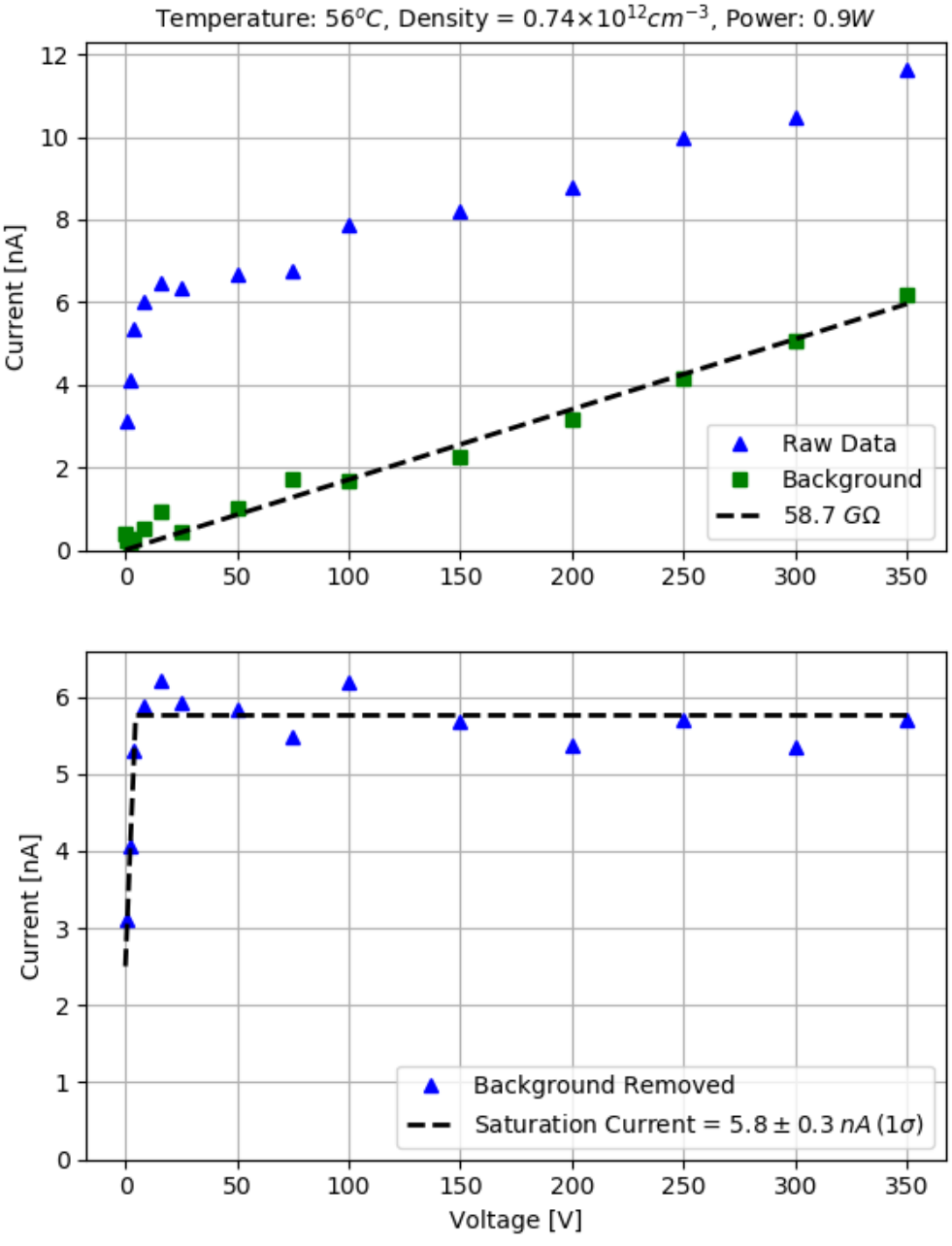

Figure D.22: Electrode measurement A3

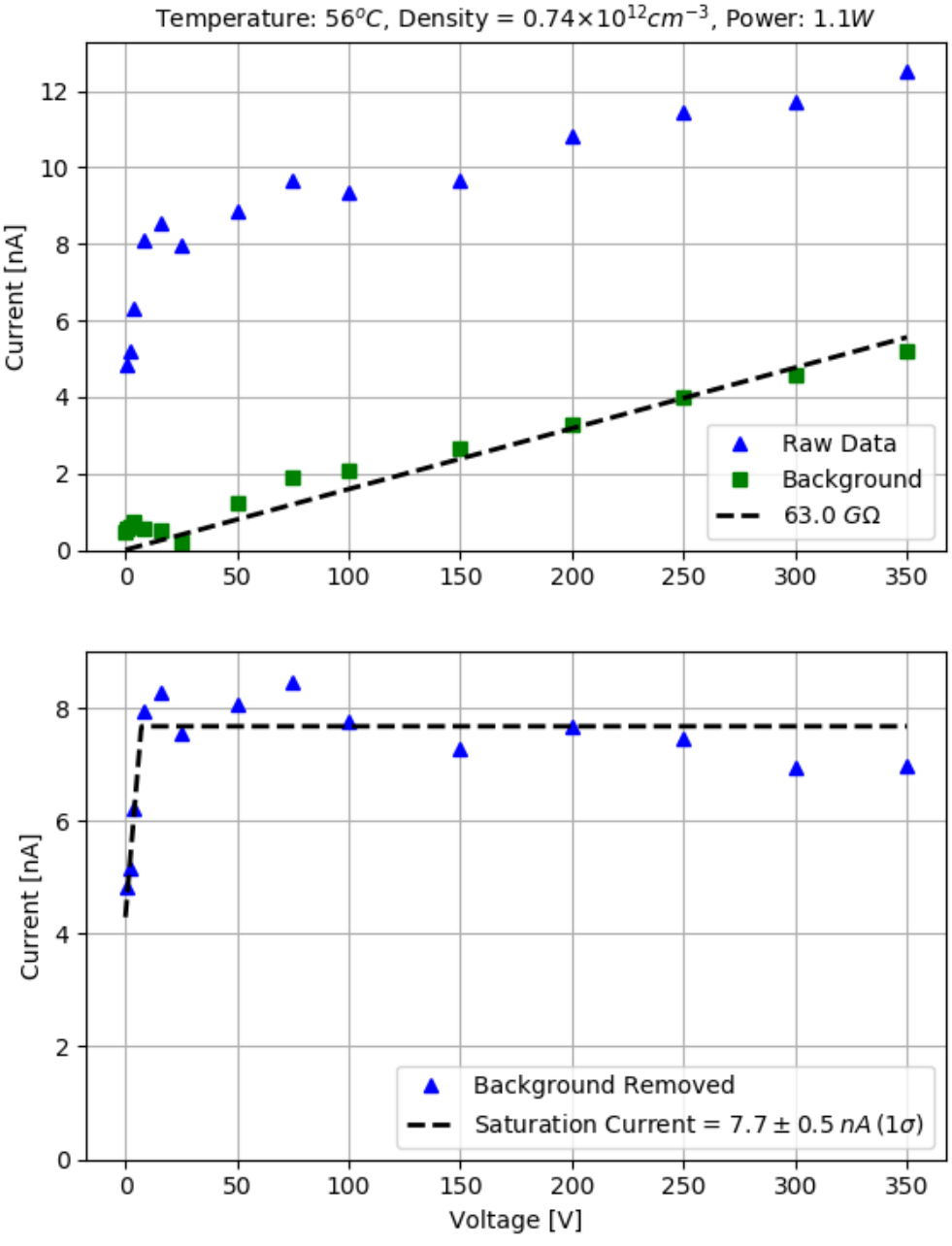

Figure D.23: Electrode measurement A4

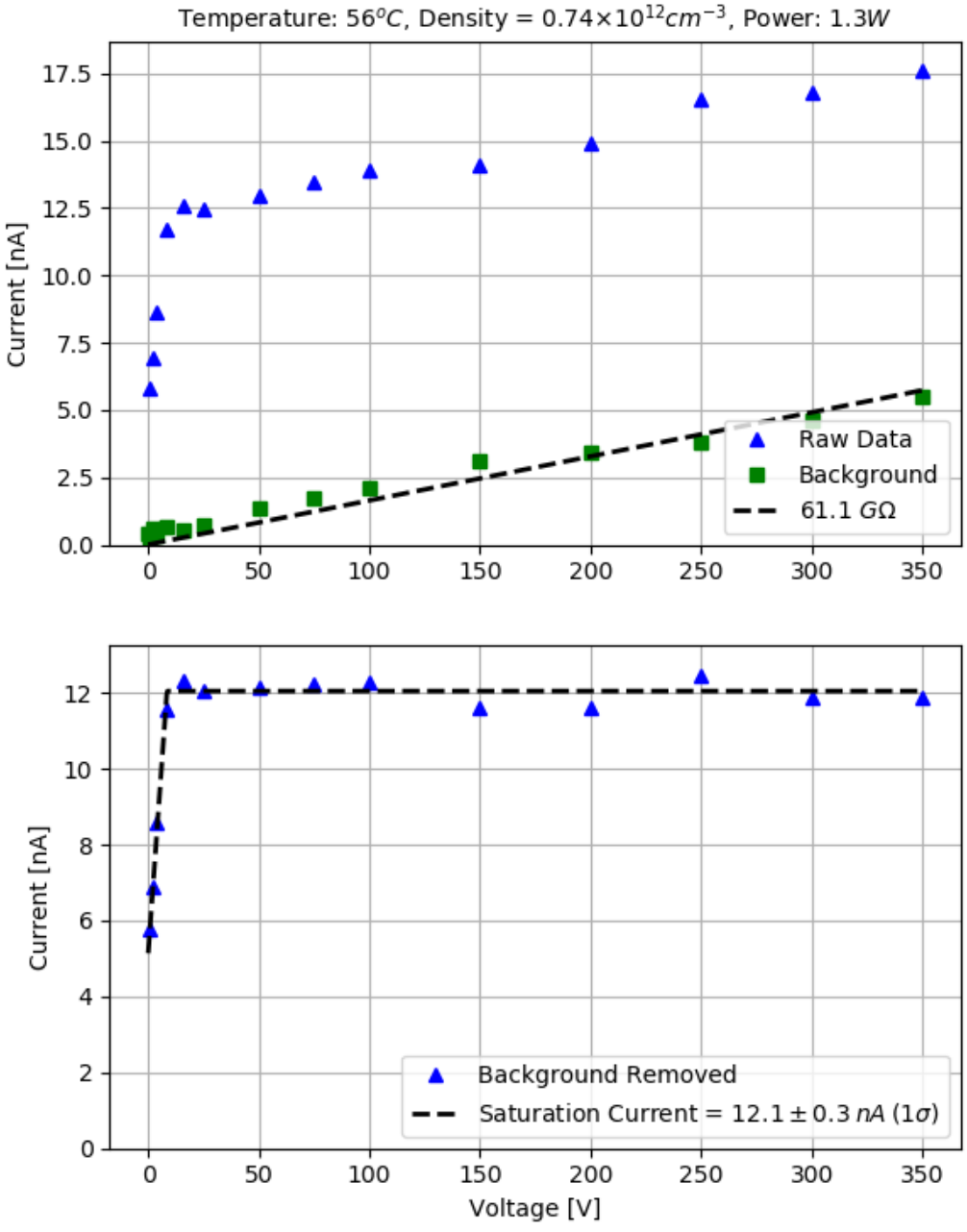

Figure D.24: Electrode measurement A5

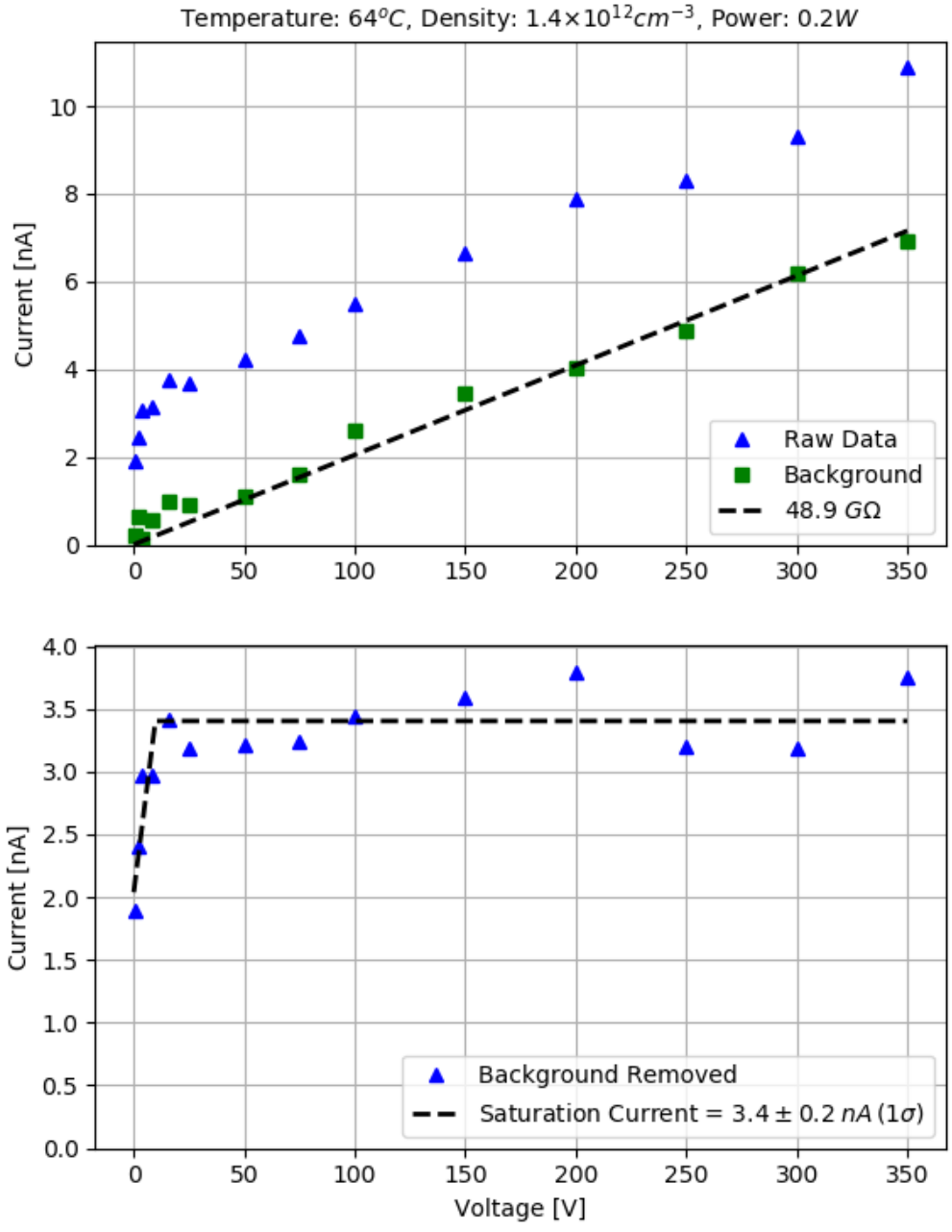

Figure D.25: Electrode measurement B1

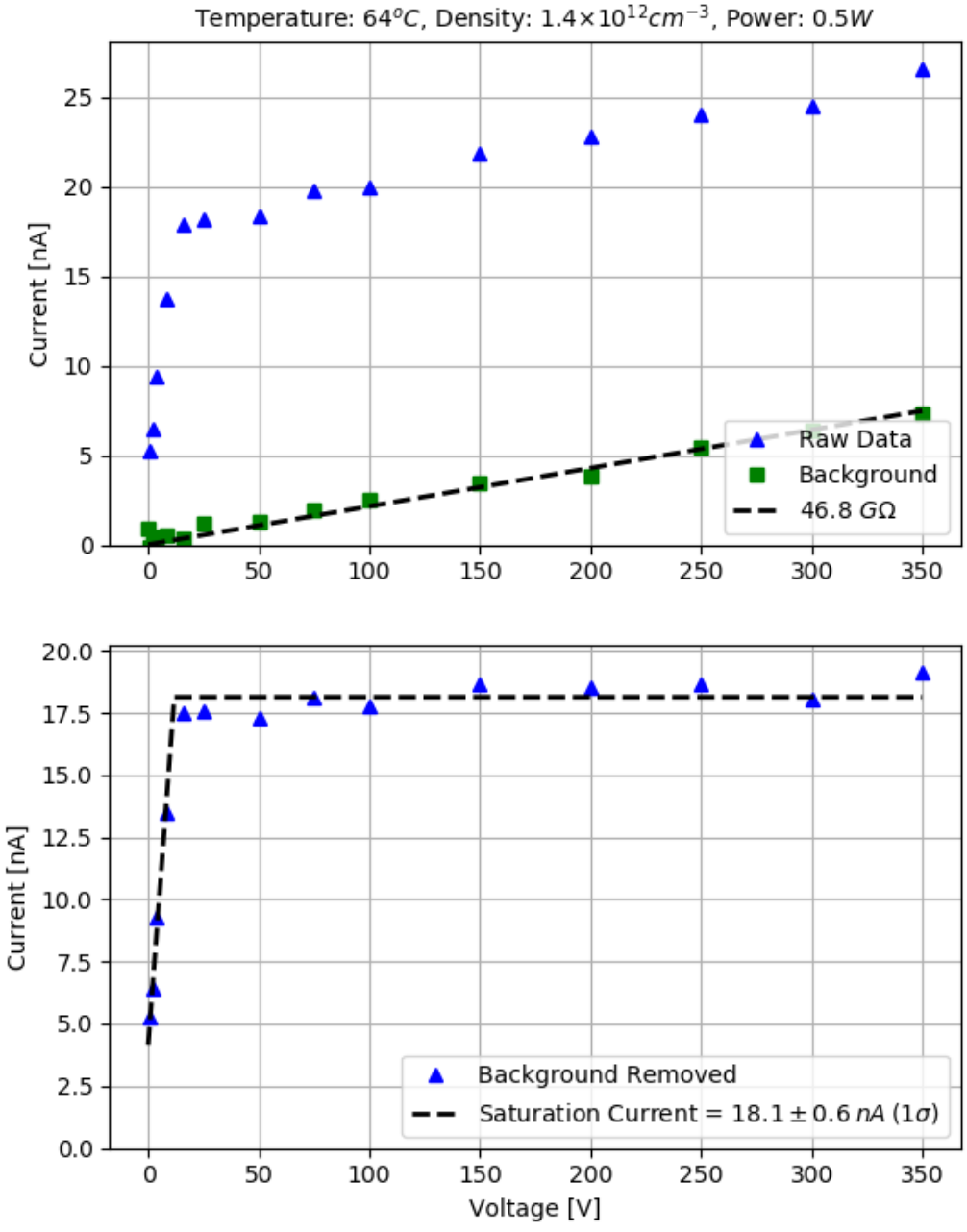

Figure D.26: Electrode measurement B2

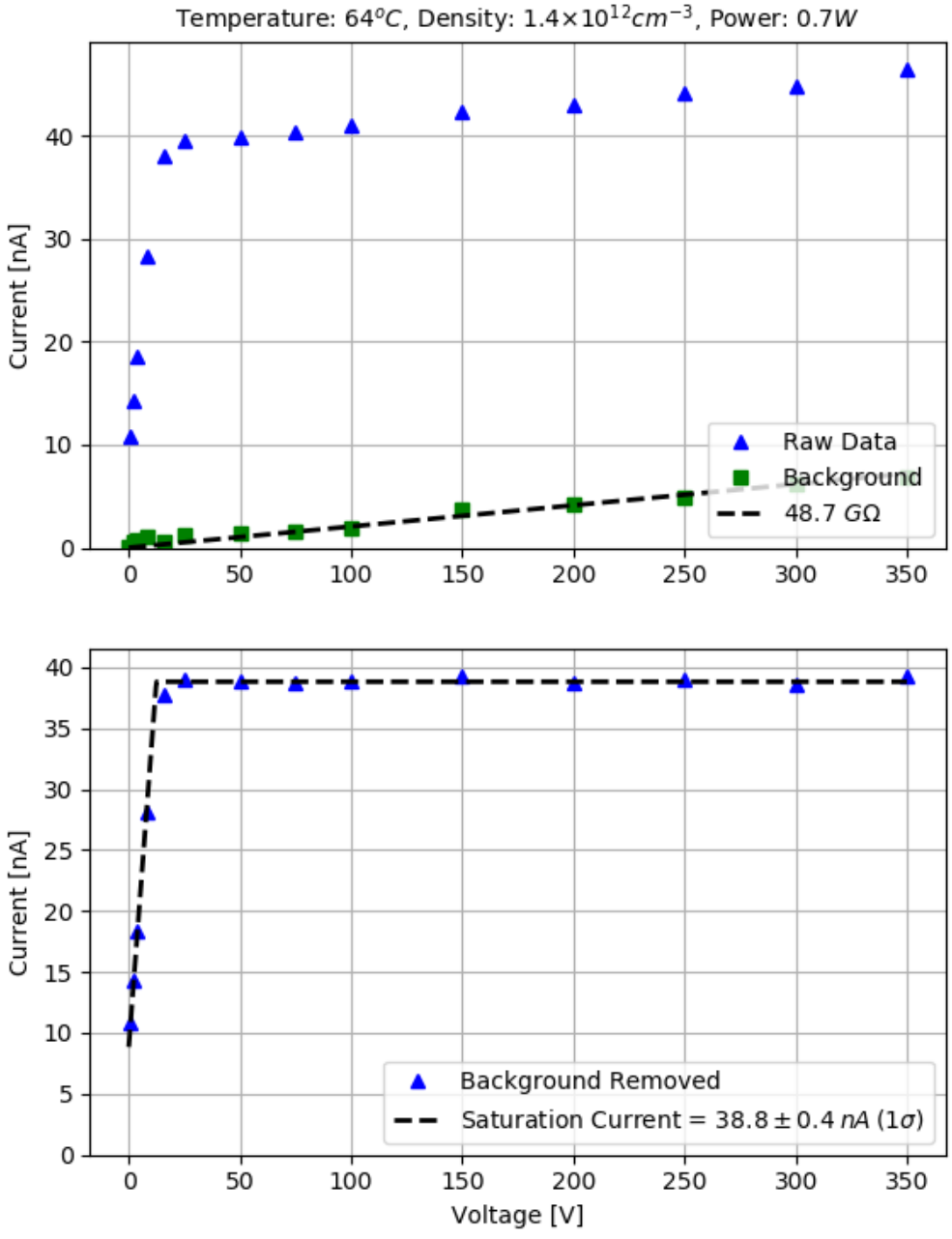

Figure D.27: Electrode measurement B3

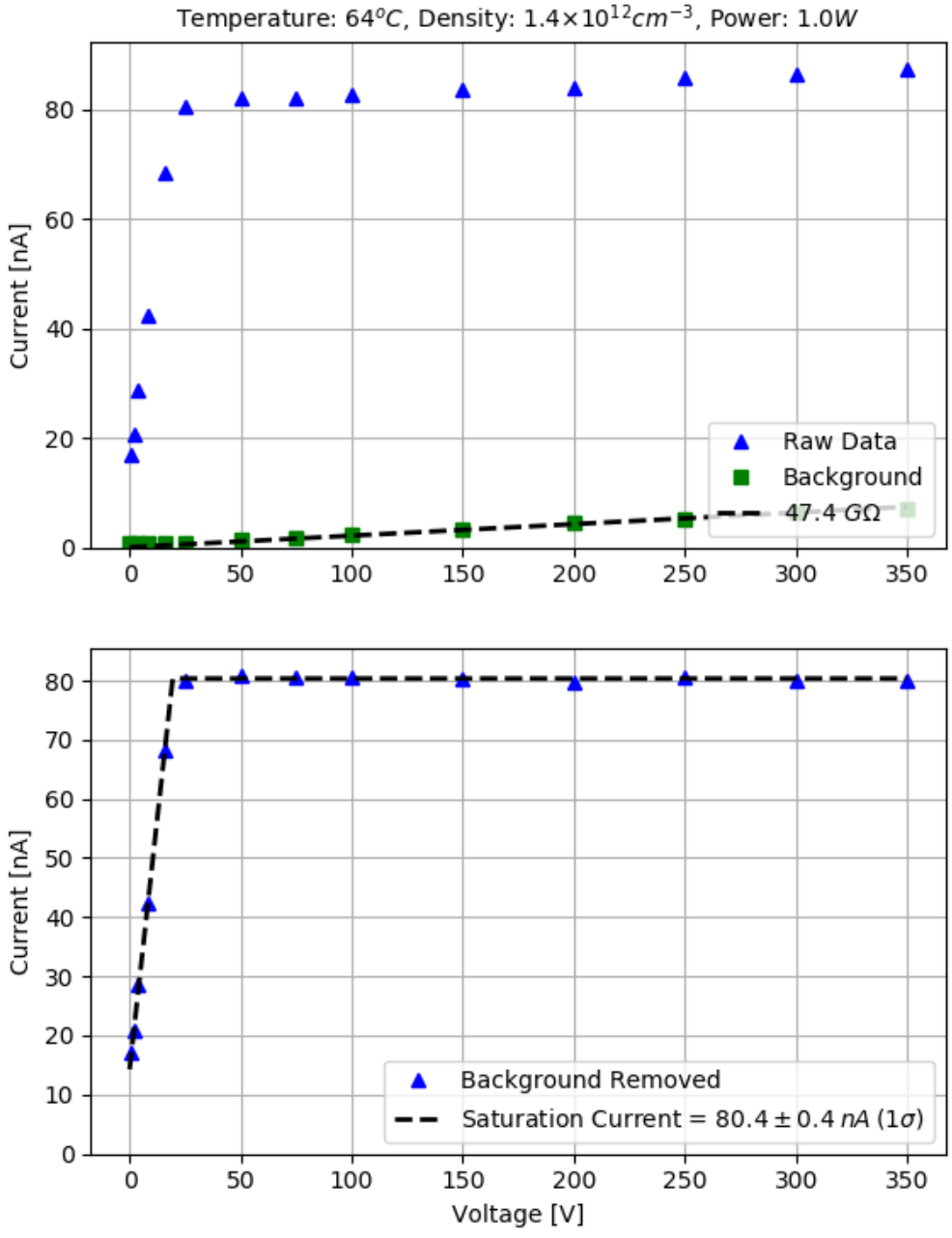

Figure D.28: Electrode measurement B4

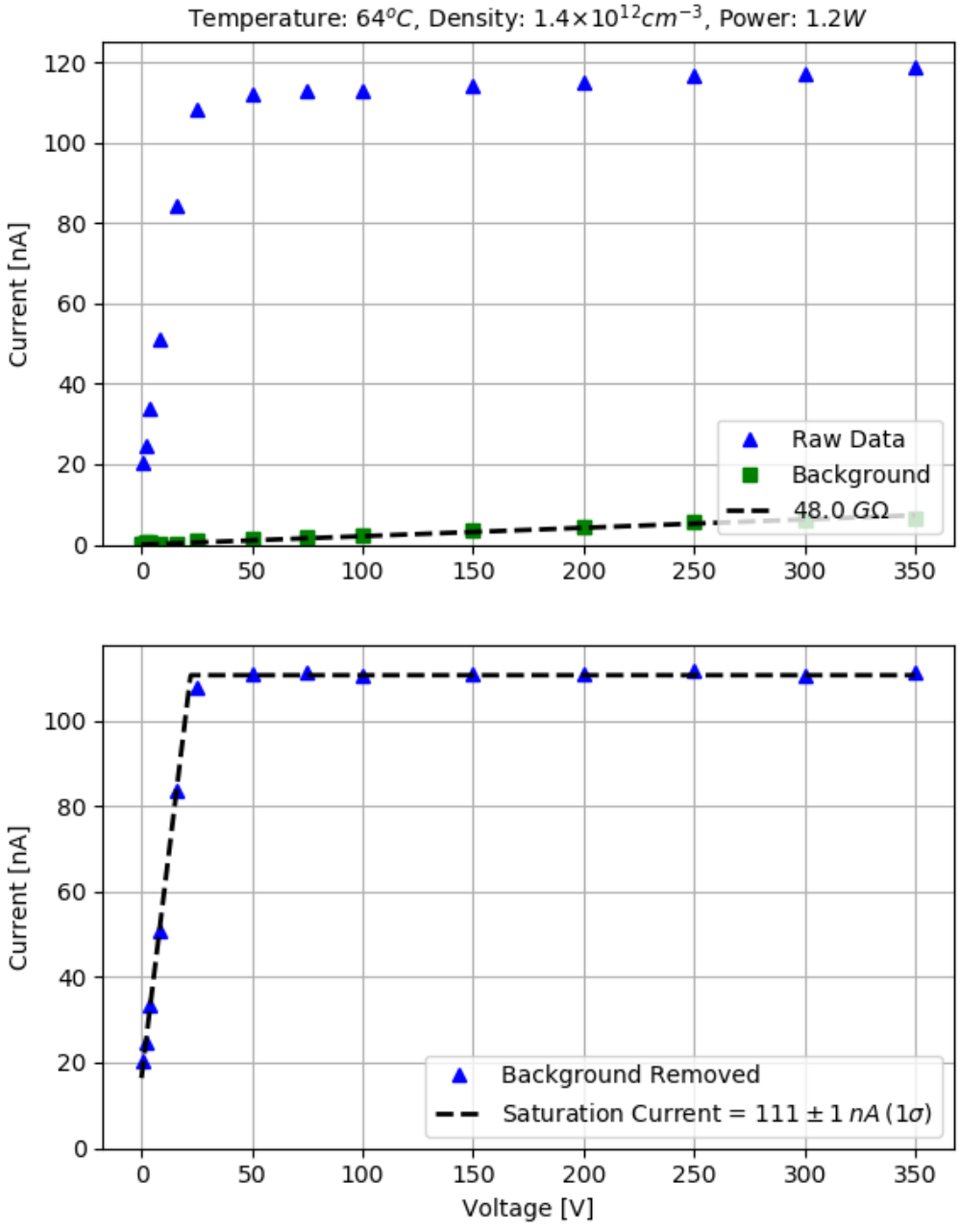

Figure D.29: Electrode measurement B5

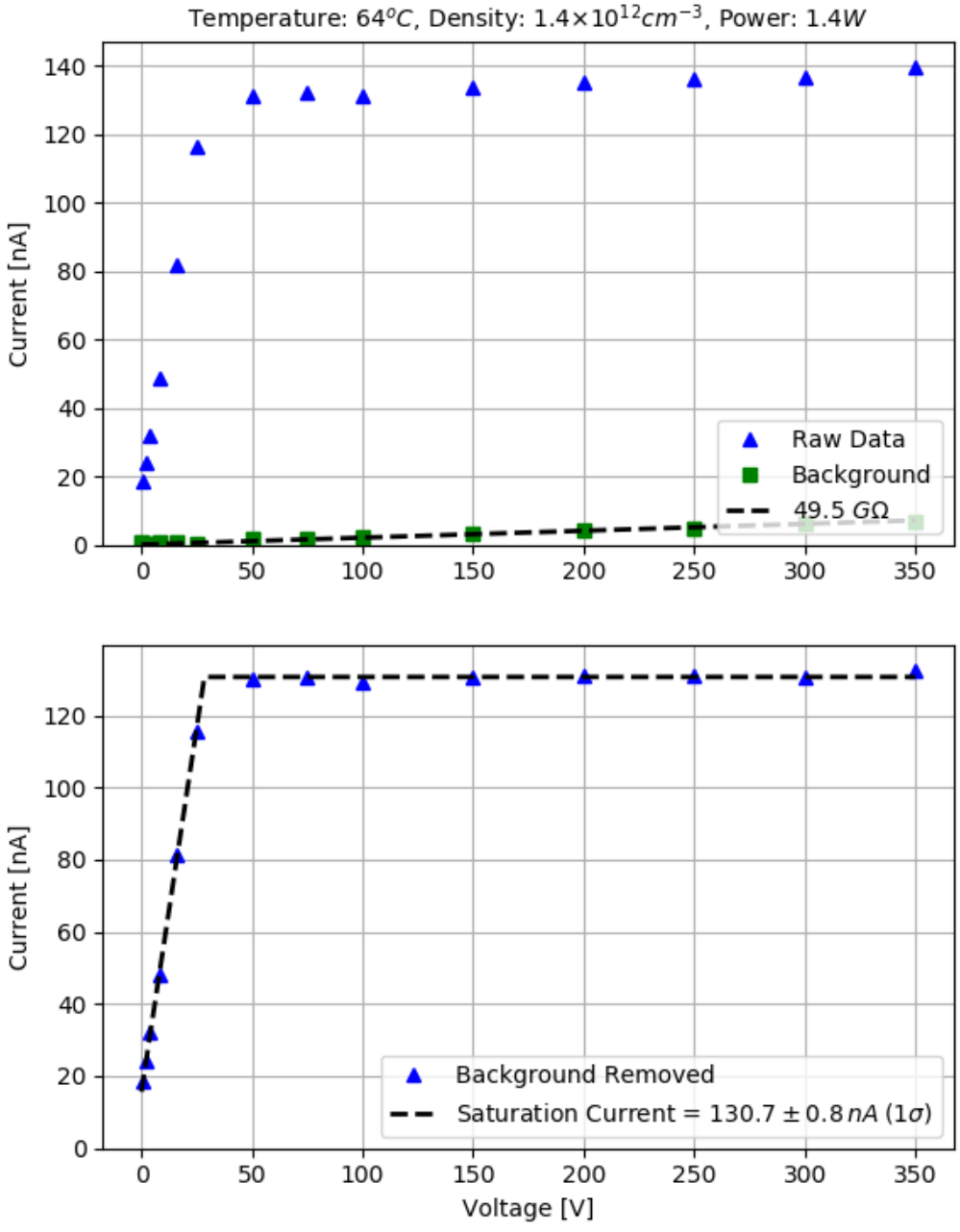

Figure D.30: Electrode measurement B6

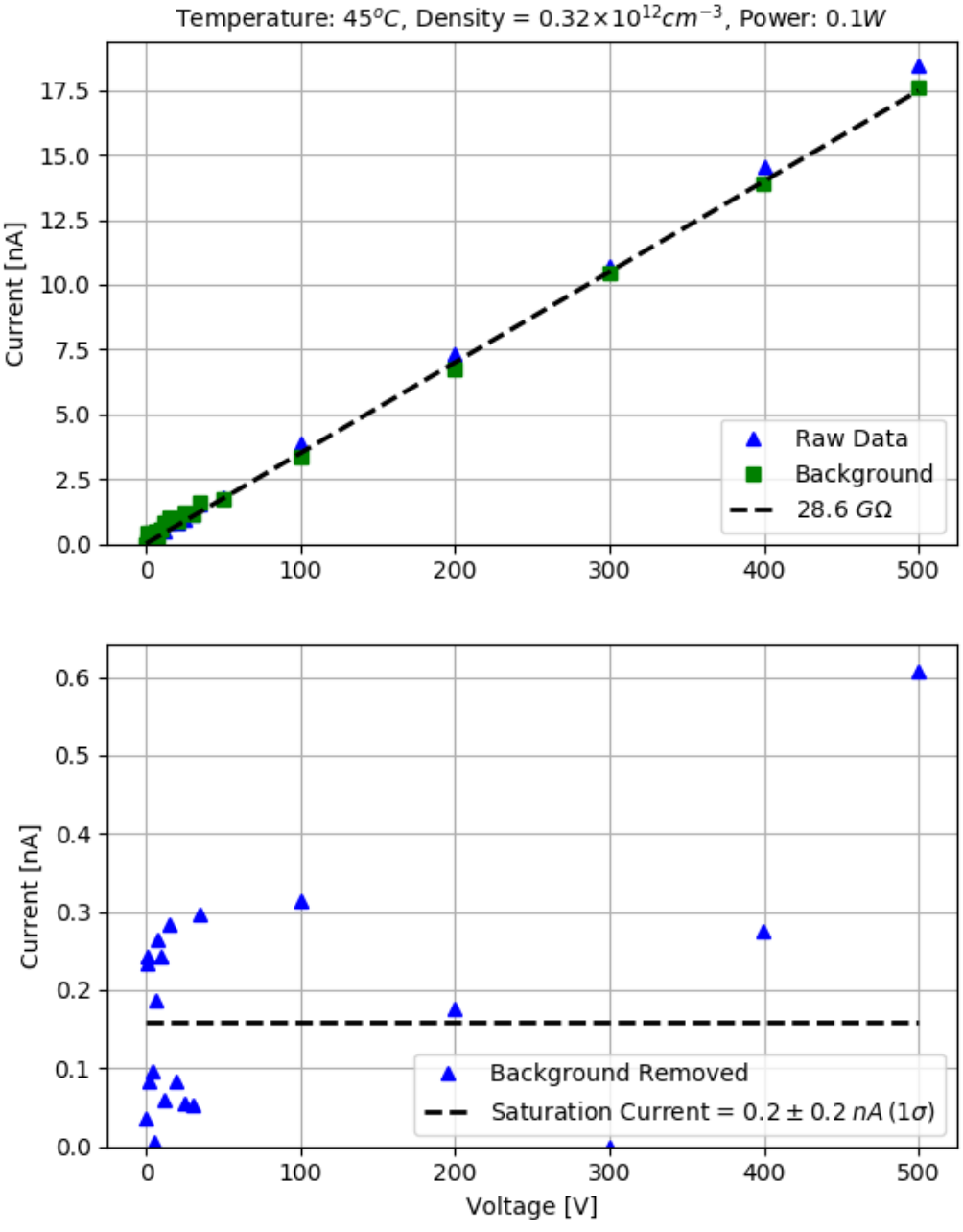

Figure D.31: Electrode measurement C1

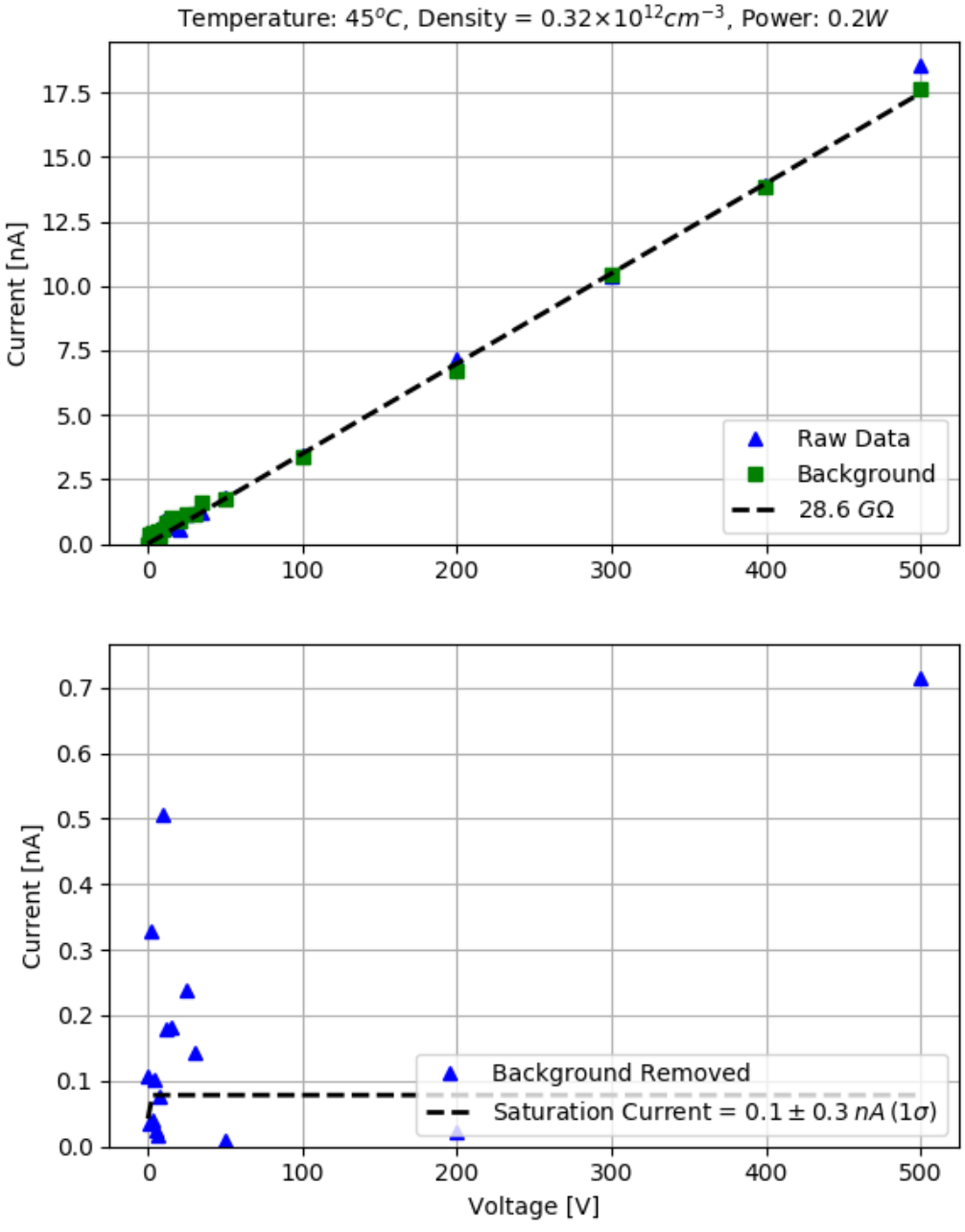

Figure D.32: Electrode measurement C2

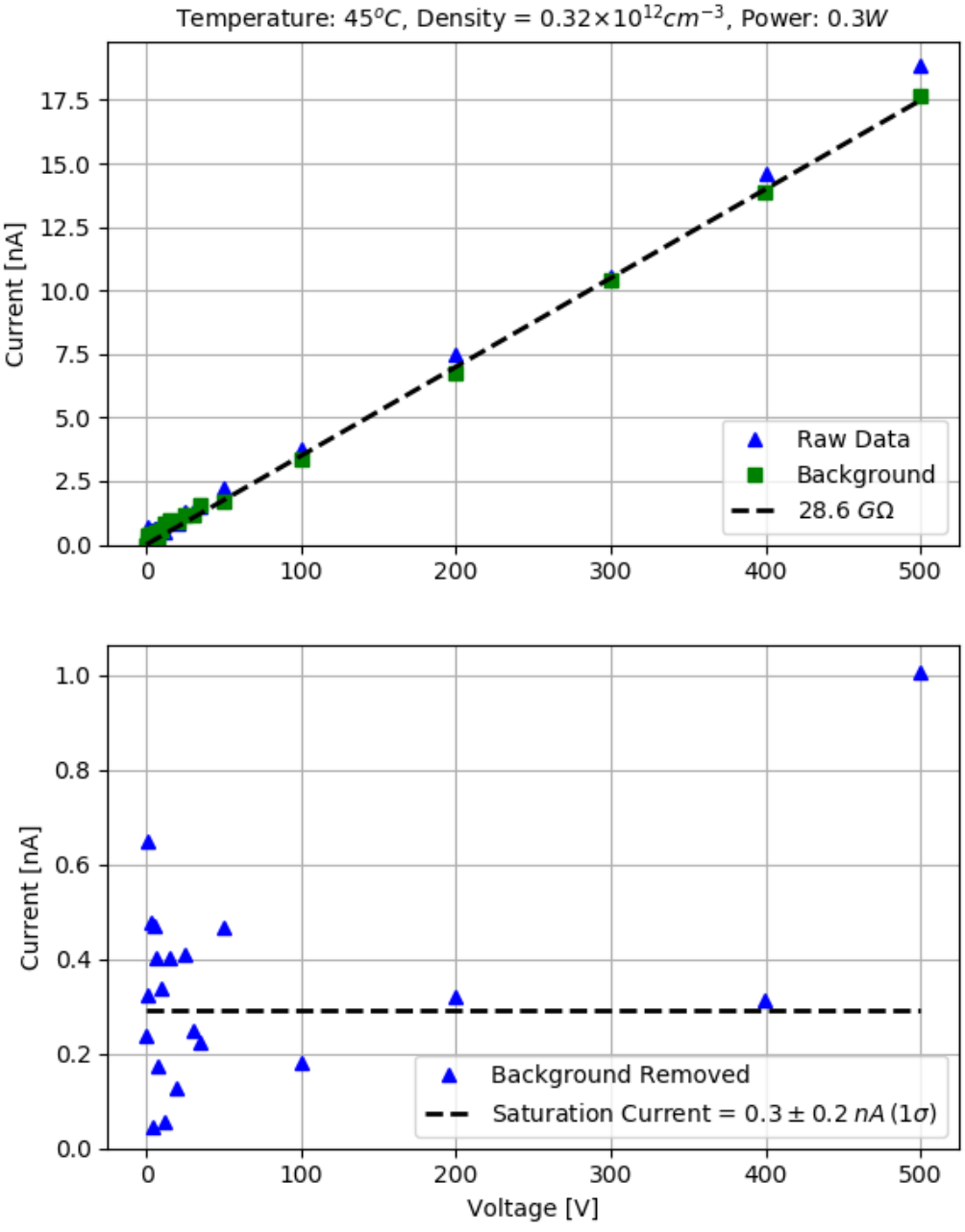

Figure D.33: Electrode measurement C3

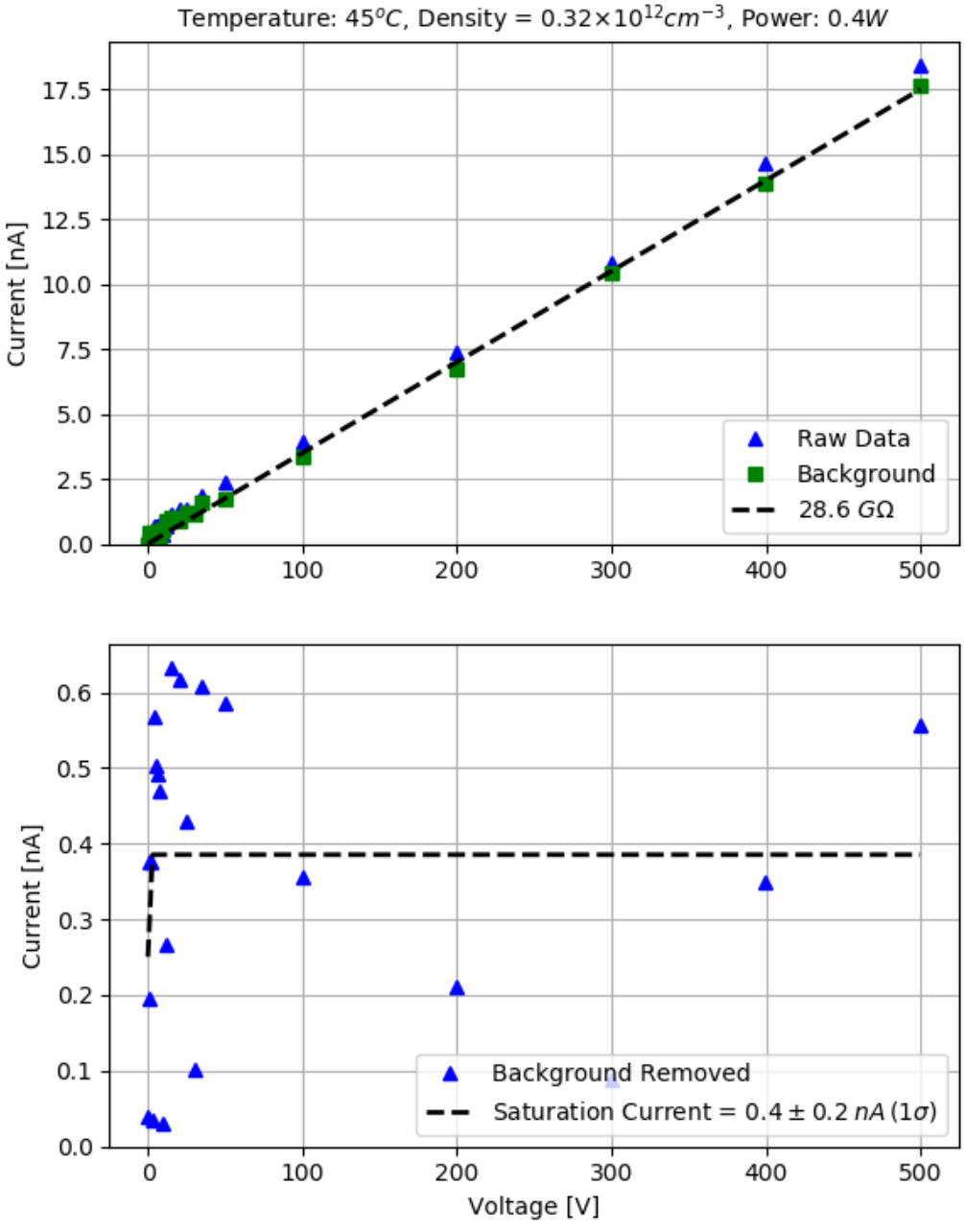

Figure D.34: Electrode measurement C4

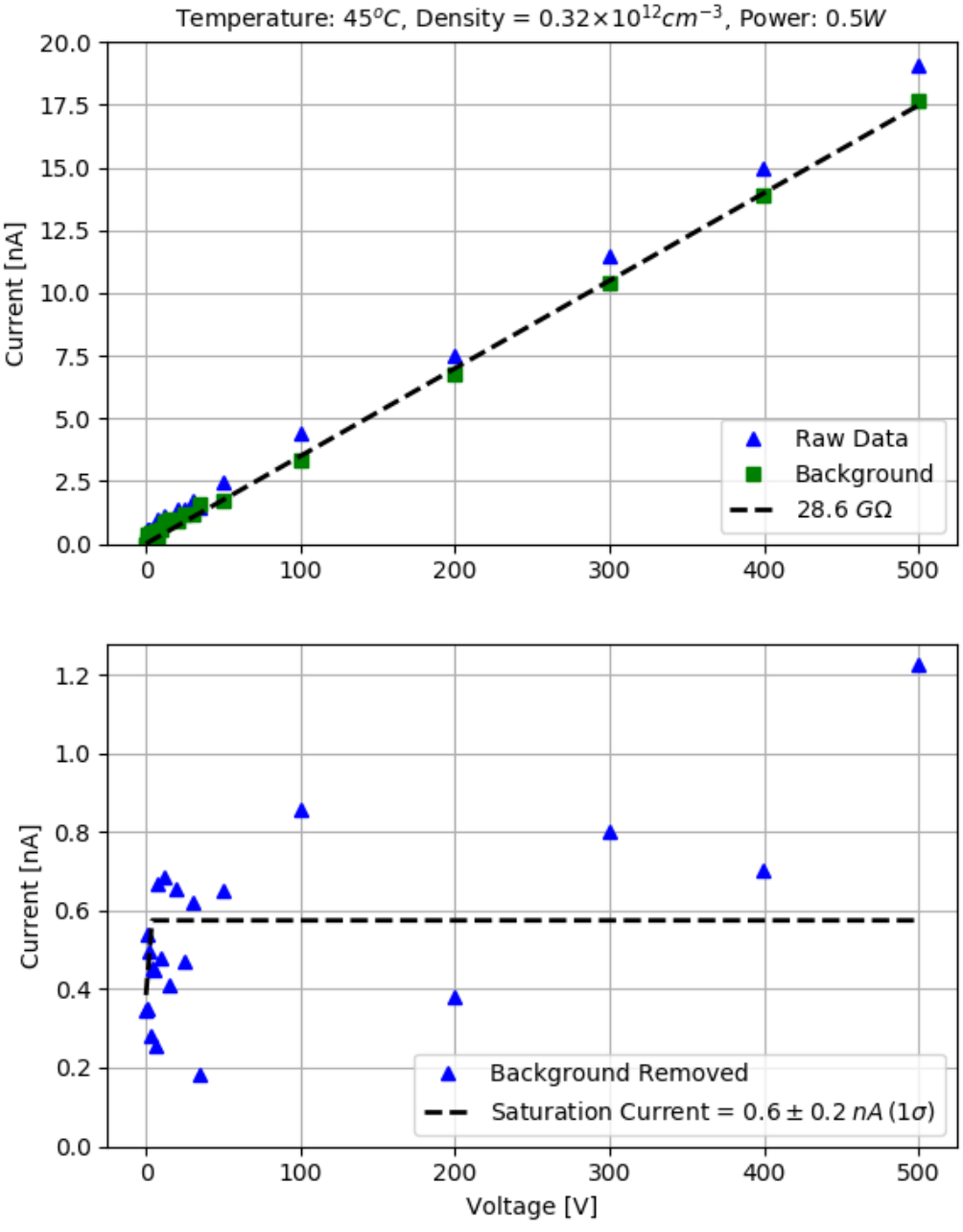

Figure D.35: Electrode measurement C5

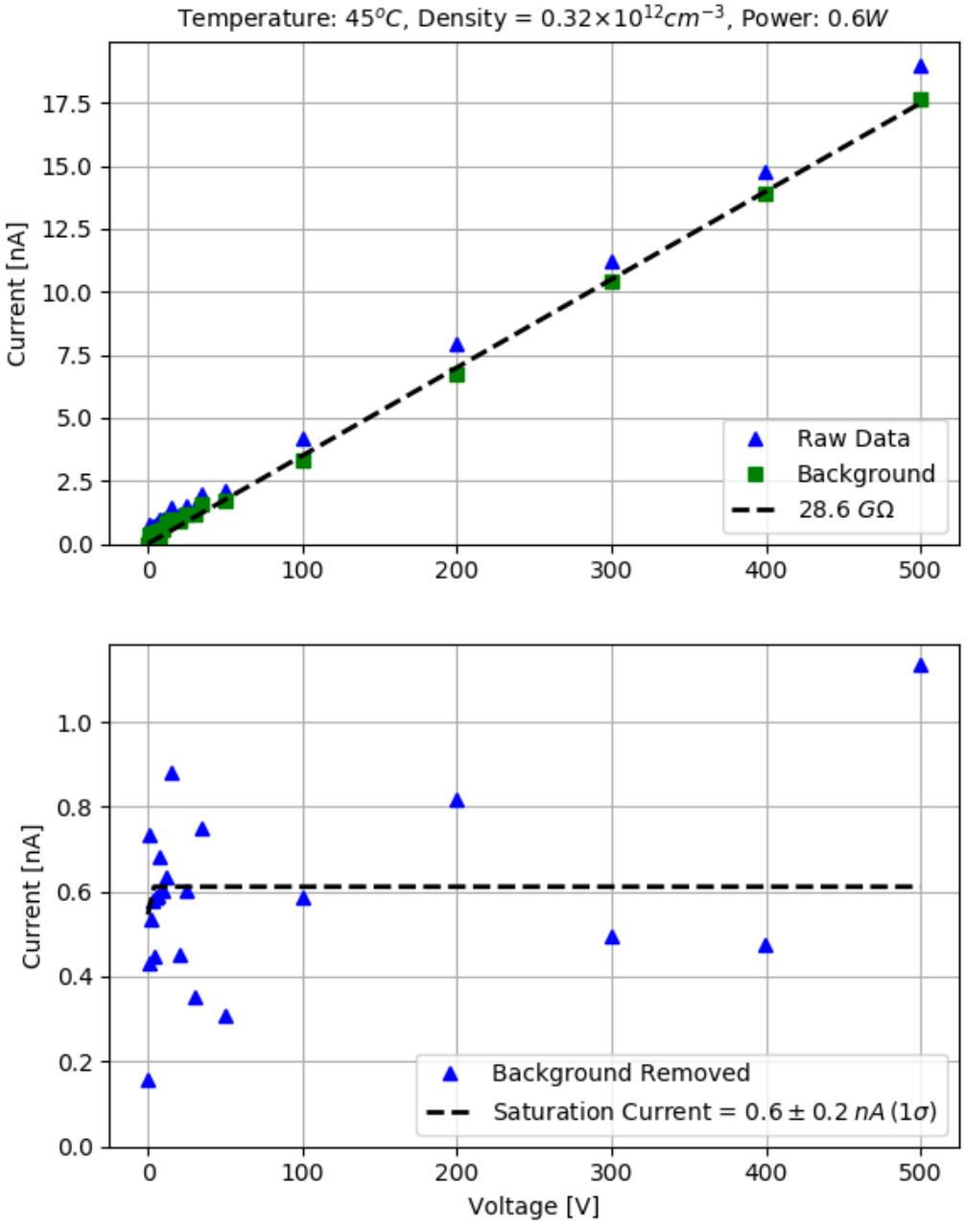

Figure D.36: Electrode measurement C6

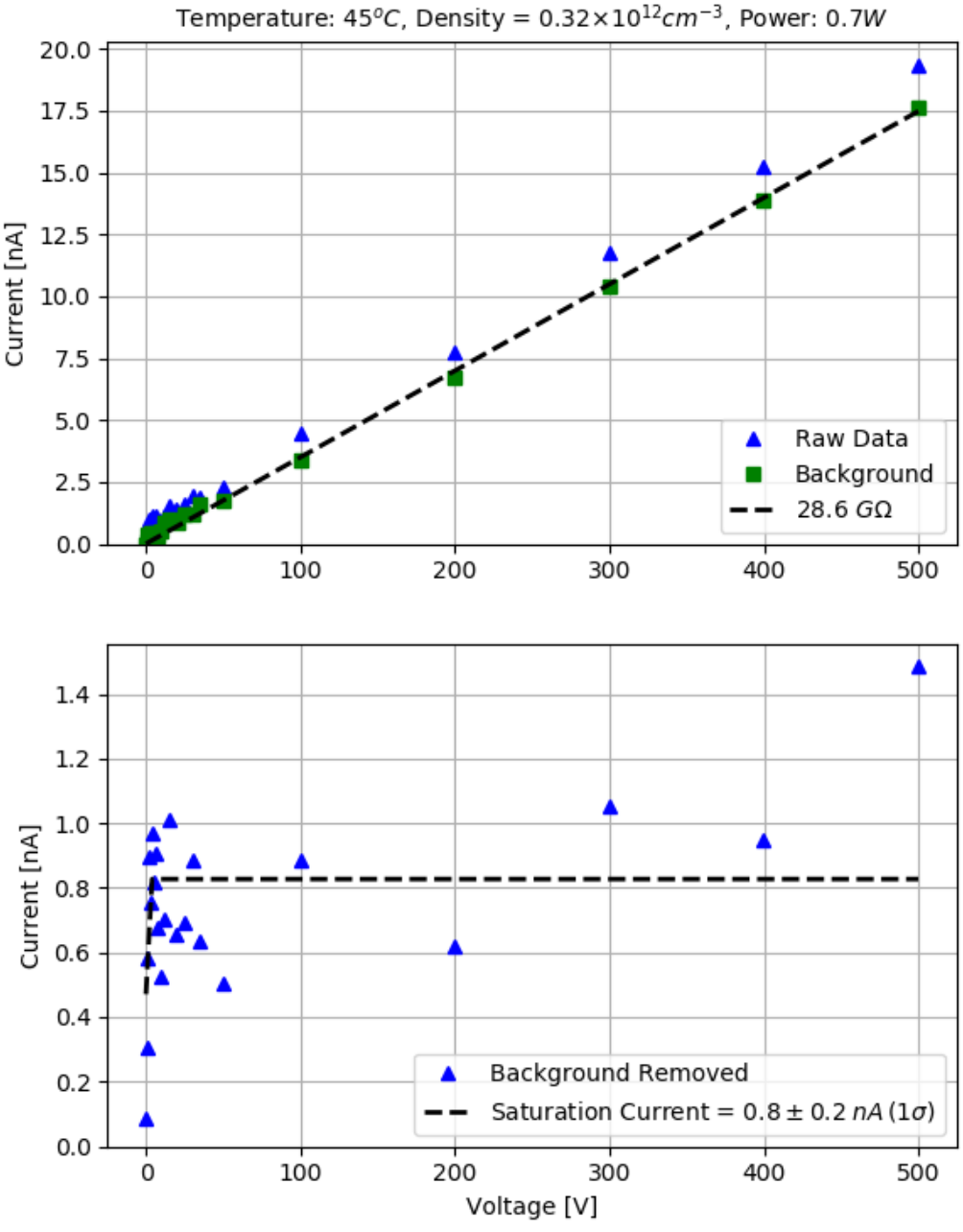

Figure D.37: Electrode measurement C7

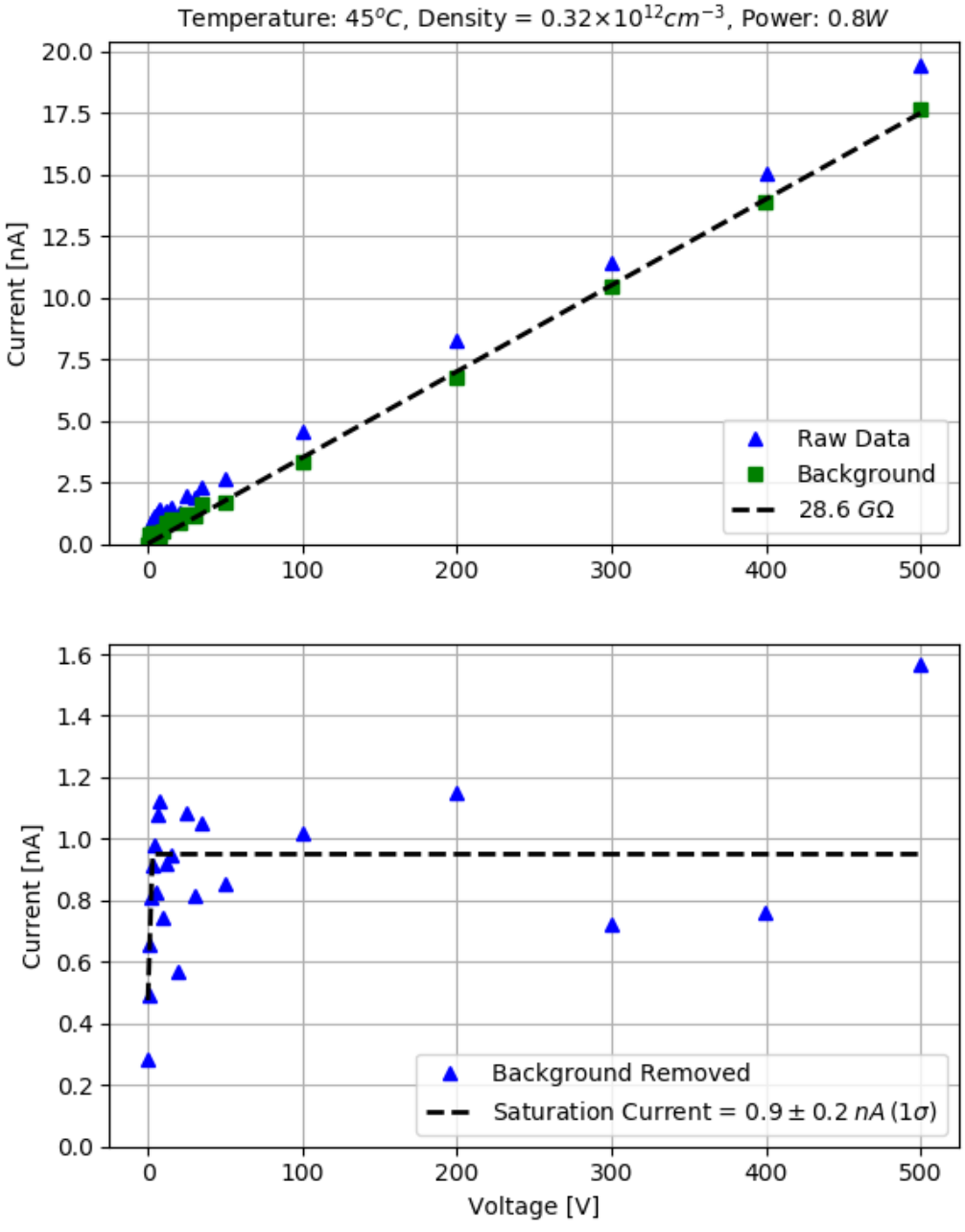

Figure D.38: Electrode measurement C8

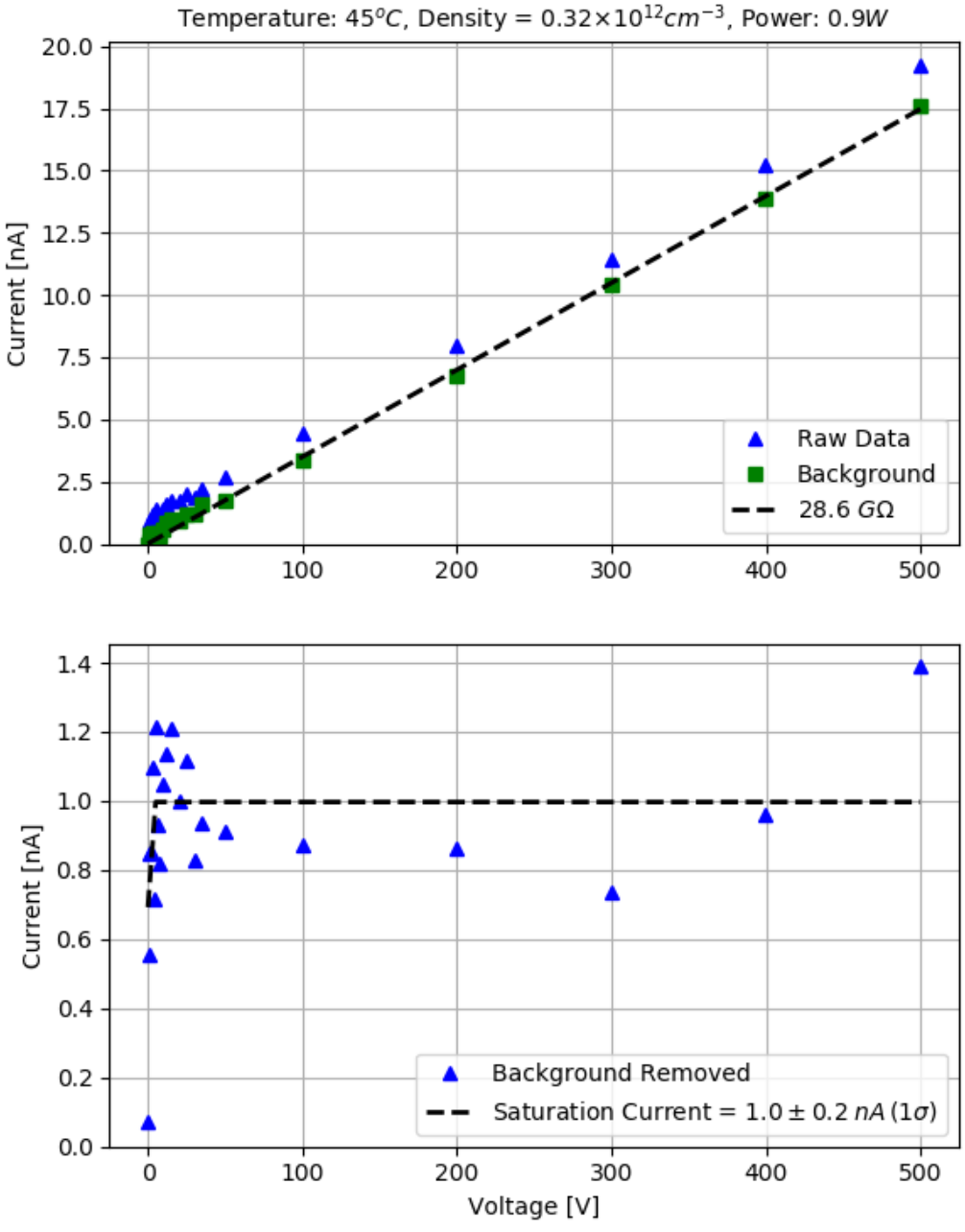

Figure D.39: Electrode measurement C9

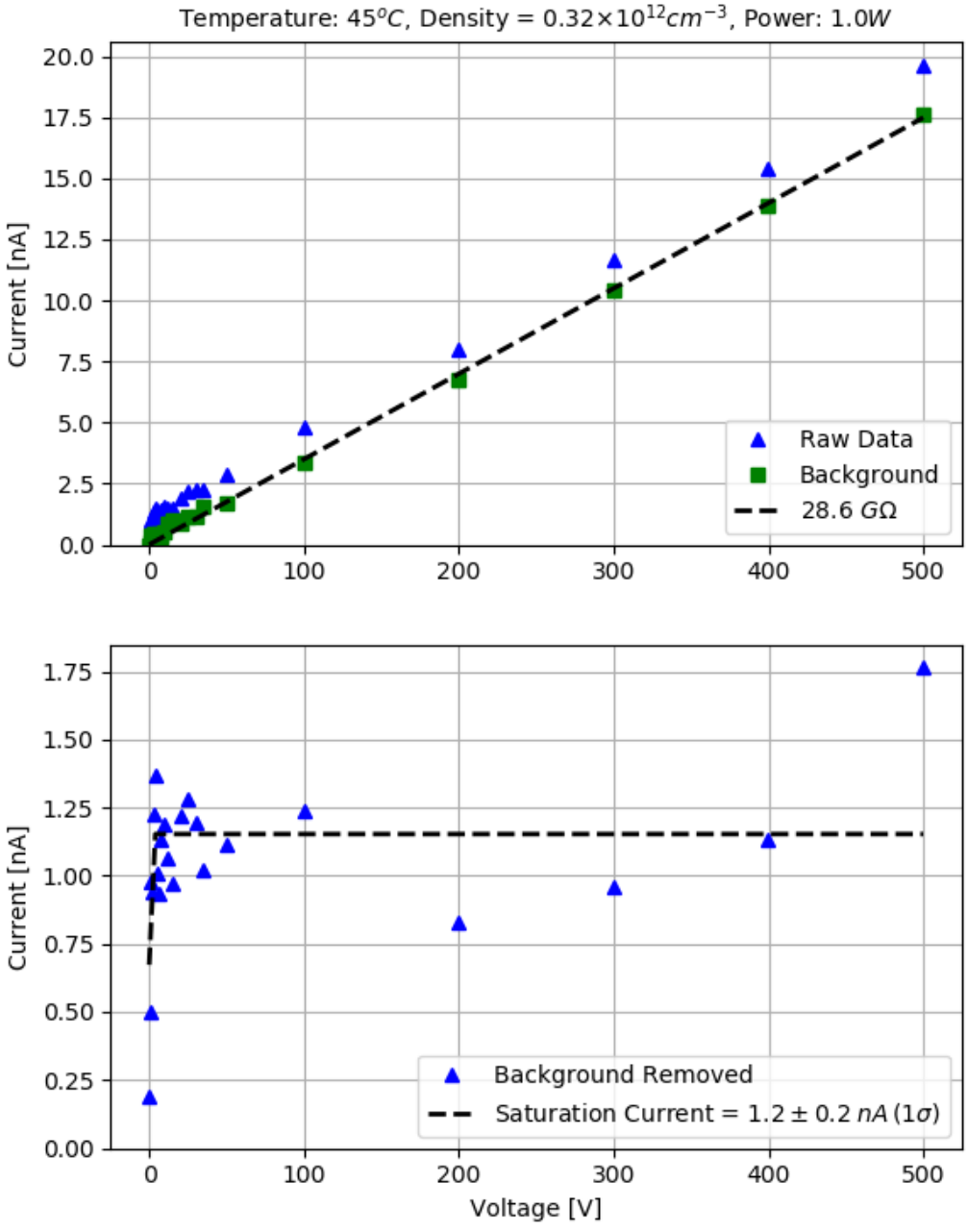

Figure D.40: Electrode measurement C10

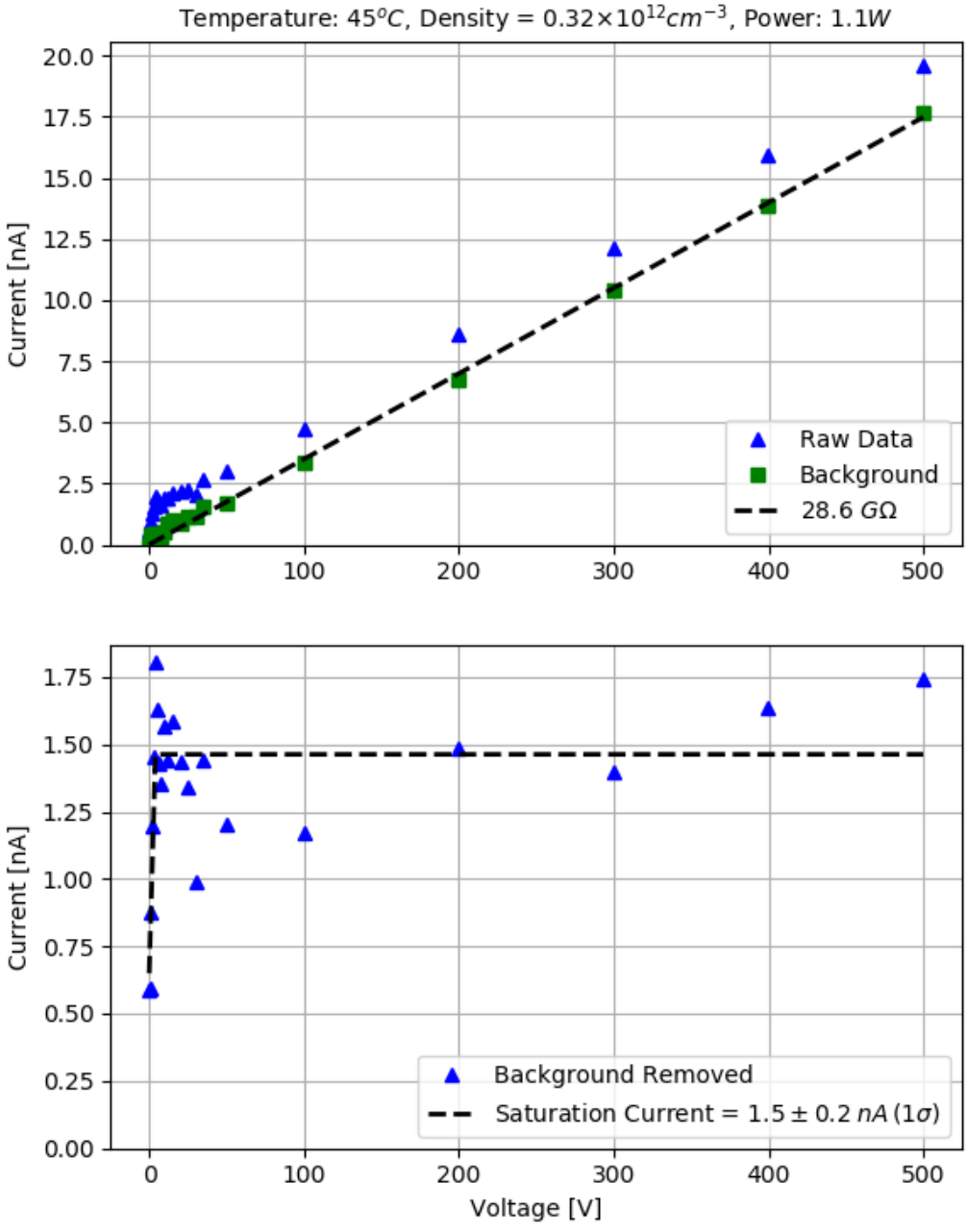

Figure D.41: Electrode measurement C11

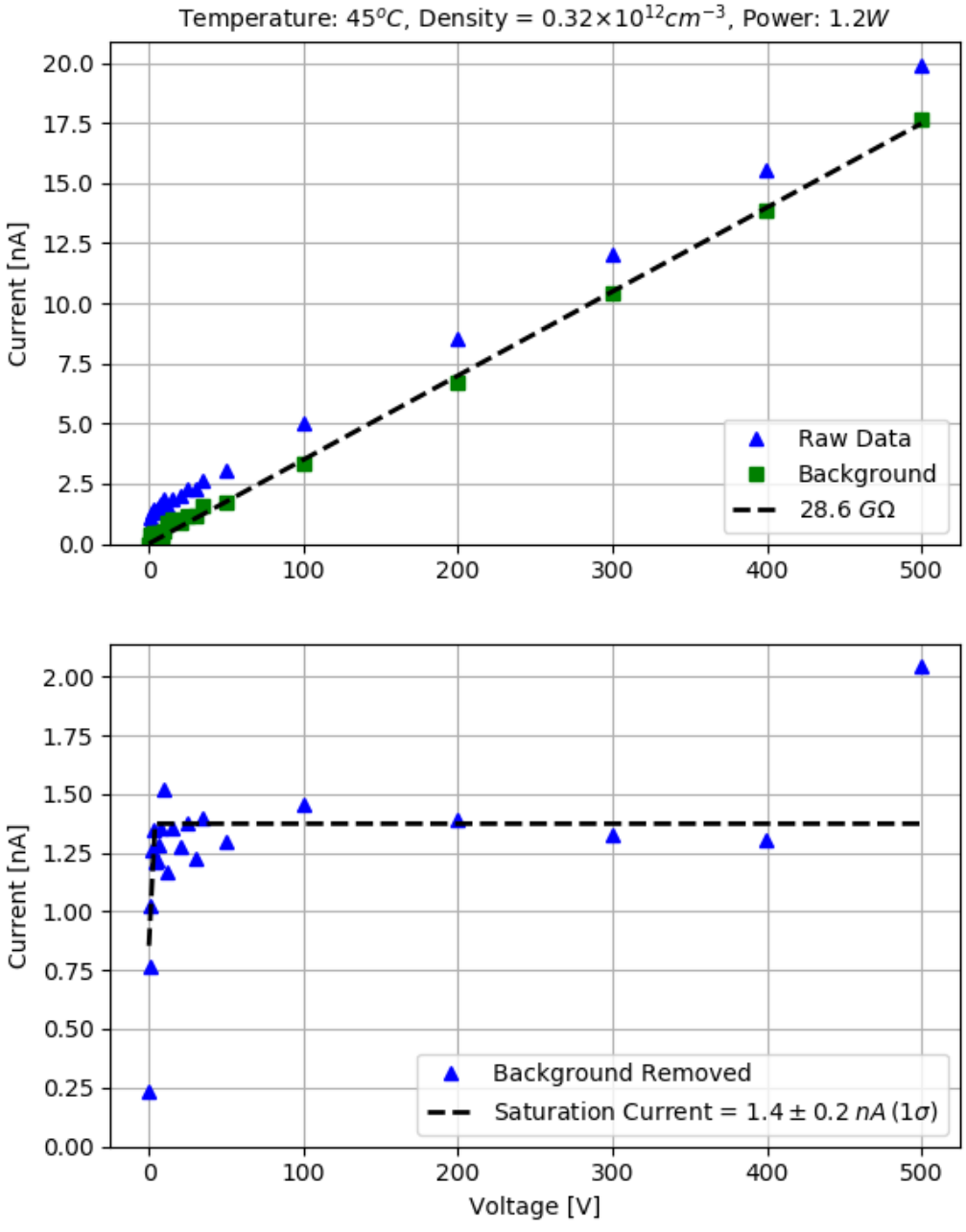

Figure D.42: Electrode measurement C12

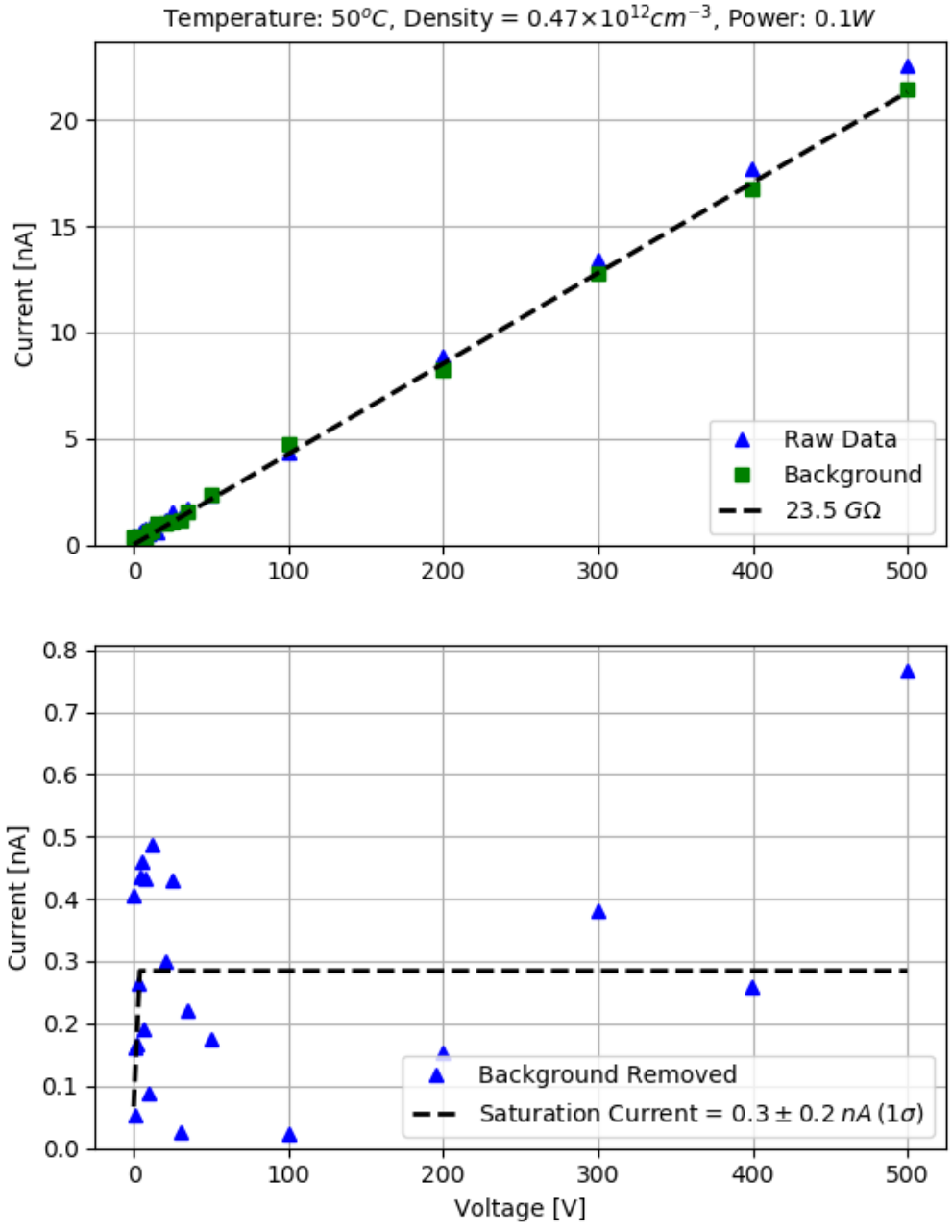

Figure D.43: Electrode measurement D1

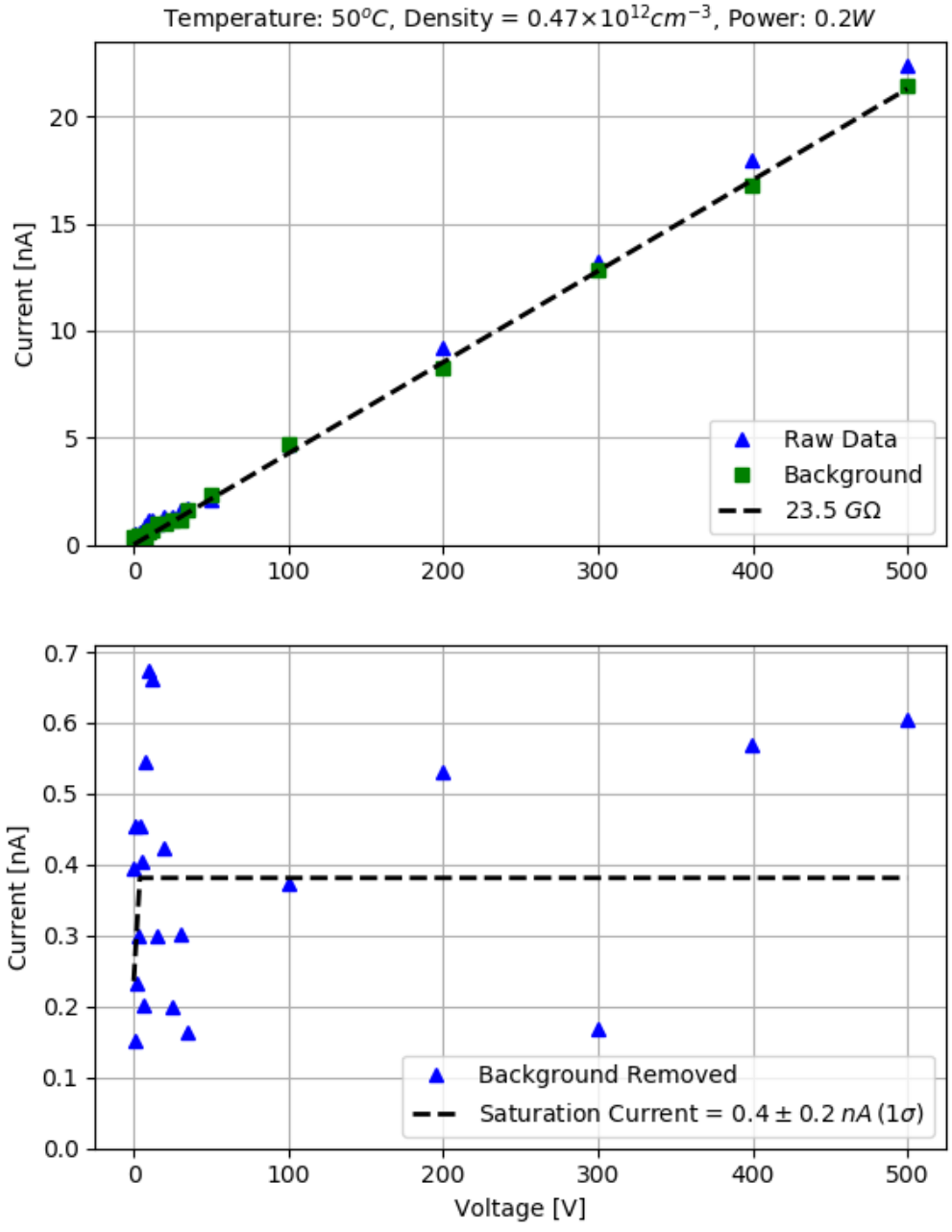

Figure D.44: Electrode measurement D2

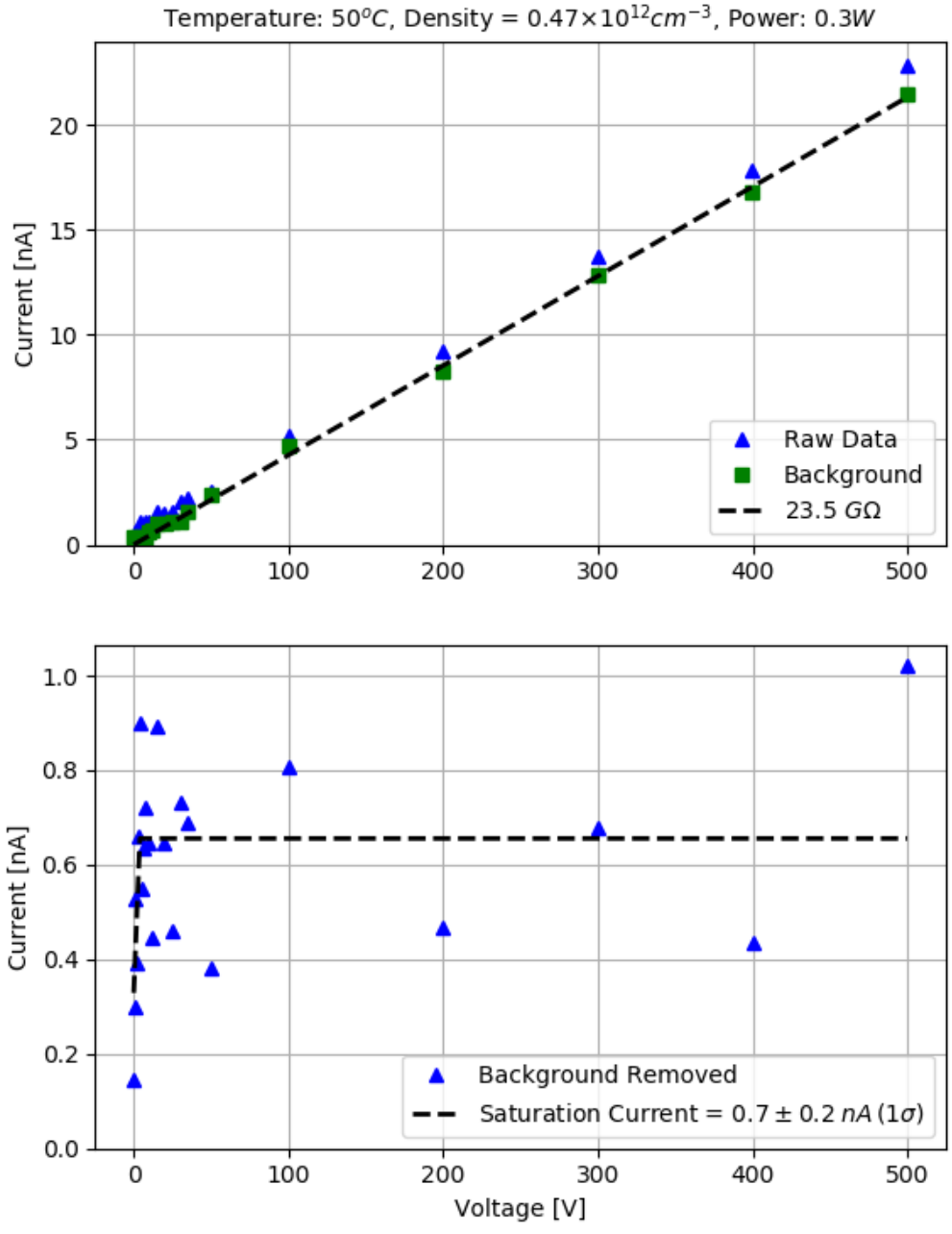

Figure D.45: Electrode measurement D3

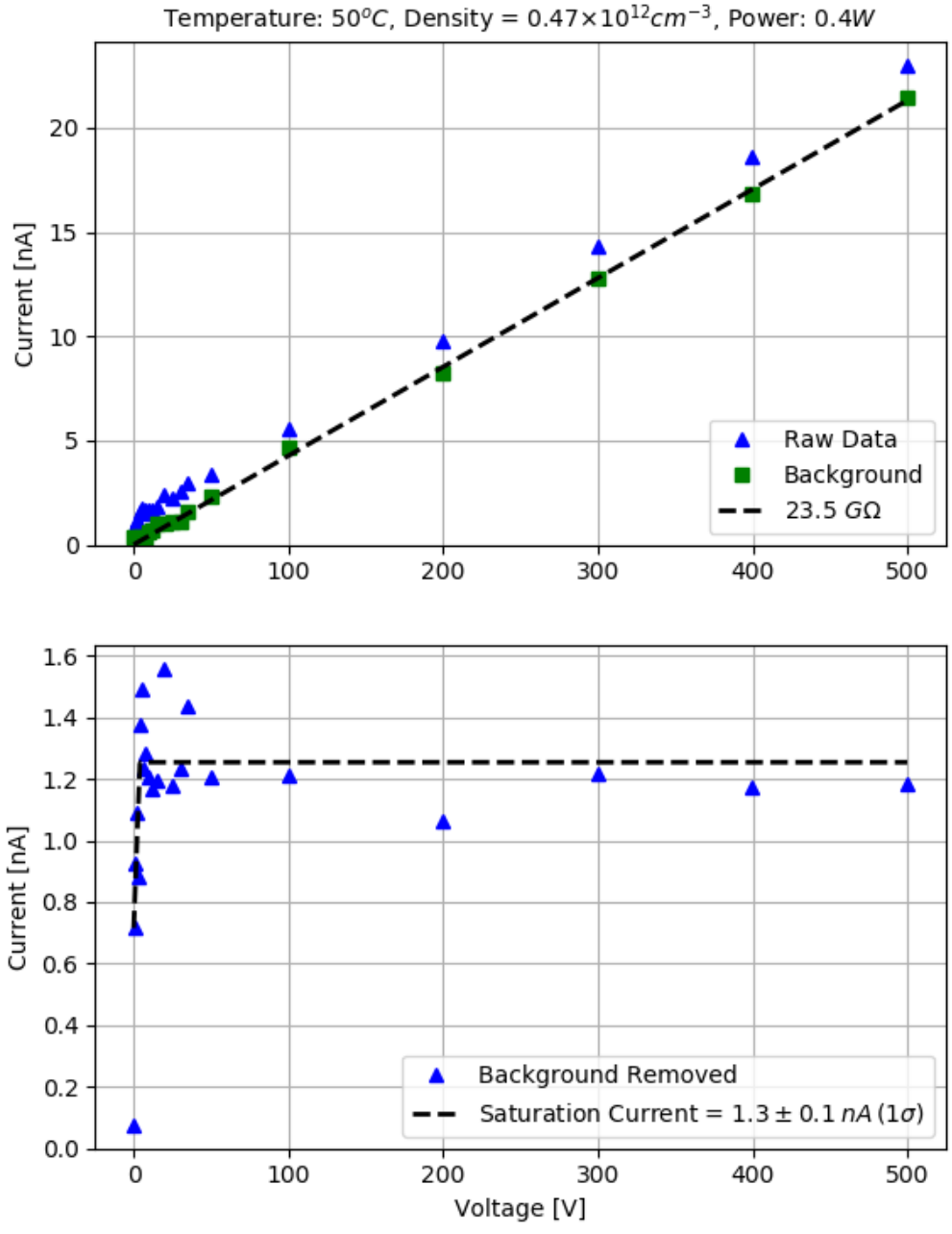

Figure D.46: Electrode measurement D4

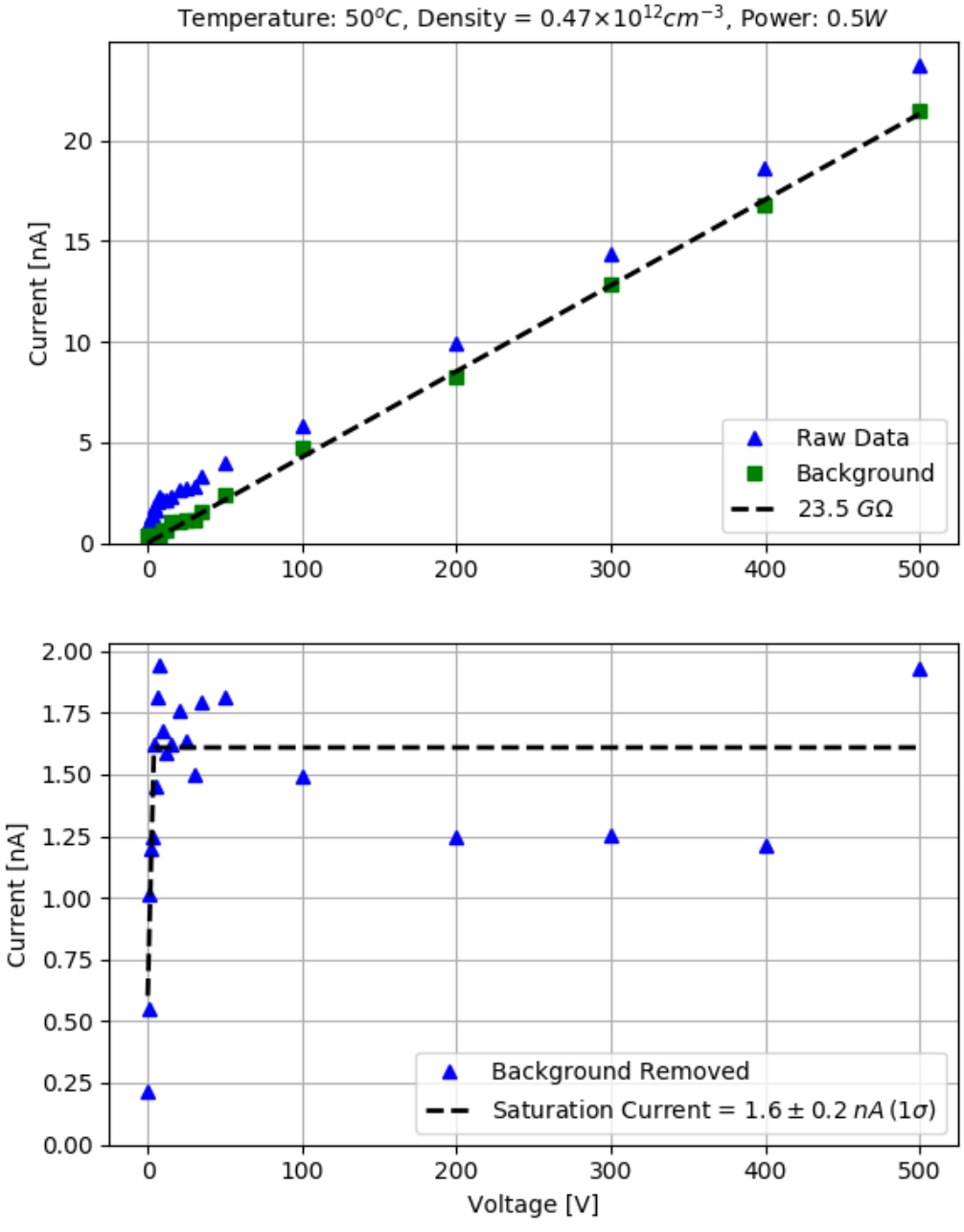

Figure D.47: Electrode measurement D5

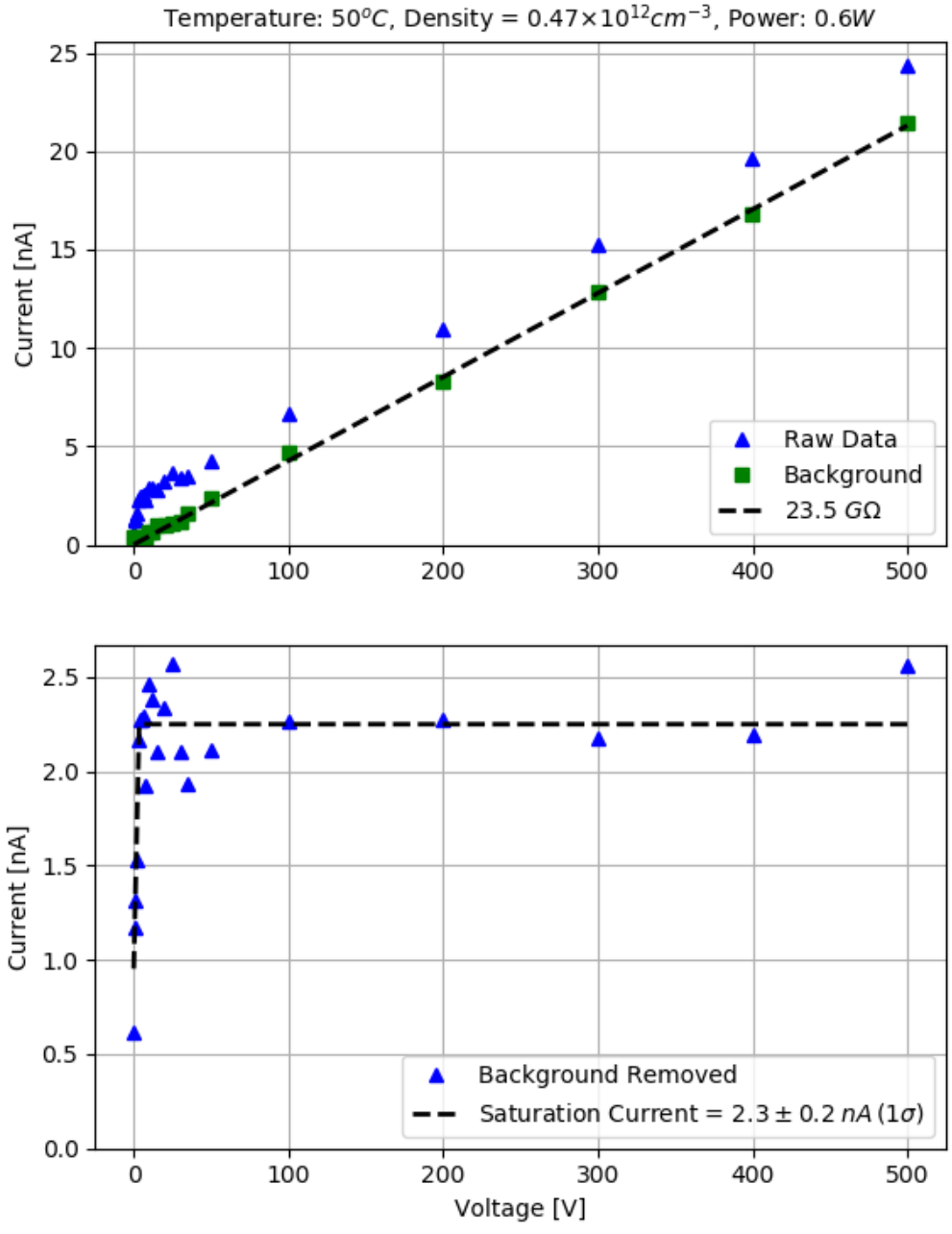

Figure D.48: Electrode measurement D6

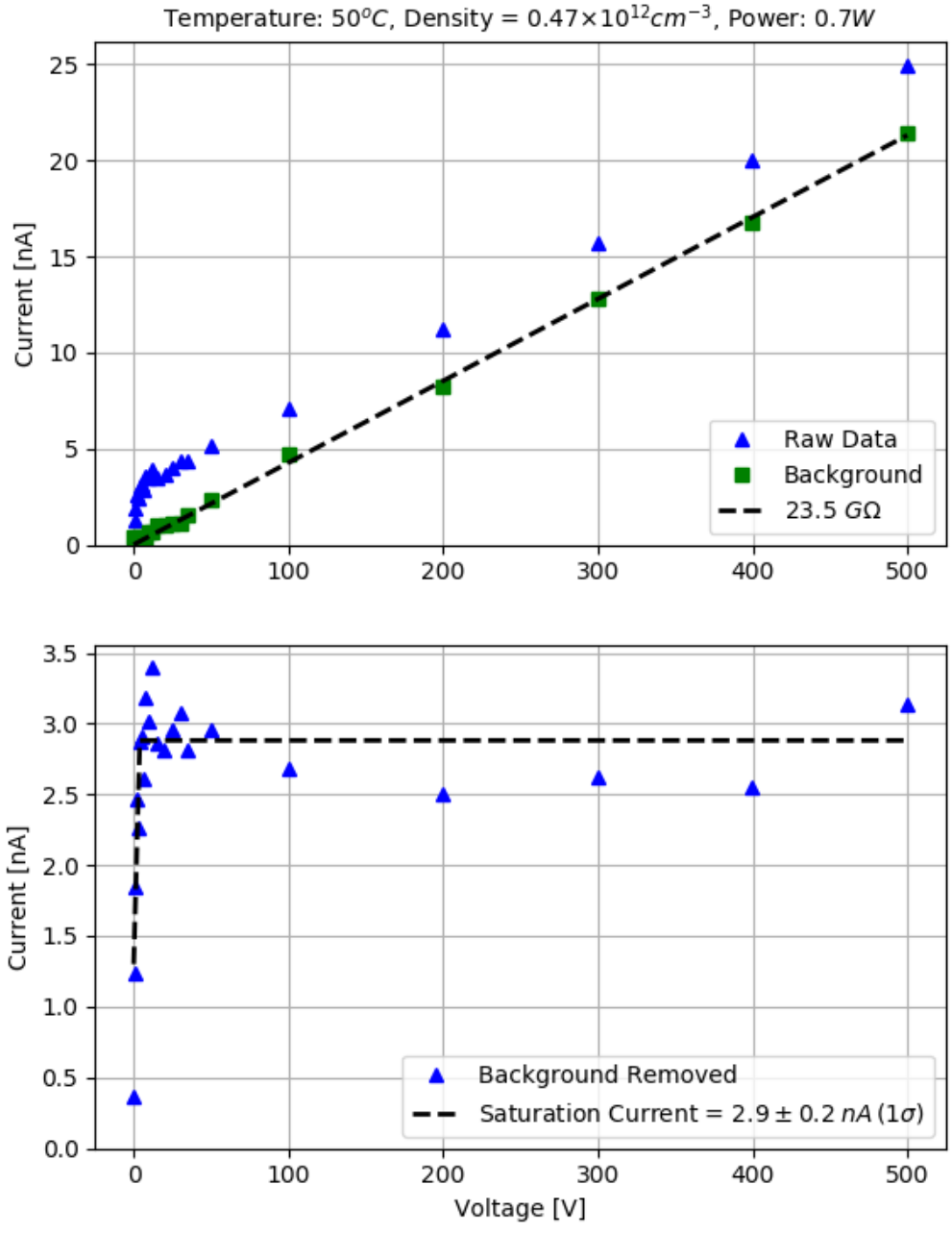

Figure D.49: Electrode measurement D7

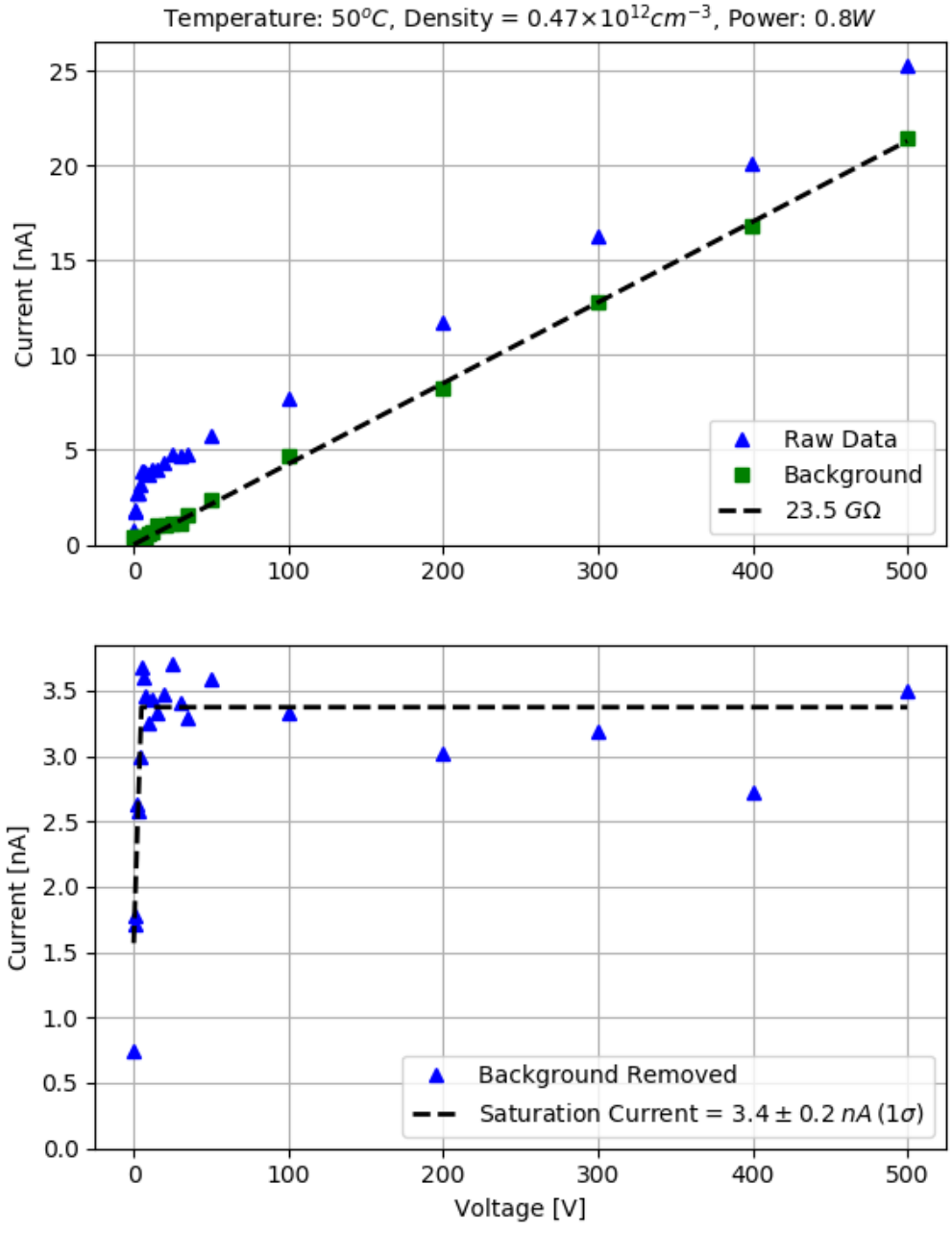

Figure D.50: Electrode measurement D8

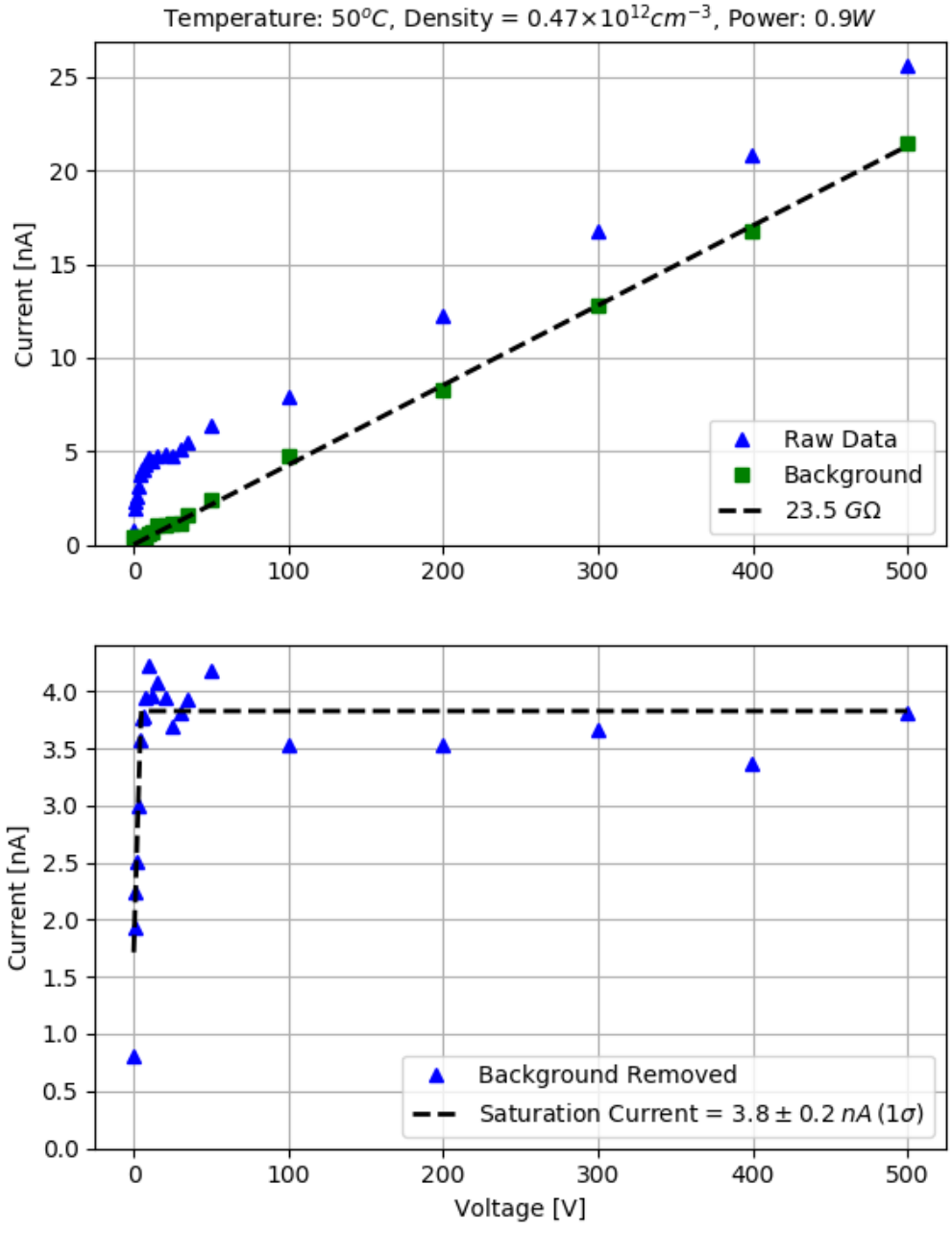

Figure D.51: Electrode measurement D9

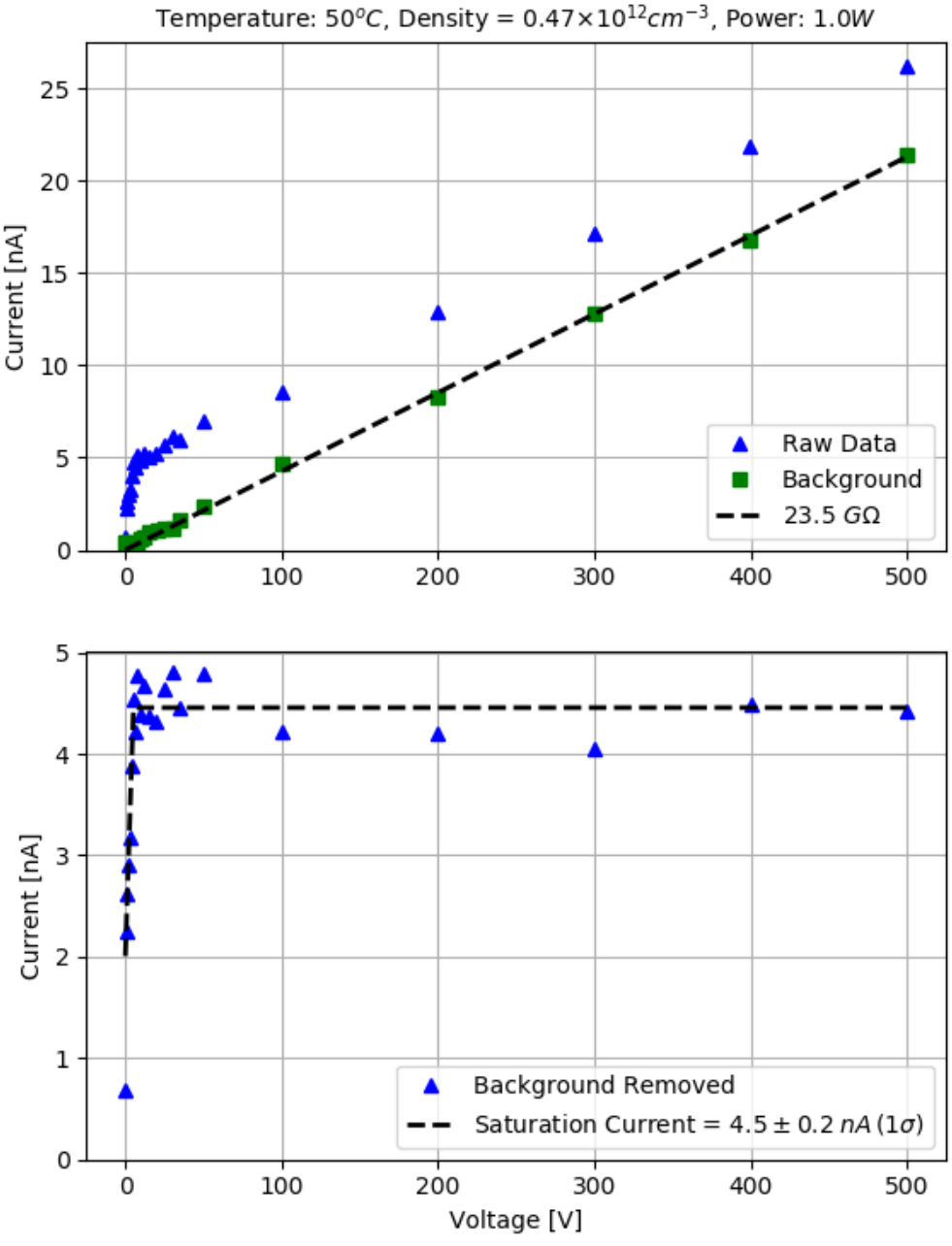

Figure D.52: Electrode measurement D10

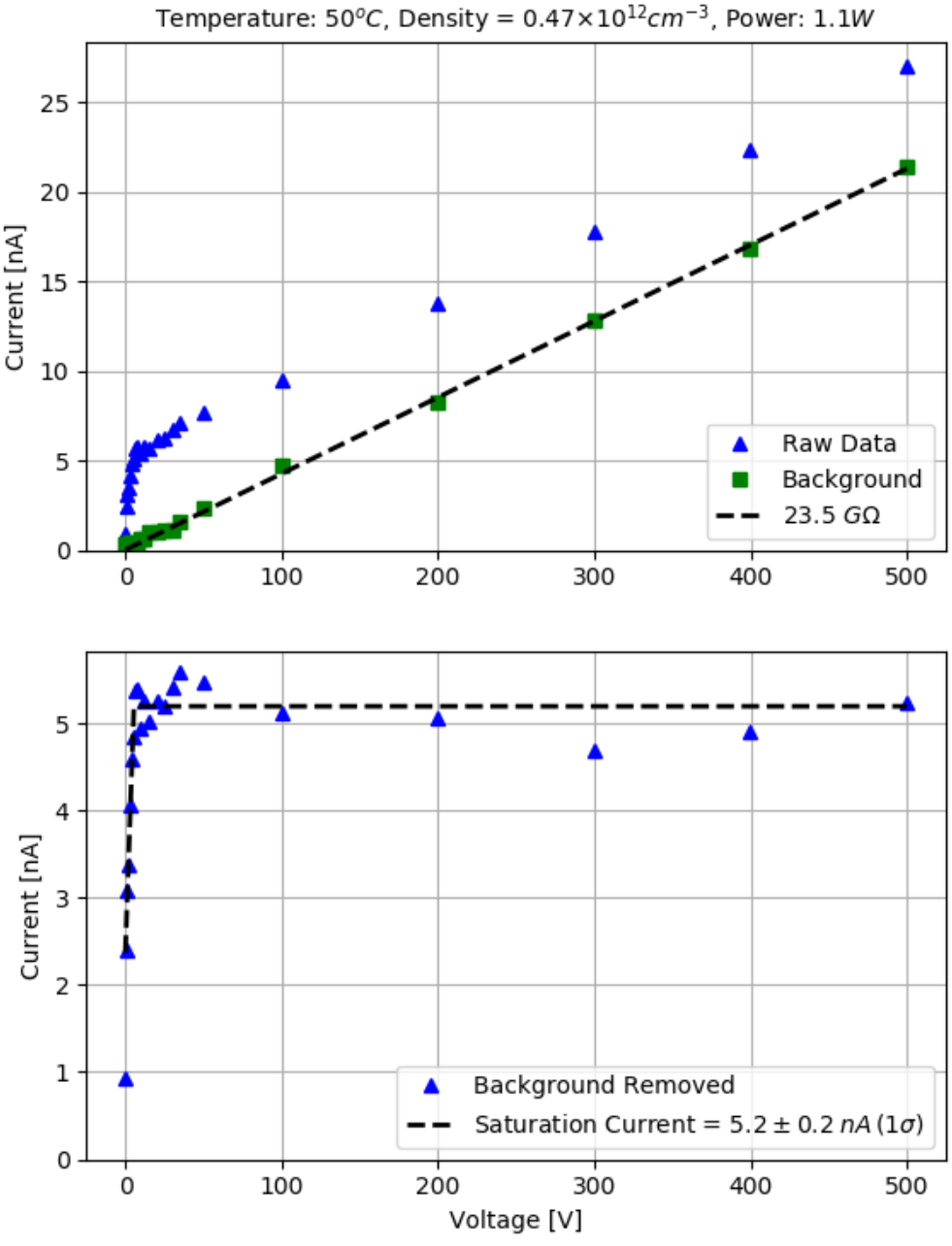

Figure D.53: Electrode measurement D11

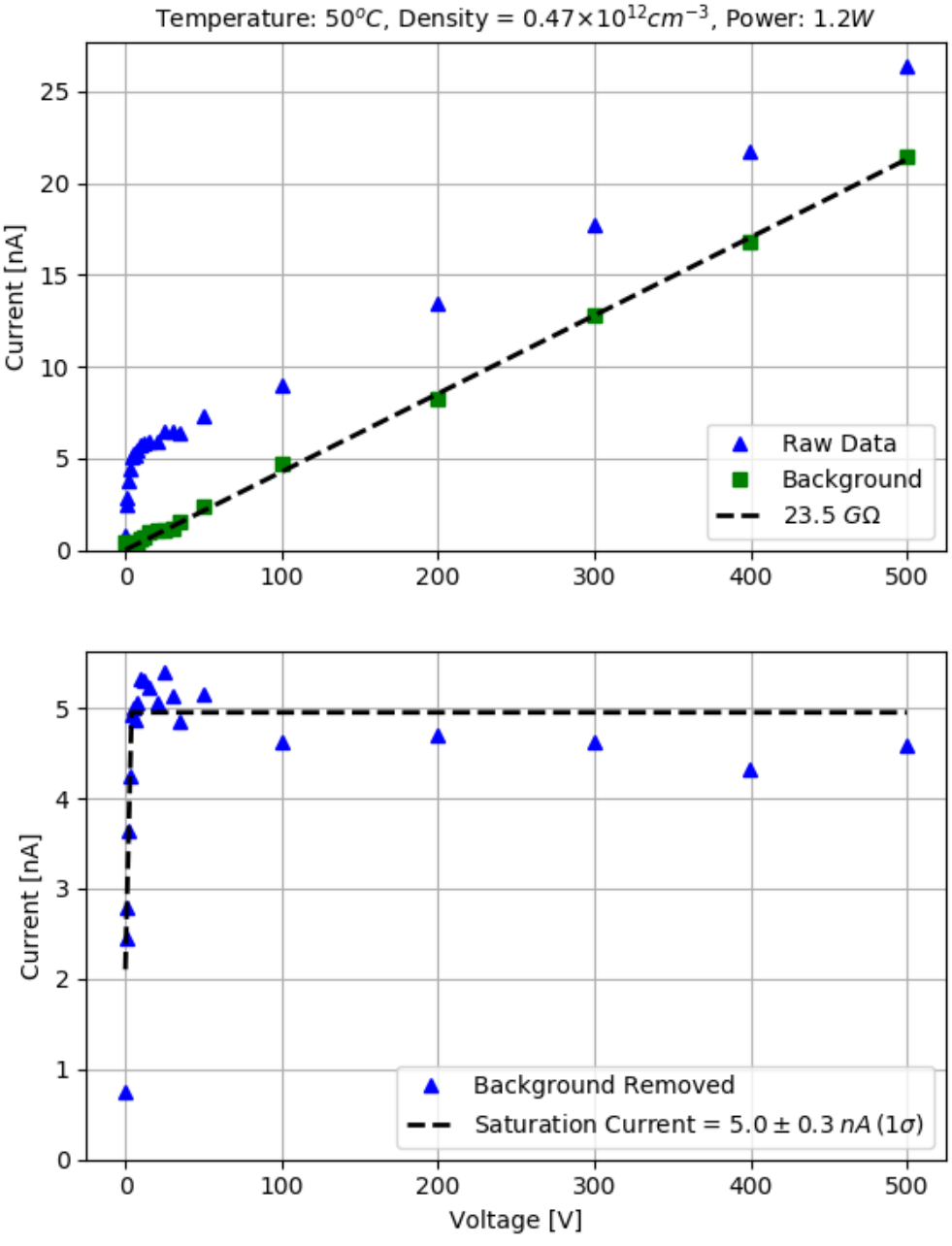

Figure D.54: Electrode measurement D12

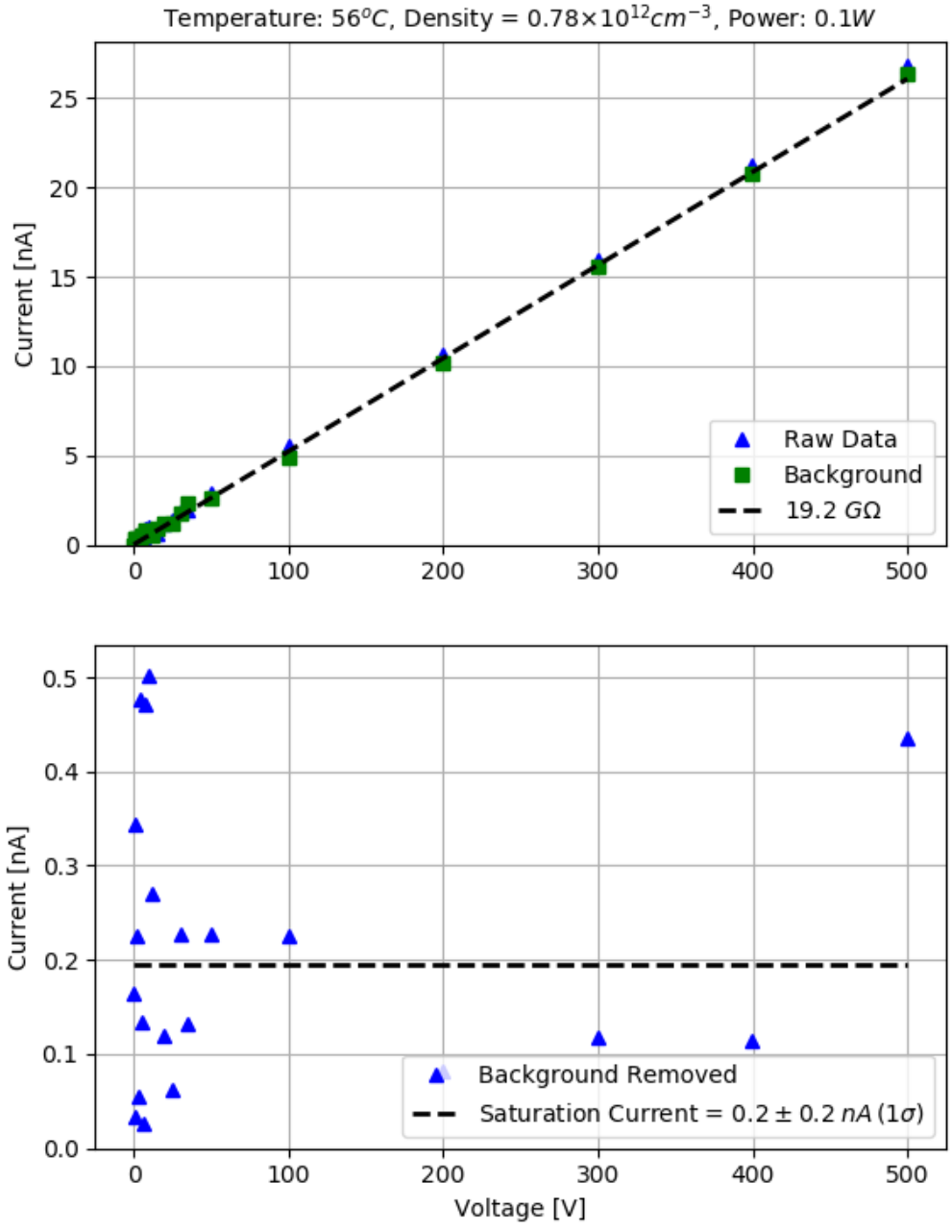

Figure D.55: Electrode measurement E1

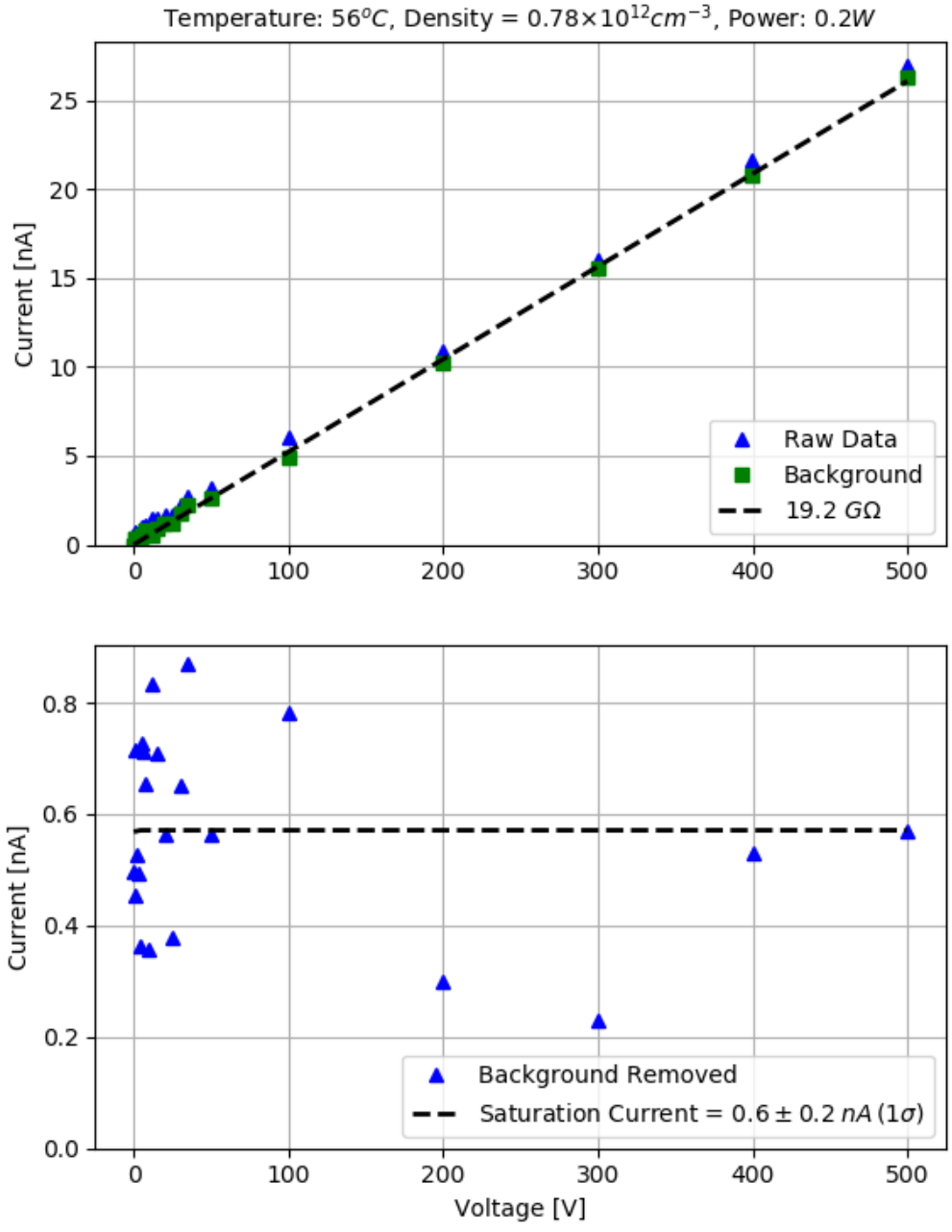

Figure D.56: Electrode measurement E2

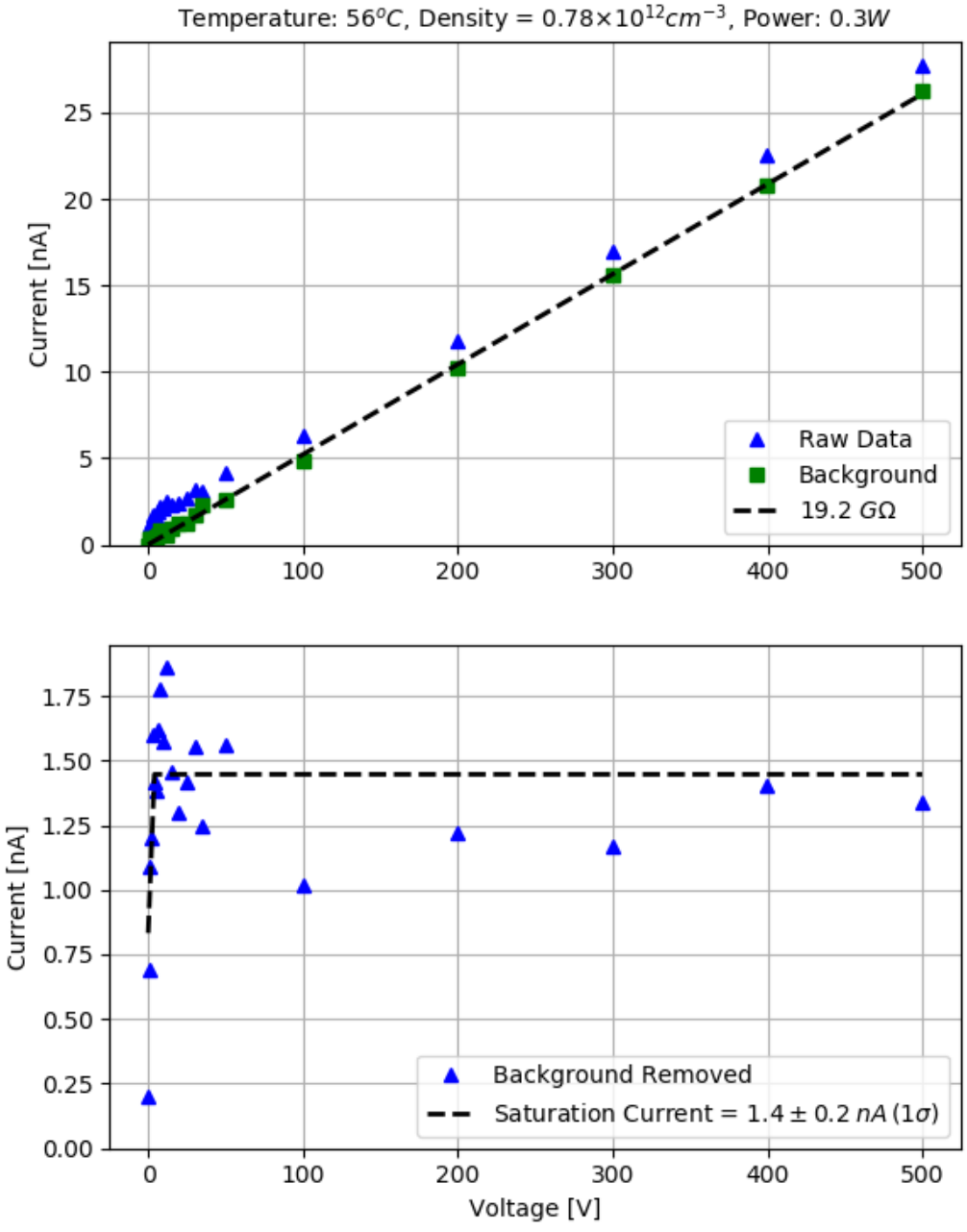

Figure D.57: Electrode measurement E3

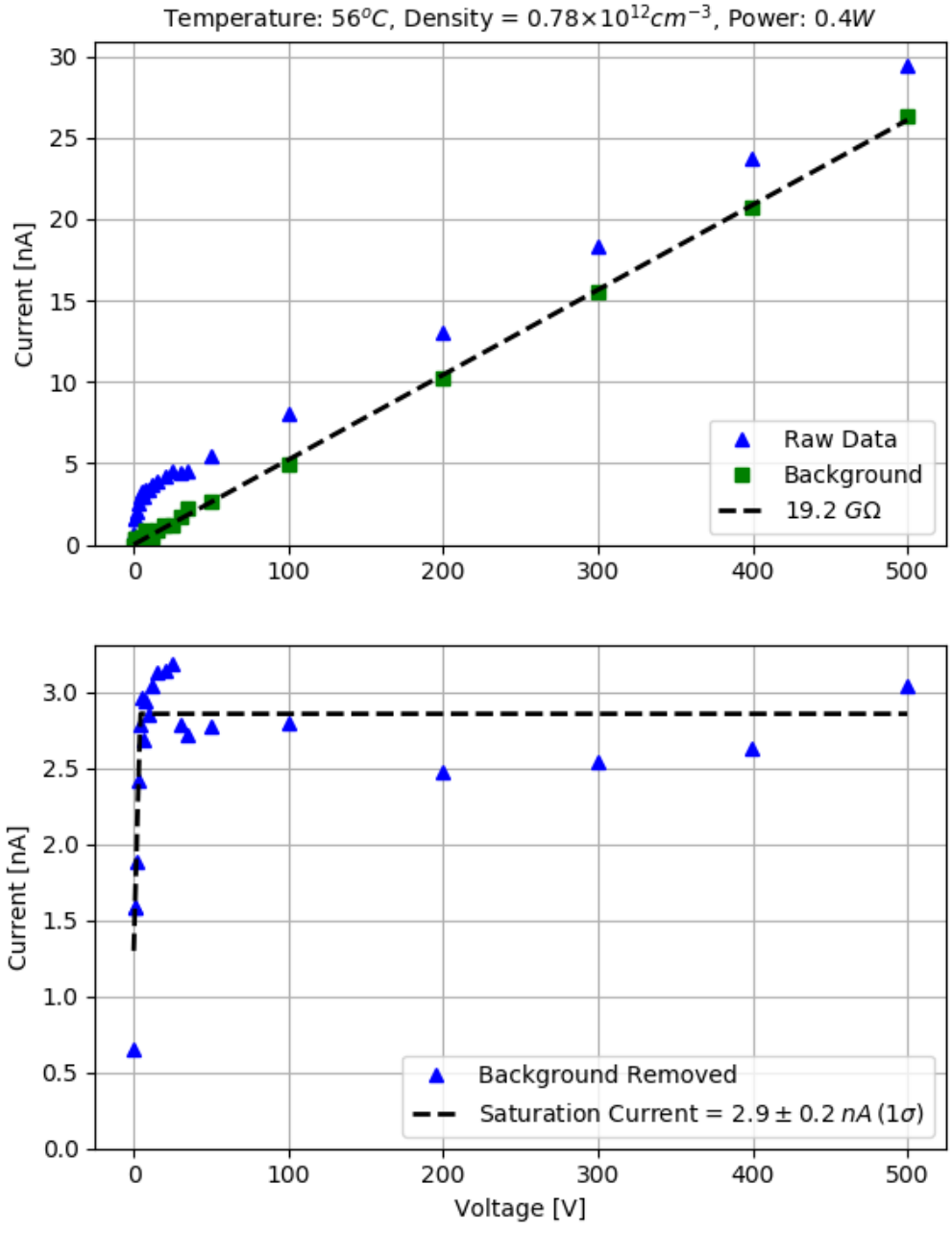

Figure D.58: Electrode measurement E4

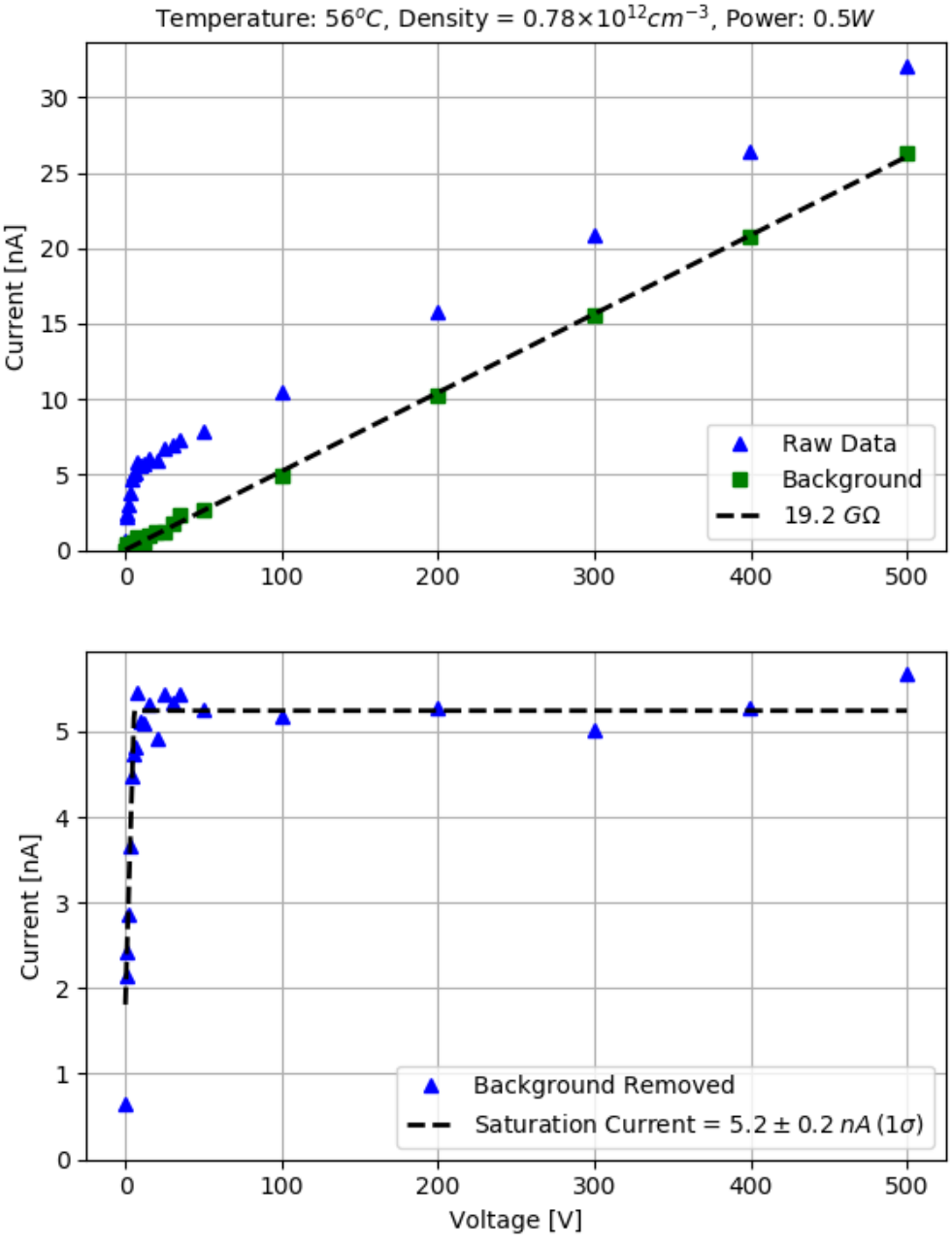

Figure D.59: Electrode measurement E5

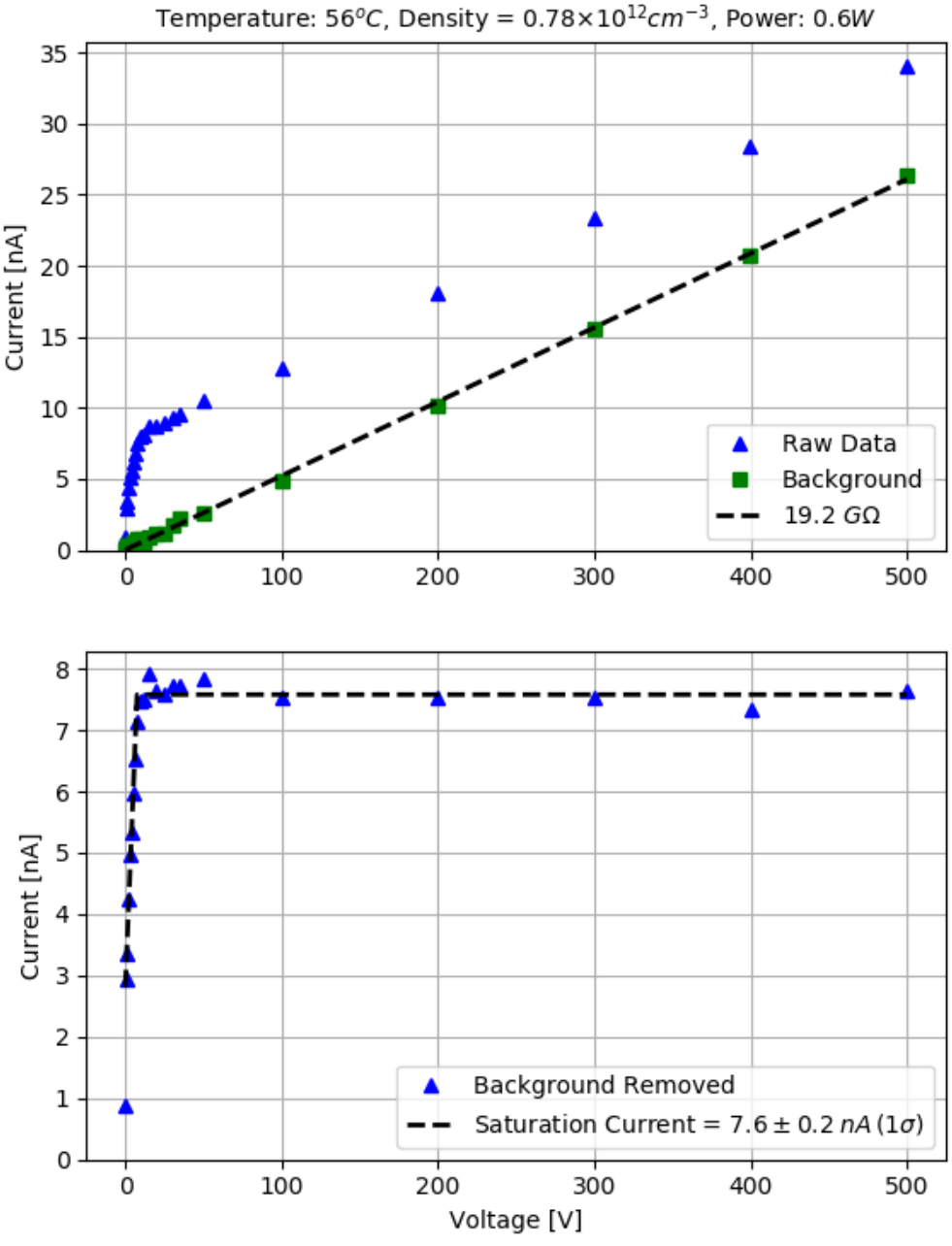

Figure D.60: Electrode measurement E6

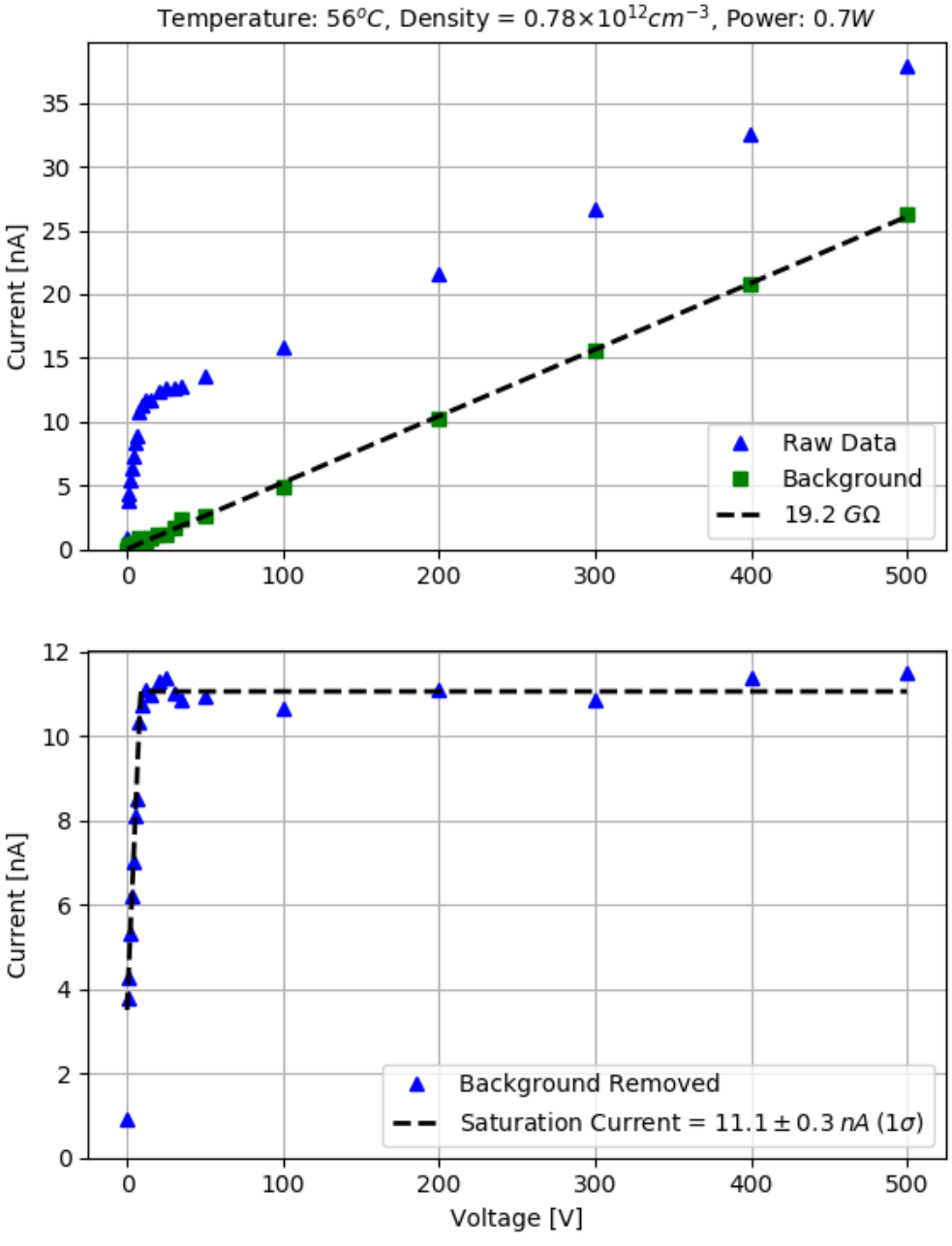

Figure D.61: Electrode measurement E7

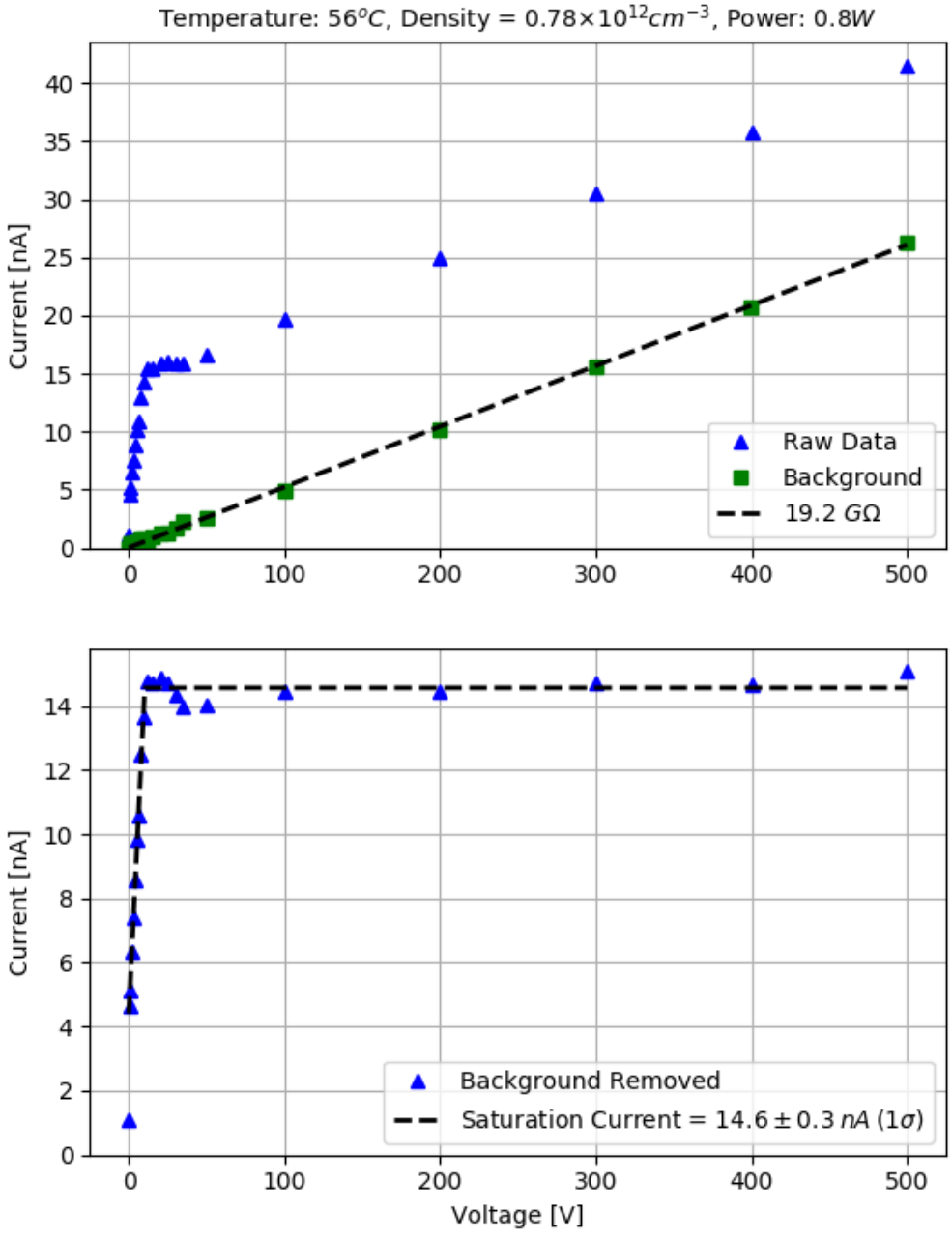

Figure D.62: Electrode measurement E8

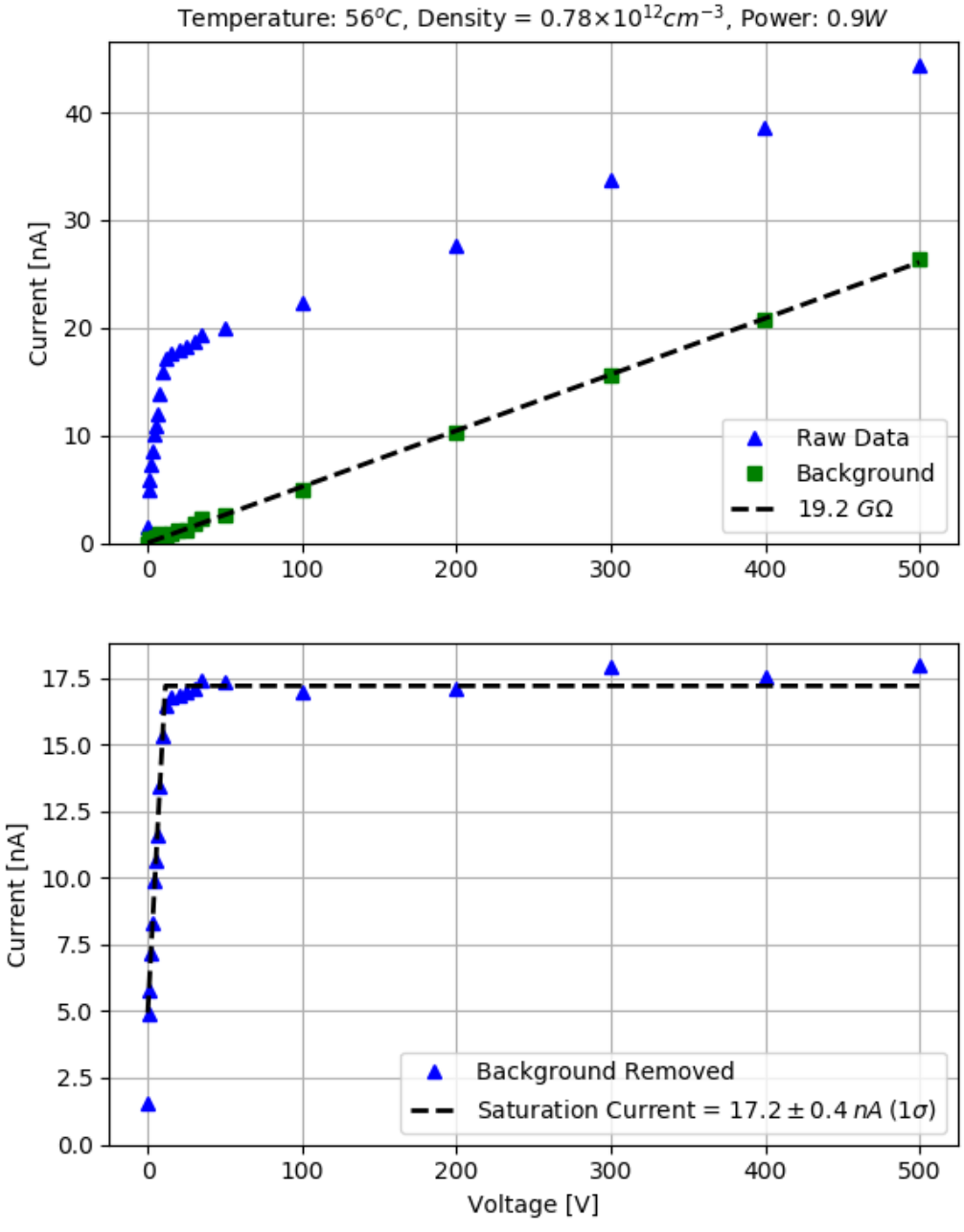

Figure D.63: Electrode measurement E9

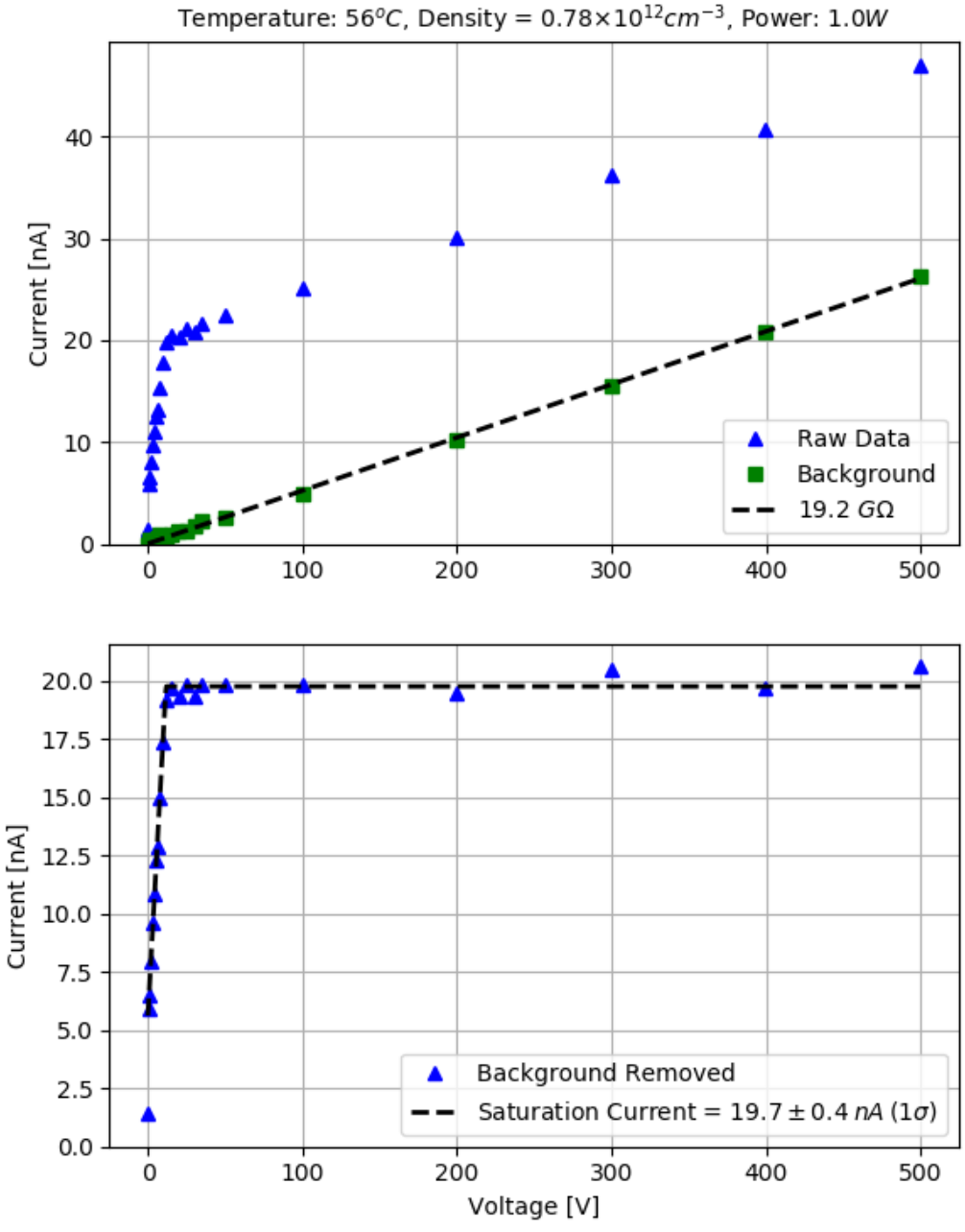

Figure D.64: Electrode measurement E10

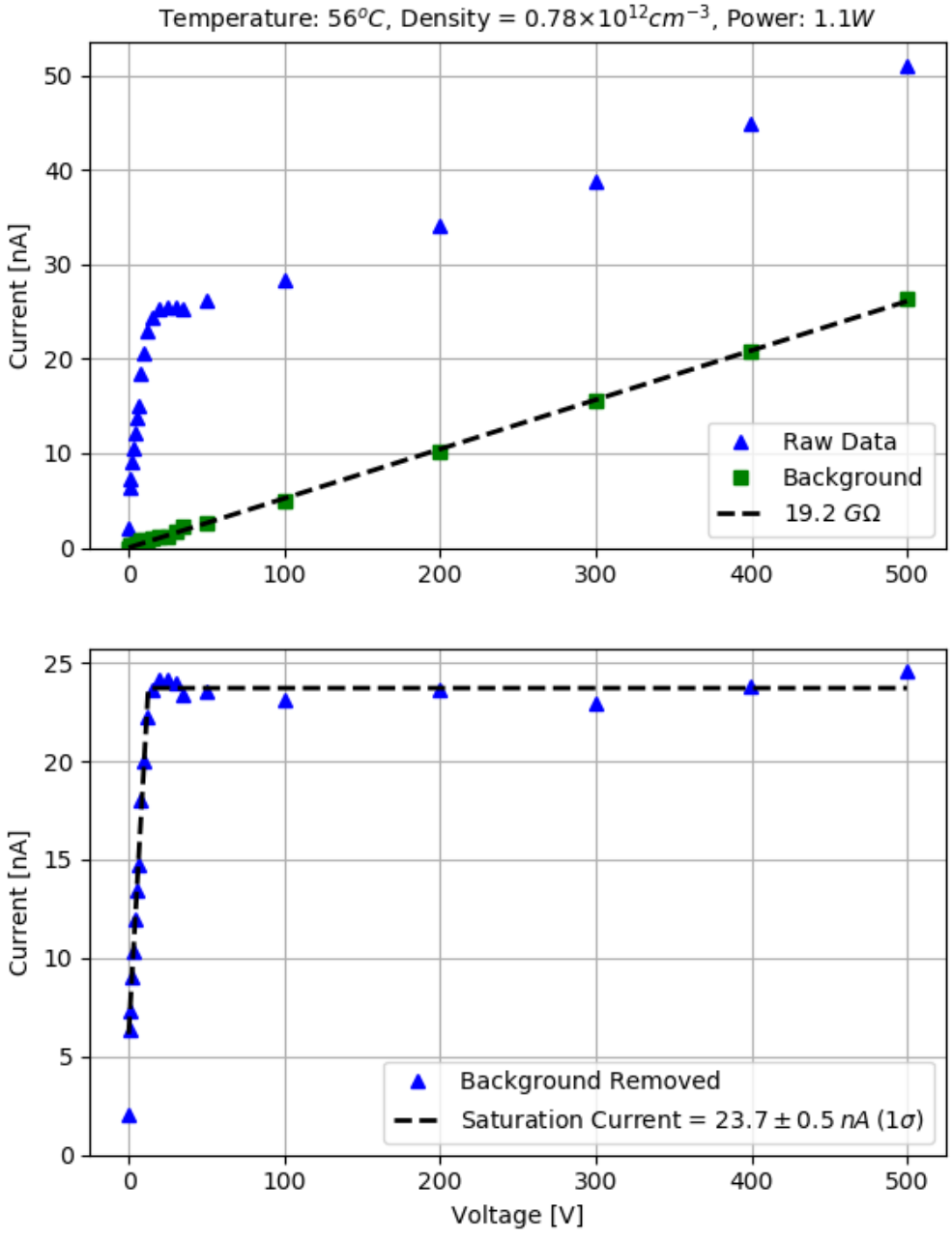

Figure D.65: Electrode measurement E11

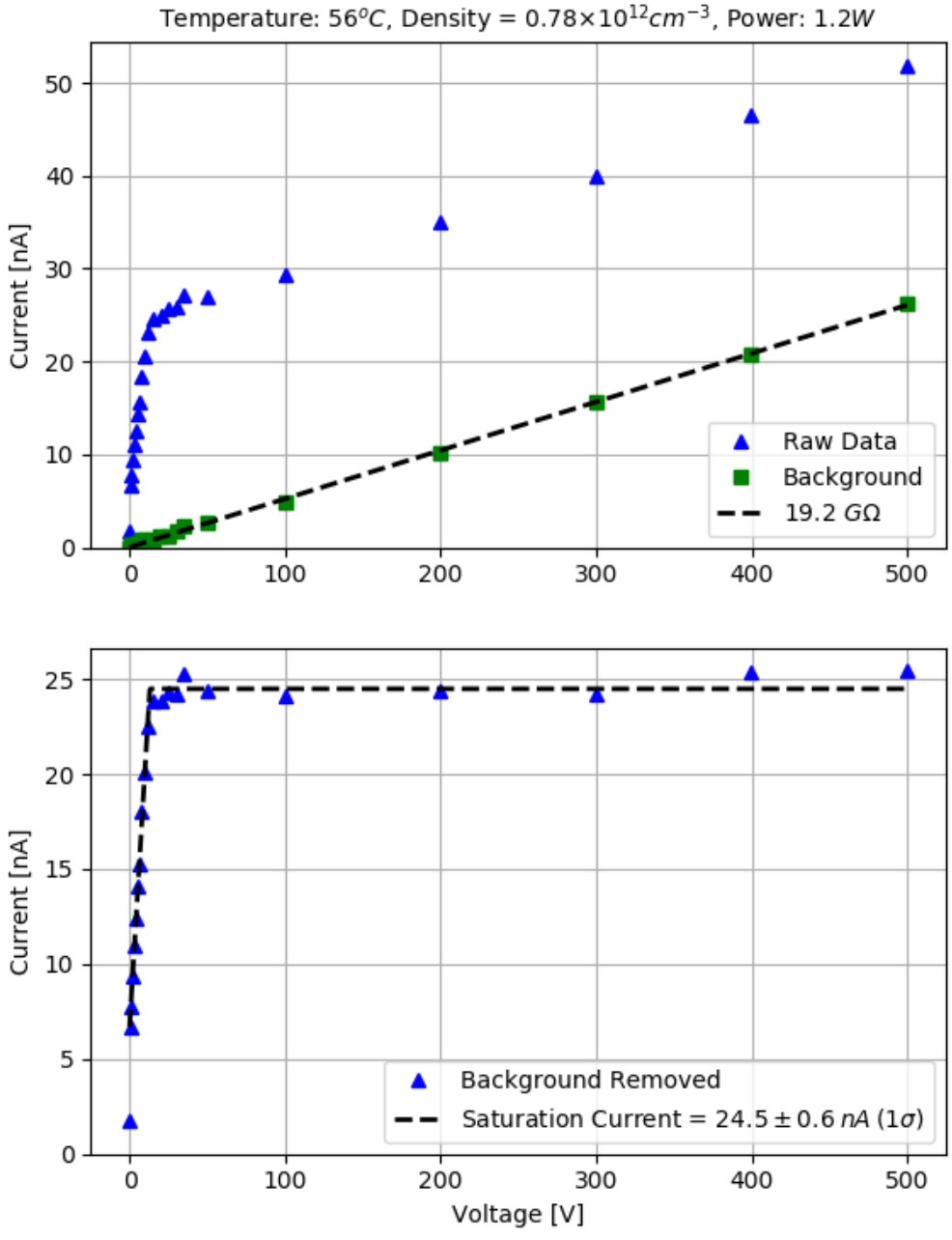

Figure D.66: Electrode measurement E12

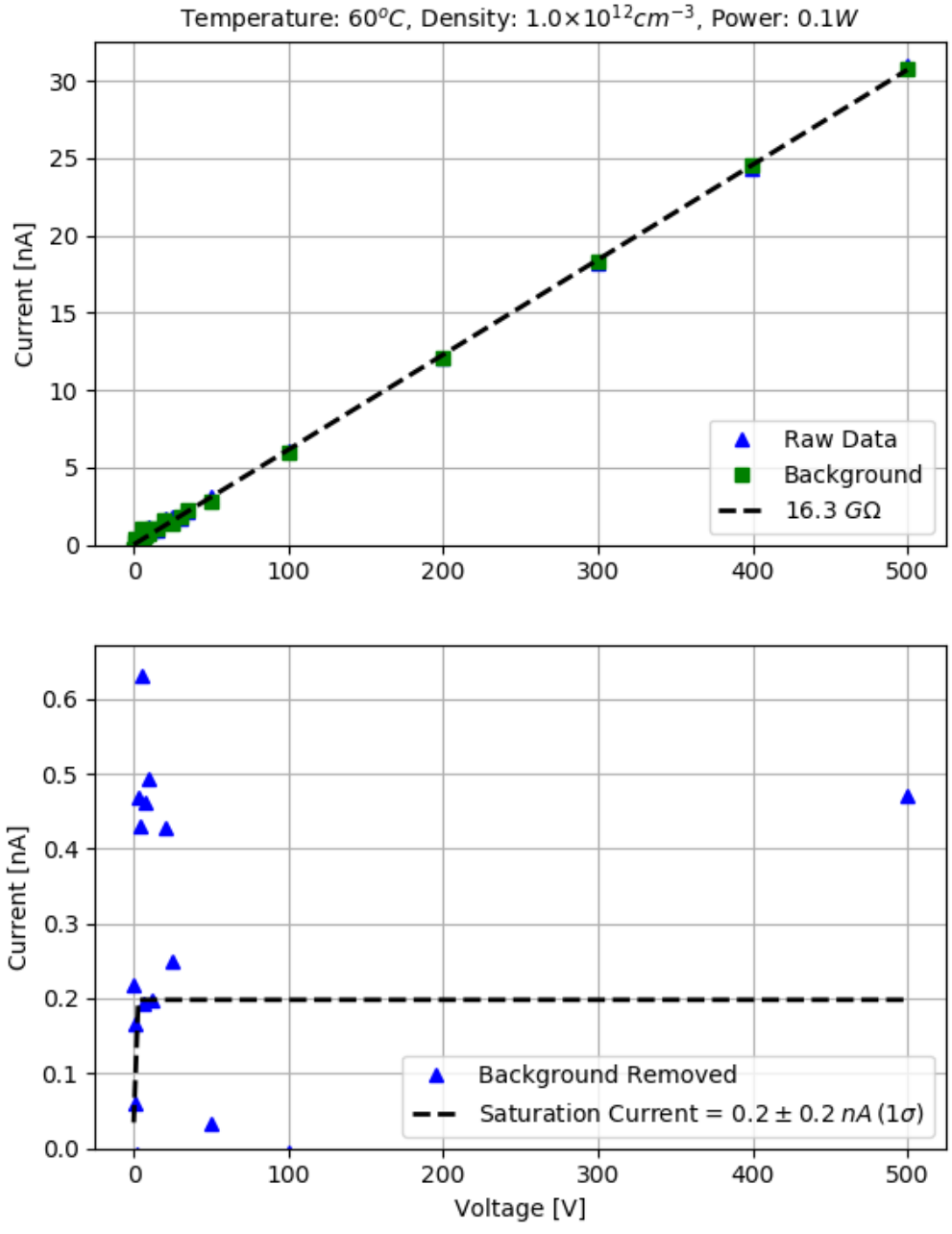

Figure D.67: Electrode measurement F1

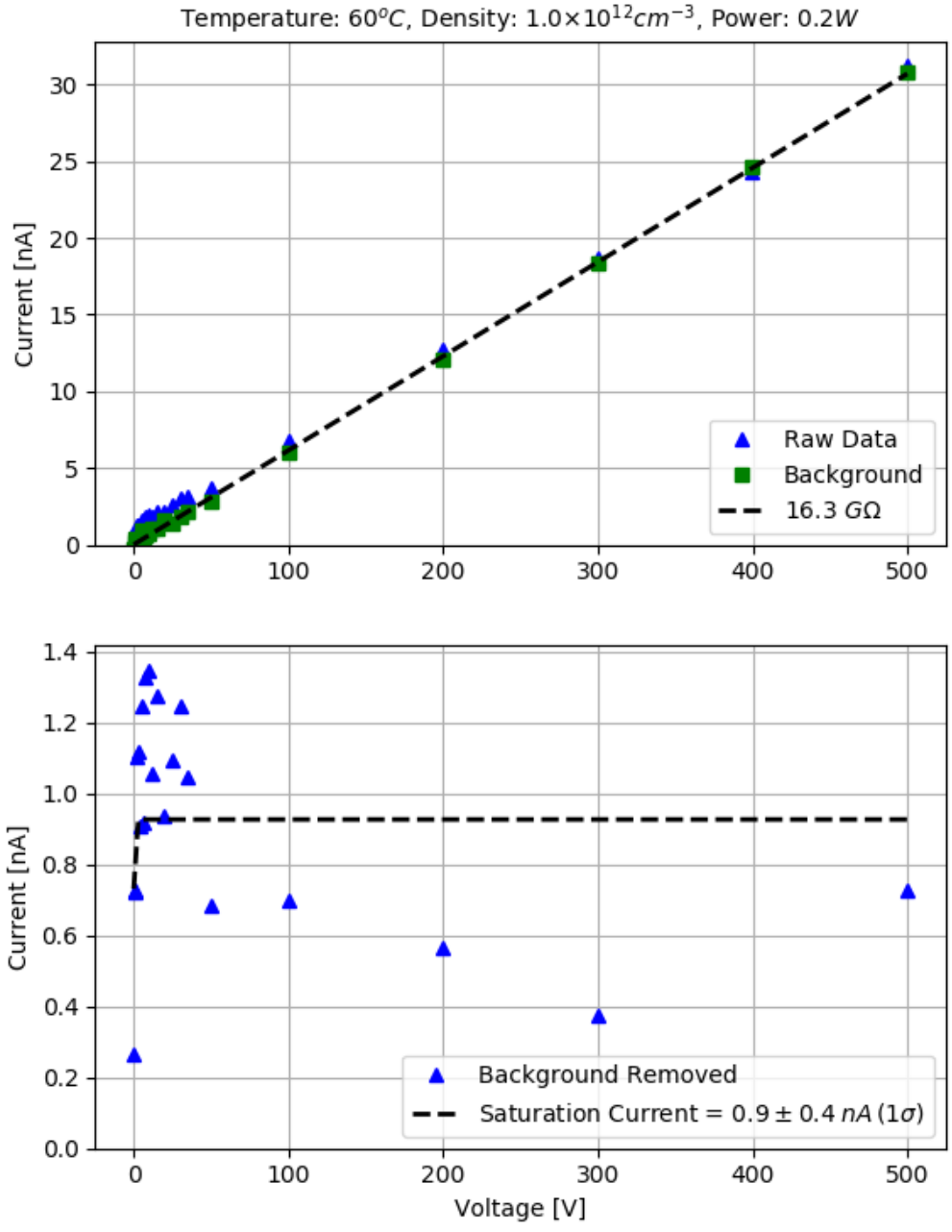

Figure D.68: Electrode measurement F2

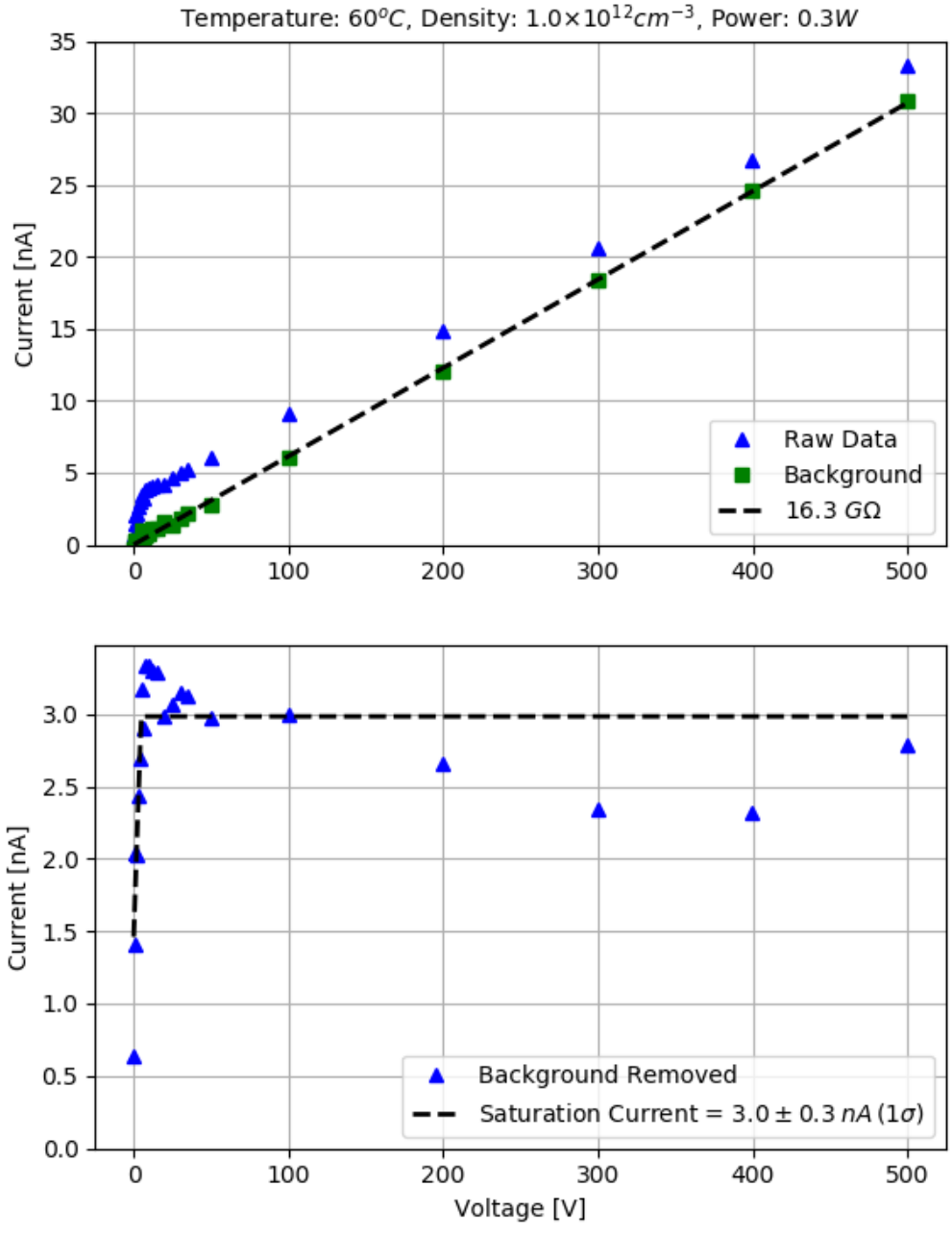

Figure D.69: Electrode measurement F3

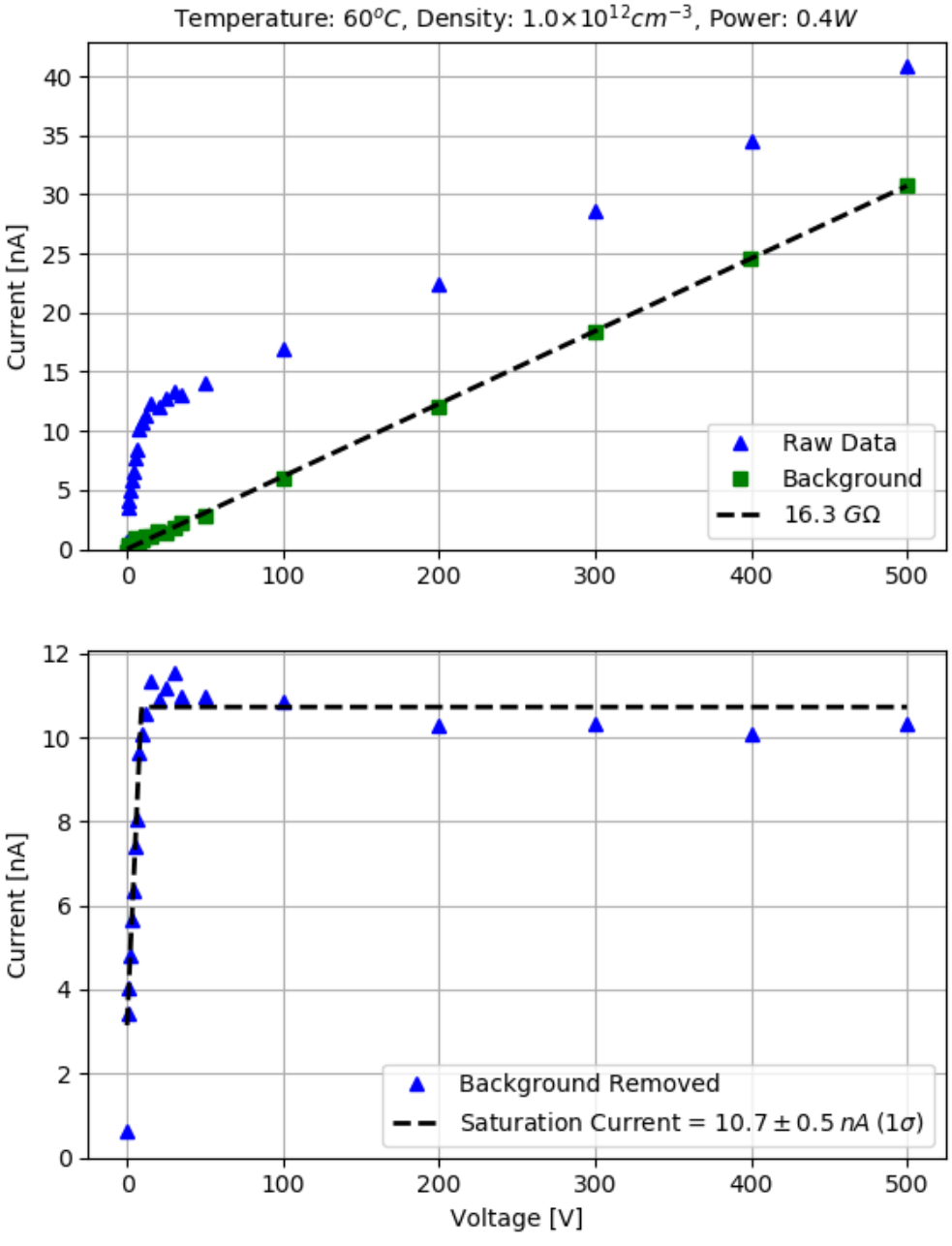

Figure D.70: Electrode measurement F4

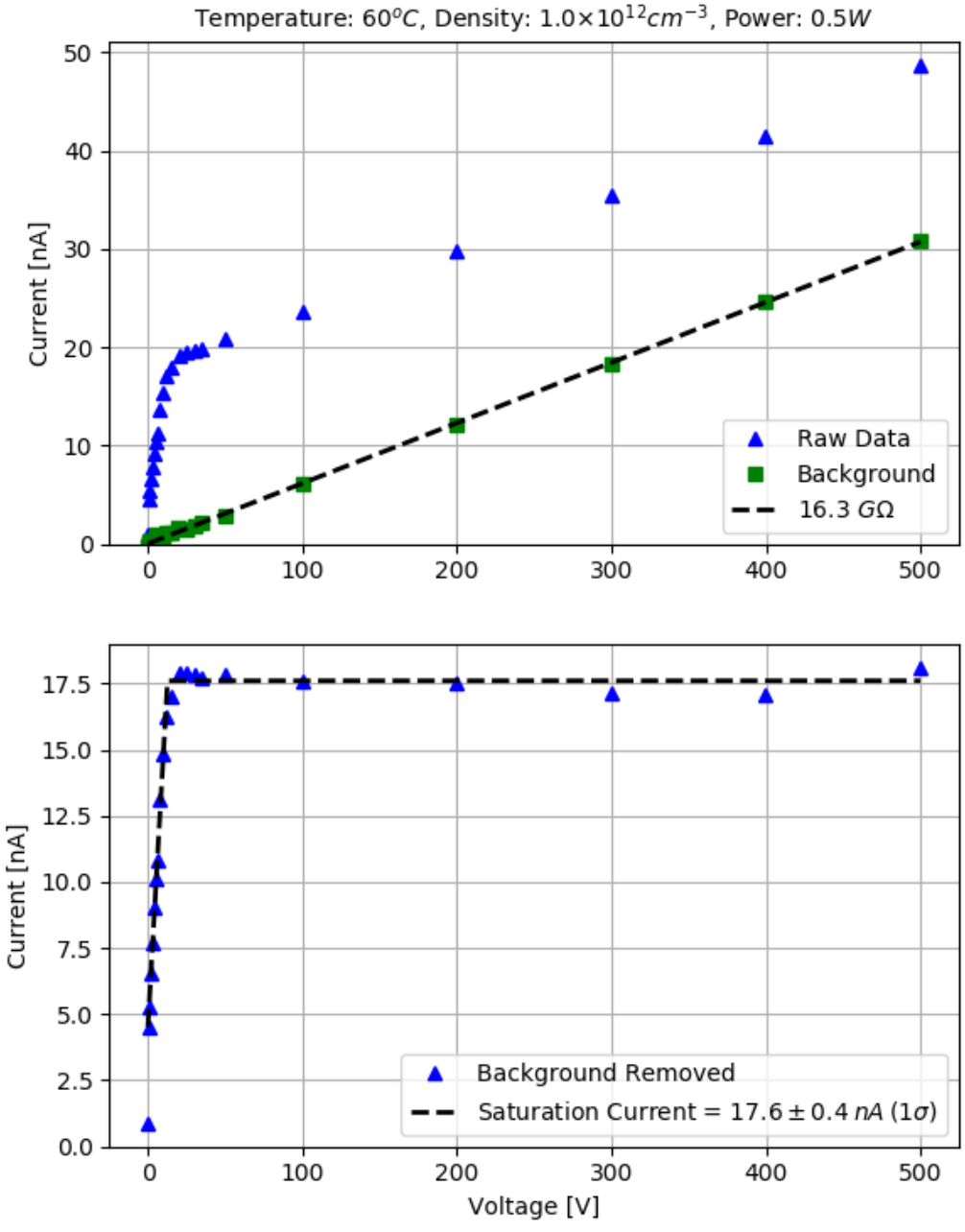

Figure D.71: Electrode measurement F5

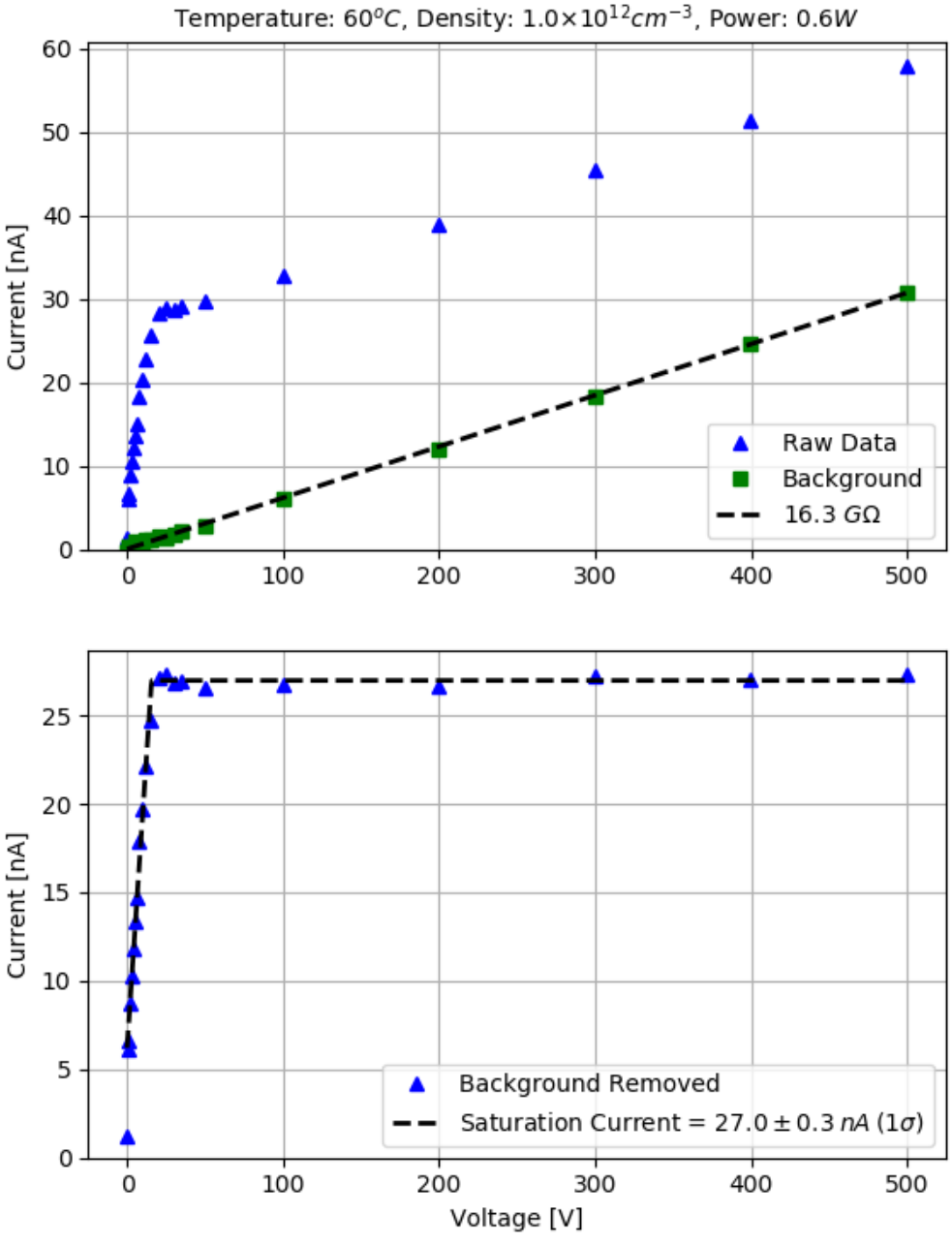

Figure D.72: Electrode measurement F6

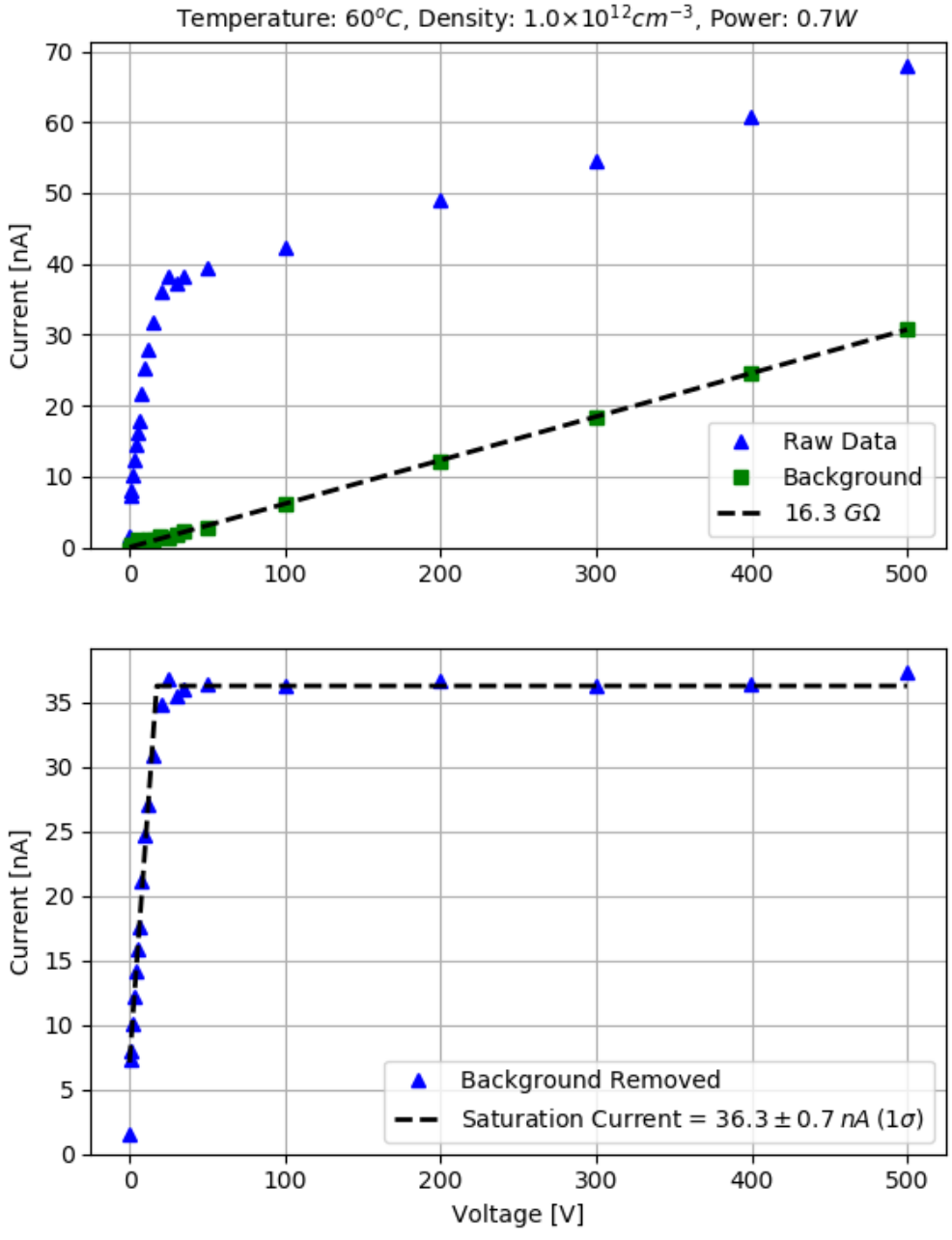

Figure D.73: Electrode measurement F7

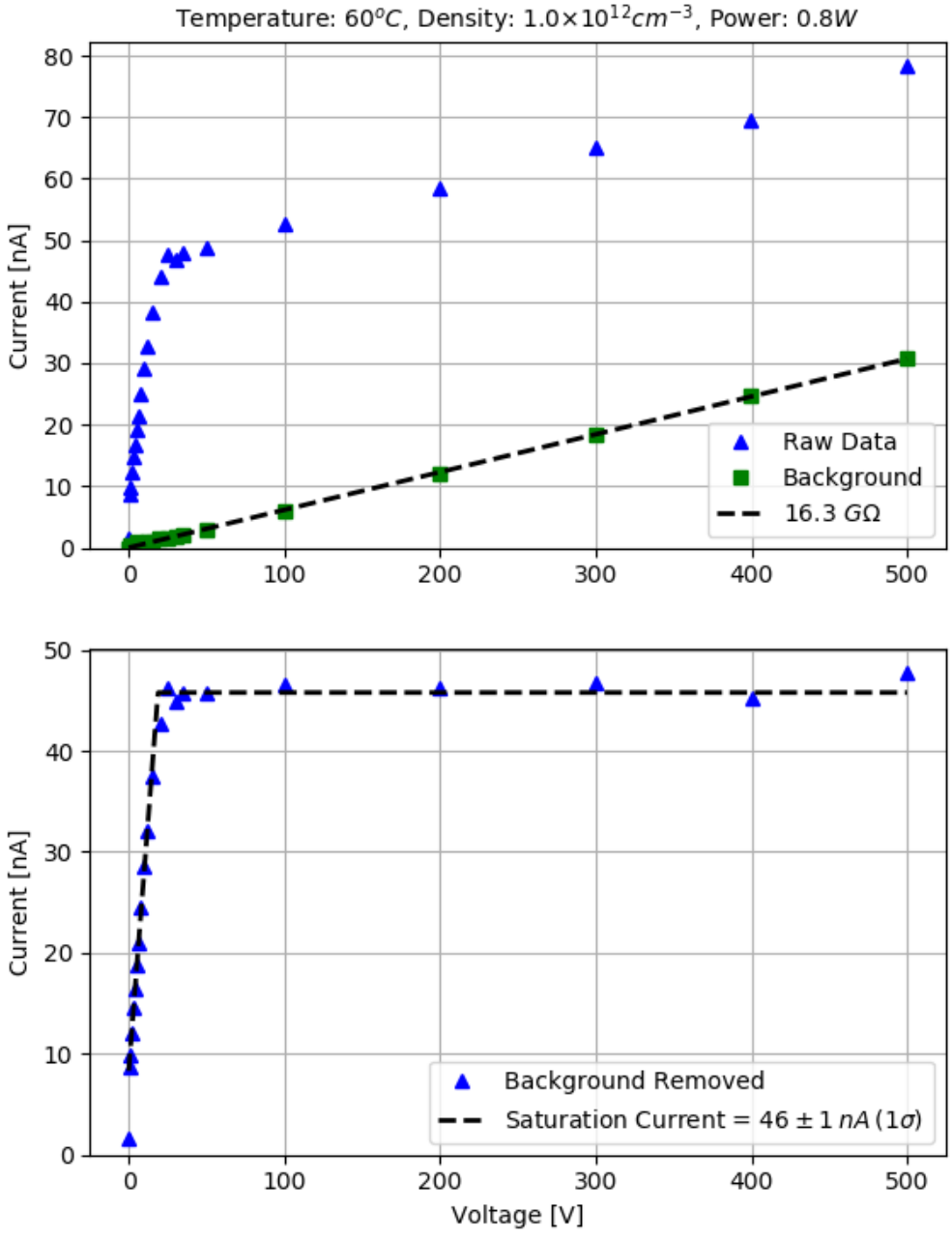

Figure D.74: Electrode measurement F8

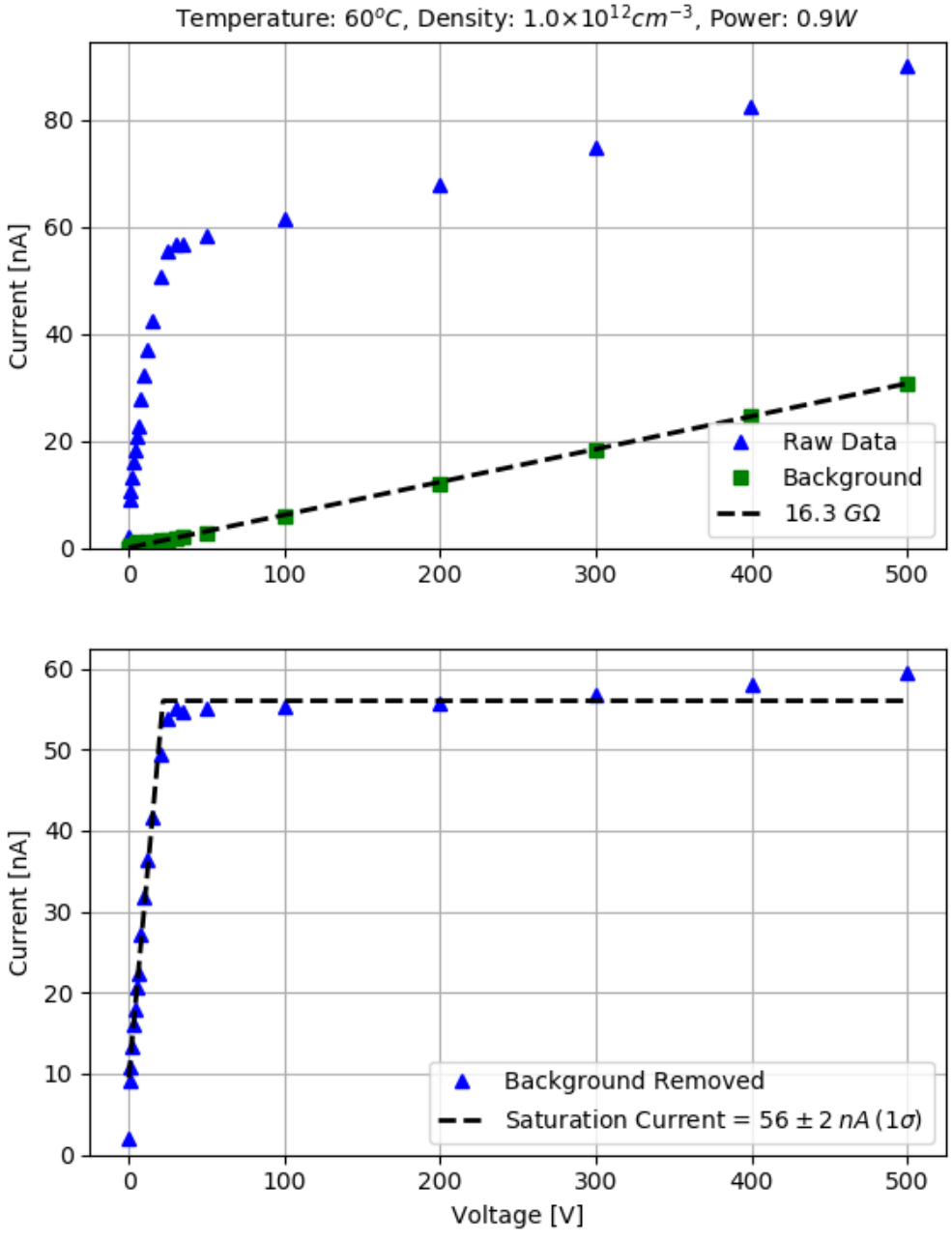

Figure D.75: Electrode measurement F9

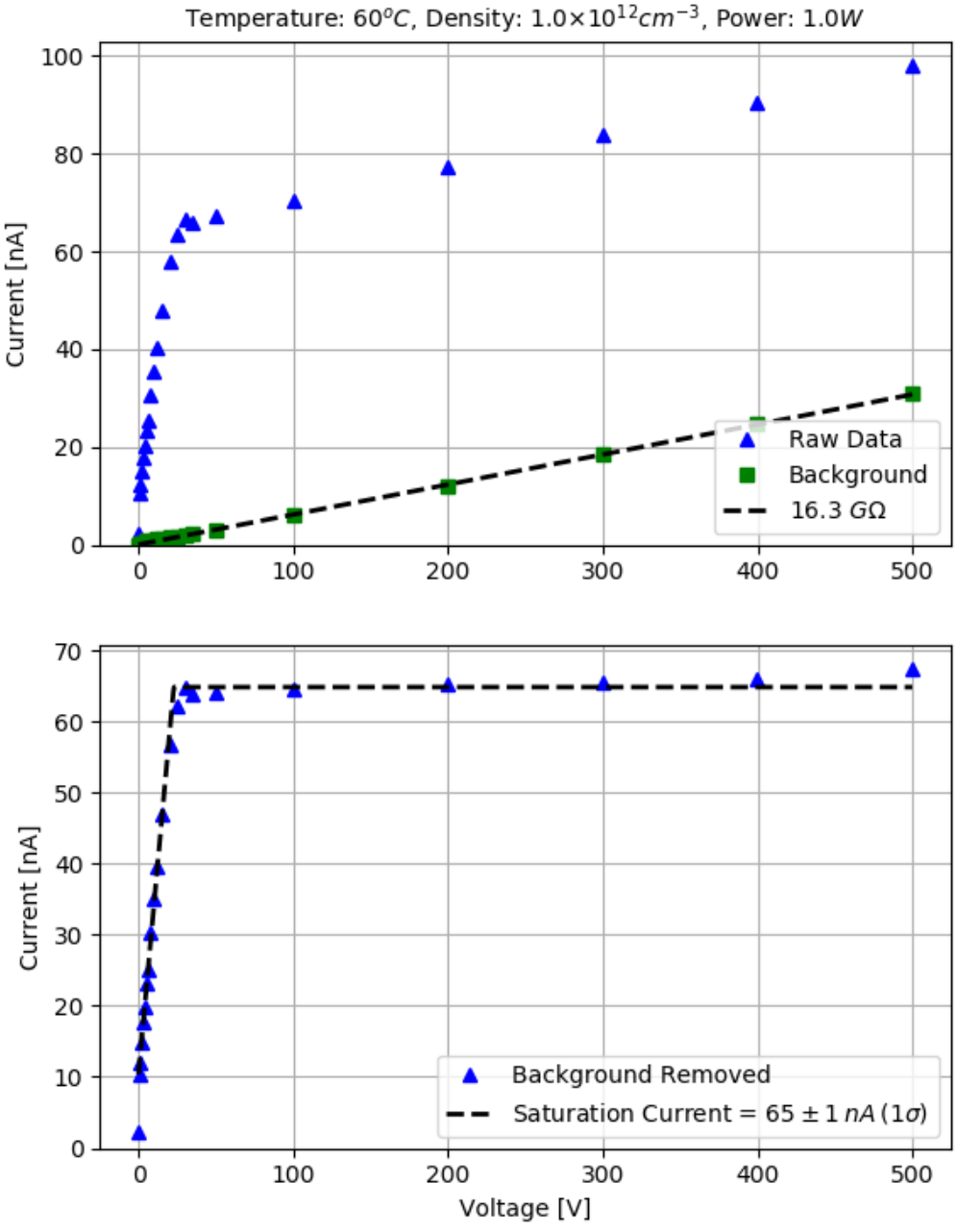

Figure D.76: Electrode measurement F10

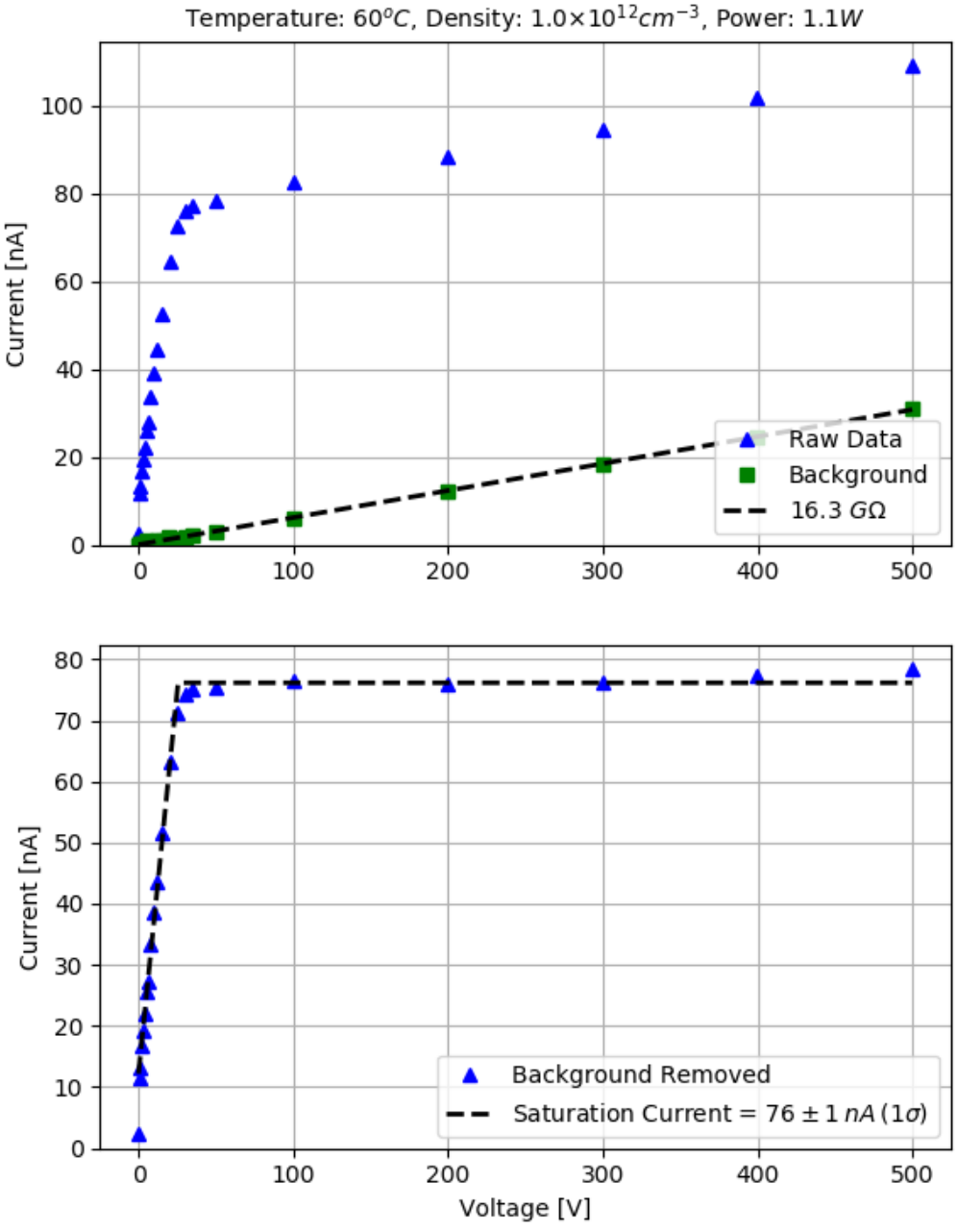

Figure D.77: Electrode measurement F11

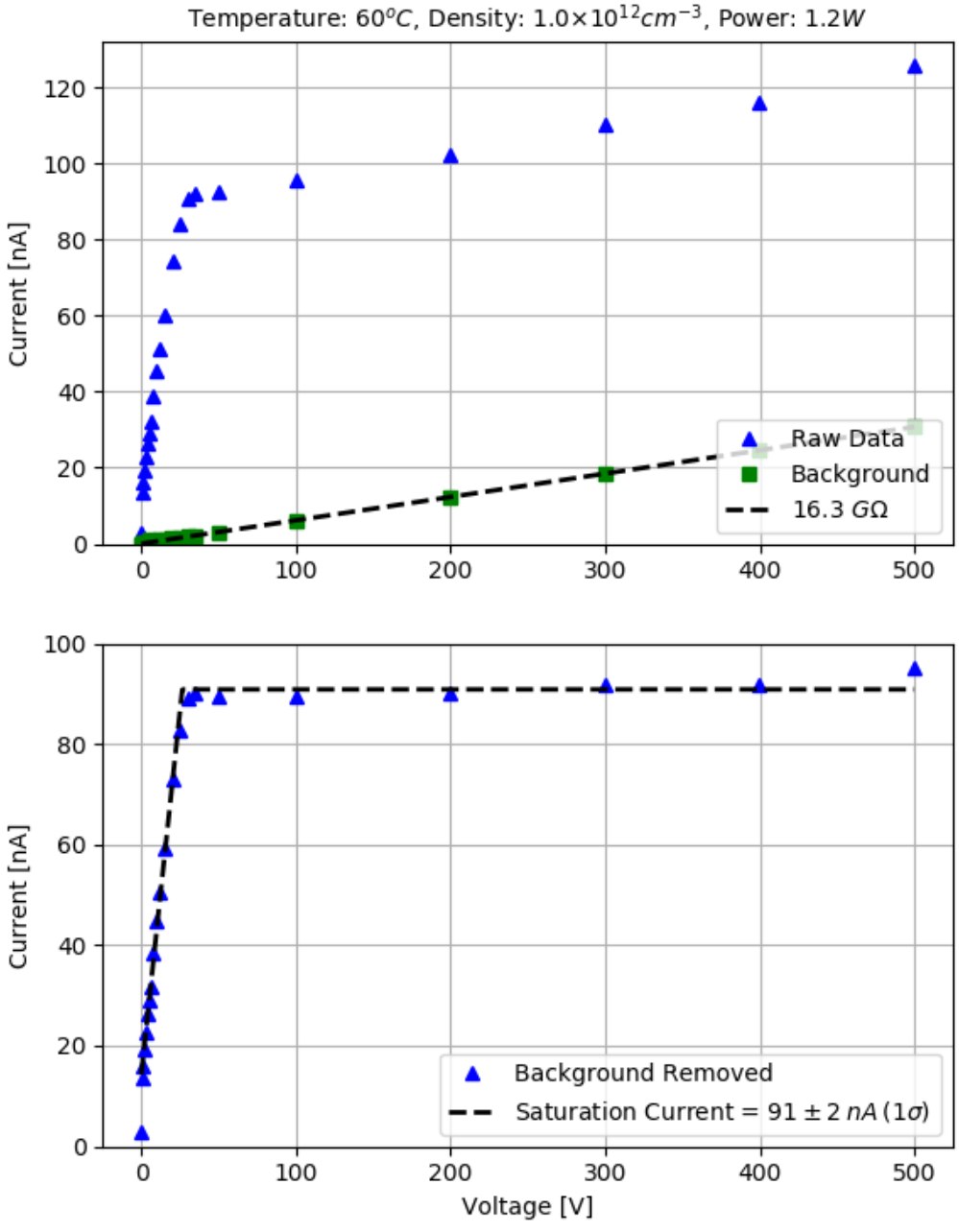

Figure D.78: Electrode measurement F12

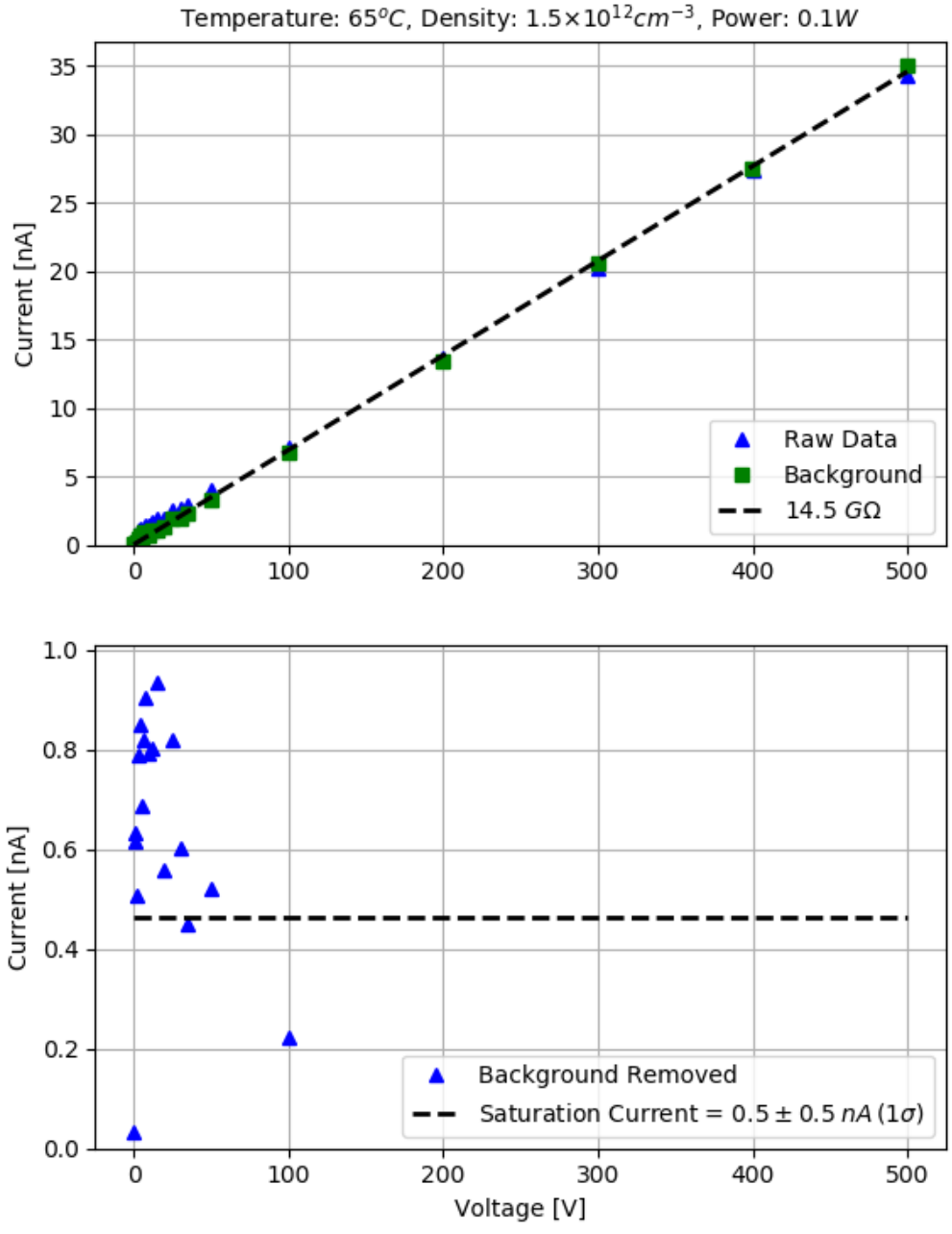

Figure D.79: Electrode measurement G1

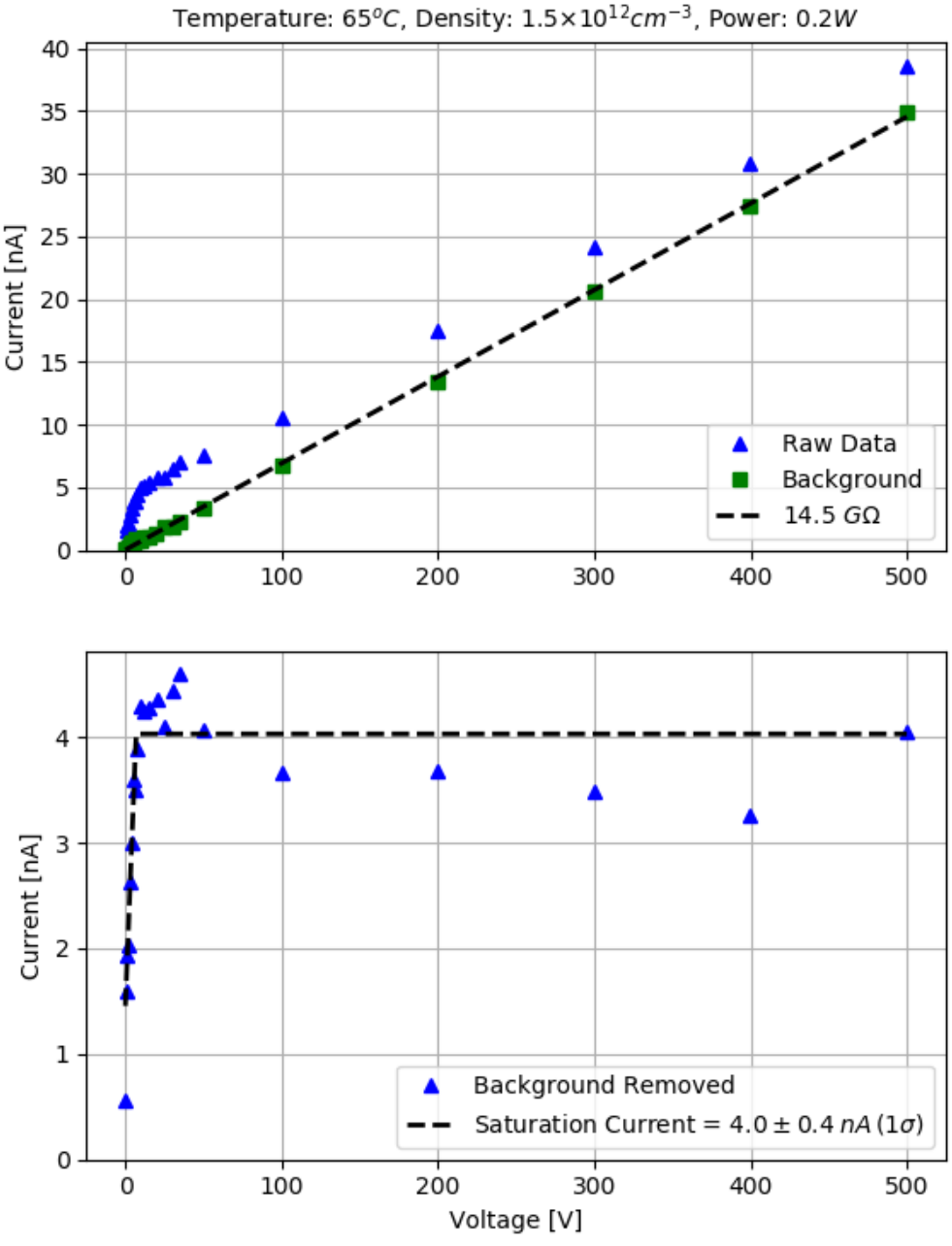

Figure D.80: Electrode measurement G2

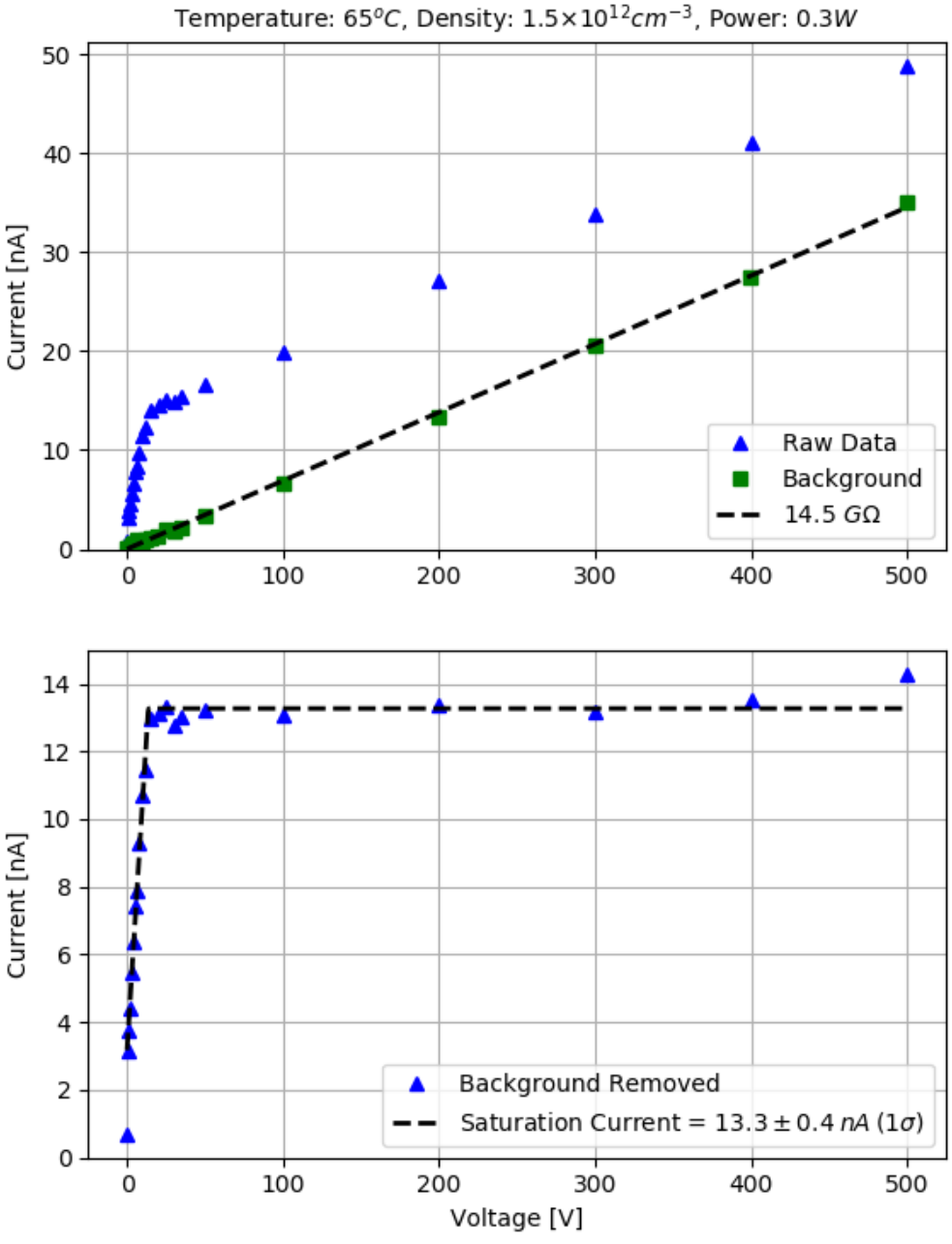

Figure D.81: Electrode measurement G3

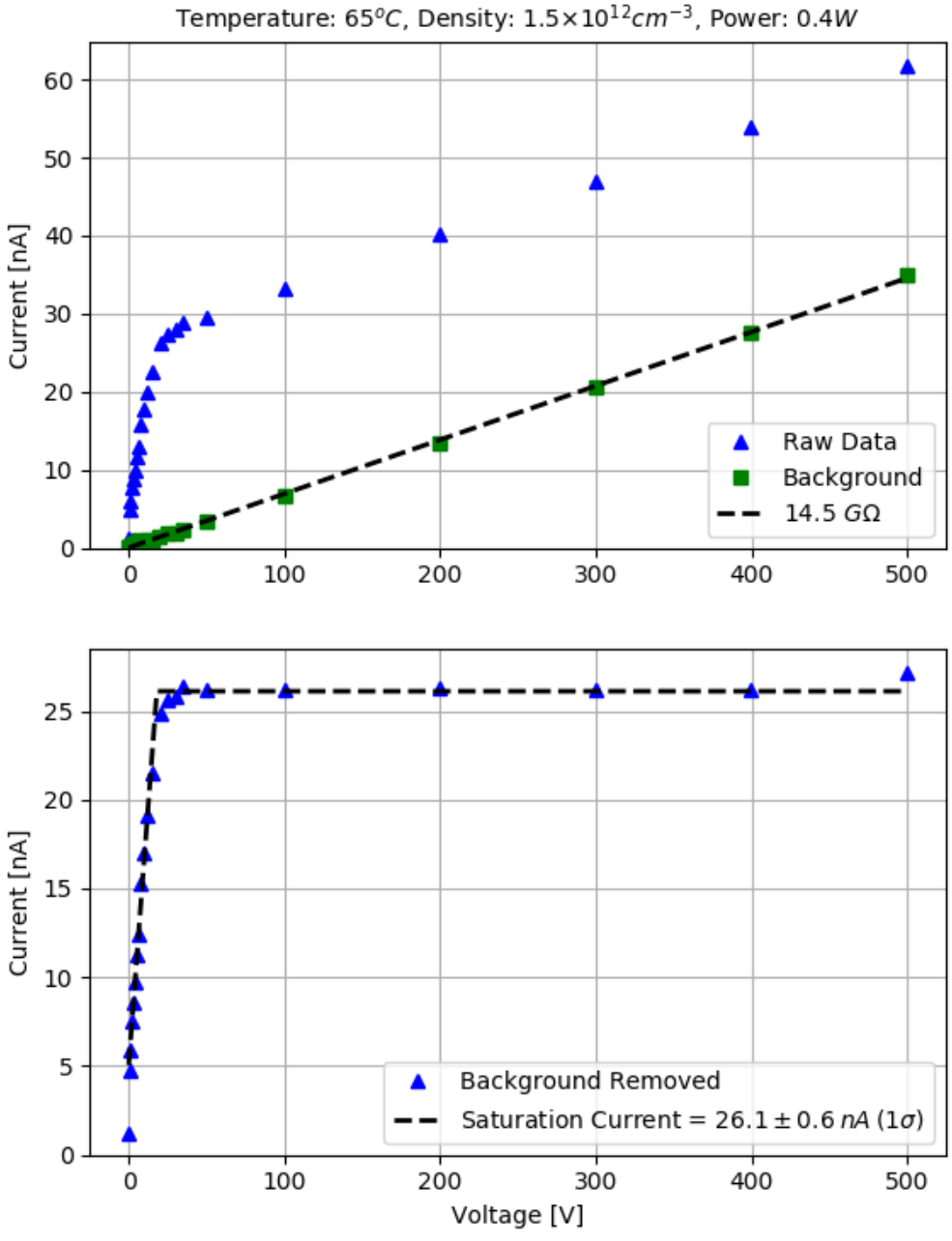

Figure D.82: Electrode measurement G4

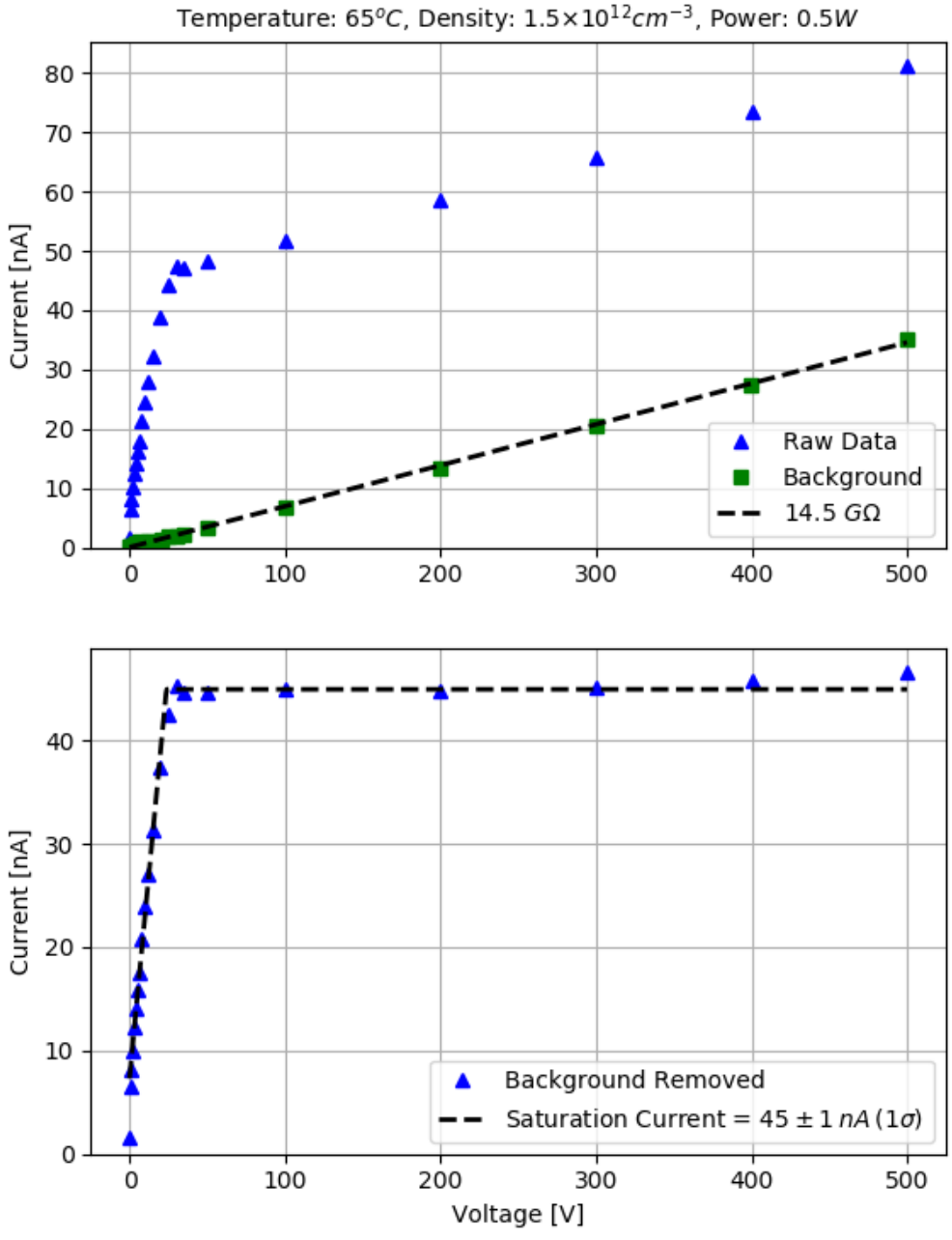

Figure D.83: Electrode measurement G5

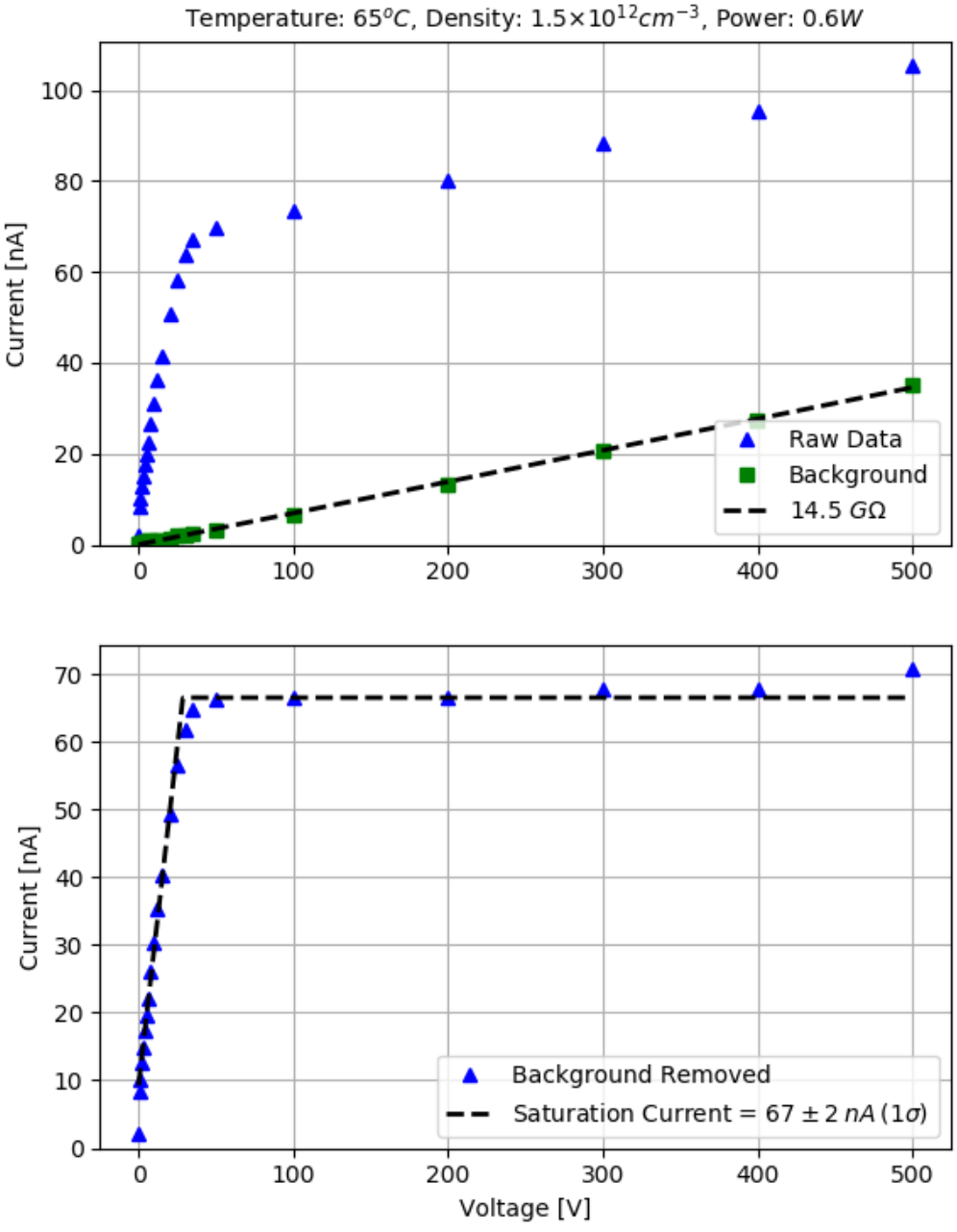

Figure D.84: Electrode measurement G6

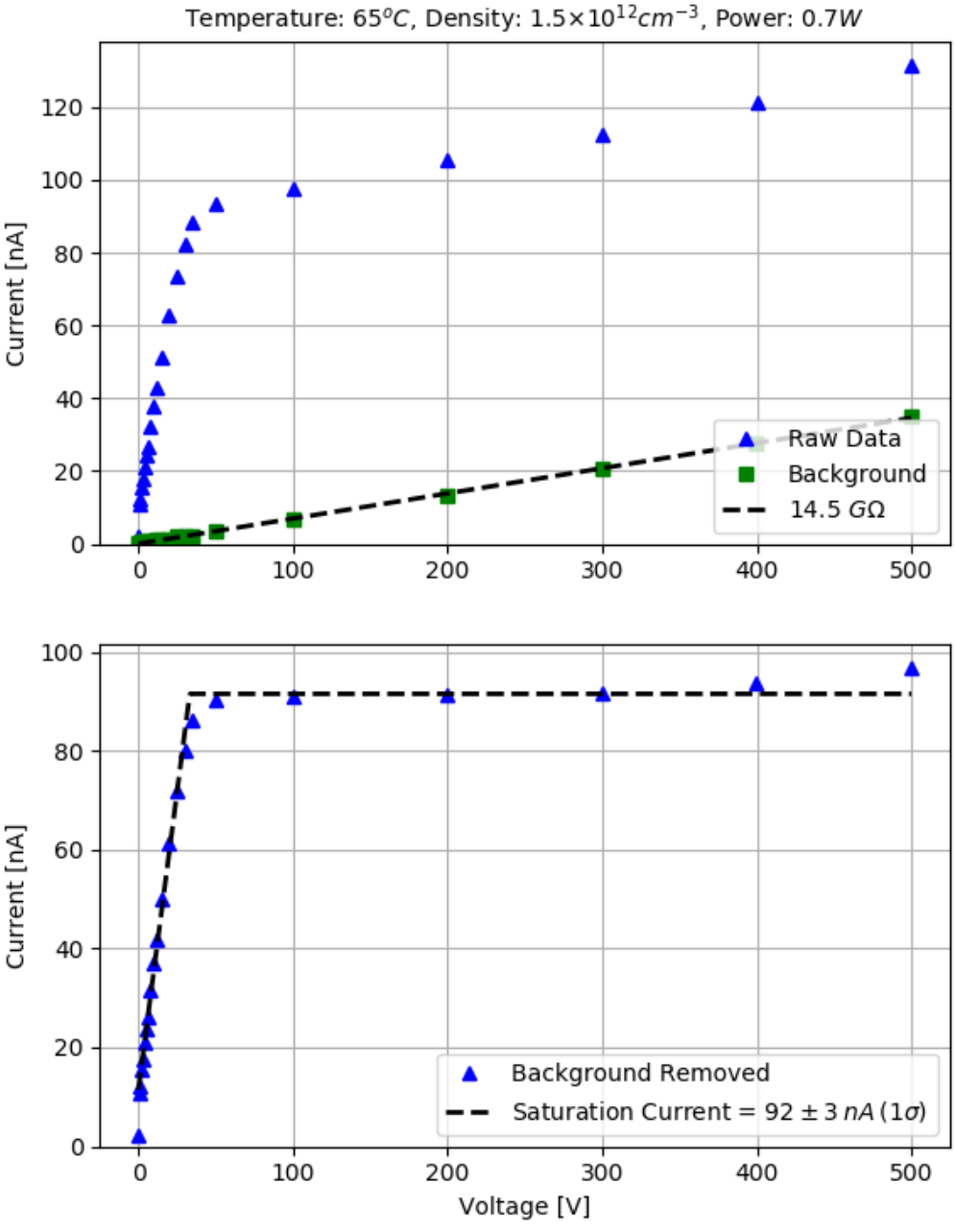

Figure D.85: Electrode measurement G7

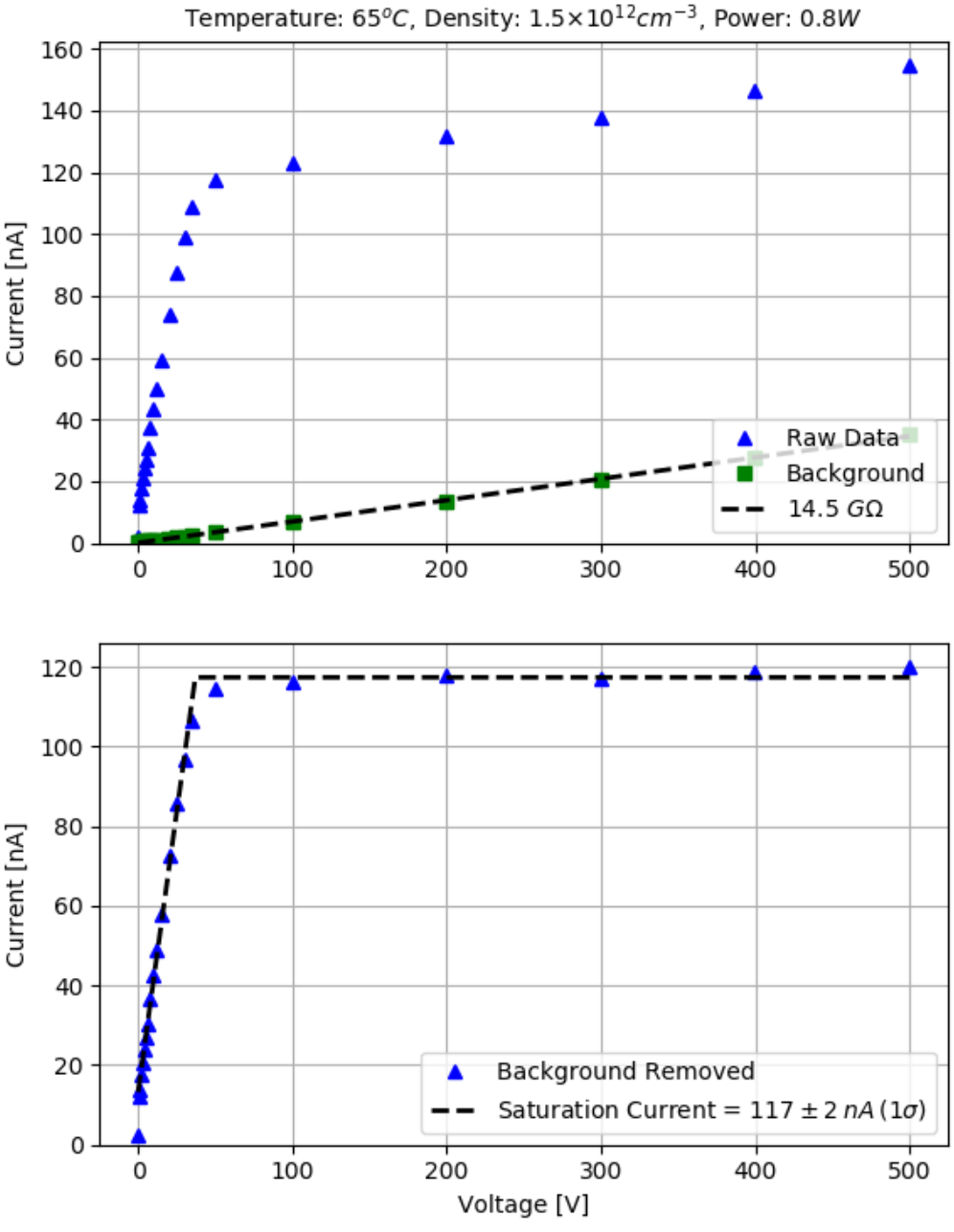

Figure D.86: Electrode measurement G8

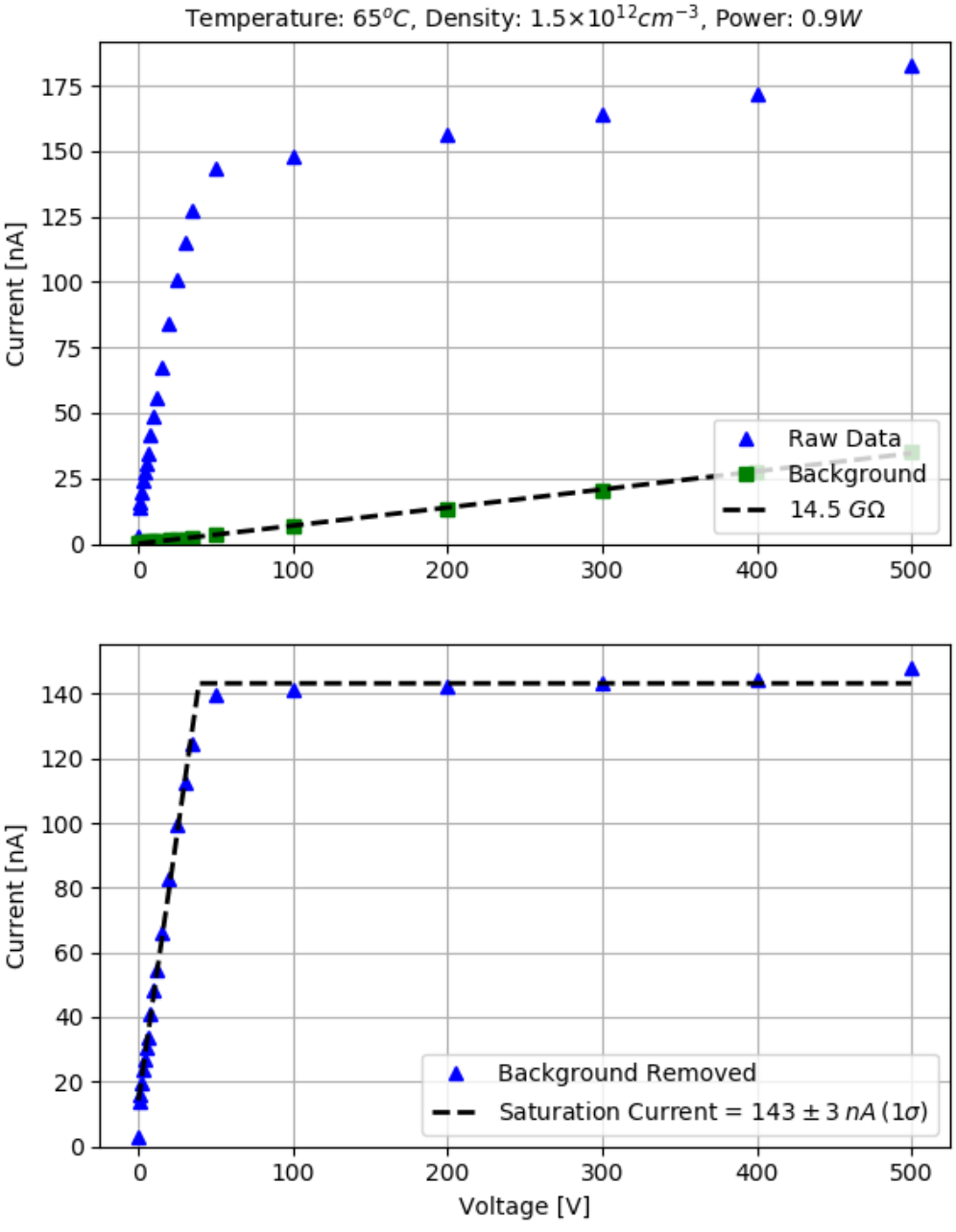

Figure D.87: Electrode measurement G9

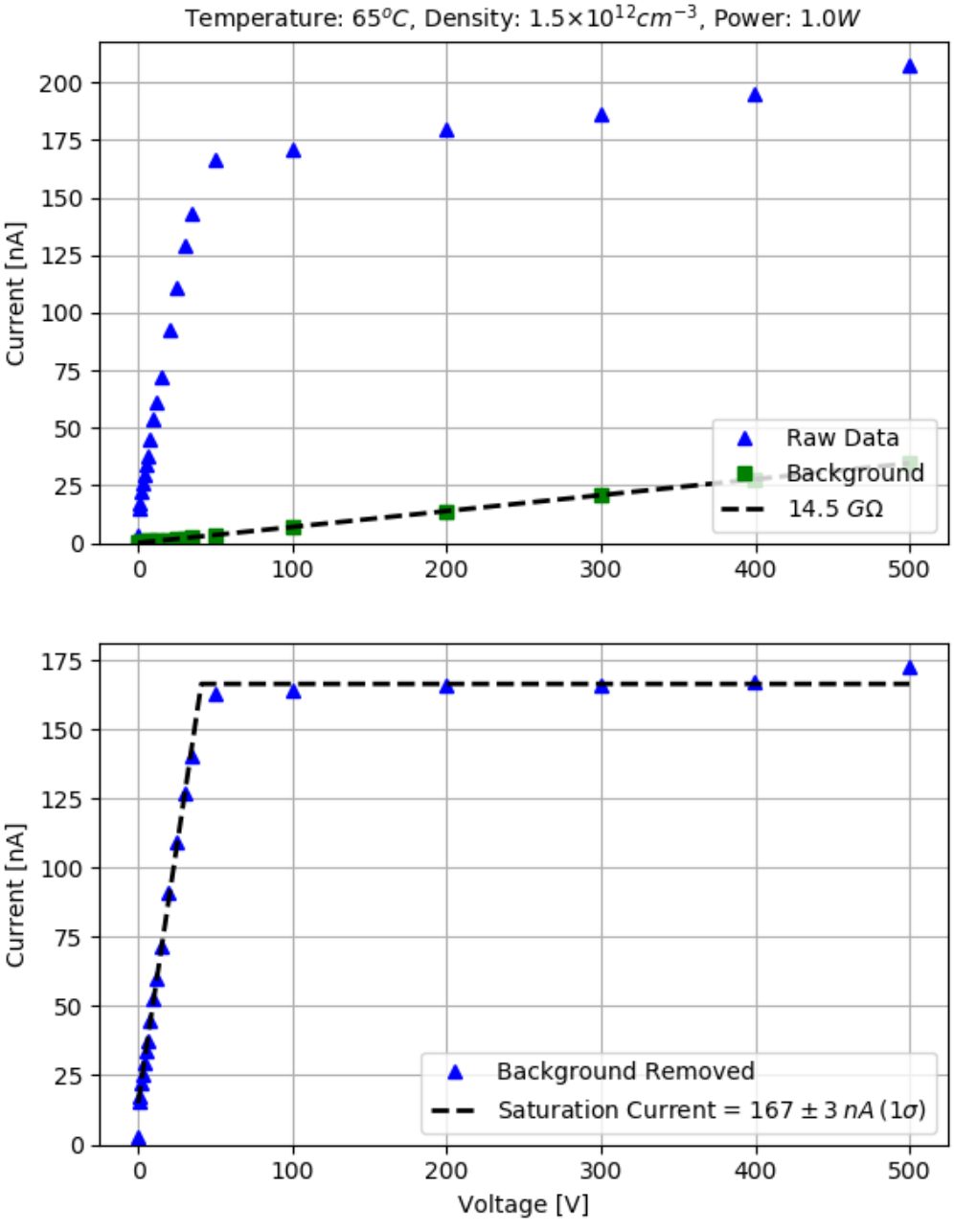

Figure D.88: Electrode measurement G10

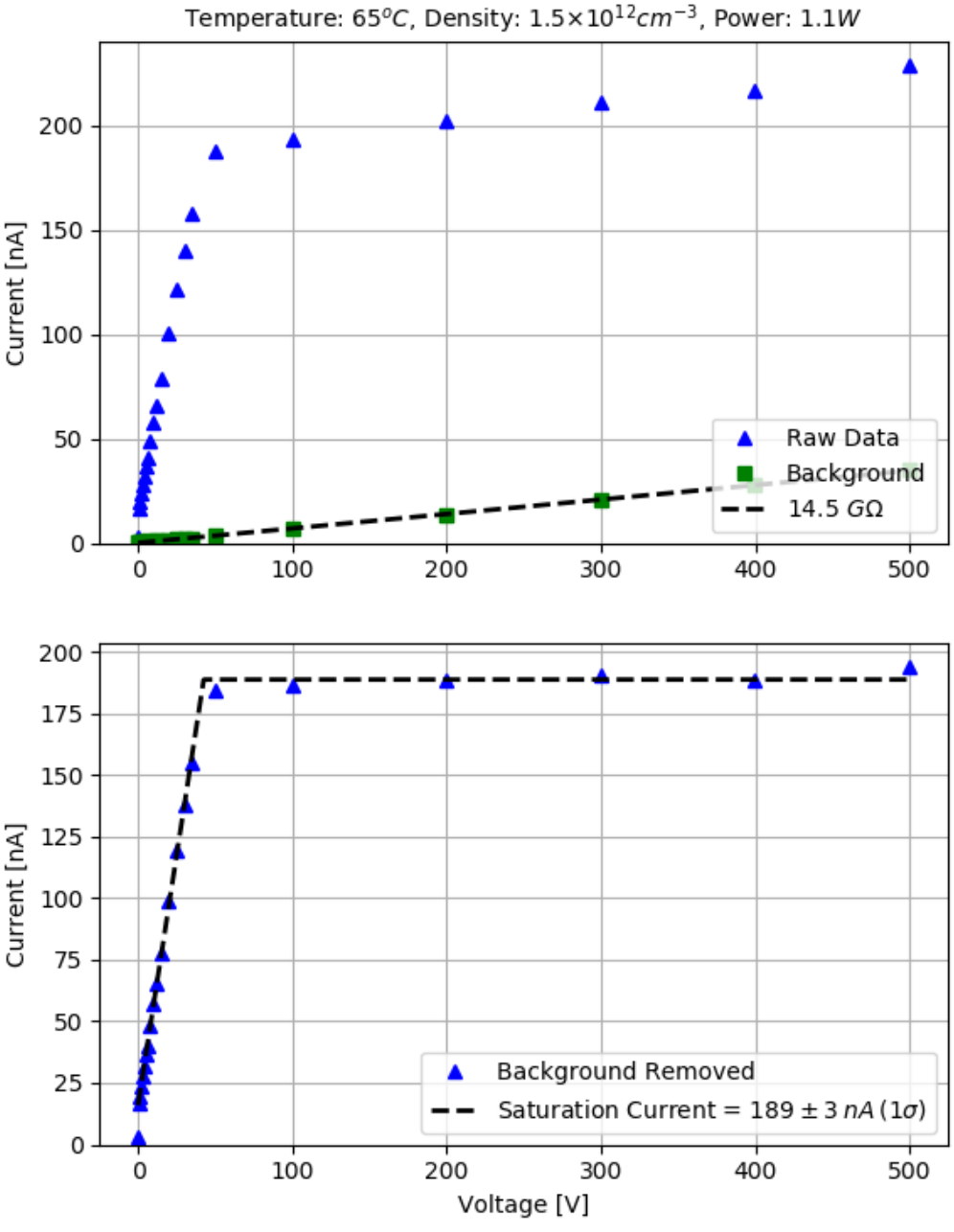

Figure D.89: Electrode measurement G11

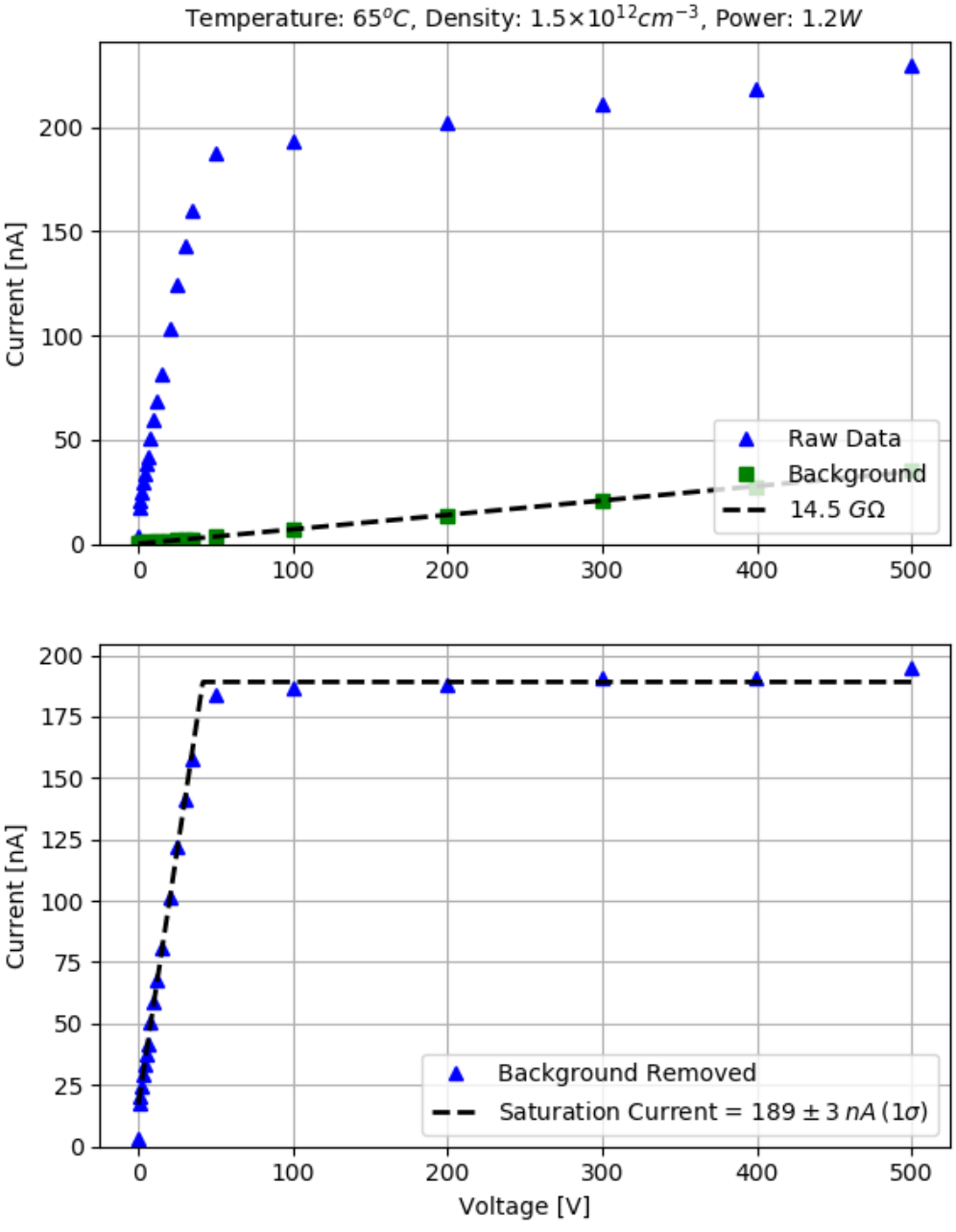

Figure D.90: Electrode measurement G12

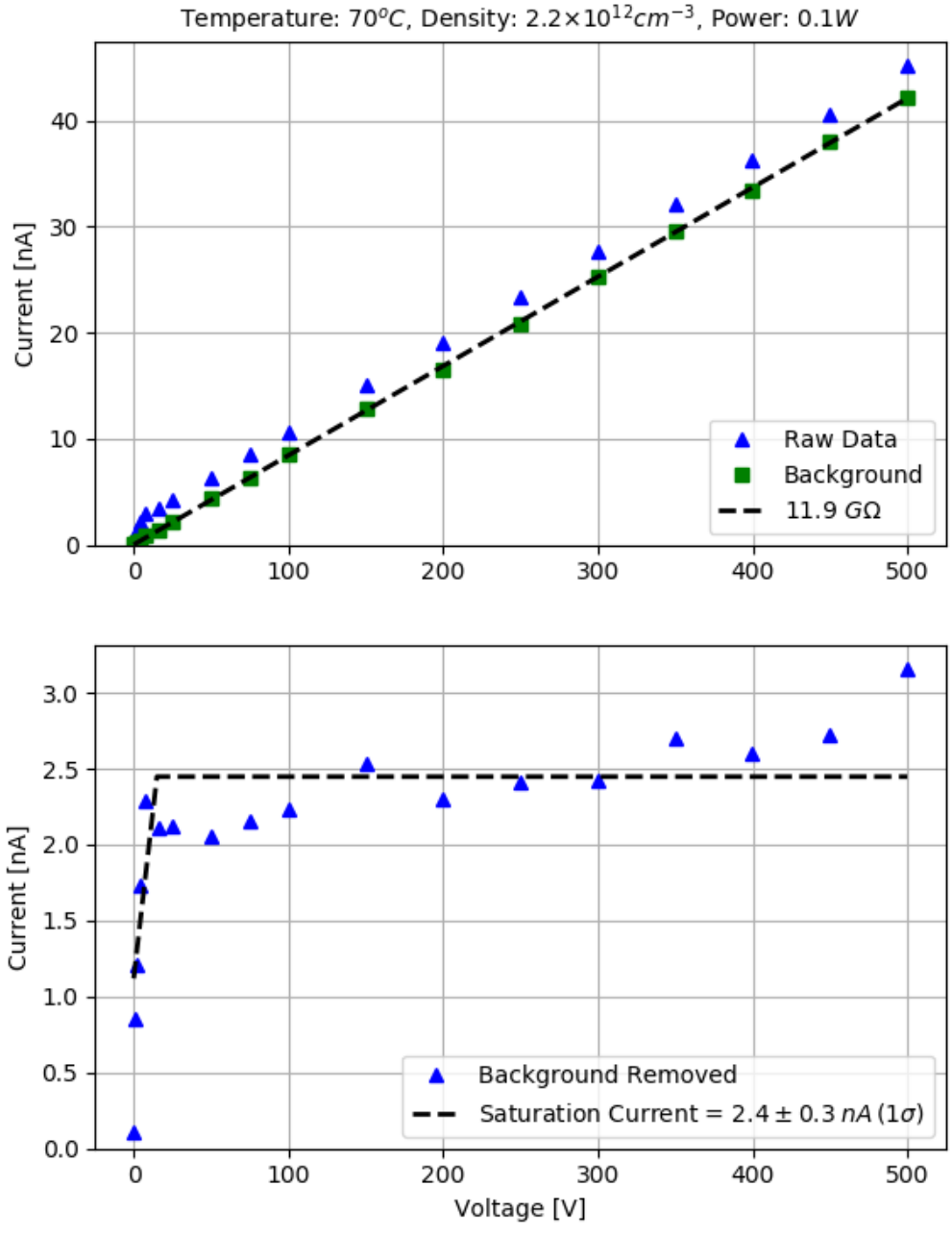

Figure D.91: Electrode measurement H1

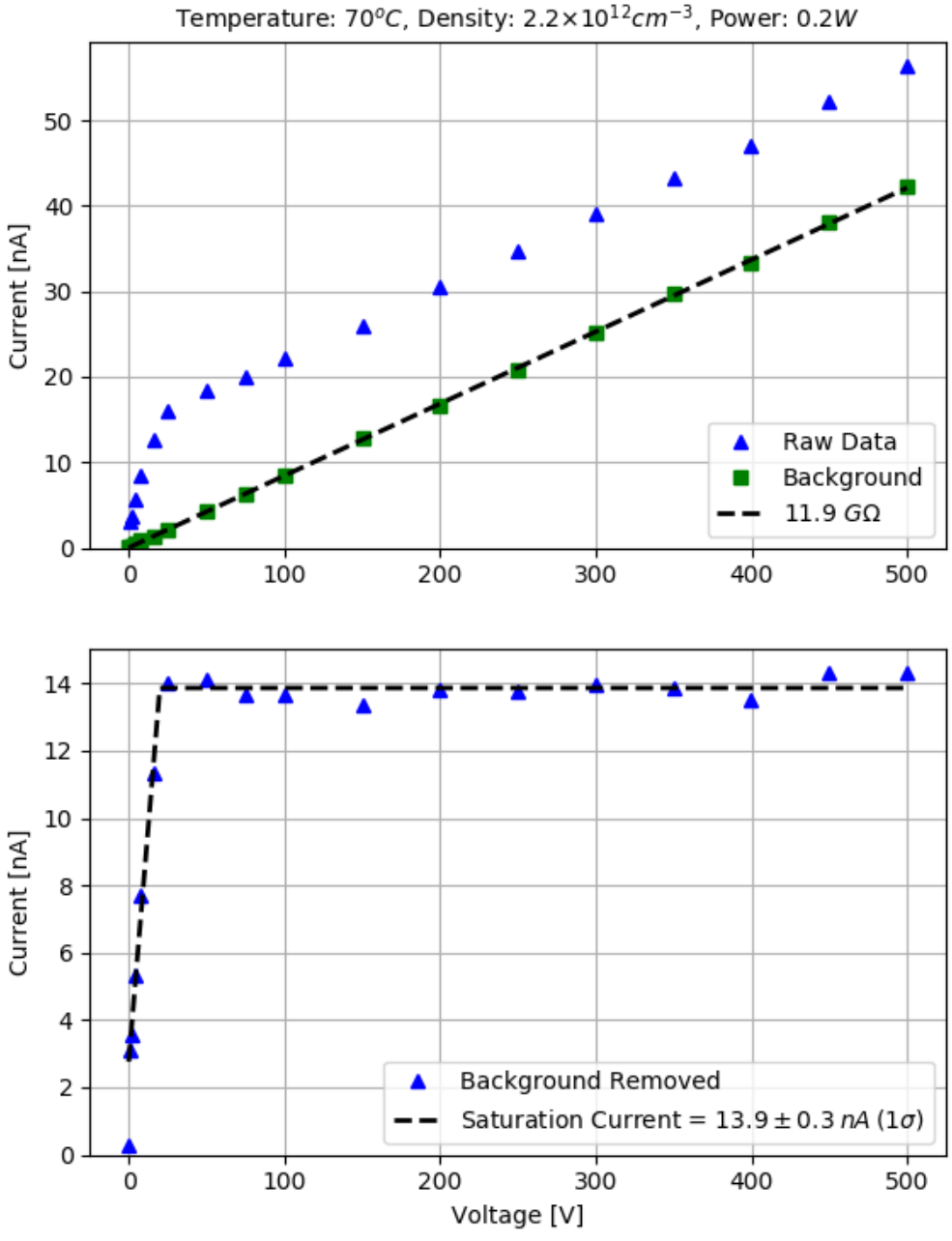

Figure D.92: Electrode measurement H2

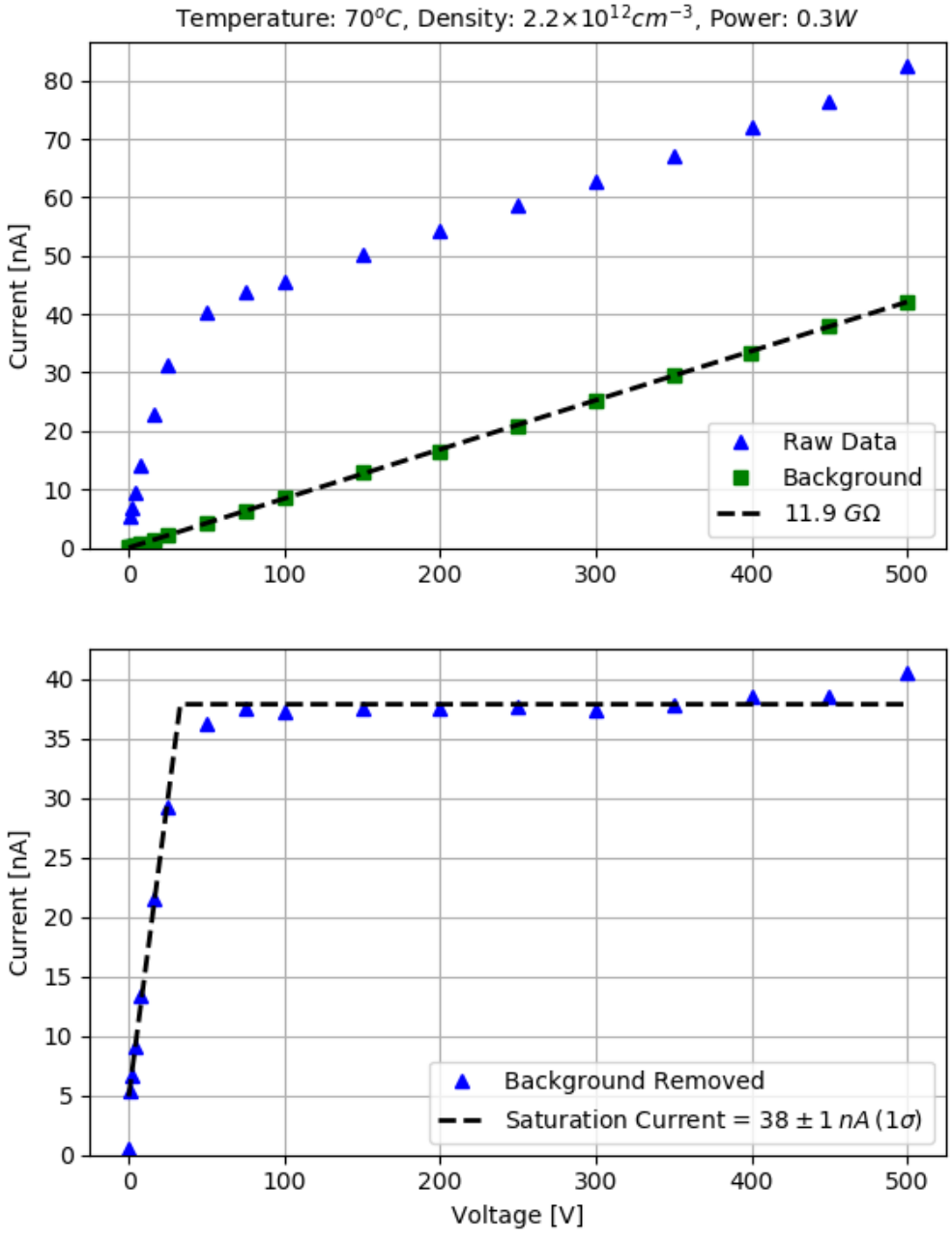

Figure D.93: Electrode measurement H3

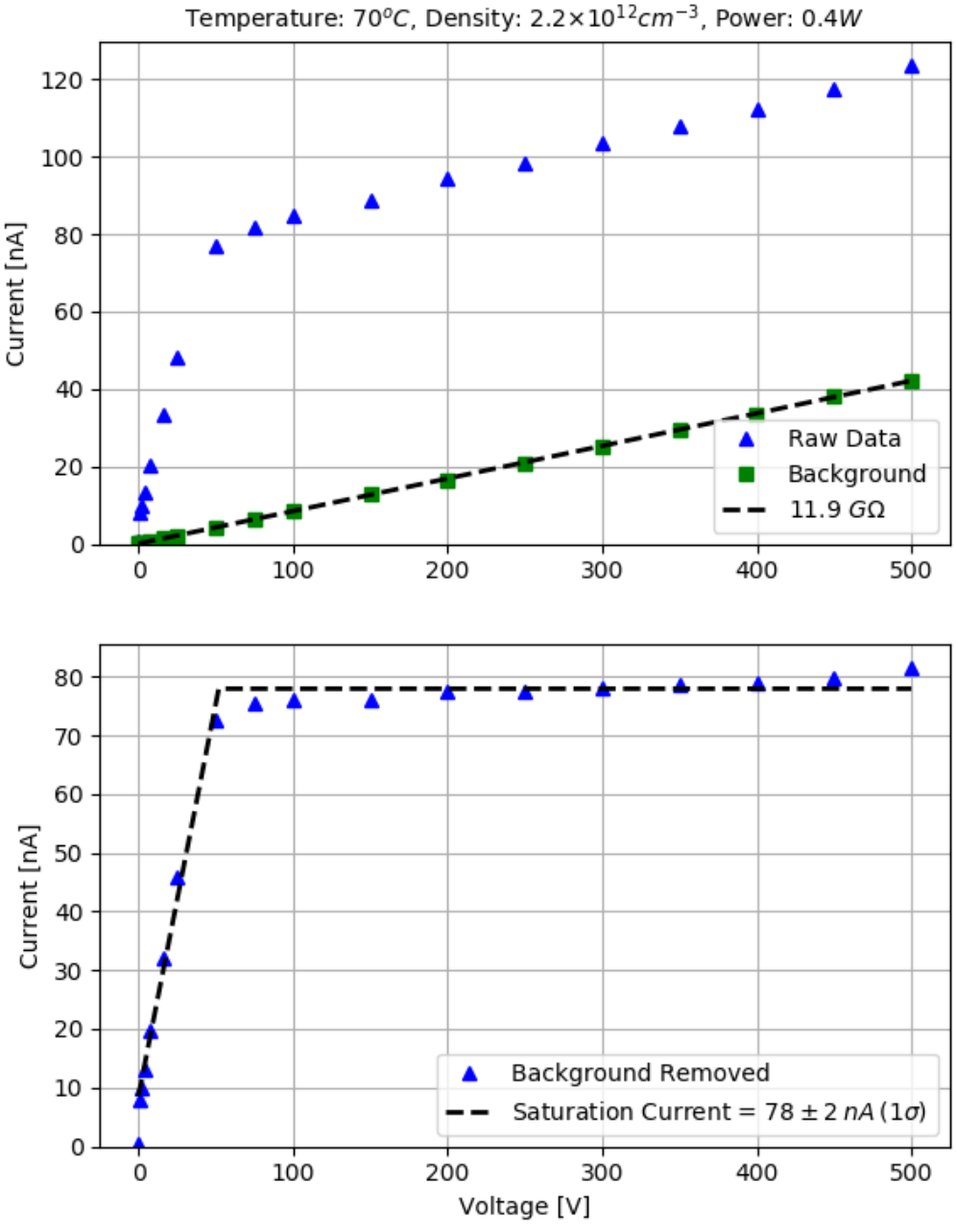

Figure D.94: Electrode measurement H4

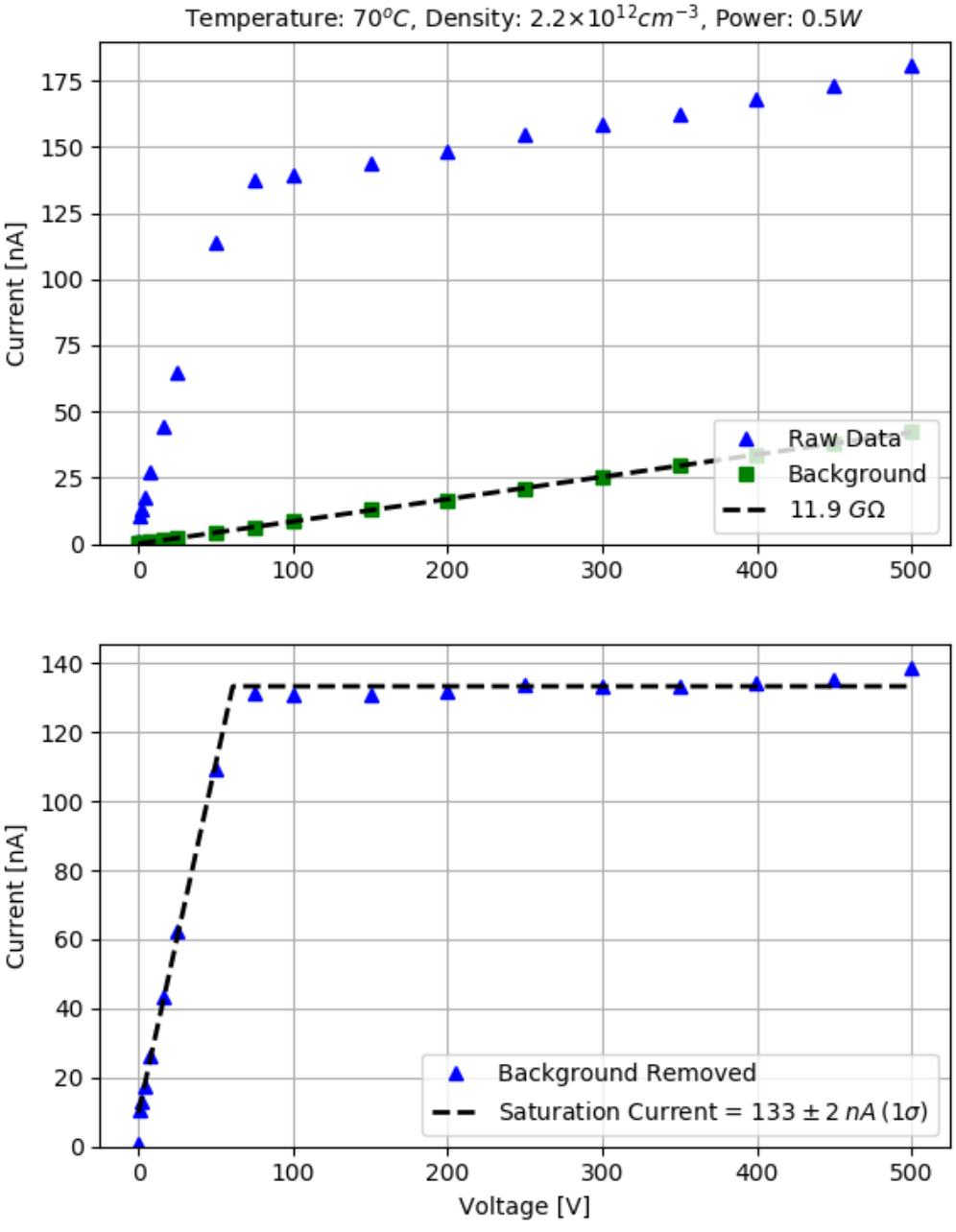

Figure D.95: Electrode measurement H5

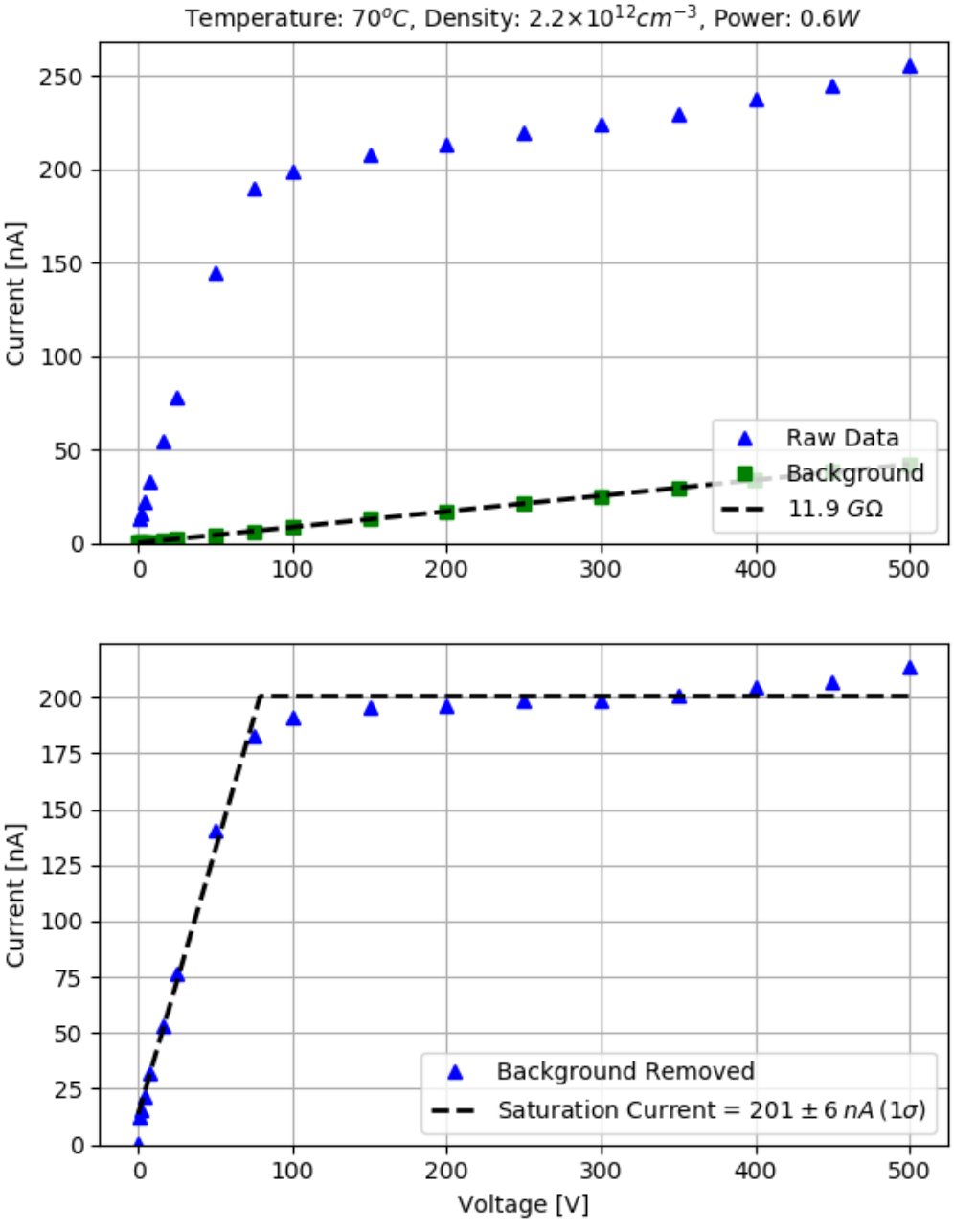

Figure D.96: Electrode measurement H6

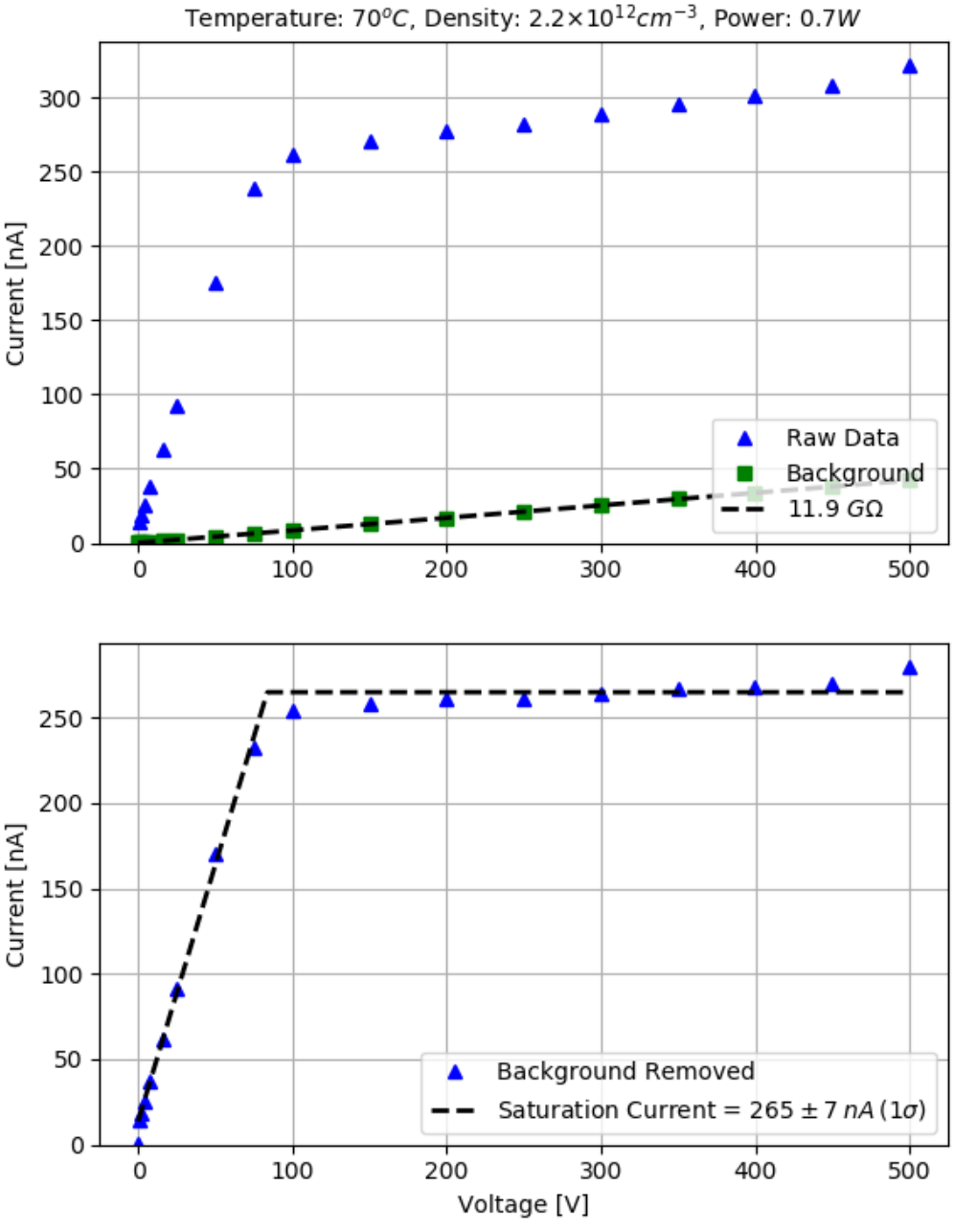

Figure D.97: Electrode measurement H7

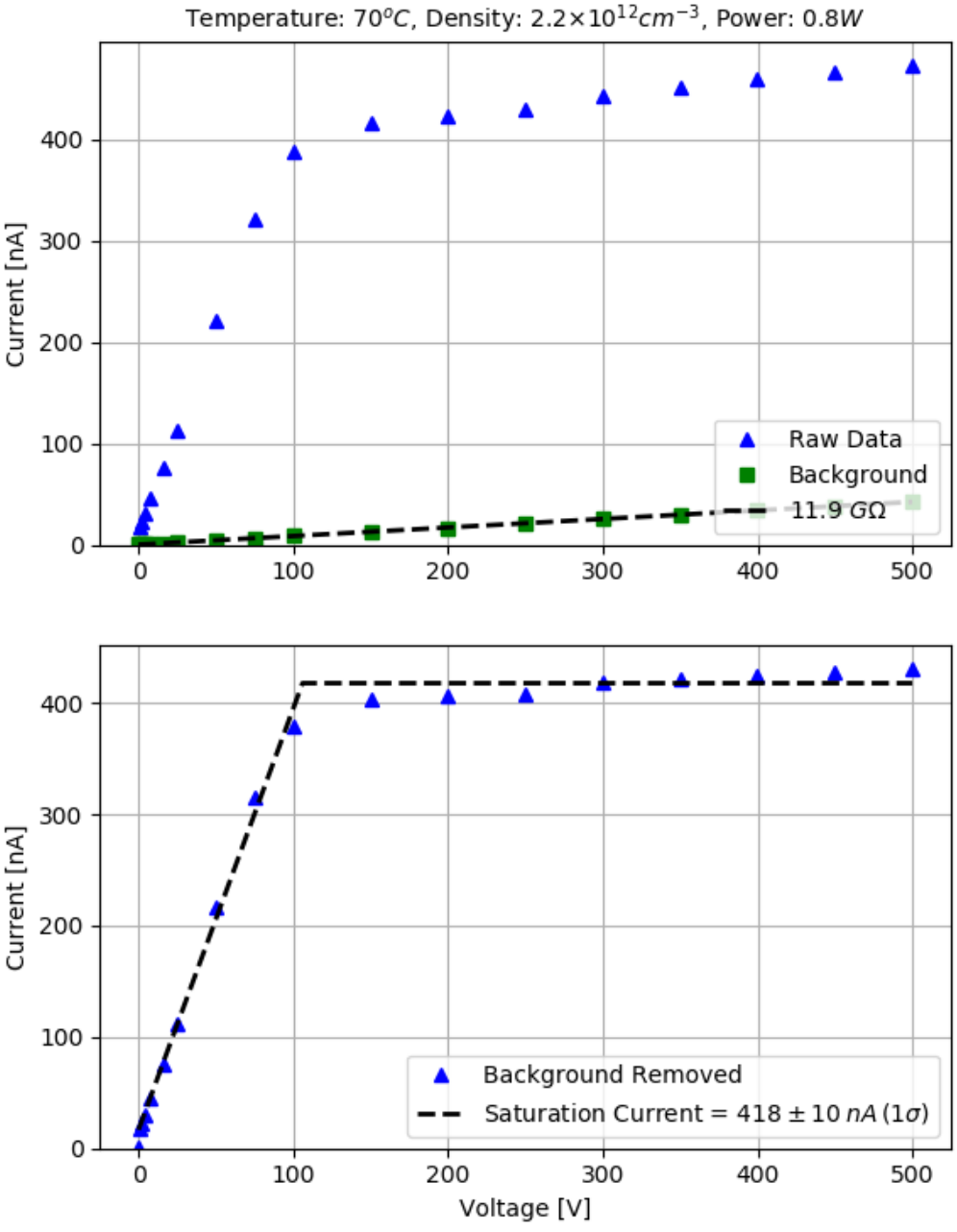

Figure D.98: Electrode measurement H8

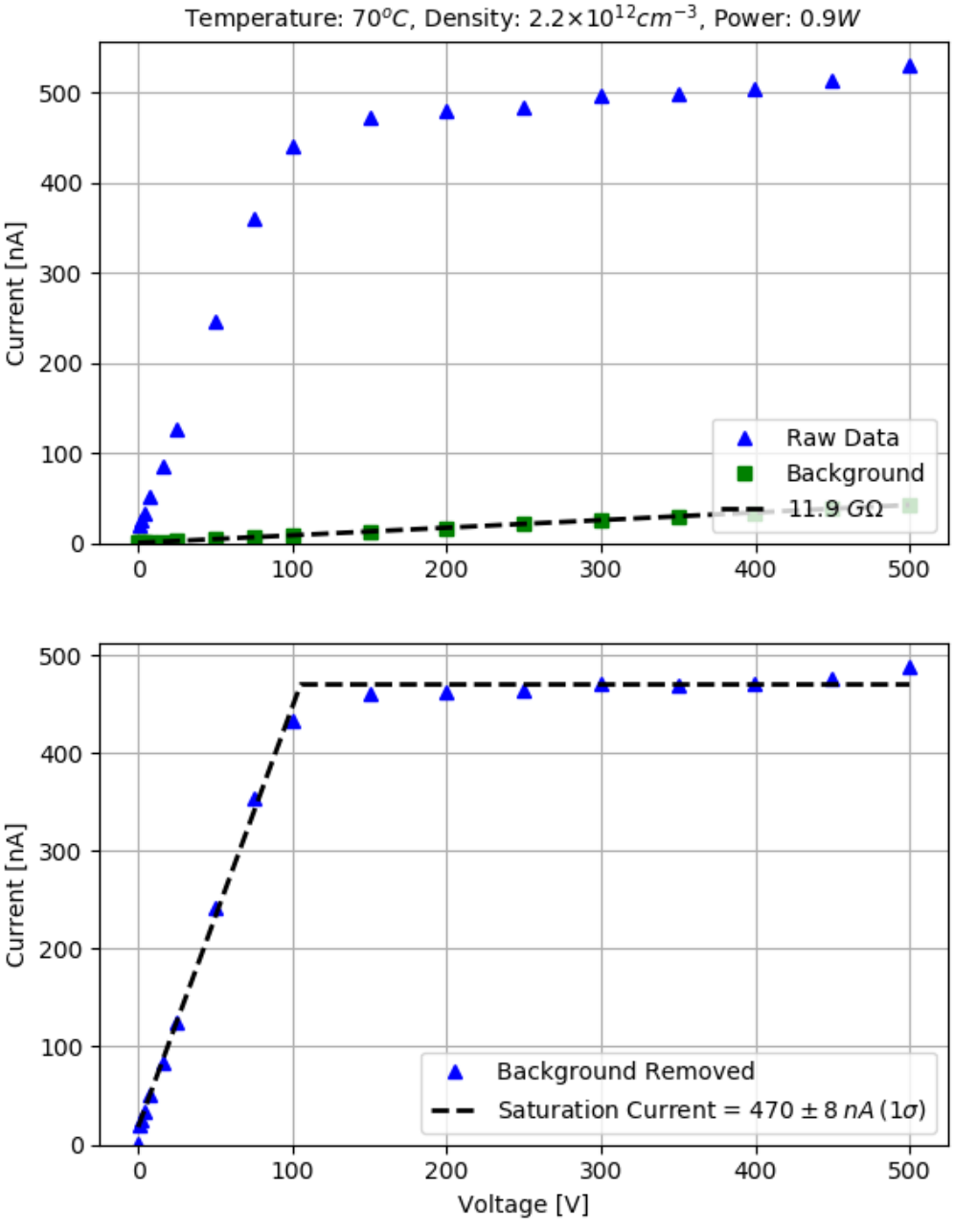

Figure D.99: Electrode measurement H9

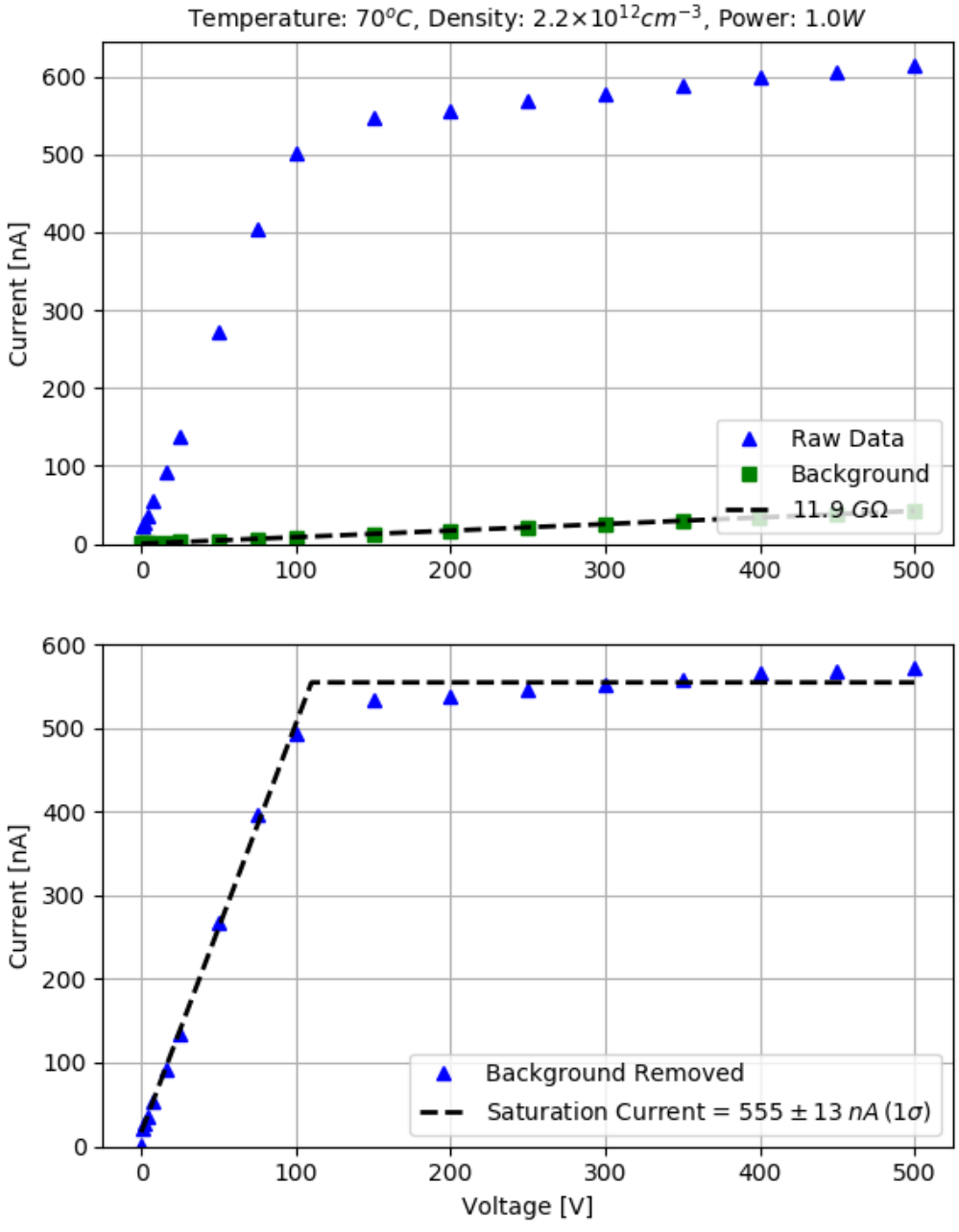

Figure D.100: Electrode measurement H10

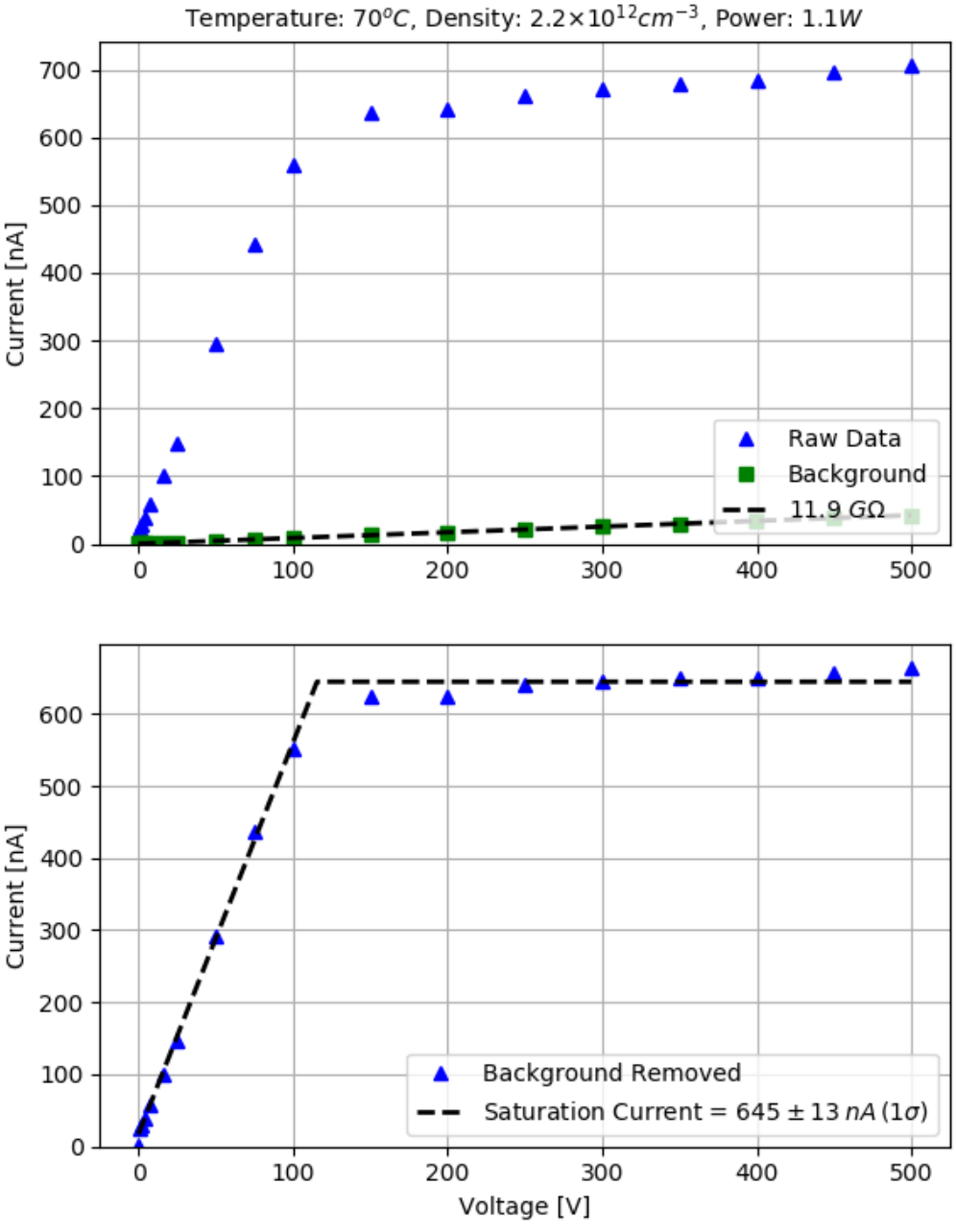

Figure D.101: Electrode measurement H11

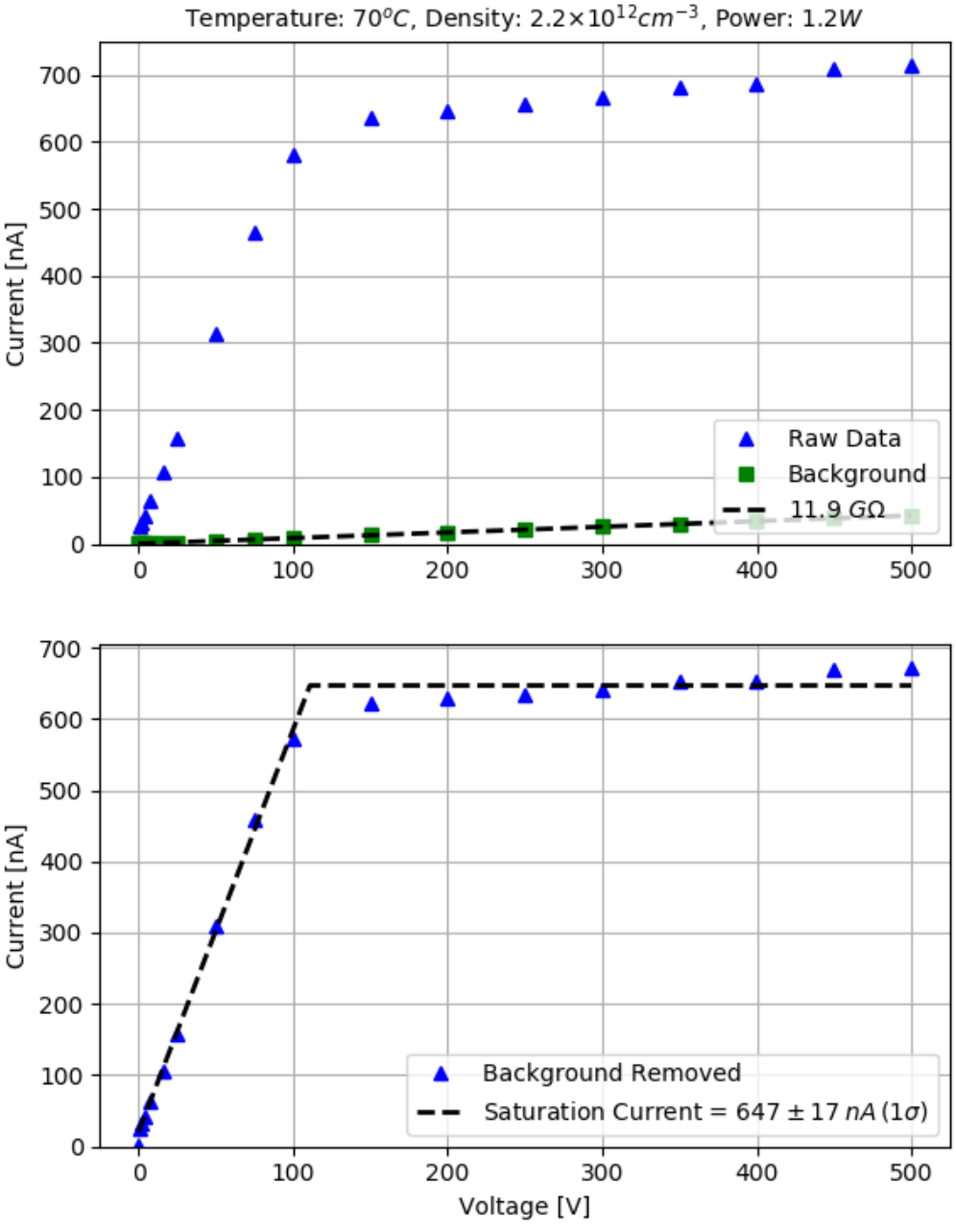

Figure D.102: Electrode measurement H12

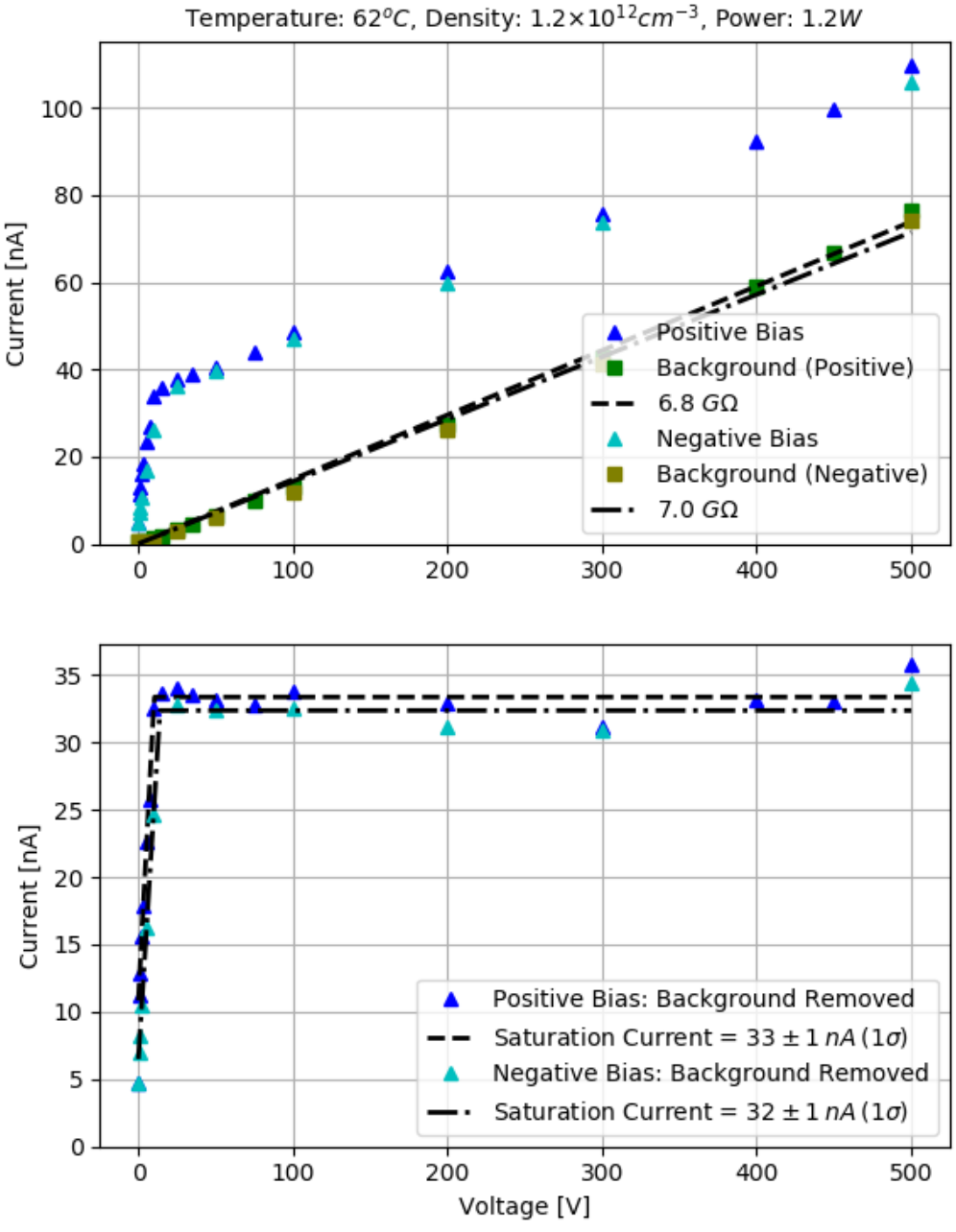

Figure D.103: Electrode measurement I1

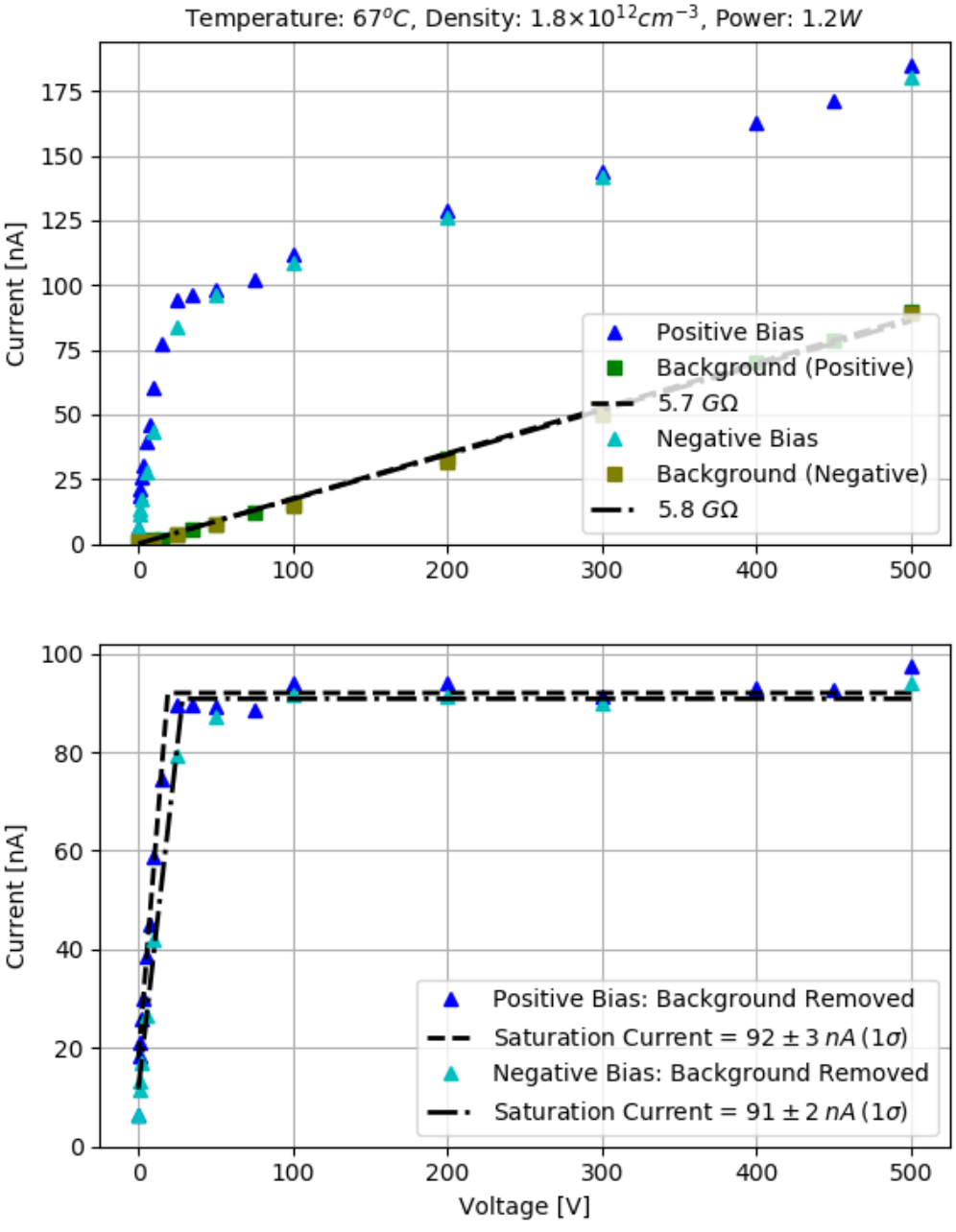

Figure D.104: Electrode measurement J1

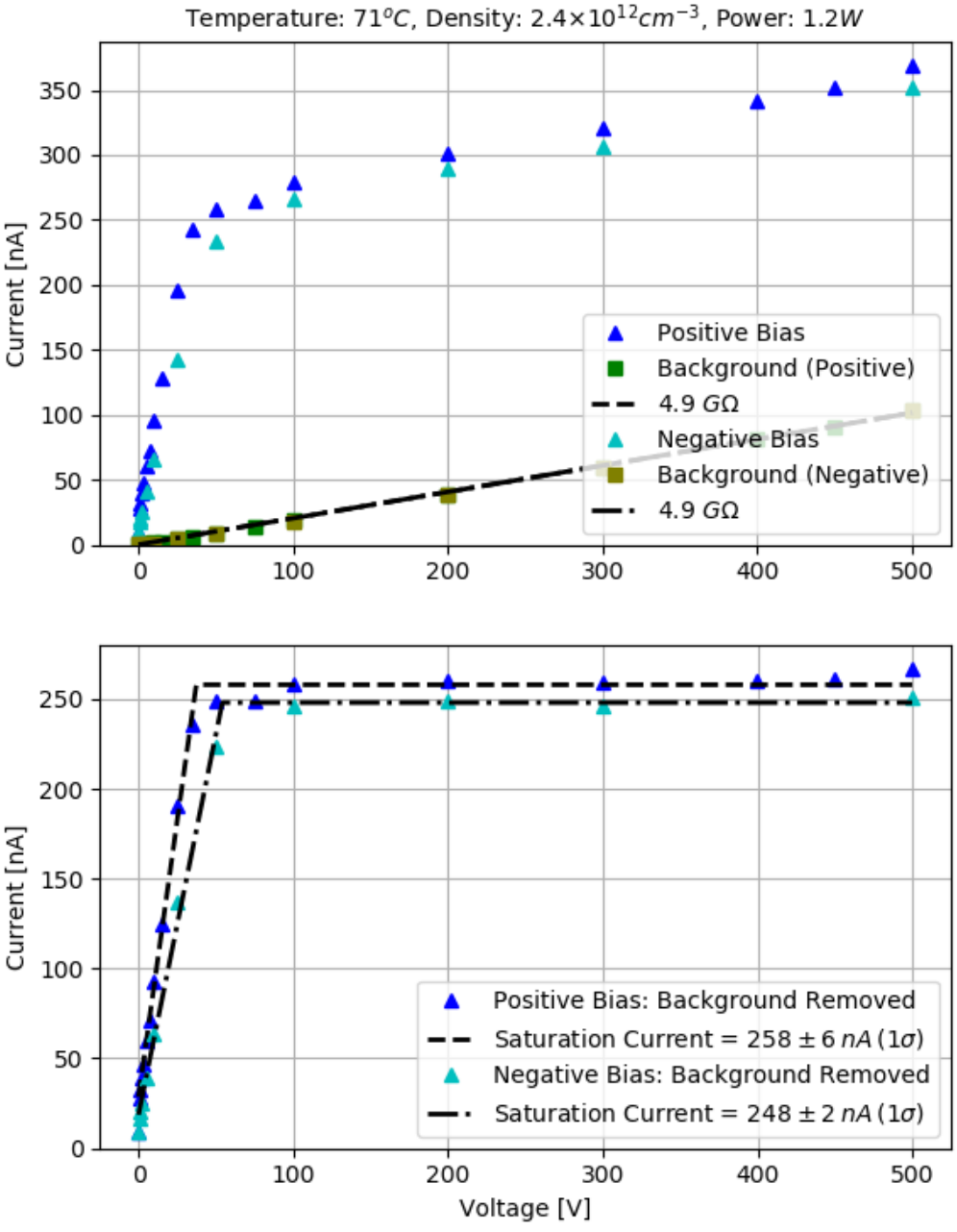

Figure D.105: Electrode measurement K1

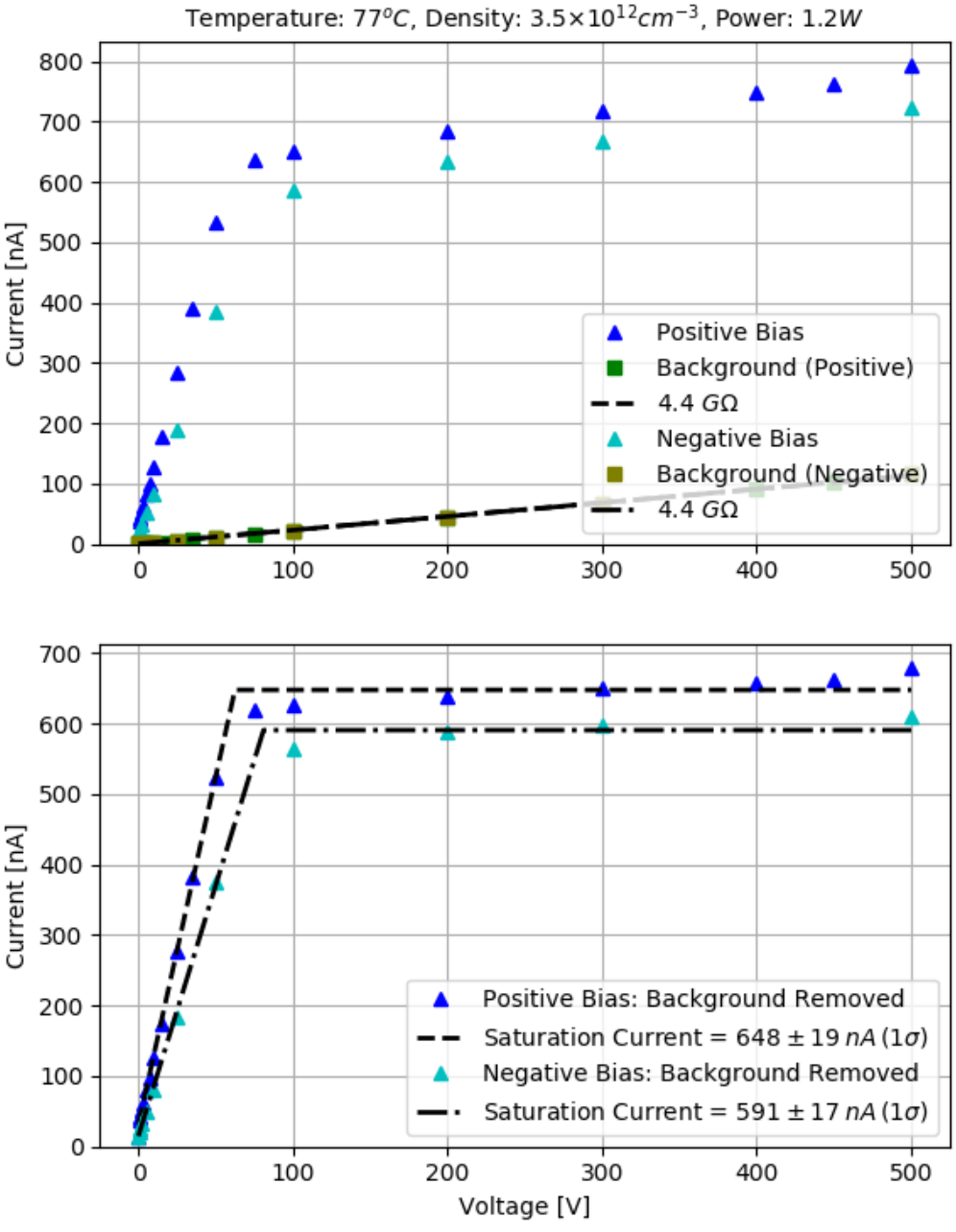

Figure D.106: Electrode measurement L1

D.6 Fluorescence Measurements

Simulataneous fluorescence and ion chamber measurements were made during test series I-L. Fluorescent lines were monitored for three transitions, $7P_{3/2} \rightarrow 6S_{1/2}$ at 455 nm, $7P_{1/2} \rightarrow 6S_{1/2}$ at 459 nm, and $7D_{5/2} \rightarrow 6P_{3/2}$ at 697 nm, as was previously discussed in Sec. 5.2.

Fluorescence measurement of the $7P_{1/2}$ state are shown in Fig. D.107, measurement of the $7P_{3/2}$ state are shown in Fig. D.107, and measurement of the $7D_{5/2}$ state are shown in Fig. D.109. The measurements were made with varying cesium density and at two different pump laser powers, 0.4 and 1.2 W.

A green filter was used when monitoring fluorescence from the $7P$ states, which removed wavelengths longer than 500 nm and significantly reduced scattered light. To determine the relative fluorescent energy when varying alkali density, the measurements were fit with a Lorentzian funtion, which is shown as a black dashed line in the figures. The Lorentzian function included a constant off-set, which was assumed to be due to scattered light in the spectrometer, and not fluorescence at the tracked transition. The integrated Lorentzian function determined the relative fluorescent power of the transition, and error in this measurement was determined by the root-mean-square (RMS) of the data to the Lorentzian fit.

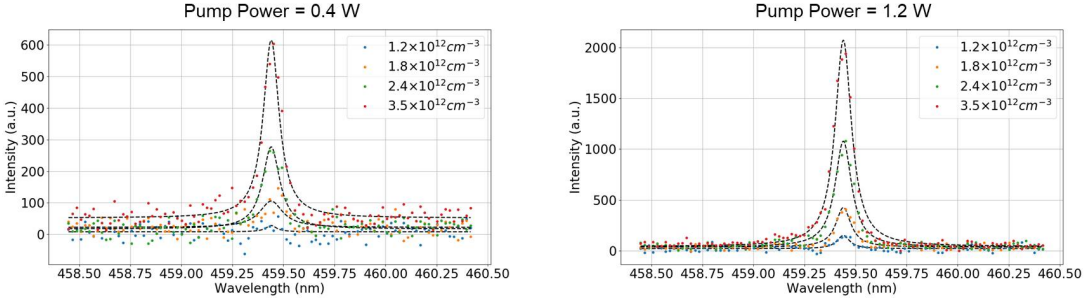

Figure D.107: Fluorescence measurements of the $7P_{1/2}$ state varying cesium density and at two different pump laser powers. The black dashed lines are the Lorentzian fits used to calculate the total integrated fluorescent power of each transition.

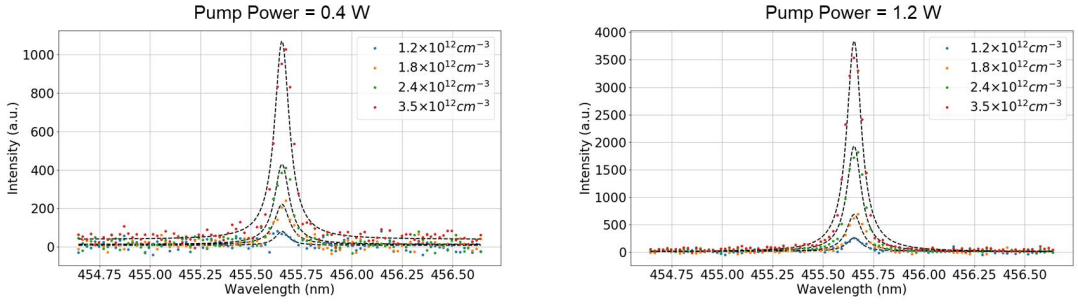

Figure D.108: Fluorescence measurements of the $7P_{3/2}$ state varying cesium density and at two different pump laser powers. The black dashed lines are the Lorentzian fits used to calculate the total integrated fluorescent power of each transition.

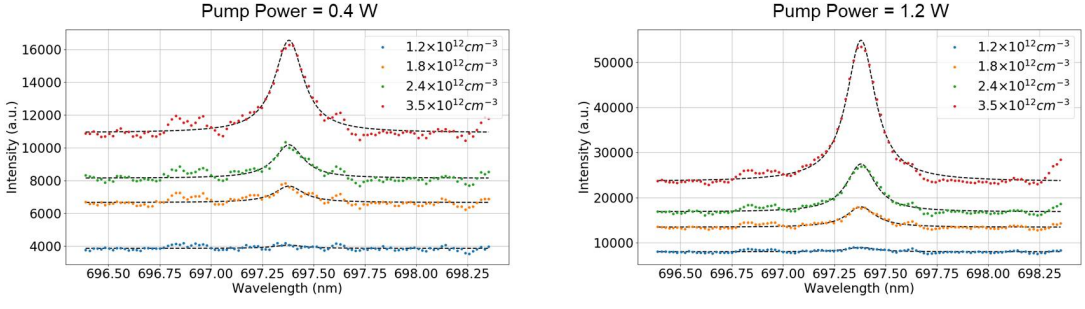

Figure D.109: Fluorescence measurements of the $7D_{5/2}$ state varying cesium density and at two different pump laser powers. The black dashed lines are the Lorentzian fits used to calculate the total integrated fluorescent power of each transition.

Appendix E

Ion Chamber Experimental / Simulation Comparisons

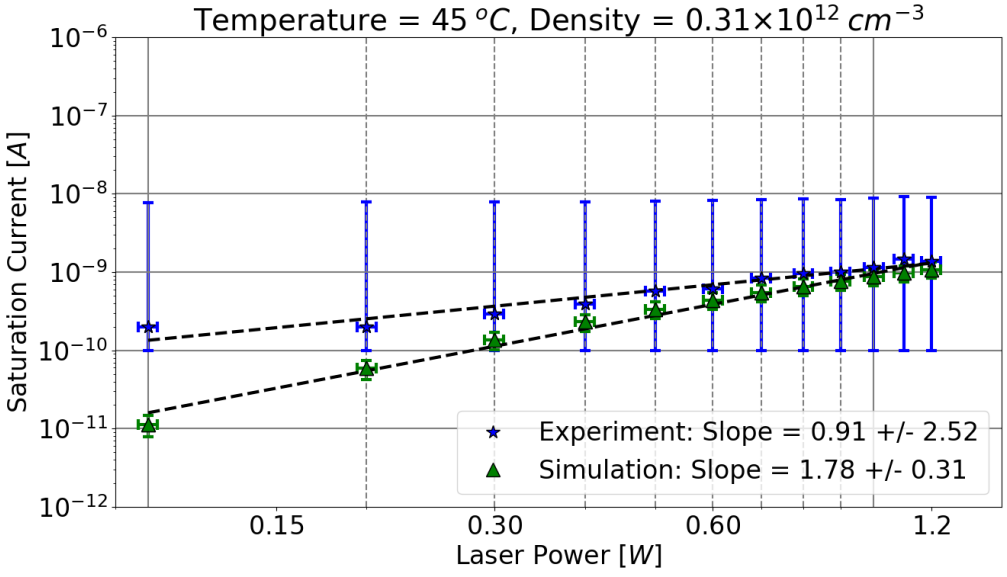

Figure E.1: Comparison of measured and simulated ion chamber saturation current with varying pump power at constant cesium density of 0.31 $\times$ 10^{12} cm^{-3} in a 6:1 He:CH_4 buffer gas mixture

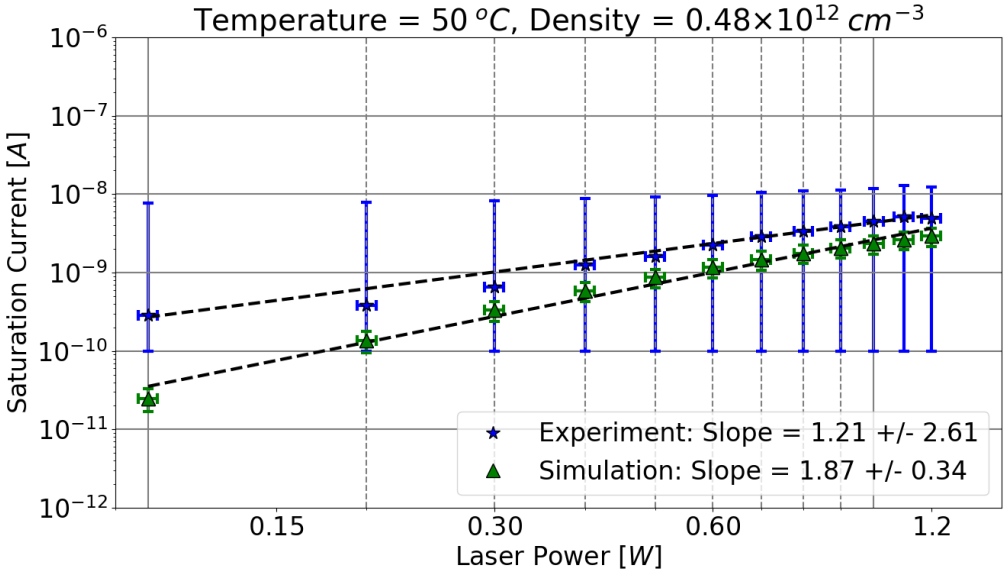

Figure E.2: Comparison of measured and simulated ion chamber saturation current with varying pump power at constant cesium density of 0.48 $\times$ 10^{12} cm^{-3} in a 6:1 He:CH_4 buffer gas mixture

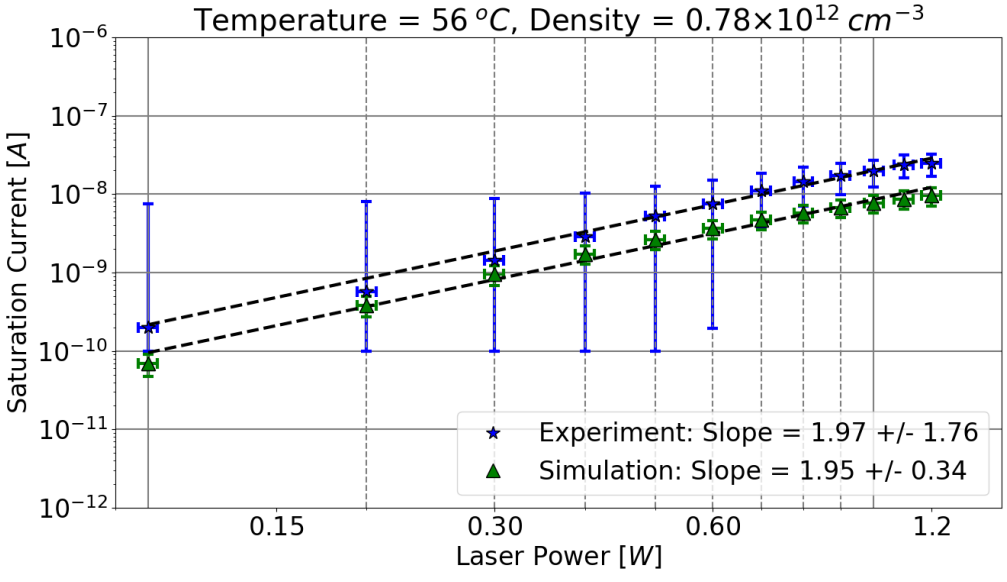

Figure E.3: Comparison of measured and simulated ion chamber saturation current with varying pump power at constant cesium density of 0.78 $\times$ 10^{12} cm^{-3} in a 6:1 He:CH_4 buffer gas mixture

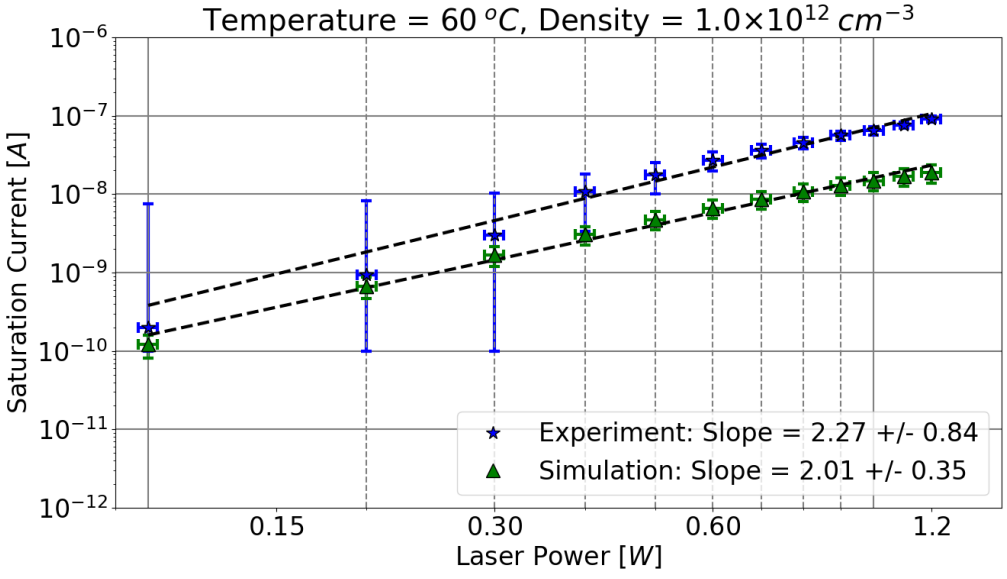

Figure E.4: Comparison of measured and simulated ion chamber saturation current with varying pump power at constant cesium density of 1.0 × 10^{12} cm^{-3} in a 6:1 He:CH_4 buffer gas mixture

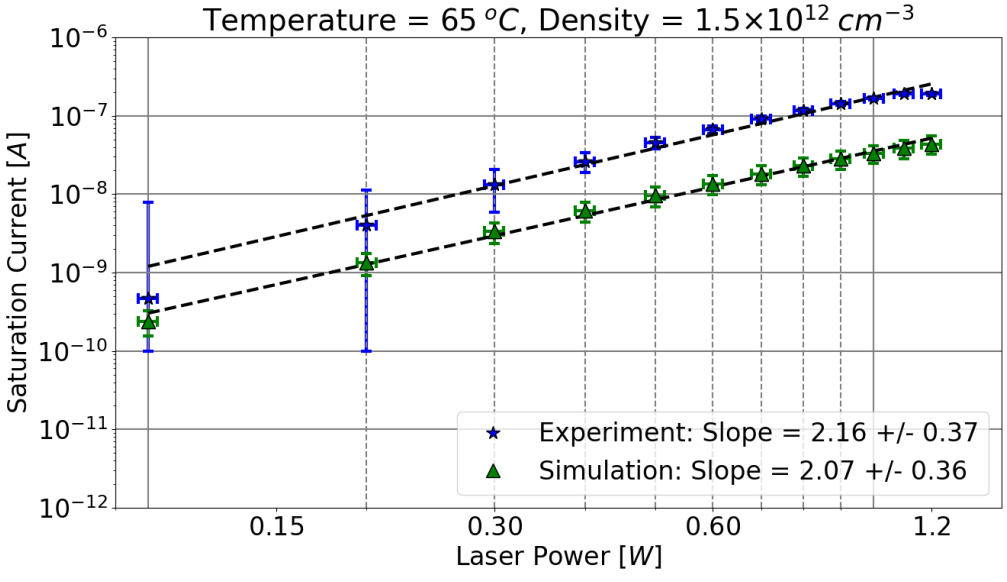

Figure E.5: Comparison of measured and simulated ion chamber saturation current with varying pump power at constant cesium density of 1.5 × 10^{12} cm^{-3} in a 6:1 He:CH_4 buffer gas mixture

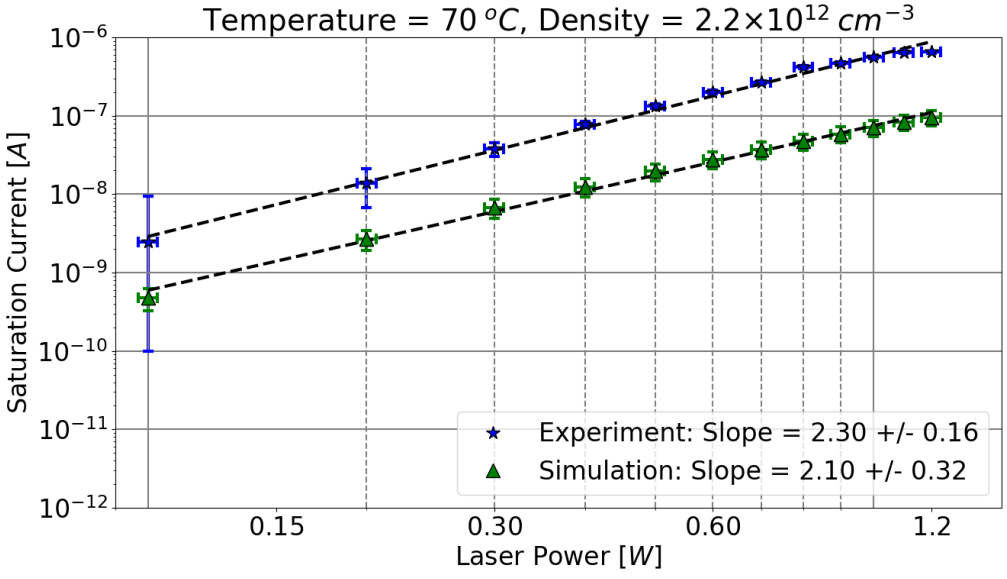

Figure E.6: Comparison of measured and simulated ion chamber saturation current with varying pump power at constant cesium density of 2.2 × 10^{12} cm^{-3} in a 6:1 He:CH_4 buffer gas mixture

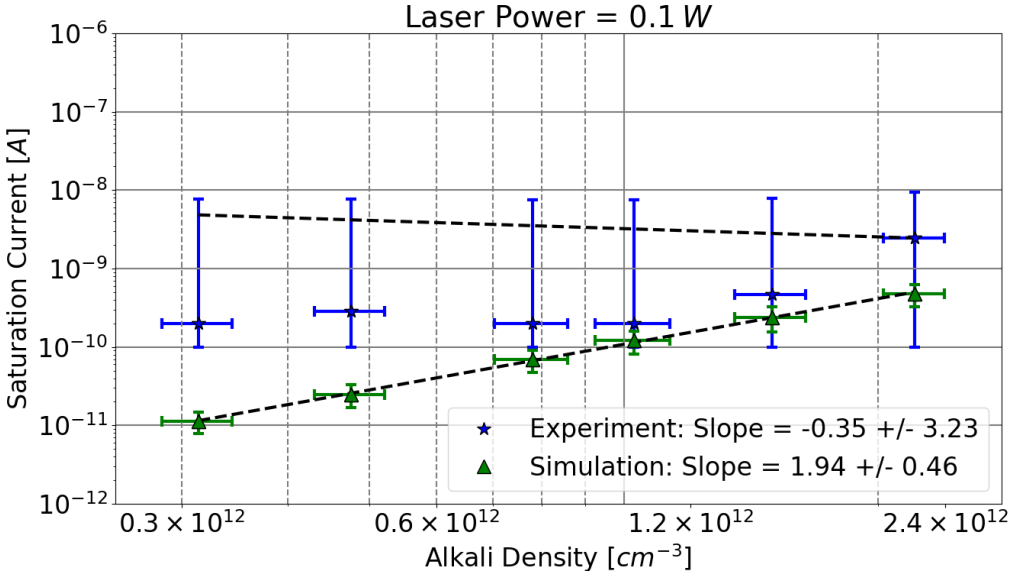

Figure E.7: Comparison of measured and simulated ion chamber saturation current with varying cesium density at constant pump power of 0.1 W in a 6:1 He:CH_4 buffer gas mixture

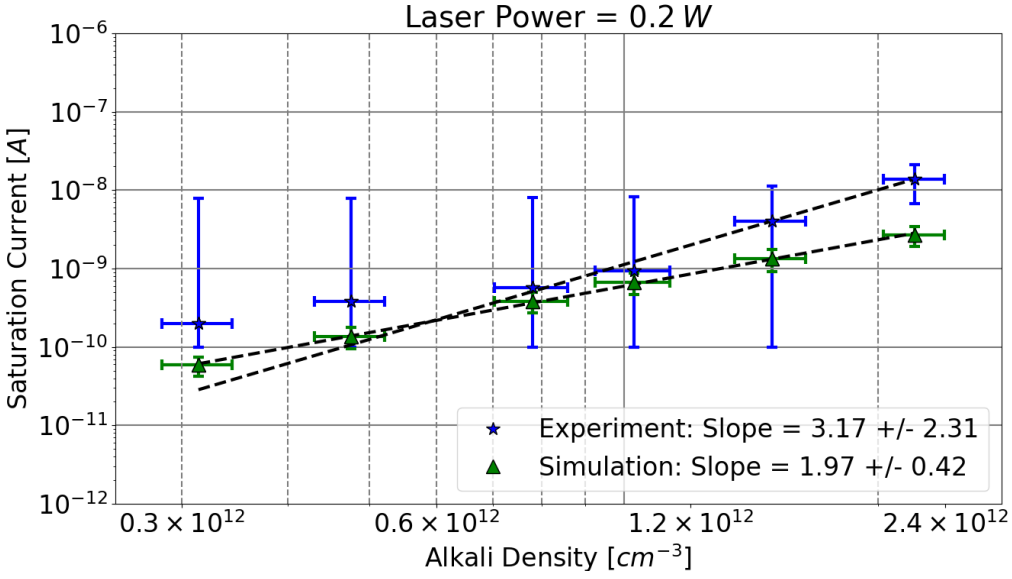

Figure E.8: Comparison of measured and simulated ion chamber saturation current with varying cesium density at constant pump power of 0.2 W in a 6:1 He:CH_4 buffer gas mixture

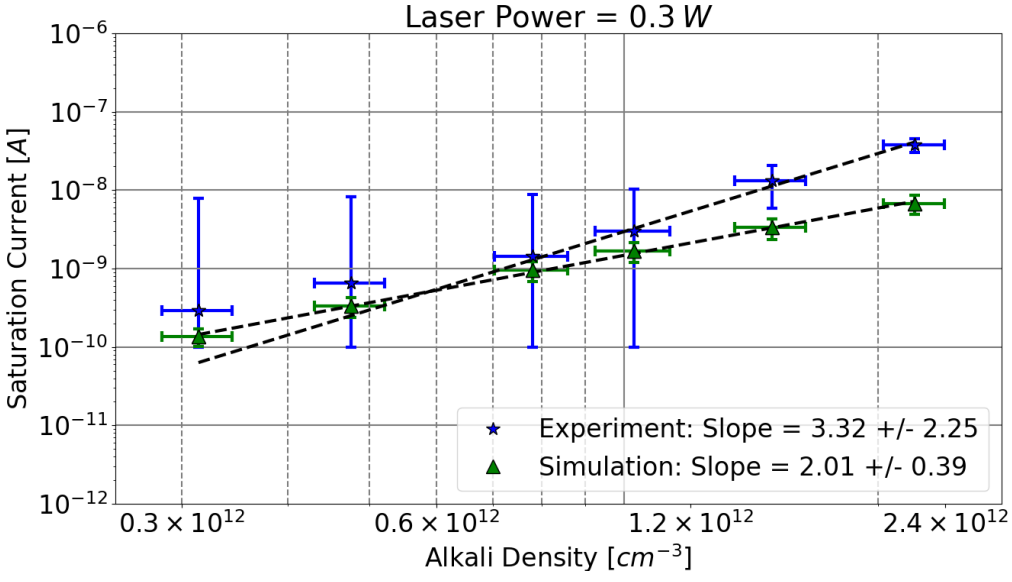

Figure E.9: Comparison of measured and simulated ion chamber saturation current with varying cesium density at constant pump power of 0.3 W in a 6:1 He:CH_4 buffer gas mixture

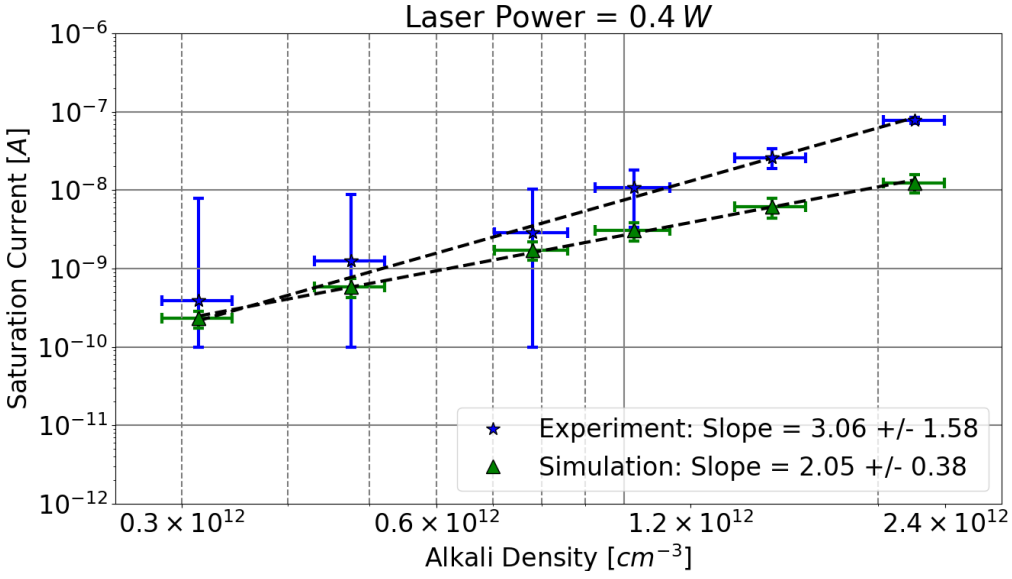

Figure E.10: Comparison of measured and simulated ion chamber saturation current with varying cesium density at constant pump power of 0.4 W in a 6:1 He:CH_4 buffer gas mixture

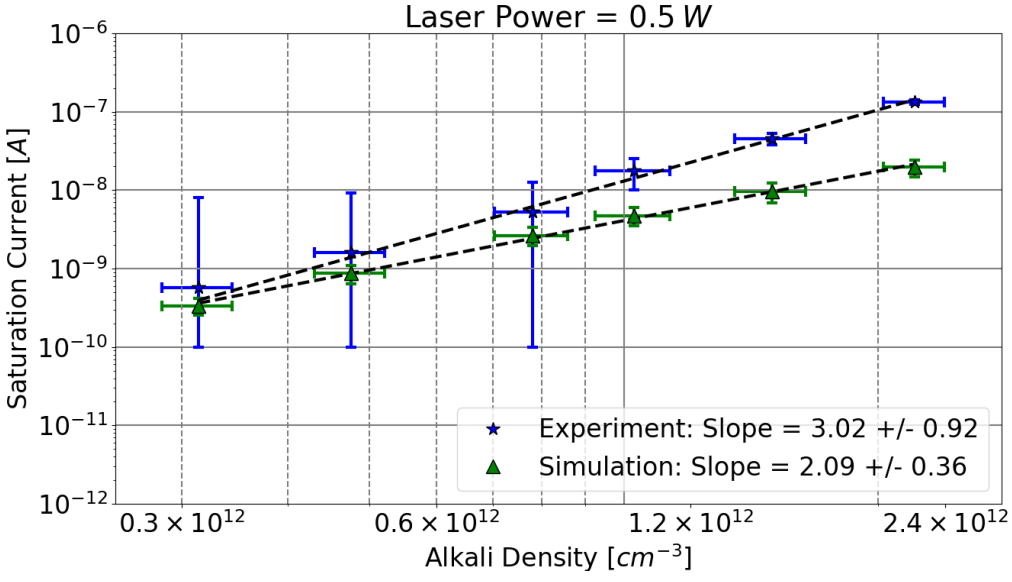

Figure E.11: Comparison of measured and simulated ion chamber saturation current with varying cesium density at constant pump power of 0.5 W in a 6:1 He:CH_4 buffer gas mixture

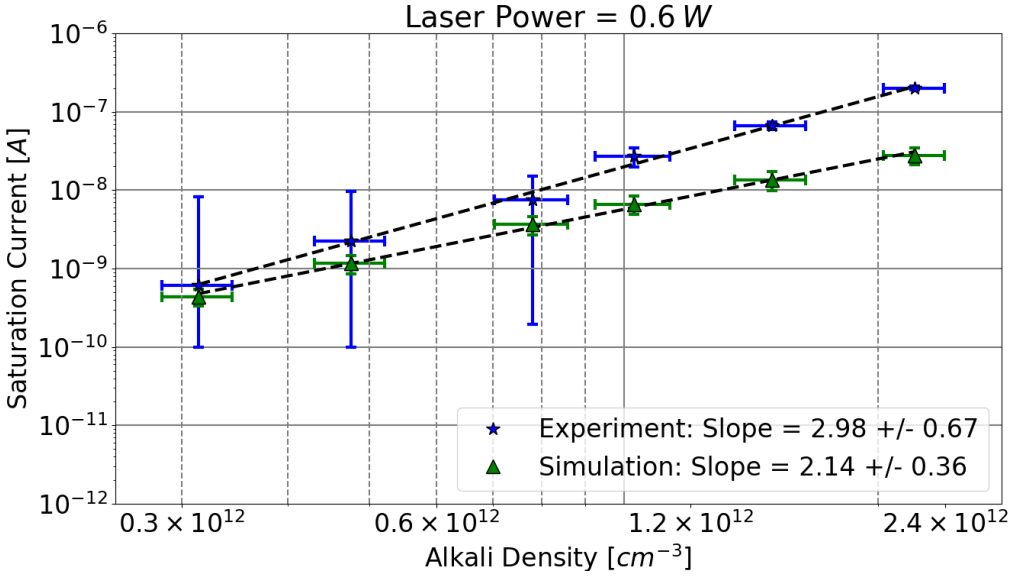

Figure E.12: Comparison of measured and simulated ion chamber saturation current with varying cesium density at constant pump power of 0.6 W in a 6:1 He:CH_4 buffer gas mixture

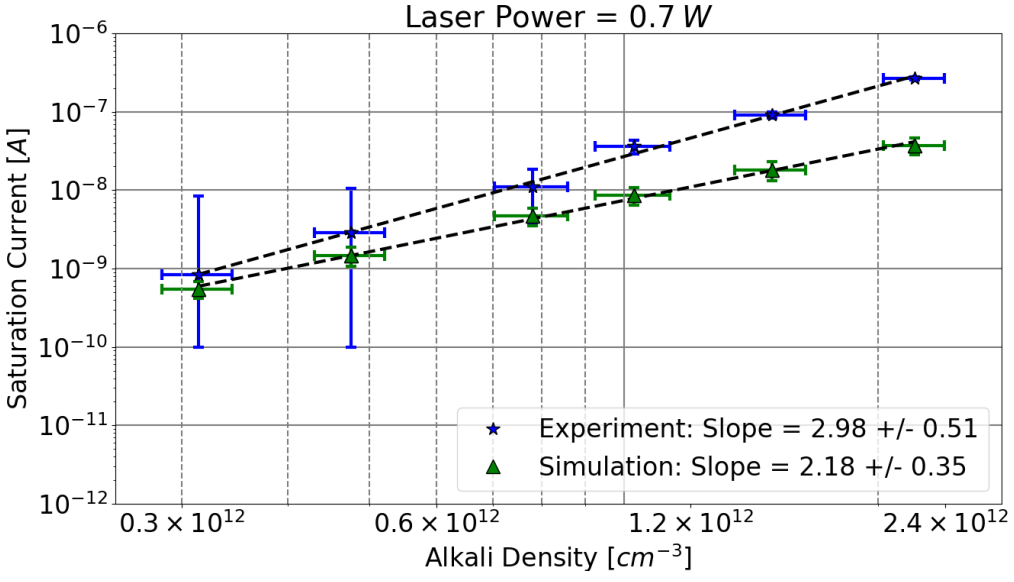

Figure E.13: Comparison of measured and simulated ion chamber saturation current with varying cesium density at constant pump power of 0.7 W in a 6:1 He:CH_4 buffer gas mixture

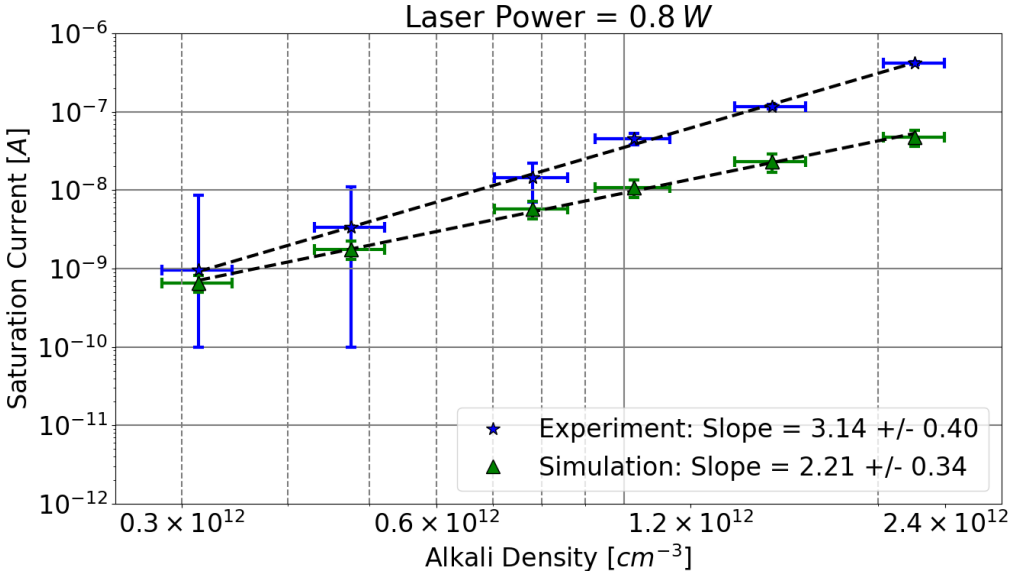

Figure E.14: Comparison of measured and simulated ion chamber saturation current with varying cesium density at constant pump power of 0.8 W in a 6:1 He:CH_4 buffer gas mixture

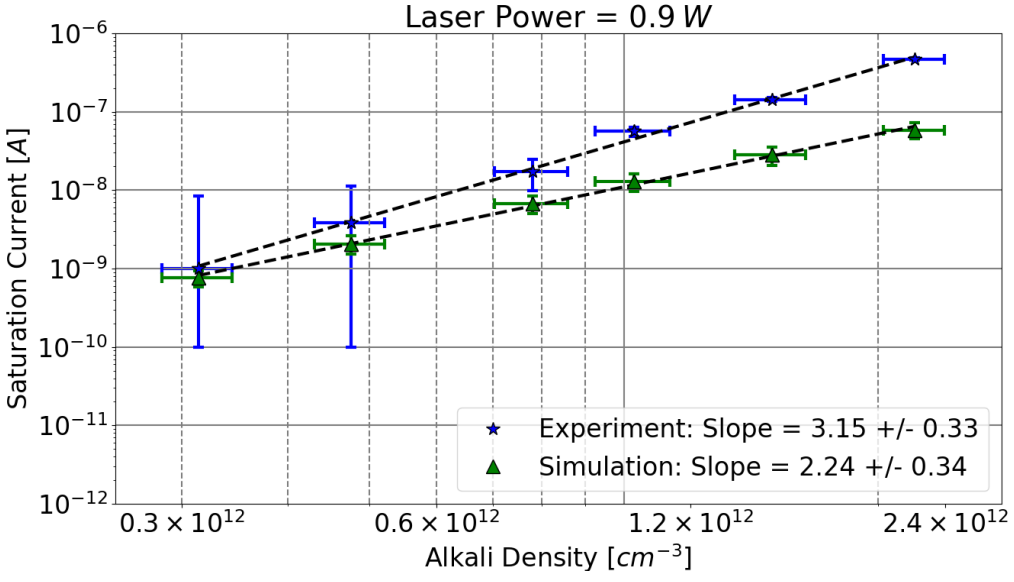

Figure E.15: Comparison of measured and simulated ion chamber saturation current with varying cesium density at constant pump power of 0.9 W in a 6:1 He:CH_4 buffer gas mixture

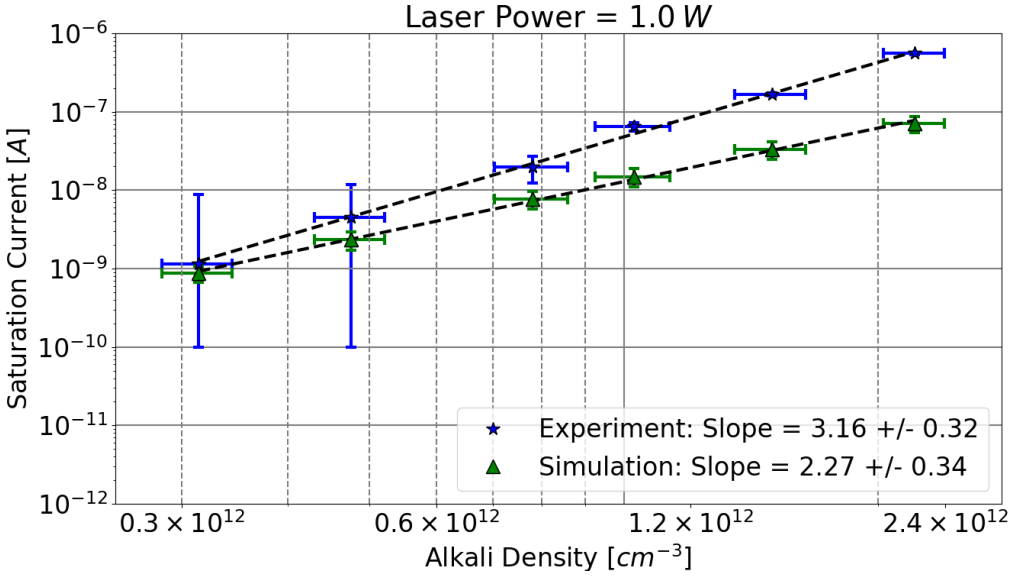

Figure E.16: Comparison of measured and simulated ion chamber saturation current with varying cesium density at constant pump power of 1.0 W in a 6:1 He:CH_4 buffer gas mixture

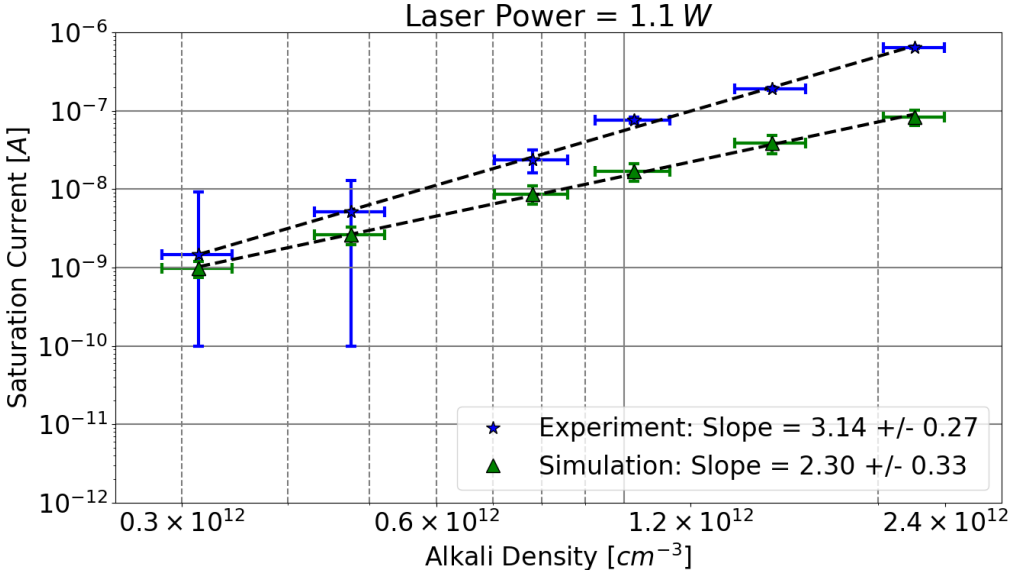

Figure E.17: Comparison of measured and simulated ion chamber saturation current with varying cesium density at constant pump power of 1.1 W in a 6:1 He:CH_4 buffer gas mixture

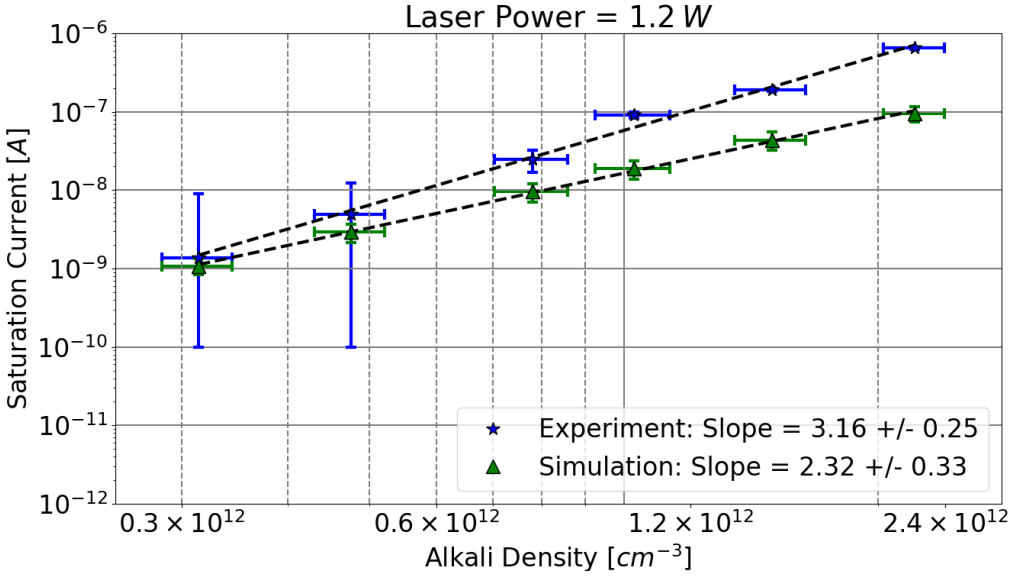

Figure E.18: Comparison of measured and simulated ion chamber saturation current with varying cesium density at constant pump power of 1.2 W in a 6:1 He:CH_4 buffer gas mixture

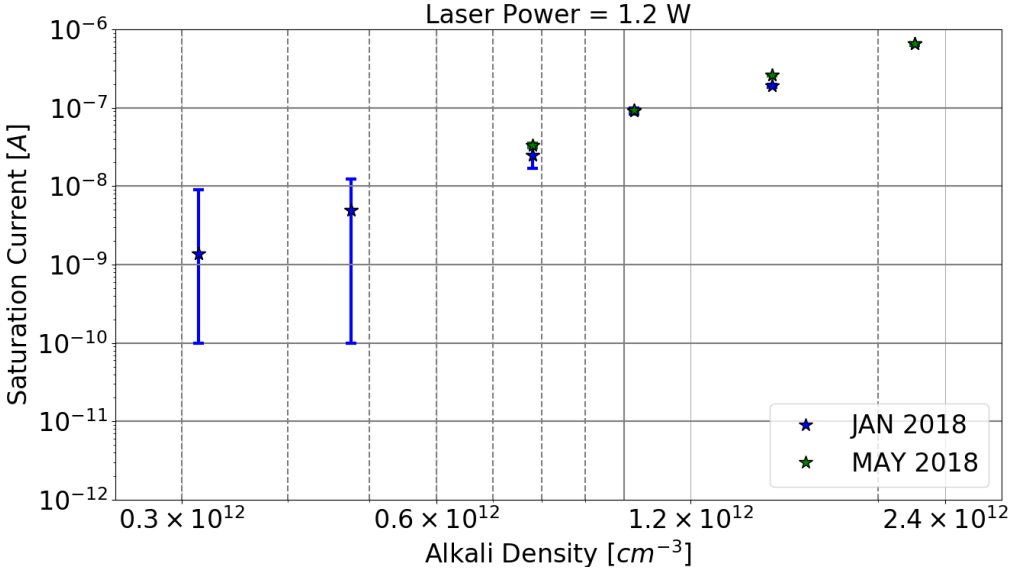

Figure E.19: Comparison of ion chamber test results recorded months apart with varying cesium density at constant pump power of 1.2 W in a 6:1 He:CH_4 buffer gas mixture

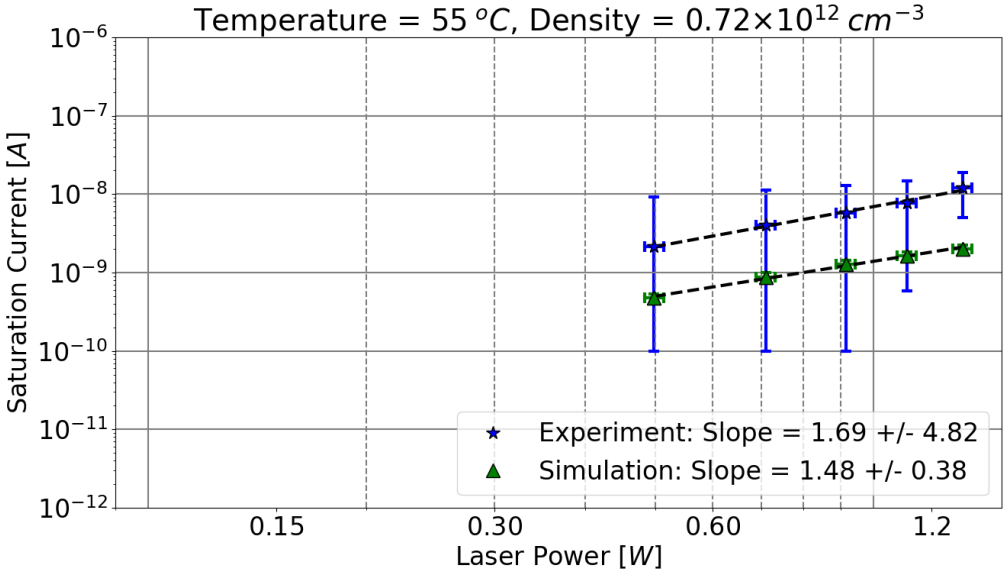

Figure E.20: Comparison of measured and simulated ion chamber saturation current with varying pump power at constant cesium density of 0.72 $\times$ 10^{12} cm^{-3} in helium buffer gas

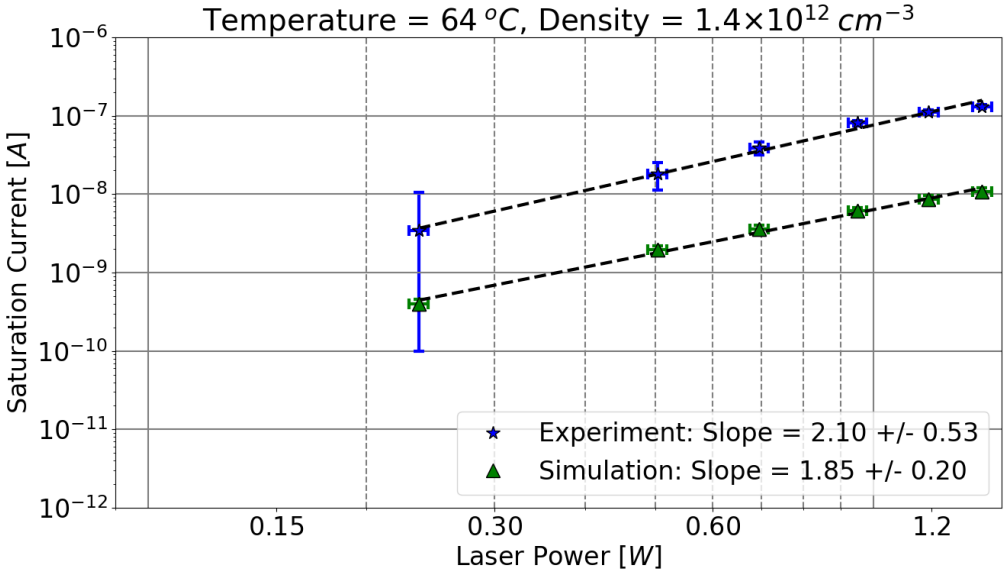

Figure E.21: Comparison of measured and simulated ion chamber saturation current with varying pump power at constant cesium density of 1.4 $\times$ 10^{12} cm^{-3} in helium buffer gas

References

[1] W. F. Krupke, Diode-pumped alkali laser, US Patent 6,643,311 (Nov. 4 2003).

[2] G. A. Pitz, D. M. Stalnaker, E. M. Guild, B. Q. Oliker, P. J. Moran, S. W. Townsend, D. A. Hostutler, Advancements in flowing diode pumped alkali lasers, in: High Energy/Average Power Lasers and Intense Beam Applications IX, Vol. 9729, International Society for Optics and Photonics, 2016.

[3] A. E. Siegman, Unstable optical resonators for laser applications, Proceedings of the IEEE 53 (3) (1965) 277–287.

[4] G. A. Pitz, C. D. Fox, G. P. Perram, Transfer between the cesium $6^2P_{1/2}$ and $6^2P_{3/2}$ levels induced by collisions with H_2, HD, D_2, CH_4, C_2H_6, CF_4, AND C_2F_6, Physical Review A 84 (3) (2011) 032708.

[5] N. D. Zameroski, W. Rudolph, G. D. Hager, D. A. Hostutler, A study of collisional quenching and radiation-trapping kinetics for Rb (5p) in the presence of methane and ethane using time-resolved fluorescence, Journal of Physics B: Atomic, Molecular and Optical Physics 42 (24) (2009) 245401.

[6] T. Koenning, D. McCormick, D. Irwin, D. Stapleton, T. Guiney, S. Patterson, DPAL pump system exceeding 3kW at 766nm and 30 GHz bandwidth, in: High-Power Diode Laser Technology and Applications XIV, Vol. 9733, International Society for Optics and Photonics, 2016, p. 97330E.

[7] M. K. Shaffer, T. Lilly, B. Zhdanov, R. Knize, In situ non-perturbative temperature measurement in a cs alkali laser, Optics Letters 40 (1) (2015) 119–122.

[8] A. Fletcher, D. Turner, S. Fairchild, C. Rice, G. Pitz, Tof-sims characterization of robust window material for use in diode pumped alkali lasers, physica status solidi (a) 215 (2) (2018) 1700728.

[9] B. Zhdanov, M. Rotondaro, M. Shaffer, R. Knize, Potassium diode pumped alkali laser demonstration using a closed cycle flowing system, Optics Communications 354 (2015) 256–258.

[10] E. Yacoby, I. Auslender, B. D. Barmashnko, S. Rosewaks, Continuous wave diode pumped flowing-gas cesium laser, in: XXII International Symposium on High Power Laser Systems and Applications, Vol. 11042, International Society for Optics and Photonics, 2019, p. 110420D.

[11] V. N. Azyazov, A. P. Torbin, A. M. Mebel, S. M. Bresler, M. C. Heaven, Product channels of the reactions of Rb (6p) with H_2, CH_4 and C_2H_6, Journal of Quantitative Spectroscopy and Radiative Transfer 196 (2017) 46–52.

[12] A. J. Wallerstein, Kinetics of higher lying potassium states after excitation of the D_2 transition in the presence of helium, Ph.D. thesis, Wright-Patterson Air Force Base, Ohio (2018).

[13] B. V. Zhdanov, M. D. Rotondaro, M. K. Shaffer, R. J. Knize, Examination of potassium diode pumped alkali laser using He, Ar, CH_4 and C_2H_6 as buffer gas, Optics express 25 (24) (2017) 30793–30798.

[14] J. Thomson, XIX. On the theory of the conduction of electricity through gases by charged ions, The London, Edinburgh, and Dublin Philosophical Magazine and Journal of Science 47 (286) (1899) 253–268.

[15] B. Zhdanov, J. Sell, R. Knize, Multiple laser diode array pumped Cs laser with 48W output power, Electronics Letters 44 (9) (2008) 582–583.

[16] R. Measures, Electron density and temperature elevation of a potassium seeded plasma by laser resonance pumping, Journal of Quantitative Spectroscopy and Radiative Transfer 10 (2) (1970) 107–125.

[17] A. Tam, G. Moe, W. Happer, Particle formation by resonant laser light in alkali-metal vapor, Physical Review Letters 35 (24) (1975) 1630.

[18] M. Sakuntala, Discharges in potassium seeded argon at elevated temperatures, British Journal of Applied Physics 16 (6) (1965) 821.

[19] H. Ellington, The value of the breakdown voltage in hot alkali-metal-seeded rare gases, Journal of Physics D: Applied Physics 1 (8) (1968) 1082.

[20] H. Ellington, Breakdown voltage measurements in alkali-metal-seeded rare gases at elevated temperatures and atmospheric pressure, Journal of Physics D: Applied Physics 1 (1) (1968) 49.

[21] C. Vadla, V. Horvatic, K. Niemax, Radiative transport and collisional transfer of excitation energy in cs vapors mixed with ar or he, Spectrochimica Acta Part B: Atomic Spectroscopy 58 (7) (2003) 1235–1277.

[22] S. S. Wu, Hydrocarbon-free resonance transition 795 nm rubidium laser, Ph.D. thesis, San Diego, CA (2009).

[23] R. Knize, B. Zhdanov, M. Shaffer, Photoionization in alkali lasers, Optics Express 19 (8) (2011) 7894–7902.

[24] A. H. Markosyan, M. J. Kushner, Plasma formation in diode pumped alkali lasers sustained in cs, Journal of Applied Physics 120 (19) (2016) 193105.

[25] K. Waichman, B. D. Barmashenko, S. Rosenwaks, Dependence of static K DPAL performance on addition of methane to He buffer gas: 3D CFD modeling and comparison with experimental results, JOSA B 36 (12) (2019) 3464–3470.

[26] H. J. Cambier, T. J. Madden, Implementing and constraining higher fidelity kinetics for dpal models, arXiv preprint arXiv:1902.10776 (2019).

[27] B. Q. Oliker, J. D. Haiducek, D. A. Hostutler, G. A. Pitz, W. Rudolph, T. J. Madden, Simulation of deleterious processes in a static-cell diode pumped alkali laser, in: High Energy/Average Power Lasers and Intense Beam Applications VII, Vol. 8962, International Society for Optics and Photonics, 2014, p. 89620B.

[28] B. Barmashenko, S. Rosenwaks, M. Heaven, Static diode pumped alkali lasers: model calculations of the effects of heating, ionization, high electronic excitation and chemical reactions, Optics Communications 292 (2013) 123–125.

[29] M. Endo, R. Nagaoka, H. Nagaoka, T. Nagai, F. Wani, Output power characteristics of diode-pumped cesium vapor laser, Japanese Journal of Applied Physics 54 (12) (2015) 122701.

[30] L. Ge, W. Hua, H. Wang, Z. Yang, X. Xu, Study on photoionization in a rubidium diode-pumped alkali laser gain medium with the optogalvanic method, Optics letters 38 (2) (2013) 199–201.

[31] Z. Yang, L. Zuo, W. Hua, H. Wang, X. Xu, Experimental measurement of ionization degree in diode-pumped rubidium laser gain medium, Optics letters 39 (22) (2014) 6501–6504.

[32] X. Zhao, Z. Yang, W. Hua, H. Wang, X. Xu, Ionization degree measurement in the gain medium of a hydrocarbon-free rubidium vapor laser operating in pulsed and cw modes, Optics express 25 (8) (2017) 9458–9470.

[33] G. Mie, The electric current in ionized air in a plane parallel condenser, Ann. Phys.(Leipzig) 13 (1904) 857–889.

[34] R. Seeliger, The theory of the conduction of electricity in dense gases, Ann. Phys.(Leipzig) 33 (1910) 319–380.

[35] H. Seeman, Measurement of the saturation curve in air, ionized by x-rays, Ann. Phys., Lpz 38 (1912) 781–829.

[36] J. S. Townsend, Electricity in gases, Oxford University Press, 1915.

[37] J. Thomson, G. Thomson, Conduction of electricity through gases, Vol. 1, Cambridge University Press, 1928.

[38] J. Boag, T. Wilson, The saturation curve at high ionization intensity, British Journal of Applied Physics 3 (7) (1952) 222.

[39] R. Rosen, E. George, Ion distributions in plane and cylindrical chambers, Physics in Medicine & Biology 20 (6) (1975) 990.

[40] S. P. Chabod, A perturbation method to examine the steady-state charge transport in the recombination and saturation regimes of ionization chambers, Nuclear Instruments and Methods in Physics Research Section A: Accelerators, Spectrometers, Detectors and Associated Equipment 595 (2) (2008) 419–425.

[41] M. Ridenti, P. Pascholati, J. Gonçalves, C. Bueno, On the interpretation of current–voltage curves in ionization chambers using the exact solution of the thomson problem, Nuclear Instruments and Methods in Physics Research Section A: Accelerators, Spectrometers, Detectors and Associated Equipment 795 (2015) 32–38.

[42] J. Boag, Ionization chambers, The dosimetry of ionizing radiation 2 (1987) 169–243.

[43] G. F. Knoll, Radiation detection and measurement, John Wiley & Sons Incorporated, 1989.

[44] M. Huyse, M. Facina, Y. Kudryavtsev, P. V. Duppen, ISOLDE collaboration, Intensity limitations of a gas cell for stopping, storing and guiding of radioactive ions, Nuclear Instruments and Methods in Physics Research Section B: Beam Interactions with Materials and Atoms 187 (4) (2002) 535–547.

[45] J. Boag, Space charge distortion of the electric field in a plane-parallel ionization chamber, Physics in Medicine & Biology 8 (4) (1963) 461.

[46] S. P. Chabod, Impact of space charges on the saturation curves of ionization chambers, Nuclear Instruments and Methods in Physics Research Section A: Accelerators, Spectrometers, Detectors and Associated Equipment 602 (2) (2009) 574–580.

[47] N. Esplen, M. S. Mendonca, M. Bazalova-Carter, Physics and biology of ultra-high dose-rate (FLASH) radiotherapy: A topical review, Physics in Medicine & Biology 65 (23) (2020) 23TR03.

[48] M. McManus, F. Romano, N. Lee, W. Farabolini, A. Gilardi, G. Royle, H. Palmans, A. Subiel, The challenge of ionisation chamber dosimetry in ultra-short pulsed high dose-rate very high energy electron beams, Scientific reports 10 (1) (2020) 1–11.

[49] B. Singh, B. Mehta, Relationship between nature of metal-oxide contacts and resistive switching properties of copper oxide thin film based devices, Thin Solid Films 569 (2014) 35–43.

[50] N. F. Mott, R. W. Gurney, Electronic processes in ionic crystals, Clarendon Press, 1948.

[51] V. E. Krohn Jr, Emission of negative ions from metal surfaces bombarded by positive cesium ions, Journal of applied physics 33 (12) (1962) 3523–3525.

[52] D. A. Steck, Cesium D line data, available online at `http://steck.us/alkalidata` (revision 2.2.1, 21 November 2019).

[53] G. A. Pitz, A. J. Sandoval, T. B. Tafoya, W. L. Klennert, D. A. Hostutler, Pressure broadening and shift of the rubidium D_1 transition and potassium D_2 transitions by various gases with comparison to other alkali rates, Journal of Quantitative Spectroscopy and Radiative Transfer 140 (2014) 18–29.

[54] J. Dodd, E. Enemark, A. Gallagher, Quenching of cesium resonance radiation by helium, The Journal of Chemical Physics 50 (11) (1969) 4838–4842.

[55] A. J. Wallerstein, G. P. Perram, C. A. Rice, Excitation of higher lying states in a potassium diode-pumped alkali laser, Applied Physics B 125 (8) (2019) 1–18.

[56] L. Barbier, M. Chéret, Experimental study of penning and hornbeck-molnar ionisation of rubidium atoms excited in a high s or d level ($5d \leq nl \leq 11s$), Journal of Physics B: Atomic and Molecular Physics 20 (6) (1987) 1229.

[57] O. Zatsarinny, S. Tayal, Photoionization of potassium atoms from the ground and excited states, Physical Review A 81 (4) (2010) 043423.

[58] B. Duncan, V. Sanchez-Villicana, P. Gould, H. Sadeghpour, Measurement of the Rb ($5D_{5/2}$) photoionization cross section using trapped atoms, Physical Review A 63 (4) (2001) 043411.

[59] S. Geltman, Laser-induced ionising collisions in alkali vapours, Journal of Physics B: Atomic and Molecular Physics 10 (15) (1977) 3057.

[60] L. Harris, Ionization and recombination in cesium-seeded plasmas near thermal equilibrium, Journal of Applied Physics 36 (5) (1965) 1543–1553.

[61] E. Arimondo, F. Giammanco, A. Sasso, M. Schisano, Laser ionization and time-resolved ion collection in cesium vapor, Optics communications 55 (5) (1985) 329–334.

[62] Y. Momozaki, M. S. El-Genk, Dissociative recombination coefficient for low temperature equilibrium cesium plasma, Journal of applied physics 92 (2) (2002) 690–697.

[63] R. Bergman, L. Chanin, Mass spectrometer analysis studies of cesium discharges, Journal of Applied Physics 42 (11) (1971) 4208–4215.

[64] C. Alcock, V. Itkin, M. Horrigan, Vapour pressure equations for the metallic elements: 298–2500k, Canadian Metallurgical Quarterly 23 (3) (1984) 309–313.

[65] J. C. Slater, Atomic radii in crystals, The Journal of Chemical Physics 41 (10) (1964) 3199–3204.

[66] C. E. Klots, R. Compton, Effects of dc electric fields on multiphoton ionization spectra in cesium, in: Multiphoton Processes, Springer, 1984, pp. 58–66.

[67] C. E. Klots, R. Compton, Effects of uniform dc electric fields on multiphoton ionization of cesium atoms, Physical Review A 31 (1) (1985) 525.

[68] R. R. Freeman, N. P. Economou, Electric field dependence of the photoionization cross section of rb, Physical Review A 20 (6) (1979) 2356.

[69] G. Belin, L. Holmgren, S. Svanberg, Hyperfine interaction, zeeman and stark effects for excited states in cesium, Physica Scripta 14 (1-2) (1976) 39.

[70] J. Dawson, C. Oberman, High-frequency conductivity and the emission and absorption coefficients of a fully ionized plasma, The Physics of Fluids 5 (5) (1962) 517–524.

[71] S. Pfalzner, P. Gibbon, Direct calculation of inverse-bremsstrahlung absorption in strongly coupled, nonlinearly driven laser plasmas, Physical Review E 57 (4) (1998) 4698.

[72] J. Sansonetti, Wavelengths, transition probabilities, and energy levels for the spectra of cesium (Cs I–Cs LV), Journal of Physical and Chemical Reference Data 38 (4) (2009) 761–923.

[73] Y.-t. Lee, B. H. Mahan, Photosensitized ionization of alkali-metal vapors, The Journal of Chemical Physics 42 (8) (1965) 2893–2896.

[74] W. H. Press, B. P. Flannery, S. A. Teukolsky, W. T. Vetterling, et al., Numerical recipes, Cambridge university press Cambridge, 1989.

[75] K.-C. Ng, Hypernetted chain solutions for the classical one-component plasma up to γ= 7000, The Journal of Chemical Physics 61 (7) (1974) 2680–2689.

[76] D. G. Anderson, Iterative procedures for nonlinear integral equations, Journal of the ACM (JACM) 12 (4) (1965) 547–560.

[77] H. F. Walker, P. Ni, Anderson acceleration for fixed-point iterations, SIAM Journal on Numerical Analysis 49 (4) (2011) 1715–1735.

[78] E. Gilliland, Diffusion coefficients in gaseous systems, Industrial & Engineering Chemistry 26 (6) (1934) 681–685.

[79] M. Santos, M. Kaja, A. Cortez, R. Veenhof, P. Neves, F. Santos, F. Borges, C. Conde, Experimental ion mobility measurements for the LCTPC collaboration — Ar-CF_4 mixtures, Journal of Instrumentation 13 (04) (2018) P04012.

[80] R. Bergman, L. Chanin, Afterglow studies in helium-cesium mixtures, Physical Review A 8 (2) (1973) 1076.

[81] C. Chen, M. Raether, Collision cross section of slow electrons and ions with cesium atoms, Physical Review 128 (6) (1962) 2679.

[82] E. Clementi, D. Raimondi, W. P. Reinhardt, Atomic screening constants from SCF functions. II. Atoms with 37 to 86 electrons, The Journal of chemical physics 47 (4) (1967) 1300–1307.

[83] Z. Mao, S. B. Sinnott, Separation of organic molecular mixtures in carbon nanotubes and bundles: molecular dynamics simulations, The journal of physical chemistry B 105 (29) (2001) 6916–6924.

[84] M. A. Lieberman, A. J. Lichtenberg, Principles of plasma discharges and materials processing, John Wiley & Sons, 2005.

[85] P. Windham, P. Joseph, J. Weinman, Negative helium ions, Physical Review 109 (4) (1958) 1193.

[86] J. De Urquijo, C. Arriaga, C. Cisneros, I. Alvarez, A time-resolved study of ionization, electron attachment and positive-ion drift in methane, Journal of Physics D: Applied Physics 32 (1) (1999) 41.

[87] G. Gousset, B. Sayer, J. Berlande, Electron-cs+-ion recombination in the presence of neutral helium atoms, Physical Review A 16 (3) (1977) 1070.

[88] W. L. Morgan, Molecular-dynamics simulation of electron-ion recombination in a nonequilibrium, weakly ionized plasma, Physical Review A 30 (2) (1984) 979.

[89] B. Sayer, J. Jeannet, J. Lozingot, J. Berlande, Collisional and radiative processes in a cesium afterglow, Physical Review A 8 (6) (1973) 3012.

[90] L. Pitaevskii, Recombination of electrons in a monoatomic gas, Zhur. Eksptl'. i Teoret. Fiz. 42 (1962).

[91] G. A. Pitz, G. P. Perram, Pressure broadening of the d1 and d2 lines in diode pumped alkali lasers, in: High-power laser ablation VII, Vol. 7005, International Society for Optics and Photonics, 2008, p. 700526.

[92] R. Rafac, C. Tanner, A. Livingston, K. Kukla, H. Berry, C. Kurtz, Precision lifetime measurements of the 6 p 2 p 1/2, 3/2 states in atomic cesium, Physical Review A 50 (3) (1994) R1976.

[93] K. C. Brown, G. P. Perram, Spin-orbit relaxation and quenching of cesium 7 2 p in mixtures of helium, methane, and ethane, Physical Review A 85 (2) (2012) 022713.

[94] M. Safronova, C. W. Clark, Inconsistencies between lifetime and polarizability measurements in cs, Physical Review A 69 (4) (2004) 040501.

[95] D. DiBerardino, C. Tanner, A. Sieradzan, Lifetime measurements of cesium 5 d 2 d 5/2, 3/2 and 11 s 2 s 1/2 states using pulsed-laser excitation, Physical Review A 57 (6) (1998) 4204.

[96] O. Heavens, Radiative transition probabilities of the lower excited states of the alkali metals, JOSA 51 (10) (1961) 1058–1061.

[97] A. Vasilyev, I. Savukov, M. Safronova, H. Berry, Measurement of the 6 s- 7 p transition probabilities in atomic cesium and a revised value for the weak charge q w, Physical Review A 66 (2) (2002) 020101.

[98] E. Walentynowicz, R. Phaneuf, W. Baylis, L. Krause, Inelastic collisions between excited alkali atoms and molecules IX. an isotope effect in the cross sections for $6^2P_{1/2} \leftrightarrow 6^2P_{3/2}$ mixing in cesium, induced in collisions with deuterated methanes, Canadian Journal of Physics 52 (7) (1974) 584–588.

[99] Z. Jabbour, R. Namiotka, J. Huennekens, M. Allegrini, S. Milošević, F. De Tomasi, Energy-pooling collisions in cesium: 6 p j+ 6 p j→ 6s+ (nl= 7p, 6d, 8s, 4f), Physical Review A 54 (2) (1996) 1372.

[100] T. Yabuzaki, A. Tam, M. Hou, W. Happer, S. Curry, Preferential excitation transfer in cs*(6d32)-cs (6s12) collisions, Optics Communications 24 (3) (1978) 305–310.

[101] C. Vadla, Energy pooling in caesium vapour, The European Physical Journal D-Atomic, Molecular, Optical and Plasma Physics 1 (3) (1998) 259–264.